The application of wavefront sensing methods to optical surface metrology

Bharath Reddy Adapa

To cite this version:

Bharath Reddy Adapa. The application of wavefront sensing methods to optical surface metrology. Instrumentation and Detectors [physics.ins-det]. Université Grenoble Alpes [2020-..], 2020. English. NNT : 2020GRALY032 . tel-03144377

HAL Id: tel-03144377
https://theses.hal.science/tel-03144377

Submitted on 17 Feb 2021

Université
Grenoble Alpes

THÈSE

Pour obtenir le grade de

DOCTEUR DE L'UNIVERSITE GRENOBLE ALPES

Spécialité : **PHYSIQUE APPLIQUEE**

Arrêté ministériel : 25 mai 2016

Présentée par

Bharath Reddy ADAPA

Thèse dirigée par **Nicholas BROOKES**
et Co-encadrement par **Raymond BARRETT,** European Synchrotron Radiation Facility
et Co-encadrement par **Guillaume DOVILLAIRE,** Imagine Optic

préparée au sein du **Laboratoire European Synchrotron Radiation Facility**
dans **l'École Doctorale Physique**

L'analyse de front d'onde appliquée à la métrologie de surface optique

The application of wavefront sensing methods to optical surface metrology

Thèse soutenue publiquement le **19 octobre 2020**,
devant le jury composé de :

Monsieur Josep NICOLÁS
DOCTEUR EN SCIENCES, ALBA SYNCHROTRON - ESPAGNE, Rapporteur
Monsieur François POLACK
INGENIEUR HDR, SYNCHROTRON SOLEIL - GIF-SUR-YVETTE, Rapporteur
Monsieur Philippe ZEITOUN
DIRECTEUR DE RECHERCHE, CNRS ILE-DEFRANCE GIF-SURYVETTE, Examinateur
Monsieur Jean-Louis HAZEMANN
DIRECTEUR DE RECHERCHE, CNRS DELEGATION ALPES, Président

Declaration

This dissertation is the result of my own work and includes nothing, which is the outcome of work done in collaboration except where specifically indicated in the text. It has not been previously submitted, in part or whole, to any university of institution for any degree, diploma, or other qualification.

Signed:_______ADAPA Bharath Reddy_______________________

Date:_________18/01/2021________________________________

Bharath Reddy ADAPA,

PhD student, ESRF / Imagine Optic,

Grenoble

ABSTRACT

Synchrotrons are quite a recent development in the history of science but have seen tremendous improvements since their inception in middle of 20th century. Synchrotrons provide X-rays with very high brilliance generally many orders of magnitude larger than X-ray tube sources and thus require very high quality optics for their operations. X-ray mirrors of different sizes (10 mm – 1500 mm lengths) and different shapes (flat, spherical, elliptical, toroidal…) are some of the most commonly used optics at the synchrotron facilities. The mirrors should be highly polished with surface figure errors often <1 nm rms to maintain the beam quality and require sophisticated metrology instruments for both mirror manufacturing and quality control. Synchrotron mirror metrology instrumentation has evolved in parallel to the increasing quality demands and the most commonly currently used instruments for such applications are Long Trace Profilers (LTP), Nanometer Optical Component Measuring Machines (NOM), Fizeau interferometers, and Micro interferometers. The Stitching Shack-Hartmann wavefront sensor (SHARPeR) is a relatively new addition to the synchrotron mirror metrology instruments. It is a 2D slope measuring instrument developed by Imagine Optic and Q-Sys and is available as a complete commercial product. SHARPeR uses subaperture stitching algorithms to measure synchrotron mirrors which are typically larger than most of the optical metrology instrument apertures.

The initial SHARPeR instrument presented problems for the accurate measurement of long and/or highly curved mirrors and my PhD focused primarily on improving the performance of the system. The SHARPeR instrument installed at the ESRF has been validated using other ESRF instruments such as LTP, Fizeau and Micro- interferometers for performance qualification and for insights into the types of errors displayed by SHARPeR. Different types of systematic and random errors have been studied which include errors from CCD detector (of the wavefront sensor), SHARPeR head optical aberrations, translation errors and environmental errors. Instrument errors such as retrace errors are shown to be a significant limit to the accuracy of measurements of highly curved mirrors by SHARPeR. New measurement techniques have been developed which showed significant improvement in the accuracy of slope errors and figure errors for such mirrors. The SHARPeR instrument has also been calibrated for retrace errors with mirror tilt using a standard Michelson interferometer and improved calibration methods have

allowed improvements in measured shape parameters such as radius of curvature. Environmental effects during measurements such as thermal fluctuations and air turbulences were shown to be major influence in degrading the accuracy of measurements of long mirrors. Instrument design has been improved in many iterations to insulate the optical path and to avoid heat sources near the measurement path. Measurement speed has been improved using ‘on the fly’ scanning method which also reduces long term drift influences from the environment.

SHARPeR uses a proprietary stitching software StitchWave provided by Imagine Optic. As an alternative offering more flexibility, a new open source stitching software (PyLOSt) has been developed to stitch measurements from various instruments including SHARPeR. Different stitching algorithms have been developed to stitch 2D slope and height data scanned along one axis (1D), such as Progressive Stitching (PROG), Matrix overlap error (MO) and global optimization (GO). Algorithms to extract reference errors within the stitching process have also been implemented. The performance of stitching algorithms has been tested using synthetic SHARPeR and Fizeau datasets and has provided satisfying results. PyLOSt has been used for most of the SHARPeR measurements presented in this thesis manuscript.

RESUME

Le développement des synchrotrons est relativement récent dans l'histoire de la science, cependant ces instruments ont connu d'importantes améliorations depuis leur création au milieu du 20e siècle. Les synchrotrons fournissent des rayons X avec une brillance très élevée généralement supérieure de plusieurs ordres de grandeurs comparée aux sources de rayons X à tube et nécessitent donc des optiques de très haute qualité pour leur opération. Les miroirs à rayons X couramment utilisés dans les installations synchrotron offrent une grande diversité de tailles (longueurs de 10 mm à 1500 mm) et de formes (plans, sphériques, elliptiques, toroïdales…). Leur surface optique doit répondre à des critères de polissage de très haute qualité avec des erreurs de forme souvent <1 nm afin de conserver la qualité du faisceau ce qui implique des instruments de métrologie de pointe pour assurer leur fabrication et garantir le contrôle qualité. L'instrumentation pour la métrologie des miroirs synchrotrons a évolué pour répondre aux exigences de qualité croissante et les instruments les plus couramment utilisés pour ces applications sont les profilomètres optiques tels que le LTP (Long Trace Profiler) ou le NOM (Nanometer Optical Component Measuring Machines), des interféromètres de type Fizeau ou encore des micro-interféromètres. Le capteur de front d'onde nommé SHARPeR (Stitching Shack-Hartmann wavefront sensor) est venu s'ajouter récemment à cette liste. Il s'agit d'un instrument de mesure de pentes 2D développé par Imagine Optic et Q-Sys, disponible en tant que produit commercial complet. Le SHARPeR utilise des algorithmes de recollement de sous-pupilles pour mesurer des miroirs synchrotrons dont la longueur excède l'ouverture de la plupart des instruments de métrologie optique.

L'instrument SHARPeR ayant révélé des problèmes de précision lors de la mesure de miroirs longs et/ou fortement courbés, ma thèse s'est donc principalement orientée sur l'amélioration des performances du système installé à l'ESRF. Ces dernières ont été évaluées à l'aide des autres instruments du laboratoire de métrologie de l'ESRF tels que le LTP, l'interféromètre de Fizeau et le micro-interféromètre, permettant également d'avoir un aperçu des types d'erreurs engendrées par la mesure SHARPeR. Différents types d'erreurs systématiques et aléatoires ont été étudiés, notamment les erreurs du capteur de front d'onde (détecteur CCD), les aberrations optiques de la tête optique du

SHARPeR, les erreurs de translation et les erreurs environnementales. Les erreurs de retour de faisceau (connues sous le terme « retrace error » en anglais) se révèlent être une limite à la précision des mesures de miroirs fortement courbés avec le SHARPeR. Les nouvelles techniques de mesure développées ont montré une amélioration significative de la précision des erreurs de pente et des erreurs de forme pour ce type de miroir. Une calibration des erreurs de retour de faisceau réalisée en mesurant simultanément l’inclinaison d’un miroir avec le SHARPeR et avec un interféromètre Michelson standard mais aussi d’autres méthodes d'étalonnage ont permis d'améliorer la précision des paramètres de forme mesurés tels que le rayon de courbure. Il a été démontré que la précision de l’instrument lors des mesures de longs miroirs est sérieusement dégradée par les instabilités environnementales telles que les gradients thermiques ou les turbulences de l’air. La conception de l’instrument a été notablement améliorée par itérations successives visant à réduire les perturbations induites par les sources de chaleur locales dans le chemin optique ou à proximité. L’augmentation de la vitesse de mesure en utilisant une méthode de mesure à la volée à également contribué à la réduction de l’influence des dérives long terme.

SHARPeR utilise un logiciel propriétaire, StitchWave, fourni par Imagine Optic pour le recollement des sous-pupilles. Un nouveau logiciel de type open source (PyLOSt) offrant plus de flexibilité a été développé pour la reconstruction de mesures issues de divers instruments incluant le SHARPeR. Différents algorithmes sont proposés permettant de travailler à partir de données 2D de pente ou de hauteur obtenues le long d’un axe de mesure (1D) tels que le recollement progressif (PROG), la matrice des erreurs dans la zone de recouvrement (MO) ou l’optimisation globale (GO). Des algorithmes spécifiques permettant d’extraire les erreurs de la référence à partir des données ont également été implémentés. Les performances de ces différents algorithmes évaluées à partir d’un jeu de données simulées pour chacun des instruments SHARPeR et Fizeau, ont donné des résultats satisfaisants. PyLOSt a été utilisé pour traiter la plupart des mesures SHARPeR présentées dans ce manuscrit de thèse.

SOMMAIRE

Chapitre 1 - Introduction:

Les synchrotrons sont de grands instruments scientifiques conçus pour générer un rayonnement électromagnétique hautement intense et cohérent principalement dans le domaine des rayons X. Parmi les divers composants optiques qui permettent de guider, focaliser ou conditionner le faisceau de rayons X, les miroirs sont fréquemment utilisés. Ces miroirs doivent répondre à des spécifications très pointues définissant leur état de surface en termes de forme et de rugosité, ce qui implique des instruments de métrologie de très haute précision. Ces instruments doivent donc permettre de contrôler la forme (i.e. le rayon de courbure), mais aussi les défauts de polissage qui se répartissent en deux catégories les erreurs de pente ou de hauteur à basses fréquences et la microrugosité pour les hautes fréquences. Les instruments couramment utilisés pour la métrologie de ces miroirs sont les profilomètres optiques tels que le LTP (Long Trace Profiler) ou le NOM (Nanometer Optical Component Measuring Machines), des interféromètres de type Fizeau ou encore des micro-interféromètres. La technique de recollement de sous-pupilles pour mesurer des miroirs synchrotrons dont la longueur excède souvent l'ouverture de la plupart des instruments de métrologie optique est couramment utilisée. Les profilomètres cités précédemment ne fournissent qu'un profil le long de la ligne mesurée sur le miroir (1D). Les instruments capables de donner une image 2D, principalement des interféromètres, nécessitent la plupart de temps le développement et l'implémentation des outils permettant l'acquisition des sous-pupilles. Un instrument basé sur la technologie de détection de front d'onde, nommé SHARPeR (Stitching Shack-Hartmann wavefront sensor), a été développé pour offrir une alternative de mesure 2D des miroirs rayons X et concurrencer les instruments existants.

Chapitre 2 – L'instrument SHARPeR:

Le SHARPeR est un instrument conçu par Imagine Optic et Q-Sys qui mesure les pentes des miroirs rayons X en 2D en combinant la technique de recollement de sous-pupilles à celle de détection de front d'onde Shack-Hartmann. Les prototypes de SHARPeR développés en collaboration avec les synchrotrons SOLEIL et BNL, ont donné lieu par la suite au développement d’un instrument commercial dans le cadre d’un projet faisant partie du programme Eurostars. Cet instrument est actuellement installé au Synchrotron européen (ESRF). Le SHARPeR est disponible en tant que produit commercial complet avec logiciel de recollement de sous-pupilles StitchWave inclus. Il présente certains avantages par rapport à d’autres instruments tels que (1) la fourniture d’une cartographie de surface 2D, (2) une configuration optique simple sans pièces mobiles, et (3) pas de problème inhérent à l interférométrie tel que le phénomène de persistance des franges (communément appelé « fringe-print-through » en anglais).

La tête optique du SHARPeR se déplace au-dessus du miroir à mesurer et acquière tout le long les données des sous-pupilles qui se chevauchent. L’ensemble des données ainsi collectées est ensuite traité par le logiciel StitchWave pour reconstruire, telle une image panoramique, la totalité de la surface mesurée. Un nouveau logiciel (PySHARPeR), développé en langage Python, permet d’aligner automatiquement le miroir par rapport à l’axe de déplacement de la tête de mesure mais aussi de mettre en œuvre des mesures plus complexes. L’acquisition peut se faire en mode pas à pas avec arrêt du déplacement de la tête à chaque position ou en mode à la volée avec déplacement continu à vitesse constante. Une mesure dite de référence obtenue avec un miroir très plan est soustraite à chacune des sous-pupilles dans le but de corriger les erreurs systématiques résultant des aberrations optiques et désalignement de l’instrument. La résolution spatiale du SHARPeR dépend de la taille de la microlentille du capteur de front d'onde (~ 1,2 mm), et la présente étude a démontré que pour obtenir cette résolution spatiale le pas d’échantillonnage des sous-pupilles doit être inférieur ou égal à la moitié de la taille d’une microlentille. Cependant pour des raisons de simplification du code permettant la reconstruction de la surface dans le logiciel StitchWave, le pas d’échantillonnage est resté fixé à la taille d’une microlentille.

Diverses sources d’erreurs systématiques et aléatoires peuvent entacher les résultats de mesures SHARPeR. Le capteur de front d’onde inclut un détecteur CCD qui est source d’erreurs comme le bruit de photon, le bruit de lecture ou encore les erreurs d’échantillonnage, mais celles-ci ne limitent pas les performances de l’instrument. Une ou plusieurs sous-pupilles à mesurer peuvent être hors du plan focal à cause d’un mauvais alignement du miroir ou de sa courbure intrinsèque. La contribution des erreurs engendrées par une défocalisation reste théoriquement minime dans la mesure des pentes ou des rayons de courbure. La principale source d’erreur mise en évidence concerne le capteur de front d’onde et les divers composants optiques de la tête de mesure SHARPeR pour des raisons d’aberrations optiques ou d’alignement. Les aberrations optiques du détecteur de front d’onde sont habituellement caractérisées avant sa mise en place dans la tête de mesure de façon à les prendre en compte pour corriger les pentes pendant la mesure. Les erreurs systématiques dues aux autres composants optiques sont minimisées grâce à l’acquisition, préalable à toute mesure de miroir, d’une mesure dite de référence faite avec un miroir très plan en incidence normale. Cependant cette méthode ne permet pas de de s’affranchir des erreurs de retour de faisceau (‘retrace error’ en anglais) générées lorsque le miroir n’est pas en incidence normale ou lorsque sa courbure est importante, dans ce cas le faisceau réfléchi s’éloigne fortement du chemin optique initial rendant la mesure de référence initiale obsolète. Deux nouvelles techniques de mesure nommées « incidence normale » et « multi-incidences » ont été développées afin de corriger les erreurs de retour de faisceau. La première méthode qui consiste à mesurer chaque sous-pupille en incidence normale, et la deuxième qui mesure chaque sous–pupille sous différentes inclinaisons, fournissent un grand nombre de données redondantes qui seront utilisées pour corriger les erreurs de retour de faisceau. La translation qui assure le déplacement de la tête de mesure est aussi sujette à engendrer des erreurs dues au lacet, roulis, tangage. Ces erreurs sont corrigées dans une large mesure grâce à la redondance des données dans les zones de recouvrement des sous-pupilles. Enfin les turbulences de l’air, les gradients thermiques, les variations de température constituent des sources d’erreurs pseudo-aléatoires très importantes. La conception du SHARPeR a été progressivement modifiée afin de réduire significativement l’impact de l’environnement sur la mesure.

Chapitre 3 – Algorithmes de recollement de données:

La technique de recollement de sous-pupilles pour mesurer un miroir dont la longueur excède l’ouverture de l’instrument est couramment utilisée dans le domaine de la métrologie des miroirs rayons X. Les logiciels des instruments commerciaux dotés de cette capacité de mesure permettent en général de reconstruire la surface à partir des données collectées, cependant l’algorithme utilisé n’est pas accessible et reste donc inconnu. C’est le cas pour StitchWave, logiciel du SHARPeR, MetroPro & MX logiciels permettant de piloter de nombreux instruments Zygo tels que les interféromètres de Fizeau et les micro-interféromètres, ou encore Vision64 logiciel utilisé par les instruments

Bruker comme les micro-interféromètres. De nouveaux algorithmes pour effectuer le recollement des données ont donc été développés sur la base de codes déjà existants utilisés dans d'autres synchrotrons tels que (a) le recollement progressif (PROG), (b) la matrice des erreurs dans la zone de recouvrement (MO) ou (c) l'optimisation globale (GO). Ils ont été intégrés dans un logiciel de type open source (PyLOSt) développé dans le cadre d'une collaboration pour un projet européen MooNpics (Metrology on One-Nanometer-Precise Optics). Ces algorithmes permettent de traiter des données de pente ou de hauteur, issues de différents instruments. L'étude de leur performance à partir du traitement de données simulées est présentée dans ce mémoire.

Chapitre 4 – Résultats obtenus avec le SHARPeR:

Différents miroirs synchrotrons ont été mesurés avec l'instrument SHARPeR dans différentes conditions, et l'ensemble des résultats obtenus est présenté dans ce manuscrit. Ces mesures ont permis d'appréhender les performances et les limites du SHARPeR. Le bruit statistique de l'instrument a été analysé à l'aide d'images prises sans aucun mouvement de la tête de mesure pendant plusieurs heures (~ 35 heures). Moyenner de nombreuses images sur de courtes périodes (<15 heures) permet de réduire le bruit en raison de sa nature aléatoire (fluctuations de l'environnement), en revanche sur des périodes plus longues (> 25 heures) il augmente, dominé par une dérive long terme. Le bruit dynamique de l'instrument a été évalué en mesurant un miroir fixé sur la tête optique pendant son déplacement aller/retour sur toute la course de la translation. Ces mesures de bruit dynamique ont permis de travailler activement sur l'isolation du chemin optique et de le réduire d'un facteur 10 (de 1,4 à 0,15 µrad sur les erreurs de pente tangentielle). Dans ces nouvelles conditions, la mesure avec le SHARPeR d'un petit miroir plan (100mm de long) avec des erreurs de pente < 50 nrad rms a donné des résultats en bon accord comparé aux deux instruments de l'ESRF, le LTP et l'interféromètre de Fizeau Zygo, et ce avec une répétabilité <10 nrad rms. Par contre les résultats obtenus sur un long miroir plan (950mm) ont montré des écarts significatifs dans les erreurs de pente, en particulier dans les basses fréquences spatiales, résultant probablement de fluctuations environnementales pseudo-aléatoires sur de longues distances de translation. Des modifications de conception de la tête optique consistant à éloigner le détecteur de front d'onde (CCD) de l'environnement de mesure ont permis d'améliorer considérablement les mesures de ces longs miroirs. Les mesures de miroirs courbés ont également montré des différences sur les profils d’erreurs de pente dans le domaine des basses fréquences par rapport aux autres instruments, probablement dues dans ce cas à d’autres sources d’erreurs comme les erreurs de retour de faisceau. Pour les miroirs sphériques, la nouvelle technique de mesure basée sur l'incidence normale a permis d’améliorer la précision des mesures d’erreur de pente et cela a été conforté par la comparaison avec les autres instruments des résultats pour deux miroirs l’un avec une forte courbure (rayon ~ 10 m) et l’autre plus modérée (~ 120 m). Enfin la mesure par la méthode dite « incidence normale » d’un miroir elliptique avec une courbure moyenne importante (rayon ~ 13 m) a donné des résultats d’erreur de pente présentant des écarts dans le domaine des basses fréquences par rapport aux autres instruments probablement parce que les erreurs de retour de faisceau à chaque sous-pupille évoluent avec la courbure du miroir. En revanche la technique multi-incidence a permis d’obtenir un résultat en bon accord avec le LTP.

La plupart des mesures présentées dans ce document ont été faites dans un mode d’acquisition à la volée avec un déplacement de la tête optique à vitesse constante car ce mode s’est avéré plus performant que le mode pas à pas. Cela a été démontré par les résultats obtenus sur la mesure d’un miroir long pour lequel on a observé une réduction des erreurs de pente basse fréquence dans ce mode, qui présente par ailleurs l’avantage de réduire le temps de mesure. Ce mémoire décrit également la technique de calibration par mesure angulaire simultanée avec le SHARPeR et un interféromètre standard d’un miroir plan pour différentes inclinaisons. Malgré son échantillonnage grossier (pas de ~ 18 µrad) cette calibration réalisée sur une large de plage angulaire (~ 18 mrad), a permis d’améliorer les résultats des mesures de rayon de courbure pour des miroirs très courbés et de converger vers les valeurs fournies par les autres instruments (les méthodes incidence normale et multi-incidences n’ont pas amélioré les valeurs de rayon de courbure). Une calibration plus fine pourrait éventuellement remplacer les méthodes incidence normale et multi-incidence dont l’objectif est de corriger les erreurs de retour de faisceau.

ACKNOWLEDGEMENTS

Thank you to Raymond BARRETT (ESRF) and Guillaume DOVILLAIRE (Imagine Optic) for the continuous supervision of the thesis.

Thank you to Amparo VIVO and Francois PERRIN from ESRF for their help during every step of the thesis. Thank you to Rafael MAYER, Jerome LEGRAND and Pauline TREIMANY from Imagine Optic for their regular support.

Thank you to Mourad IDIR (BNL), Lei HUANG (BNL), Francois POLACK (SOLEIL), Josep NICOLAS (ALBA) and Simon ALCOCK (DLS) for the scientific discussions and help during my thesis. Thank you to Hans-Peter VAN DER KLEIJ (ESRF) for the help during instrument calibration. Thank you to Norman NIEWRZELLA, Sascha GENTNER and Holger LASSER from Carl Zeiss SMT for collaboration during my thesis.

Thank you to Manuel SANCHEZ DEL RIO and Nicholas BROOKES for their help as directors of thesis. Thank you also to Michael KRISCH and Kurt KUMMER for the advices as part of thesis follow up committee.

We would like to thank the funding provided by Eurostars programme (project number E!8304) for the SHARPeR project.

CONTENTS

LIST OF ABBREVIATIONS AND ACRONYMS

ESRF : European Synchrotron Radiation Facility	1
E-XFEL : European X-ray Free Electron Laser facility	135
FEL : Free Electron Laser	6
FWHM : Full Width Half Maximum	25
HASO : Imagine Optic wavefront sensor model	22
KB : Kirkpatrick-Baez	7
LTP : Long Trace Profiler	12
MI : Micro Interferometer	16
MooNpics : Metrology On One-Nanometer-Precise Optics	98
mrad : milliradians	5
MSI : Micro Stitching Interferometer	18
NOM : Nanometer Optical Component Measuring Machines	13
nrad : nanoradians	11
PSD : Power Spectral Density	9
PSF : Point Spread Function	48
PSI : Phase Shifting Interferometry	16
PV : Peak to Valley	9
PyLOSt : Python Large Optic Stitching	98
QWP : Quarter Wave Plate	22
RTT : Rotary, Tip & Tilt platform	23
SR : Synchrotron Radiation	6
SSHOH : Stitching Shack-Hartmann optical head	23
std : Standard deviation	57
WLI : White Light Interferometry	16

LIST OF APPENDICES

1 INTRODUCTION

Synchrotron radiation is electromagnetic radiation produced by accelerating charged particles moving at relativistic speeds. Experimental synchrotron facilities appeared in the middle of 20th century [1]. Synchrotron radiation was initially observed as unwarranted loss in the particle accelerator facilities, and later parasitically operated in first generation synchrotrons along with particle accelerator operations. In the second generation, storage ring facilities dedicated to the production of synchrotron light were constructed. Recognition of the opportunities for high brilliance [2] (the flux per unit area of the radiation source per unit solid angle of the radiation cone per unit spectral bandwidth) sources led to the development of third generation facilities with storage rings optimized to accommodate insertion devices (undulators [3], [4] or wigglers [4]). The first operational third-generation facility was the European Synchrotron Radiation Facility (ESRF) in Grenoble [5]. The ESRF is shown in Figure 1.1.

Synchrotron radiation was initially observed near visible frequencies, but most of the current synchrotrons operate in the UV to X-ray regime where they satisfy the large demand for short wavelength radiation. Synchrotrons have many advantages over traditional X-ray sources with brilliance several orders of magnitude larger than traditional X-ray tubes, as shown in Figure 1.2.

Figure 1.1 : The European Synchrotron Radiation Facility (ESRF) in Grenoble.

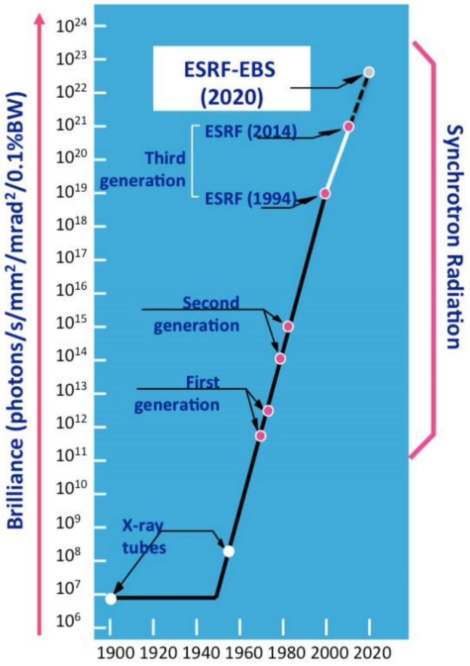

Figure 1.2 : Brilliance of ESRF compared to traditional X-ray sources [5].

Depending upon the experimental technique to be applied, the synchrotron radiation is collimated, focused, spectrally filtered, limited to an aperture size or manipulated in various other ways using different optical elements, before arriving at the samples. The ESRF beamlines deliver radiation in the soft to hard X-ray energy regime (predominantly from 300 eV to 100 keV) [6]. Some of the most common reflective / refractive / diffractive optical elements used for conditioning the X-rays are presented in section 1.1. My thesis deals with quality characterization of X-ray mirror surface topography, which is presented in section 1.2. An instrument known as SHARPeR based on stitching Shack-Hartmann wavefront sensing has been widely used during my thesis for characterization of various X-ray mirrors. This instrument is presented along with complementary instruments in sections 1.4 to 2.1.

1.1 X-ray optics for synchrotrons

X-ray optics are used to transform the beam shape / wavelength / divergence / polarization of the X-ray source in order to deliver X-rays with the specific characteristics required for an experiment. Different X-ray optics include (1) slits / pinholes, (2) filters / windows, (3) mirrors, (4) beam splitters, (5) monochromators, (6) phase plates, (7) refractive lenses, Fresnel lenses (zone plates) [7] etc. Whilst these optics have analogues in the visible light domain, due to the short wavelengths of X-rays, their appearance and sometimes operating principles may be quite different. A particularity of X-rays is that their refractive index in most materials is very close to 1 compared with typical values in the range 1.4 – 3 for visible light.

The refractive index of X-rays, n, is often expressed as a complex quantity:

$$n = 1 - \delta - i\beta$$

(1-1)

Where δ and β are known as the optical constants, δ and β are material and energy dependent as shown in Figure 1.3 [8]. The real term, δ describes the phase shift experienced by X-rays as they pass through the material whilst β describes the absorption of the X-rays.

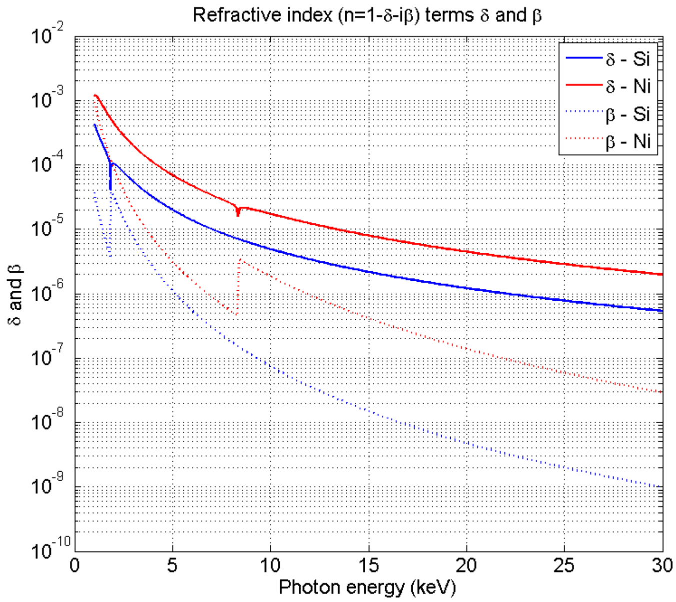

Figure 1.3 : Optical constants δ and β in the refractive index ($n = 1 - \delta - i\beta$) plotted as a function of photon energy for two materials (Si and Ni).

1.1.1 Mirrors & multilayers

Refractive index slightly less than unity means that when X-rays in vacuum (or air) impinge upon a surface they are weakly refracted or totally externally reflected [4], as shown in Figure 1.4.

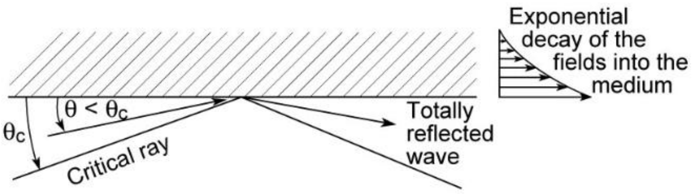

Figure 1.4 : Total external reflection of X-rays in vacuum or air [4].

Total external reflection occurs at grazing angles below a critical angle θ_c, which can be shown by Snell's law to approximate to $\theta_c \approx \sqrt{2\delta}$ [4]. By analogy, for a given grazing angle one can identify a critical energy E_c, below which X-rays are totally externally reflected. For most materials in the X-ray regime θ_c is of the order of milliradians and is approximately proportional to the square root of the material density and inversely proportional to photon energy as shown below [9].

$$\theta_{c_{[mrad]}} E_{c_{[keV]}} = 19.83\sqrt{\rho_{[g/cm^3]}} \tag{1-2}$$

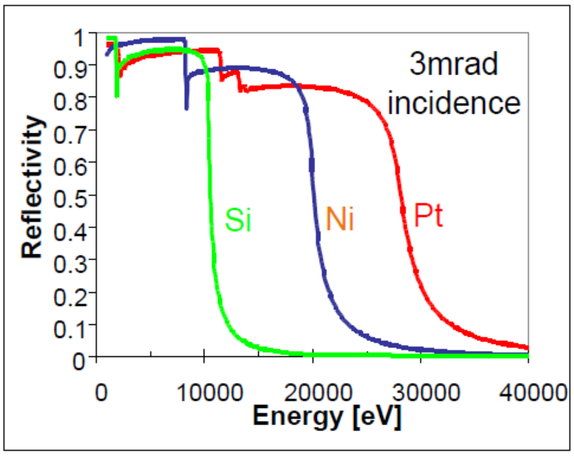

Figure 1.5 : Reflectivity of X-ray mirrors as a function of photon energy for different materials (Si, Ni, and Pt) at incidence angle of 3 mrad [8].

The calculated mirror reflectivity for different substrates (Silicon, Nickel and Platinum) at 3 mrad incidence angle for different photon energies (using XPOWER of XOP package [10]), is shown in Figure 1.5. At these small grazing incidence angles the mirrors have to be long tangentially to accept the full beam for reflection. Consequently, most X-ray mirrors have rectangular apertures and can be longer than 1m. The mirrors also need to be highly polished to preserve the beam emittance (size x divergence). The mirrors also face other constraints such as very high mechanical, thermal and vibration stabilities and need to have low gravitational sag and the ability to withstand ultra-high vacuum. Due to their favorable properties for these aspects Silicon mirrors are the most commonly used mirrors in synchrotron applications. Silicon can be coated with, for example, a high-density metal film, (like Platinum, Nickel …), which, provided the film is sufficiently thick (i.e. a few 10’s of nm), allow the mirror reflectivity below the critical angle to mimic that of a bulk mirror of the same film material. This approach can increase the critical angle consequently the incidence angles. The critical angle is also inversely proportional to the energy (spectral frequency) of the beam, consequently at a given incidence angle, the mirror acts as low pass spectral filter. The detailed reflection properties of an X-ray mirror are described by the Fresnel equations e.g.[11].

To overcome the small critical angles which are restrictive in some applications, the mirrors may be coated with multilayers [12](usually a periodic layer structure comprising of alternating low Z and high Z coatings), which can offer high reflectivity at very high energies which is usually not possible with traditional mirrors. Such multilayers can be considered as one-dimensionally periodic crystals which can reflect at Bragg angles much larger than critical angles of traditional mirrors, but much smaller than traditional crystals. Like traditional crystals the multilayers pass energy as a band pass, with central energy defined by Bragg law, although at wider bandwidth than crystals. The requirements for mirrors which will be used for multilayer coated optics are very similar to those for single layer coated mirrors and usually the techniques applied for the characterization of their surface topography are identical. The larger incidence angles lead to smaller optical sizes, and consequently crystals are typically smaller than multilayers, which in turn are smaller than mirrors. Another function that mirrors also perform are power filtering, which is much more efficient with mirror due to low incidence angles leading to low power density (per unit area). The unreflected power is absorbed and subsequently transferred out using cooling.

Other optical elements such as refractive lenses [13], crystals, diffractive lenses and capillary optics [7], [14] are also widely used by synchrotron beamlines, however for the purposes of my work only X-ray mirrors are explored here. Similar reflective optics are used in X-ray free-electron laser sources (FELs). For the state-of-the-art SR and FEL sources the required optical qualities are comparable.

The mirror designs strongly depend on various factors such as thermal load optimization [15], types of application etc. For focusing applications curved mirrors such as spherical, elliptical, toroidal shapes are used. A single spherical mirror is usually insufficient for imaging as it generates significant aberrations particularly astigmatism in beam focusing [7]. Ellipsoidal mirrors produce the best point to point imaging but they are often difficult to manufacture [16]. Toroidal mirrors [17] are sometimes used as an approximation to ellipsoids. Often two or more mirrors combination is used to minimize the aberrations such as Kirkpatrick-Baez (KB) mirrors [18] and Wolter optics [19]. In KB optics the X-rays are successively reflected from two perpendicular cylindrical surfaces whereas in Wolter optics two successive conical surfaces are used for reflection [7]. Some of the optical systems utilize mechanical bending of flat mirrors into desired shapes like cylindrical or elliptical surface [20], and active optics which can generate freeform shapes of mirror using multiple actuators [21] is an active area of research.

1.2 Introduction to surface metrology for synchrotron mirrors

Surface metrology is a critical step to evaluate the quality of synchrotron mirrors before installation. A wide range of instruments can be used for surface metrology, traditionally stylus based profilometers were used and over time new instruments based on microscopy and optical techniques were developed. After Bennet [22], the first modern profiling instrument was the Abbott profilometer, reported in 1933. It used a stylus tracing over the surface and a transducer converting the vertical motion into an electric signal. Such instruments have been continuously developed and have been used for surface metrology of X-ray mirrors during the manufacturing process [23]. Scanning probe microscopies such as Scanning Tunneling Microscopy (STM) [24] and Atomic Force Microscopy (AFM) [25], can measure surface roughness at the atomic scale (>0.1 nm) at very small lateral resolutions (< 100 nm) [26] over small field sizes (typically < 1x1 μm^2 for STM and < 200 x200 μm^2 for AFM). The AFM and mechanical stylus-based profilers are contact based, and can cause damage to the measurement surfaces. Due to the fragility of optical surfaces, non-contact optical profilers are preferred but due to their high spatial resolution, AFM measurements are commonly used for the characterization of groove profiles in X-ray diffraction gratings [27]. Despite their significantly larger aperture size, even for optical profilers the field of view can be a limitation. Synchrotron mirrors can have lengths in excess of 1m, due to the grazing incidence requirement for reflecting the X-ray beam. Most optical profilers have aperture sizes which are smaller than the typical dimensions of the optical surfaces of synchrotron mirrors. Mirror surfaces are characterized based on various parameters, which are presented in the following, and in some cases, different metrology instruments are needed to measure different parameters.

1.2.1 Definitions of measurement parameters

Synchrotron mirrors can have different surface shapes or ‘figure’ depending on the application; commonly used figures are plane, spherical, elliptical, ellipsoidal, parabolic, and toroidal [11]. The surface metrology aims to characterize deviations of shape from the specified ideal shape as shown for a toroidal mirror in Figure 1.6.

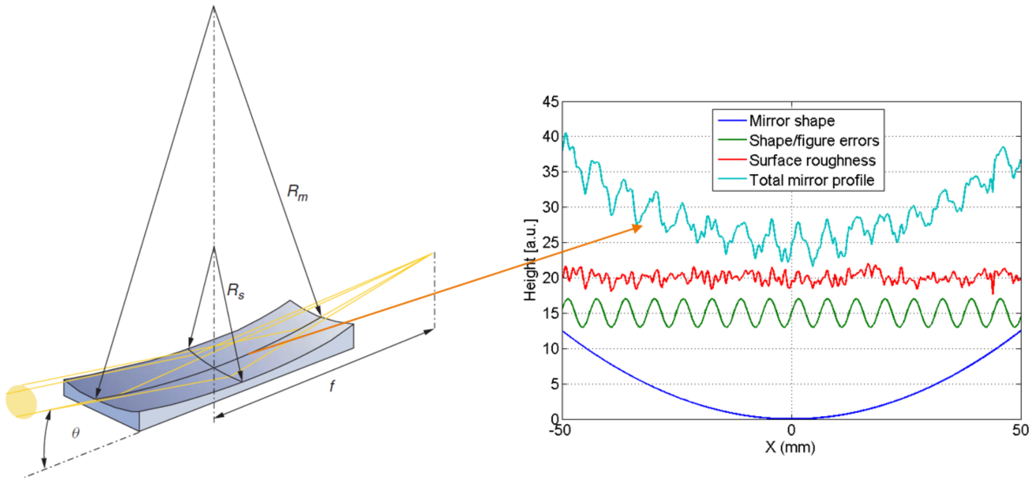

Figure 1.6 : A typical mirror shape [14] and different parameters of a mirror profile for characterization.

Slope errors: The residuals from fitting measured slopes to the ideal surface slopes are termed slope errors. The slopes of a 2D surface have two components, tangential & sagittal, where the tangential direction is along the X-ray beam propagation direction in the plane of incidence and sagittal direction is perpendicular to tangential axis in the mirror surface plane. The slopes are obtained as partial derivatives of surface along the tangential and sagittal directions. Tangential slope errors are generally of far more significance to the mirror performance, as the beam is nearly grazing incidence in tangential direction whereas it is nearly in normal incidence in sagittal direction. Unless specified as sagittal slope errors, if simply slope errors are mentioned they generally refer to tangential slope errors. Slope errors are given in 2D maps, or as 1D profiles. Globally slope errors are expressed by their rms or peak to valley (PV) values over the 2D maps or 1D line. Sometimes the profiles or maps are transformed to power spectral density (PSD) [28] plots which show the spatial frequency distribution of the errors. An example of PSD compared between different instruments is shown in Figure 1.7 [26]. The spatial periods considered are typically between 1 mm up to the mirror length.

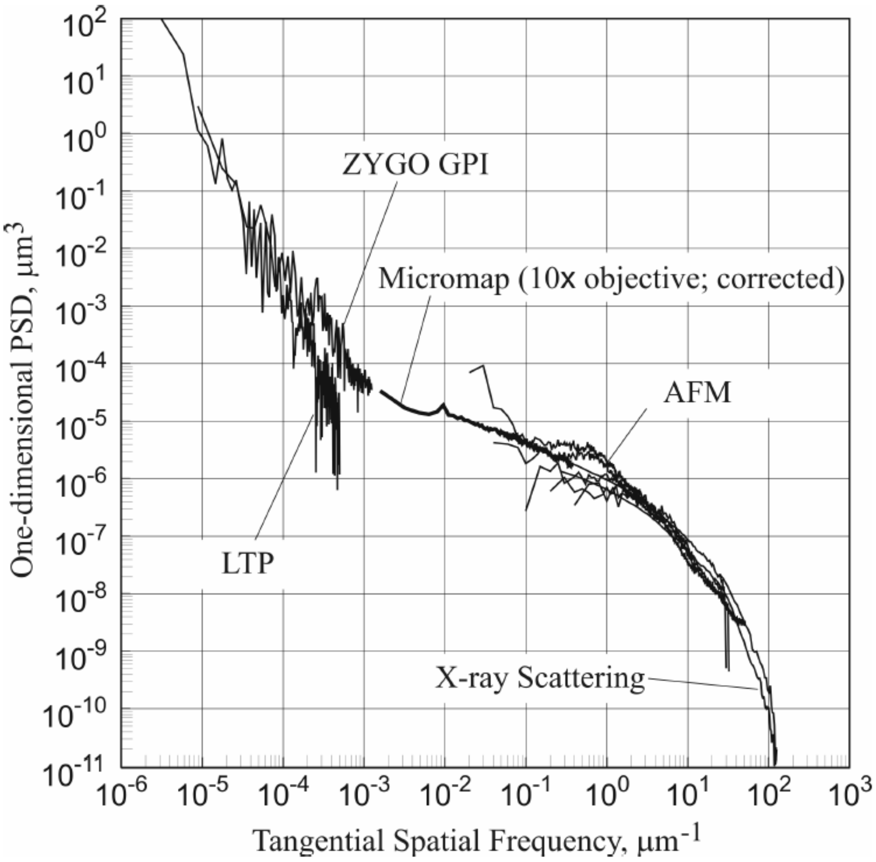

Figure 1.7 : Power Spectral Density (PSD) of different surface metrology instruments [26].

Figure errors: The residual height or shape errors from fitted shape to ideal surface, in the longer spatial period range are called figure errors. The typically considered spatial periods are the same as for the slope errors. Figure errors and slope errors affect mainly the imaging (focusing) properties of the system [29]. Similar to slope errors, figure errors are displayed as 2D maps or 1D line profiles with rms / PV values over the full profile.

Surface roughness: Surface roughness represents shape/height errors at small spatial periods typically < 1 mm (high spatial frequencies). They primarily contribute to scattering of X-rays and thus to reduction in beam intensity at the sample [29]. High resolution metrology instruments are required for surface roughness measurements at very small spatial periods (< 1 µm) instruments such as the Atomic Force Microscopes can provide the surface roughness [26] and for intermediate regions (> 1 µm and <1 mm) optical instruments, such as micro-interferometers are typically used [26]. Surface roughness is usually displayed as 2D maps or 1D profiles with rms / PV values over the full profile.

Shape parameters: The measured shape from fitting heights or slopes can deviate from ideal design shape. The shape parameters depend on the type of shape fitted, e.g. for cylindrical mirrors the shape parameters are the radius of curvatures in tangential and sagittal directions and for elliptical mirrors they are generally expressed by source distance (p), sample distance (q) and incidence angle (θ). The radius of curvature is generally expressed as radius of a sphere fitted to the 2D surface heights or slopes. For cylindrical or toroidal optics, the radius of curvature is expressed separately in the tangential and sagittal directions by fitting cylinders in respective directions to the 2D surface heights or slopes. For aspheric mirrors radius of curvature is also defined locally on the surface.

The mirror surface parameters (e.g. slope error rms, mean radius) are specified within certain tolerances and mirror manufacturers must process the mirror accordingly during the fabrication.

A typical manufacturer's specification is shown in Appendix 7. The mirrors typically range from 10 mm to 1500 mm lengths, with various shapes such as flat, spherical, toroidal, elliptical and ellipsoidal. Typical mirror slope errors can reach <100 nrad rms and figure errors < 1 nm rms. The mirrors mean curvatures can range from very flat (radius >100 km) to highly curved (radius <10 m).

1.3 Measurement uncertainties for X-ray mirror metrology

Accuracy: Accuracy is defined as the closeness of agreement between measured value and true value. The true value is usually taken as measurement of the same sample by a standard instrument, but for surface metrology of synchrotron mirrors dealing with sub nanometer height errors over long sizes, it is difficult to have a standard. For synchrotron mirror metrology, typical mirror qualities are very high and good standards are not available. To have a consensus synchrotrons have adapted round robins as a way to calibrate different instruments against few standard mirrors [30], [31]. Accuracy here is commonly referred as agreement between two or more instruments in slope & figure errors, radius of curvature and other parameters. Accuracy for slope/figure errors is expressed in difference profiles or rms / PV of difference.

Repeatability (precision): Repeatability or precision is defined by closeness of agreement between measured values in a number of repeated measurements [32]. It is commonly expressed as the standard deviation (std) or peak to valley (PV) of repeated measurement values (*x*). The repeatability of the mean, σ_{x_m} reduces by the square root of number of repeated scans given by the following.

$$x_m = \frac{\sum_{i=1}^{N} x}{N}$$

$$\sigma_{x_m} = \frac{\sigma_x}{\sqrt{N}}$$

(1-3)

Where x is the value measured N times, x_m is the mean value, σ_x is standard deviation of x and σ_{x_m} is the standard deviation of the mean.

Accuracy and precision can be visualized through a schematic shown in Figure 1.8.

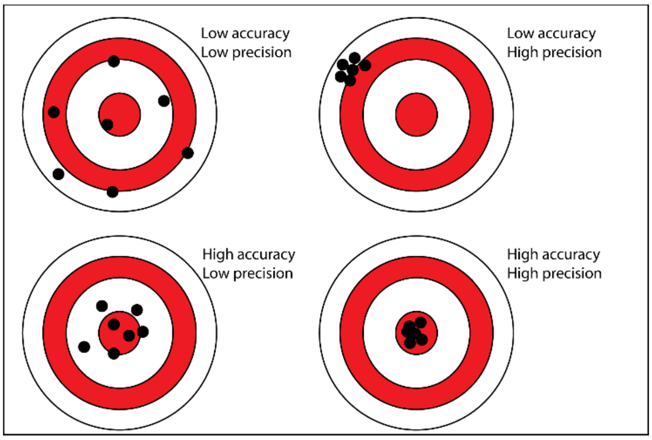

Figure 1.8 : Schematic of accuracy vs precision of repeated measurements [33].

1.4 Optical metrology for synchrotron mirrors

Mirror manufacturers and X-ray light sources use a wide range of instruments for mirror surface metrology. The more commonly used optical metrology instruments are described here. Different instruments can provide complementary metrology information over different length scales (or spatial frequencies) on the mirror with some overlap regions.

Long Trace Profiler (LTP): LTP is one of the most commonly used instruments at synchrotrons for mirror metrology. It was originally developed at the Brookhaven National Laboratory and adapted with several custom modifications by laboratories around the world [34]. The LTP is based on pencil beam interferometry [35], where two identical parallel beams (generated from a beam splitter) are reflected by a test mirror and interfere after passing through a Fourier transform lens (FTL). The interference pattern depends on the optical path difference between the beams, which changes with the slope between the points of contact of the two beams on the test mirror. LTP scans the mirror in 1D along its length to get mirror slopes (line) profile for full length. The maximum mirror size is essentially defined by the carriage translation range. The LTP developed at the ESRF (Figure 1.9) uses this approach [36]. In the ESRF LTP scanning along mirror length is facilitated by a moving optical head which primarily consists of a pentaprism whereas the rest of the optics (laser, FTL, detector) remain fixed. The pentaprism is helpful in minimizing the translation stage tilt errors while scanning; however, to avoid some of the systematic errors of the pentaprism, it is replaced with two super polished mirrors at 22.5° mimicking the pentaprism. LTPs commonly have beam sizes of few mm and measure in the low spatial frequency (periods > ~1 mm) domain relevant to the characterization of slope and figure errors.

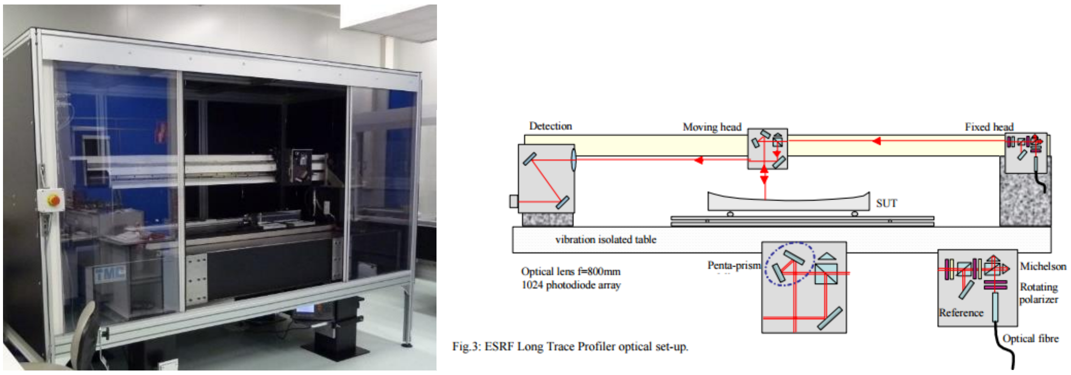

Figure 1.9 : LTP and its schematic installed at ESRF [36].

LTPs have spatial resolution typically >1 mm (ESRF LTP has 2 mm resolution) and they are able to detect slope variations <0.1 µrad rms and height variations <0.2 nm rms [37]–[40]. LTPs have been heavily customized with different modifications at different synchrotrons, which has allowed significant improvements over the years [37], [41]–[43]. ESRF LTP can measure up to 40 mm/s speed thus reducing measurement times and minimizing long term drift effects. Systematic errors from optical elements from aberrations or misalignments are a significant limitations of LTPs, although significant progress has been made [37], [44]. Stringent environmental stability requirements continues to play a significant role in measurement accuracy and repeatability of LTPs and many other mirror metrology instruments [45], [46].

Nanometer Optical Component Measuring Machines (NOM): The NOM [47] was originally developed at the Helmholtz Zentrum Berlin (Bessy II) in the early 2000s [47], similar to the one shown in Figure 1.10. The design is derived from that of the LTP with the light source and detector replaced by a commercial high precision autocollimator. Due to their relatively simple implementation and good performance they have gained increasing popularity as test systems for X-ray mirrors at many synchrotrons. As for the LTP, the maximum length is determined by the translation length. The measuring principle is based on noncontact deflectometry. The autocollimator is fixed stationary, and similar to LTP the scanning of test mirror is facilitated by a moving 45° pentaprism, which directs the collimated laser from autocollimator to test mirror and reflected beam back into autocollimator. The spatial resolution of NOM is typically 2 mm which is determined by the size of aperture/diaphragm near the test mirror (Figure 1.10). The aperture size smaller than 2 mm increases measurement noise from diffraction and interference effects [48]. NOMs have demonstrated measurements on mirrors with slope errors <0.1 µrad rms [49], [50]. NOMs face similar problems as LTPs such as systematic errors and environmental stability. Systematic errors have to be corrected for better performance either through calibration [51] or using error suppression algorithms [52].

Both the LTP and NOM instruments yield primarily 1D line profiles of the slope/height error variations. Whilst these are valuable for assessing mirror quality they are generally insufficient to provide the full surface topography of the active mirror surface – an aspect which is increasingly important as the input for deterministic mirror figuring processes [53].

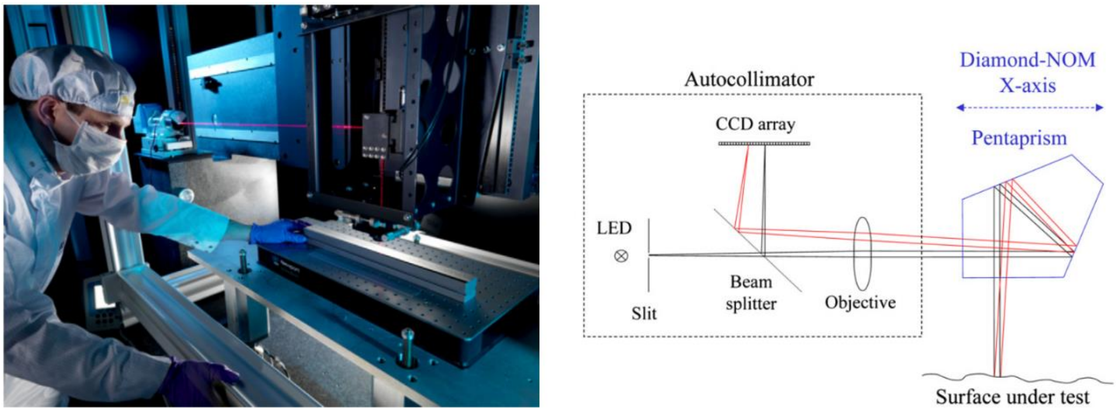

Figure 1.10 : NOM and its schematic installed at Diamond Light Source [54].

Fizeau interferometers: Fizeau interferometers are 2D height measuring surface profilers [55], in addition to their use in the testing of optical components for visible light, they are very commonly used by synchrotron facilities and X-ray mirror manufacturers. Fizeau interferometers have apertures typically between 50 mm and 300 mm. Different measurement configurations can be used with these instruments such as single-pass and double-pass [56], as shown in Figure 1.12. When used in single-pass the directly measurable mirror length is limited to the aperture size; the use of a double pass configuration with the test mirror in oblique incidence increases the measurement length at the price of a reduced spatial resolution and larger measurement cavity (leading to higher measurement errors). The ESRF has two 150 mm Fizeau instruments made by Zygo Corporation as shown in Figure 1.11, configured to measure either vertically facing or horizontal facing mirrors. The Zygo Fizeau uses Phase Shifting Interferometric techniques. The Fizeau instruments are used for height measurements in mid to low spatial frequencies (periods > ~0.1 mm) and they can measure sub nm height errors rms using single pass / double pass methods [50]. One of the major problems of Fizeau instruments is stability of environment in the cavity (beam propagation region between Fizeau and test mirror), and it becomes even more significant in double pass arrangement [57]. Double pass measurements also depend on the oblique angle, with larger measurement noise at large angles [58]. Systematic errors coming from transmission flat (TF) also play a significant role in determining measurement accuracy of the state of the art mirrors with surface deviations $\ll$ 5 nm rms [45], [50]. Unless TF is calibrated (e.g. using three flat test [59]), Fizeau instruments are limited by TF quality. Despite these problems Fizeau instruments have been very reliable and are widely used. Fizeau instruments provides accurate 2D height maps unlike LTPs and NOMs which are commonly used for 1D profile. They are also commercially available by many manufacturers (e.g. Zygo [60], Bruker [61]). Fizeau instruments can have typically very large apertures which is very advantageous as synchrotron mirrors are generally very large (<1.5 m). LTPs and NOMs typically provide only low spatial frequency information whereas Fizeau instruments can provide at much higher resolutions.

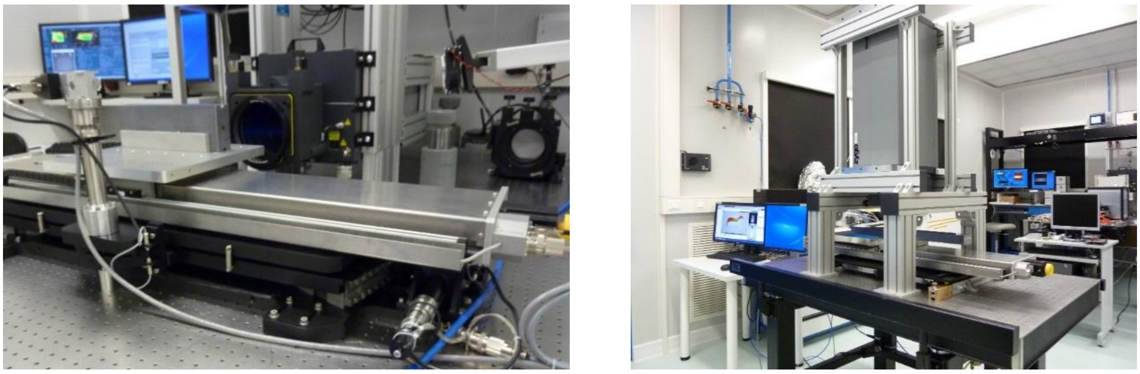

Figure 1.11 : ESRF Fizeau instruments with Zygo VeriFIRE AT+ on the left and Zygo VeriFIRE XPZ on the right.

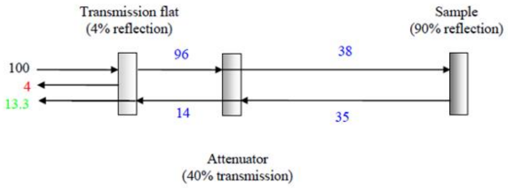

Single-pass, Fizeau geometry (the Minifiz is located at the left side of the diagram)

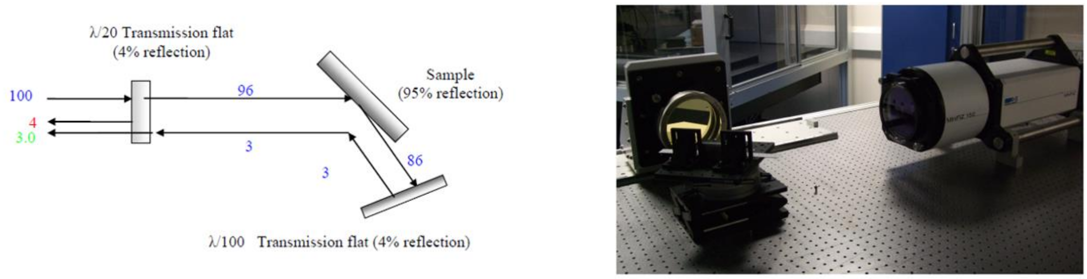

Double-Pass Geometry

Photograph of the Minifiz interferometer in double-pass configuration

Figure 1.12 : Single-pass and double-pass configurations of Fizeau instrument at Diamond Light Source (DLS) [56].

Micro-interferometers: Micro interferometers (MI) are 2D height measuring instruments used primarily for surface roughness measurements in mid-range spatial frequencies (periods > ~1 µm and < ~1 mm). The ESRF uses a modified Veeco NT9800 micro interferometer implementing both White Light Interferometry (WLI) and Phase Shifting Interferometry (PSI), as shown in Figure 1.13. Micro interferometers utilize microscopic magnification objectives to measure micro-roughness at very high resolutions. ESRF MI frequently uses objectives 2.5x, 5x and 50x, which increases resolution up to 0.5 µm at 50x from typical ~10 µm resolution at 1x [45]. However, at higher magnification the measurements are very sensitive to defocus errors which induces large curvature to the measured mirror micro-roughness map. MIs stand unique in providing 2D micro-roughness maps using non-contact based optical metrology when compared to other instruments presented here. State of the art MIs can measure micro roughness <0.1 nm [38] on synchrotron mirrors.

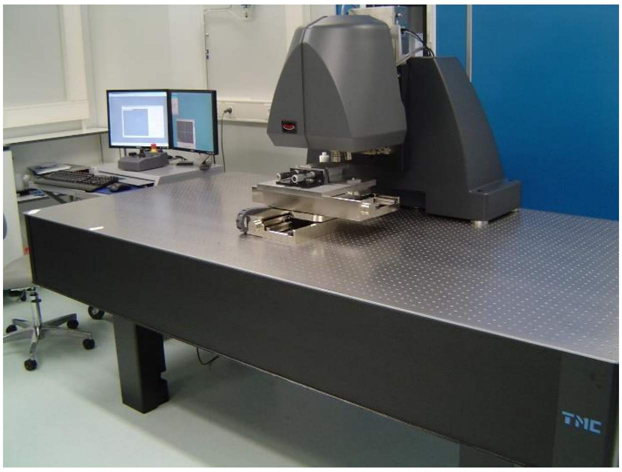

Figure 1.13 : ESRF micro-interferometer WYKO NT9300.

1.5 Stitching techniques for the measurement of large or strongly curved optics

The development of interferometric techniques has allowed for high accuracy surface metrology, but significant challenges still remain. Three major issues relevant for synchrotron mirrors are (1) optical lengths up to 1.5 m, (2) highly curved spherical and aspheric surfaces with radius of curvatures as low as < 1 m and (3) optical surface specifications which are close to the practical limits of current metrology instruments. Traditional optical metrology instruments are restricted by the size of aperture with difficulties in manufacturing large accurate optical elements such as transmission flats.

Measuring curved surfaces places a different challenge, where the instrumental errors coming from optical aberrations depend on the test surface shape itself. Interferometric instruments also face problems with resolving high fringe densities on highly curved surfaces. One of the solutions is to use stitching techniques [62], [63], which divide the test surface into many sub regions (subapertures) and measure these regions independently. The subapertures are usually measured with considerable overlap, so that joining (stitching) them would allow for compensation of orientation errors between the subapertures. This approach has been the basis of many of the recent efforts to improve the metrology of X-ray optics [64]–[68]. Stitching algorithms and different stitching software used at ESRF are presented more comprehensively in chapter 3.

Both of the ESRF Fizeau instruments are commonly used for measurement using stitching methods allowing longer mirrors to be measured in the single pass configuration. Consequently, the benches include motorized translation and alignment stages to move the mirror across the Fizeau aperture. Stitching Fizeau have shown improved measurement accuracy at ESRF compared to standard single pass technique, and it can measure surface height variations <0.2 nm [38].

The ESRF micro interferometer system also offers a stitching capability similar to “Micro-stitching interferometry” (MSI) reported by Yamauchi et al [64] to extend measurements in the low spatial frequency domain covering periods > ~1 mm to 300 mm (the latter determined by the stroke of the translation stage). However, measurements of long mirrors or at higher spatial resolutions (using larger microscope zoom objective), require large number of subapertures to be stitched. The angular errors between subapertures accumulate over large number of subaperture stitching and hence leads to low spatial frequency errors [64]. ESRF micro-interferometer measured with stitching <0.2 nm height variations, with good agreement with other instruments [38].

Mirror metrology progressed significantly over the years along with the increasingly stringent mirror specifications. Many of the third-generation synchrotrons across the world are upgrading or planning to upgrade to a more brilliant and high coherence beam. Consequently, mirrors of even higher quality and corresponding metrology is being pushed. One such project is MooNpics (Metrology On One-Nanometer-Precise Optics) collaboration among various European synchrotrons and mirror manufacturers, which aims to measure mirrors with figure errors < 1nm and slope errors < 20 nrad [69], [70]. This quality needs to be achieved on wide variety of optics; long (> 1 m) ultra-flat mirrors (radius > 3000 km) for X-ray beam transportation; and strongly curved mirrors for nano-focusing (typically radius < 100 m, but < 15 m in extreme cases). Current metrology instruments need to be further improved and new instruments may need to be developed to achieve such quality requirements.

A new variant of deflectometry measurement was investigated by combining a Shack-Hartmann-based wavefront sensor with a long LTP/NOM-type translation stage (SH-LTP), in a collaboration between Imagine Optic and SOLEIL synchrotron [71]. SH-LTP at SOLEIL was able to measure different mirrors with <1 µrad slope errors, which were verified in comparison to LTP measurements. It was able to measure highly curved mirrors with radius as low as ~1m. The measurement repeatability in the order of 0.1 µrad has been achieved with SH-LTP. The successor of this instrument forms the basis of the experimental work of this study and will be presented in more detail in section 2.1.

2 SHARPeR INSTRUMENT

2.1 Mirror metrology with stitching Shack-Hartmann wavefront sensor (SHARPeR)

In the absence of any integrated commercial test benches suitable for the surface metrology of long X-ray mirrors and in the light of the promising tests of the SH-LTP at SOLEIL [23], the two companies Imagine Optic (expert in Shack-Hartmann based wavefront sensing technologies) and Q-Sys (expert in motion technologies) initiated a product development program to provide a commercial solution.

This collaboration was consolidated through the Eurostars SHARPeR project (project number E!8304), with an optimized Imagine Optic optical head combined with highly accurate translation platform designed by Q-Sys. SHARPeR aims to be a 2D, high accuracy slope measuring instrument for high quality X-ray mirrors. The SHARPeR prototype was improved over the years in collaboration with Mourad Idir at Brookhaven National Laboratory (BNL), they were able to demonstrate accuracy and repeatability below 50 nrad with the BNL SHARPeR prototype on different mirrors (short flats, spheres and ellipses with radius > 100 m) [72].

2.1.1 Brief history of the SHARPeR project

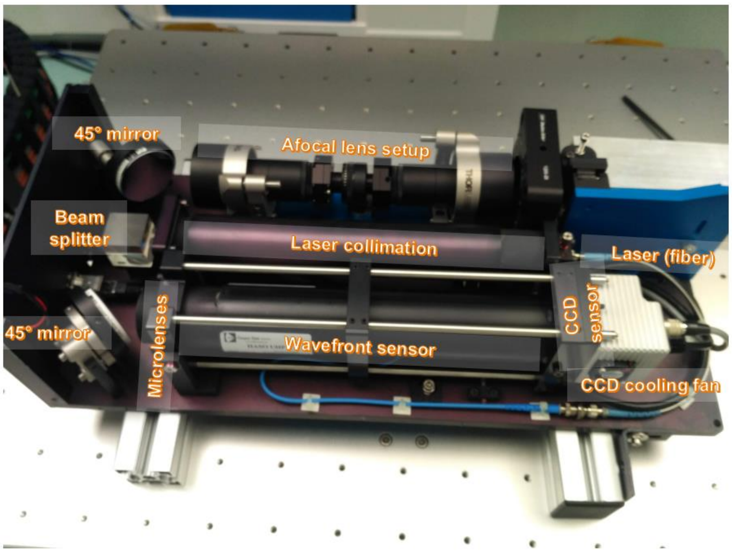

Figure 2.1 : SHARPeR optical head designed by Imagine Optic.

The Eurostars SHARPeR project required testing of the full commercial product at a user facility which lead to installation of the final SHARPeR prototype consisting of the optical head and motion platform at the ESRF as shown in Figure 2.2 and with just the optical head shown in Figure 2.1. Currently, in addition to ESRF and BNL, SHARPeR instruments are installed at Shanghai Synchrotron Radiation Facility (SSRF) and SLAC National Accelerator Laboratory.

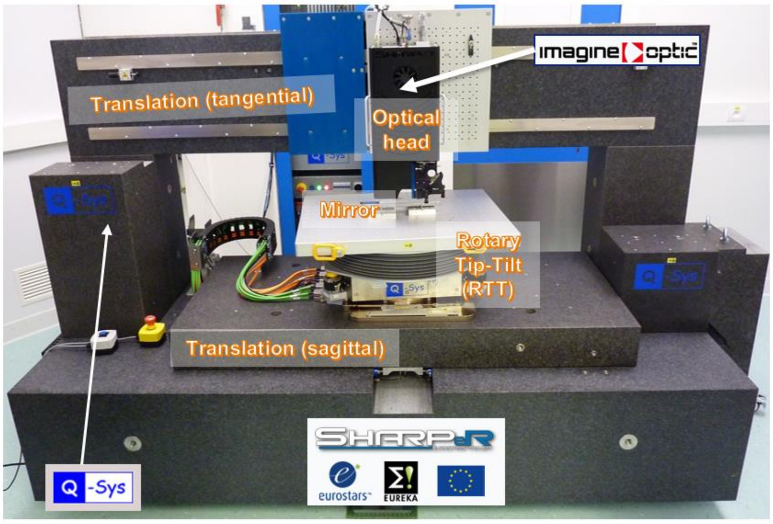

Figure 2.2 : SHARPeR installed at ESRF.

2.1.2 SHARPeR principles of operation

The SHARPeR optical head is shown in Figure 2.1, and is shown schematically in Figure 2.3. Illumination from a fibered laser (wavelength 405nm) is collimated, and after reflection by a polarizing beam splitter, passes through conditioning optics (45° mirror, afocal lens combination, quarter waveplate) before impinging on the test mirror. The beam reflected by the test mirror returns through the same afocal lens combination and other optical elements, after transmission through the beam splitter reaches the entrance pupil of the wavefront sensor (HASO UHP). The afocal lens setup projects a conjugate image of the wavefront at the mirror surface onto the entrance pupil of the HASO, at the microlens array. The wavefront sensor measures the direct wavefront slopes in tangential and sagittal directions. The laser beam is vertically polarized and the beam splitter reflects > 99% in vertical polarization and transmits > 99% in horizontal polarization. A quarter waveplate (QWP) is used to convert vertical to circular polarization in beam forward pass and from circular to horizontal polarization in return pass. The QWP plus polarized beam splitter combination also reduces the intensity from parasitic reflections entering the wavefront sensor.

The optical head is mounted on the Q-Sys tangential translation and scans over the mirror length and acquires sub-aperture images with considerable overlap (>80%), with each image measuring the reflected wavefront distortion (of the test mirror) expressed as wavefront slopes. A stitching process is used to combine the overlapping sub-aperture slope maps into a long 2D map, similar to a panoramic picture. Finally, a 2D surface profile is reconstructed through integration of the tangential and sagittal slopes. In the as-delivered version of the system the subaperture slopes are stitched with StitchWave software provided by Imagine Optic.

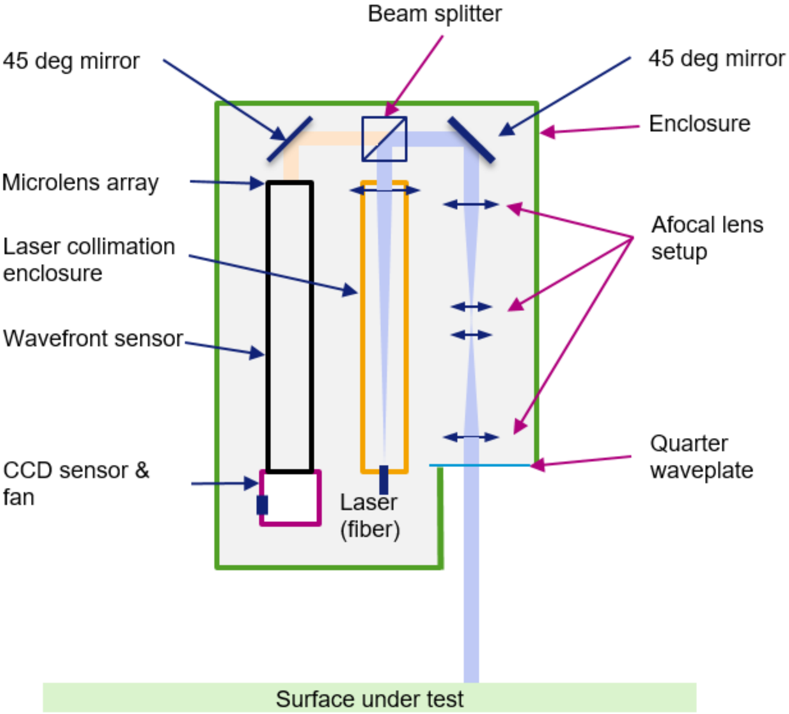

Figure 2.3 : Schematic of SHARPeR optical head. (The Afocal setup is simplified: the real instrument has more lenses with complex arrangement.)

2.1.3 Specifications of the SHARPeR at the European Synchrotron (ESRF)

SHARPeR consists of a highly accurate and precise optical head (SSHOH), stable and repeatable translation platform (STAMP) and a rotary, tip & tilt platform (RTT). The design and manufacture of the SSHOH was performed by Imagine Optic whilst that of the STAMP and RTT was produced by Q-Sys. The nominal specifications of SHARPeR installed at the ESRF are presented in Table 2.1, Table 2.2 and Table 2.3.

Table 2.1 : SHARPeR translations stage (STAMP) specifications

STAMP platform	**Sagittal axis (Y)**	**Tangential axis (X) (carrying optical head)**
Travel length	300 mm	1500 mm
Payload	≤ 200 kg	≤ 30 kg
Position accuracy	≤ 2 µm	≤ 2 µm
Repeatability	≤ 0.5 µm	≤ 0.5 µm
Maximum speed (on the fly measurements)		≤ 12.5 mm/s

Table 2.2 : SHARPeR rotation and tip-tilt (RTT) platform specifications

RTT platform	**Rotation axis**	**Tip-Tilt axes**
Range	190°	± 5°
Accuracy	≤ 15 µrad	≤ 30 µrad
Repeatability	≤ 5 µrad	≤ 5 µrad

Table 2.3 : SHARPeR optical head (SSHOH) specifications

	Specifications
Aperture size	18.0 x 13.2 mm^2
Number of microlenses	15 x 11
Tilt dynamic range	± 4 mrad
Sampling size	~1.2 mm
Microlens size	1.1993 x 1.1983 mm^2

Laser wavelength	405 nm
Weight	< 10 kg

The optical head with specifications in Table 2.3 was designed for high slope sensitivity (<100 nrad) and to achieve that the wavefront sensor microlenses were chosen with ~300 mm focal length. Microlens size has to be compromised to achieve large tilt dynamic range. The total aperture size is limited by the CCD sensor size as well as the total cost of the system.

The wavefront sensor operates at nearly diffraction limited focal spot. Figure 2.4 shows a comparison of theoretical focal spot of a microlens in the CCD focal plane for a flat incidence wavefront to a measured CCD focal spot intensity. The spot is shown only in 1D, with the measured CCD intensities averaged along sagittal pixels. The theoretical profile is obtained from the square shaped microlens of the SHARPeR wavefront sensor (sinc^2 shape), with calculated spot full width half maximum size (FWHM) of ~85 µm (or 15.5 pixels). The measured spot is very close to the theoretical diffraction limited focal spot.

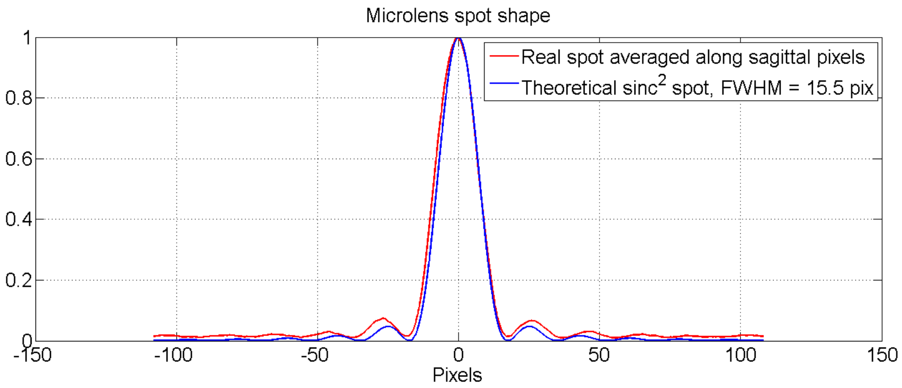

Figure 2.4 : The measured microlens spot is compared to a theoretical sinc^2 spot with FWHM of 15.5 pixels.

2.1.4 Calibration of wavefront sensor

The reference wavefront is deduced from multiple spherical wavefronts recorded by wavefront sensor using a point source between 1 to 5 m distances. Complete calibration procedure is proprietary knowledge of Imagine Optic and hence not presented here. The calibration process also corrects for manufacturing defects of the microlens array. This calibration is performed with the wavefront sensor dismounted from the SHARPeR head and was performed prior to the system assembly and assumed constant. The reference wavefront centroid positions are subtracted from test wavefront to get final slopes.

2.1.5 Advantages and disadvantages of the SHARPeR instrument

A comparison of SHARPeR with other metrology instruments used for X-ray mirror characterization at the ESRF is shown in Table 2.4. Based on its design it is possible to identify potential advantages and disadvantages of SHARPeR compared with these other instruments. Amongst them it provides 2D profiles, and (unlike LTP, NOM or stitching Fizeau benches) it is commercially available as a complete package including stitching. SHARPeR also should not face some of the problems faced by interferometric instruments. SHARPeR should offer some vibration immunity due to shorter acquisition times and has no moving parts within the measurement device (optical head). In addition, the use of an afocal optical telescope to project the wavefront at the SUT surface onto the aperture of the wavefront sensor may present advantages particularly for curved samples where propagation of the beam from the SUT to the sensor can lead to modifications of the phase profile of the beam [39].

Fizeau and micro-interferometers generally require scanning of the optics along the optical axis, usually with piezo motors, which are potential sources of instability and in-service failure. Another issue with interferometers is fringe-print-through caused by dust or vibrations, which is especially significant on highly curved mirrors and it is not a problem faced by SHARPeR. Some interferometric instruments, such as the Fizeau interferometer need to adapt their reference (transmission flats) characteristics depending upon the reflectance of mirrors, which is not the case with SHARPeR.

Some of the possible disadvantages of the SHARPeR are large systematic errors such as retrace errors and pseudo random environmental errors. Retrace errors arise from optical aberrations due to imperfections in afocal optics. Some of these systematic errors are corrected by measuring on a flat reference surface, but if the measuring mirror is steeply curved the reflected beam retraces a different optical path in the afocal optics which results in errors commonly known as retrace errors. Also, high sensitivity to environmental factors such as temperature fluctuations leads to low repeatability and low accuracy. These issues have been explored during my thesis and some solutions are proposed.

Table 2.4 : Comparison of different ESRF optical metrology instruments

	SHARPeR	**LTP**	**Zygo Fizeau VeriFIRE AT+ Interferometer**	**Veeco NT9300 Micro interferometer**
Zoom capability	no	no	1x (5x) *	1x (50x)
Aperture size (mm^2)	18.0 x 13.2	2 x 2	150 x 150 (30 x 30)	6.4 x 4.8 (0.13 x 0.10)
Spatial resolution	1.2 mm	2 mm	160 (30) µm	10 (0.5) µm
Measured dimensions	2D	1D	2D	2D
Commercial availability	Y	N	Y (stitching not available)	Y
Maximum mirror length	1.4 m	1.4 m	1 m	0.3 m
Measurement time (for 100 mm long flat mirror)	~ 3h	~45 min	~3h 30min	~2h 30min

Spatial frequency regime	Low	Low	Mid to low	Mid (Low frequencies with limited accuracy using stitching)
Method	Shack-Hartmann wavefront sensing	Deflectometry	Phase shifting interferometry	White light (coherence scanning) interferometry/phase shifting interferometry (monochromatic illumination)

*1x (5x) – implies a lower limit 1x zoom and upper limit 5x zoom, all the upper limits in the table are presented in red in brackets.

2.2 Schematic of SHARPeR measurement process

The SHARPeR measurement process can be divided into three stages, initialization, measurement and data analysis as shown in Figure 2.5.

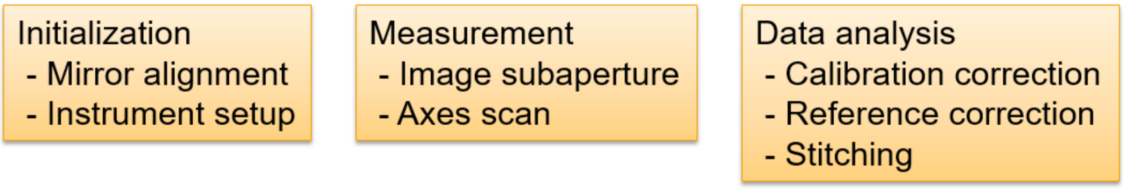

Figure 2.5 : Measurement process schematic for SHARPeR.

2.2.1 Initialization

Initialization involves setting up the test mirrors and reference mirrors (explained in section 2.2.3) under the SHARPeR instrument. Alignment of the test mirror is quite critical, not just for the measurement procedure but also for the next steps after metrology. For synchrotron mirrors the metrology is used either for process control during mirror fabrication or as a quality check before mirror installation on the beamlines. In both cases locating the measurements within a reference frame of the mirror is essential. Mirror manufacturers need to locate the figure errors unambiguously on the mirror surface in order to correct those using deterministic polishing processes. Also, synchrotron beamlines may have to locate polished regions on the mirror and align the mirror in a configuration which minimizes distortions to the x-ray beam. The approach to referencing the position of the measured zone is not unique but the optomechanical systems at the ESRF usually use the physical edges of the mirror to reference its position. Unfortunately, these edges are rarely visible within the measurement tools so metrology labs more commonly use the reflective edges of mirror to define clear aperture. Due to the presence of chamfers and roll-off effects during polishing these reflective edges do not correspond to physical edges (see Figure 2.6). Some mirrors have markings on the edges (either engraved or with ink) and increasingly have fiducials etched on the mirror to locate the clear aperture (optically active) region as shown in Figure 2.6. Metrology labs use these markings or fiducials on the mirror if available to define clear aperture and they are useful in many cases to cross check between metrologies of manufacturer and user facility, metrology verification with different tools and metrology during the iterative polishing processes. In general, the width of the clear aperture is defined to be comfortably larger than the X-ray beam width in order to relax the tolerance of alignment errors during the beamline installation of the mirrors.

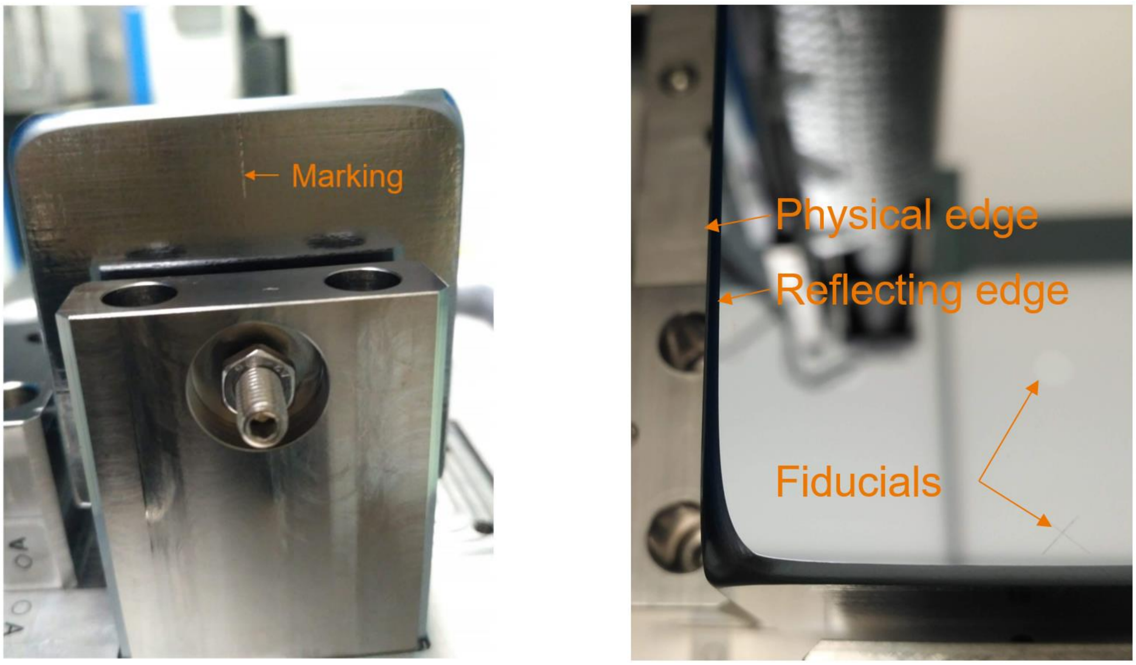

Figure 2.6 : Defining clear aperture region on the mirror using marking and fiducials. Markings and fiducials are physically engraved for this mirror.

Even with all the care taken to define the clear aperture position, the measurement processes of different instruments may lead to differences in detecting fiducial markers. Instruments having different spatial resolutions may also have difficulties in arriving at a consensus on fiducial and marking positions. The SHARPeR at the ESRF uses a focused beam with a tool lens to locate the reflecting edges or markings as shown in Figure 2.7. The estimated uncertainty between sensor center and tool lens focal spot is ~100 µm. The SHARPeR and LTP can also use visual inspection to detect the position of the measurement beam relative to markings, which is prone to inaccuracies especially if the light is monochromatic and causing specular reflections. The SHARPeR edge detection method is automated and is generally used to locate edges with <10 µm repeatability. The ESRF Zygo Fizeau interferometer uses the measured intensity from the camera image to manually define the mirror edge which is effectively the reflective edge. A new method is being tested at the ESRF to place another mirror, in parallel, behind the test mirror edge to define the physical edge [73].

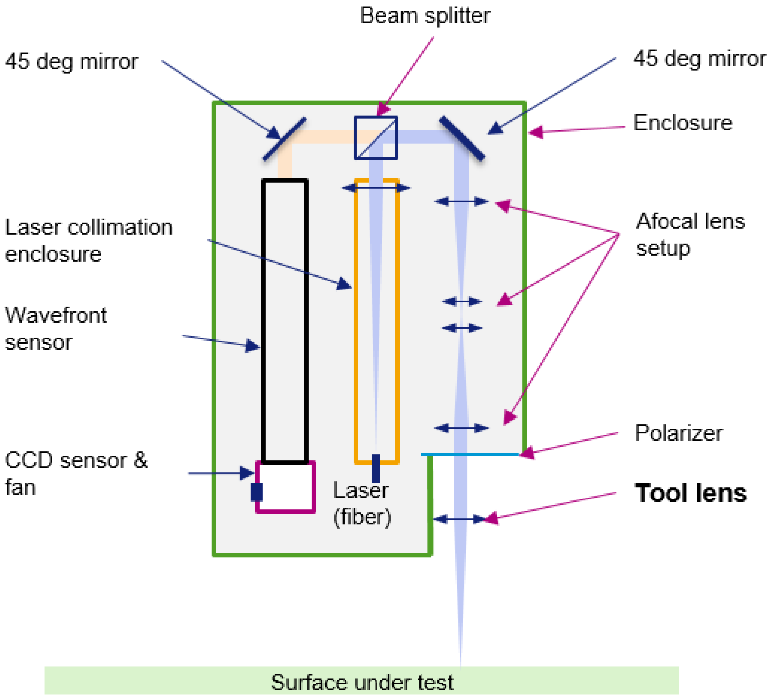

Figure 2.7 : Schematic of test mirror alignment in the focal plane of tool lens.

Another important aspect before the measurement is the supporting of the mirror. A mirror placed on a flat surface may have deformations due to non-uniformities of the holding surface. Mirror deformations such as twist in the order of few nanometers can be very significant for synchrotron mirror metrology. At the ESRF the mirrors are usually placed on two cylinders as shown in Figure 2.8, symmetrically at a distance of quarter of mirror length from center. In this setup the mirror is deformed by gravity, which can be calculated based on points of contact and thickness of mirror, and the measured data corrected accordingly [74]. However, if there are any deformations in the shape or orientation of cylinders or in the shape of the mirror back surface, it could add twist to measured surface data. The twist errors can be avoided by using spherical contacts at three points but may lead to complications for measuring the mirror in different orientations. The separation of the contact points is generally chosen to be close to the Bessel points of the mirror to minimize the gravity deformation, which for flat mirrors, should reduce the dynamic range of the angular measurements and reduce systematic measurement errors.

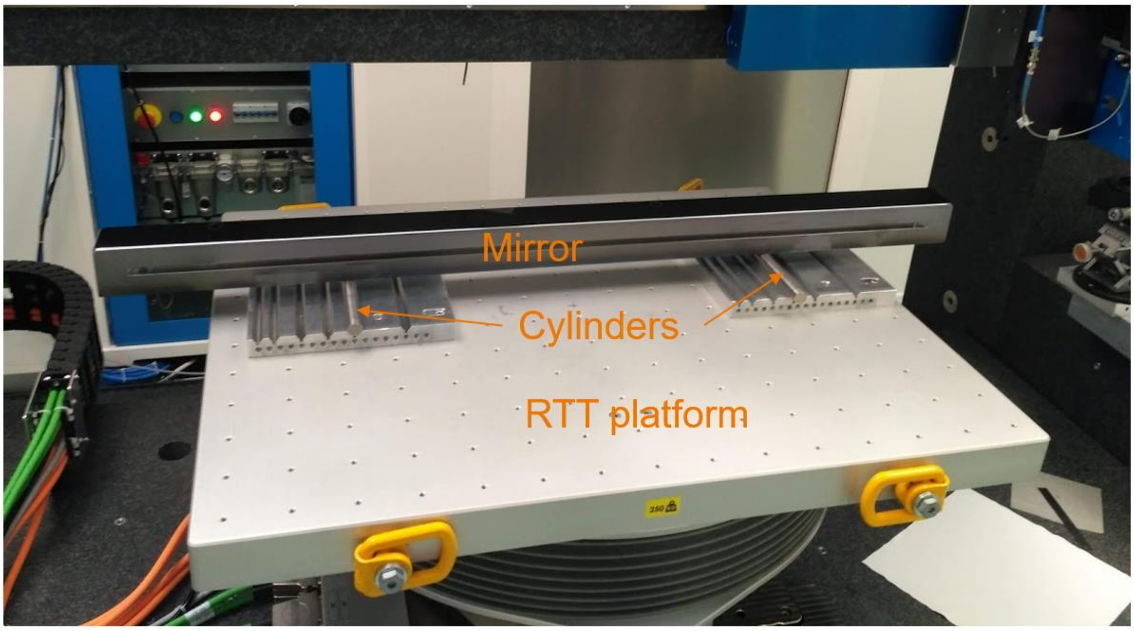

Figure 2.8: Mirror placed on cylinders during a measurement with SHARPeR.

To facilitate the stitching process SHARPeR instrument also aligns the mirror reflecting edge parallel to the CCD detector throughout the scan length, if no markings or fiducials are available as shown in Figure 2.9. The mirror edge is scanned with tool lens focal spot along the scan axis shown in Figure 2.9, and RTT is rotated until the edge is visible in SHARPeR CCD over the full mirror length (within a precision of typically <0.1 µm to account for edge nonlinearities). Subsequently the mirror is aligned to normal incidence within <2 µrad tilt in both tangential and sagittal directions, where the normal incidence corresponds to the tilt of wavefront as average of all microlens slopes. The mirror is also aligned close to the focal position within <2 µm position repeatability, using the SHARPeR tool lens. The focus and normal tilt alignments are done only at the center of clear aperture in the current measurement scheme.

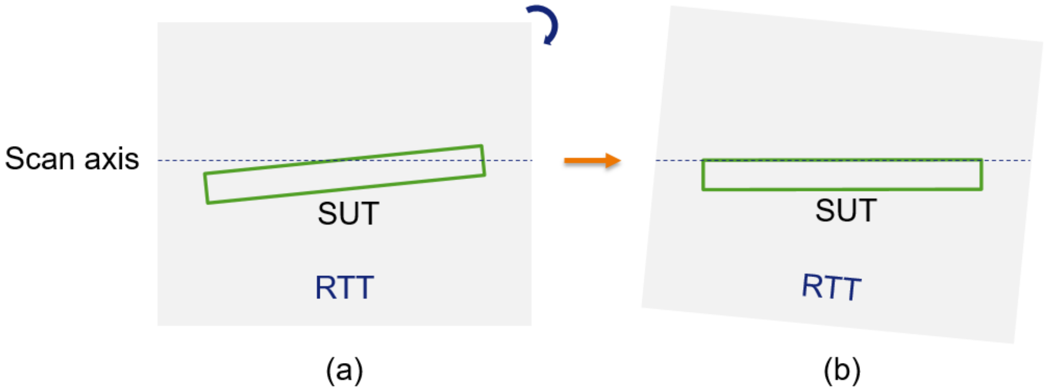

Figure 2.9 : Schematic of test mirror (SUT) alignment parallel to scan axis, which is parallel to optical head CCD.

After the mirror alignment, the SHARPeR instrument initializes the camera exposure time and laser power simultaneously to set average acquisition intensities of microlens spots within 70 to 90 percent of CCD saturation level. The laser beam intensity is not uniform across the microlenses and the mean microlens focal spot intensity on the CCD detector smaller than 90 percent is used in order to avoid saturating some of the spots. An intensity level above 70 percent to saturation is maintained to have larger signal to noise ratio.

A brief summary of typical SHARPeR alignment steps is given in the following.

1. Place the test mirror on RTT and move SHARPeR head on top of mirror.

2. With tool lens placed, roughly align the mirror close to focal position.

3. Determine the four mirror reflecting edge positions (automatic).

4. Align the mirror parallel to scan axis (Figure 2.9).

5. Re-determine mirror edge positions and the mirror center.

6. At the mirror center adjust mirror focal position more accurately.

7. Remove tool lens and adjust the mirror tilts in tangential and sagittal near normal incidence. Repeat steps 6 and 7 iteratively until the best alignment conditions.

2.2.2 Measurement procedure

The standard SHARPeR measurement procedure is shown in Figure 2.11. The optical head scans the mirror along the tangential direction from end to end in steps of ~1.2 mm (or an integer multiple of 1.2 mm), and each subaperture tangential and sagittal slopes are saved to a ‘*.***has***’ file. The step is chosen to match the optical head sampling size of ~1.2 mm, which is equivalent to the microlens size to simplify the stitching procedure. The current SHARPeR instrument can measure the test mirror in different orientations: either facing upwards or facing sideways. The sideways facing mirror measurement is performed using a 45° mirror placed at the bottom of the optical head (which rotates the beam by 90°) as shown in Figure 2.10. In this work, only measurements of mirrors in the face-up orientation are reported.

The measurement is done either in ‘**step by step**’ or ‘**onfly**’ modes, which are explained as follows. The optical head moves to a position, stops and measures the subaperture on the mirror in the step by step mode whereas in the onfly mode the head moves at a constant velocity and the camera captures subapertures at positions triggered by the stage encoder. The onfly mode is explained in more detail in section 2.5.5. All the other stage axes are not used by default, however new methods were developed during my thesis which use movement of the Rotation-Tip-Tilt (RTT) platform during the measurement; these will be explained further in section 2.5.4. The RTT axes are disabled if not used during measurement, as they can generate significant heat which has been observed to adversely influence the noise in the measurement data.

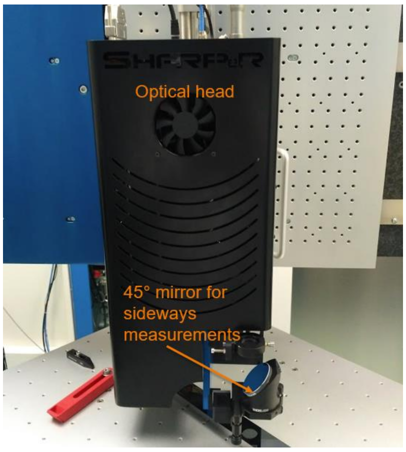

Figure 2.10 : Optical head and 45° mirror for sideways measurement.

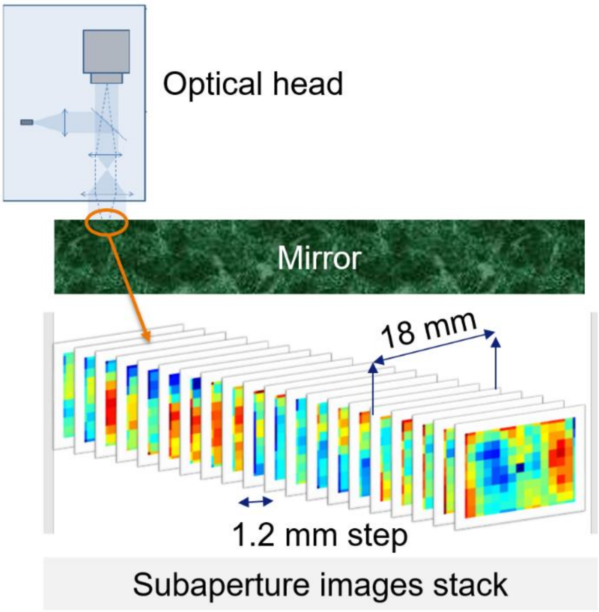

Figure 2.11: Measurement procedure with SHARPeR. The optical head scans in tangential direction with a step of ~1.2 mm equivalent to a microlens size.

2.2.3 Reference measurement procedure

Instrument errors from optical aberrations, misalignment and other factors can contribute significant errors in the measurement of synchrotron mirrors. To reduce these errors a reference measurement is taken on a good flat reference mirror. The reference measurement is subtracted from each mirror subaperture wavefront prior to stitching. One of the main criteria in selecting a reference mirror is its flatness, as the curvature of the test mirrors typically cannot be decoupled from the radius of curvature of the reference within stitching measurement techniques. However, StitchWave software can correct for reference curvature provided the translation stage is not bent. Another criteria is to generate a reference image with no errors from reference mirror and with all errors from instrument. The reference is usually captured at different locations on reference mirror and averaged to minimize reference mirror contribution, however this would still retain the reference curvature and may also retain some strong features on the reference. A reference mirror with good quality in comparison to test mirrors is required so as to capture most of the instrument errors. Still the flat reference mirror cannot capture instrument errors such as retrace errors which are explored in more detail in the next chapters. This approach is commonly used in coherence scanning micro-interferometers to reduce the influence of optical imperfections [75].

2.2.4 Data analysis

The SHARPeR subaperture data is stitched using a stitching algorithm developed by Imagine Optic (StitchWave). More stitching methods are developed and explored during my thesis which are presented in chapter 3. Prior to stitching, the reference measurement is subtracted from all subapertures. As an alternative approach the SHARPeR systematic errors were calibrated with an external standard interferometer (see section 4.7) and the calibration data is used to correct the subaperture measurements of curved mirrors before stitching. This method has shown improvements in measured curvature of test mirrors, which is presented in section 4.7.1. The measurements are repeated to minimize the statistical errors. Repeated scans are stitched separately and then averaged. The subapertures have tangential and sagittal slope errors which are stitched separately and later integrated to obtain the mirror height profile in 2D. Instrument scaling factors and magnification factor may be applied before or after stitching. A constant step equivalent to the optical head sampling (i.e. microlens spacing) is used as the stitching step, and for any other step which is not a multiple of sampling step, interpolation of data has to be done before stitching.

The stitched data is finally divided into different components for validation such as shape parameters and shape errors (or slope errors). The shapes can be flat, spherical, elliptical, toroidal and ellipsoidal or more complex freeform figures. The ideal shape for a synchrotron mirror is specified based on the application and the final manufactured mirror should have shape parameters within a defined tolerance range of the ideal shape. The shape parameters can be for example the radius of curvature for a spherical mirror, and p, q and ɵ for an elliptical mirror where p is the distance from source, q is the distance to image and ɵ is the incidence angle. The stitched data is fitted to the analytical equations of the shape and solved numerically. The shape fitting needs to consider the beamline constraints, for example for elliptical mirrors the source distance (p) is kept constant and not fitted. The fitting optimizes shape parameters to minimize the residuals (shape or slope errors) using simple least squares optimization, which is prone to inaccuracies from outliers. The features such as mirror edges, fiducials and etching edges and other outliers are usually excluded and fitting is done within clear aperture. The shape and slope errors have to be as low as possible and a tolerance level is usually defined at the beginning in terms of rms or peak to valley values.

2.2.5 Data acquisition with PySHARPeR software

Imagine Optic provided StitchWave is used for acquisition and stitching of measurements. Customization of StitchWave software is not possible, but we can use the interface libraries to design user specific applications. Using this approach, new acquisition/control software for SHARPeR (PySHARPeR) is developed in Python 3, with a full user interface using the ‘dll’ libraries from StitchWave. This approach has allowed a greater degree of flexibility in the control of the acquisition and stitching procedures than the use of the compiled StitchWave software interface. The PySHARPeR motor stage control is shown in Figure 2.12. The motors are moved by a control system designed by Q-Sys based upon a Delta Tau Power PMAC motor controller. This integrated system also manages the logic control for the air bearing pneumatics as well as the safety aspects using programs written with Delta Tau PMAC software. The high-level PySHARPeR software talks directly to the Q-Sys controller using SSH based communication protocols.

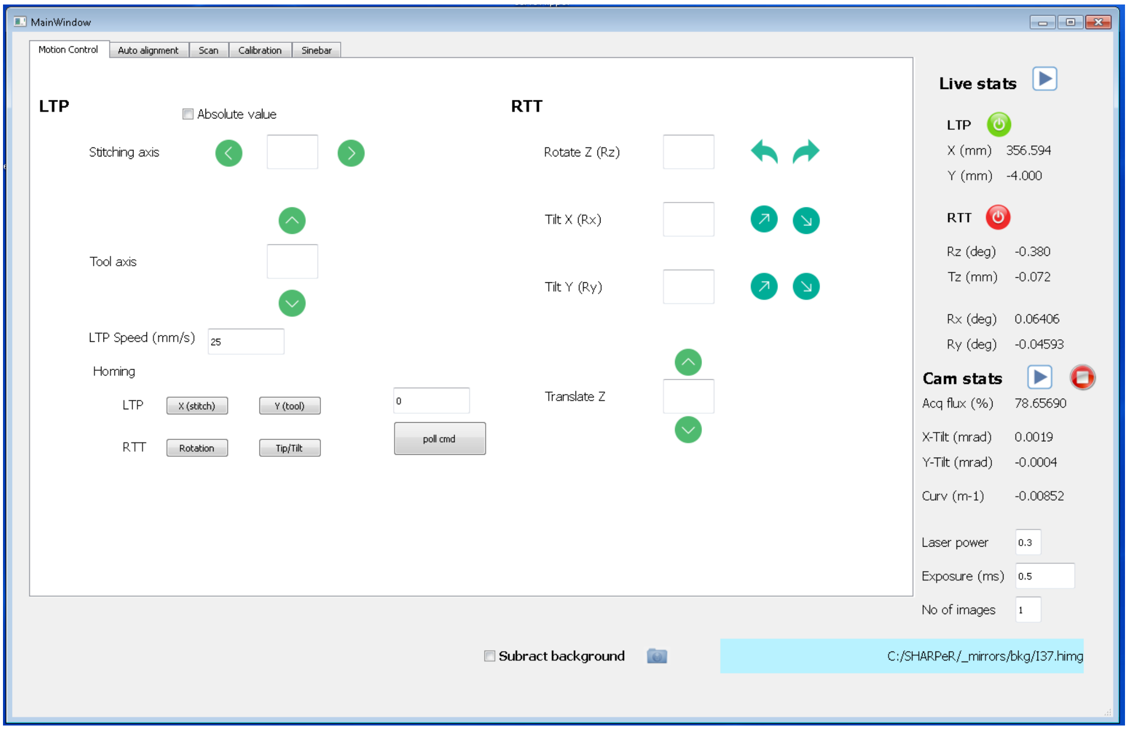

LTP Speed (mm/s) 25

0

LTP
X (mm) 356.594
Y (mm) -4.000

RTT
Rz (deg) -0.380
Tz (mm) -0.072

Rx (deg) 0.06406
Ry (deg) -0.04593

Acq flux (%) 78.65690

X-Tilt (mrad) 0.0019
Y-Tilt (mrad) -0.0004

Curv (m-1) -0.00852

Laser power 0.3
Exposure (ms) 0.5
No of images 1

C:/SHARPeR/_mirrors/bkg/I37.himg

Figure 2.12 : PySHARPeR – motion stage controls.

The Figure 2.13 shows the auto alignment functions in the PySHARPeR software. Auto alignment can center the mirror very accurately with edges detected with <0.01 mm error. It can also align the mirror surface parallel to detector so that the scanning is done along the mirror length and not skewed with respect to the mirror. It can autofocus the mirror using the tool lens, when at the focus the mirror wavefront should be optimally imaged at the entrance of microlens array. It can auto align the SUT to the normal incidence position where the total wavefront tilt is close to zero. The alignments are saved to text files, which are loaded during scanning.

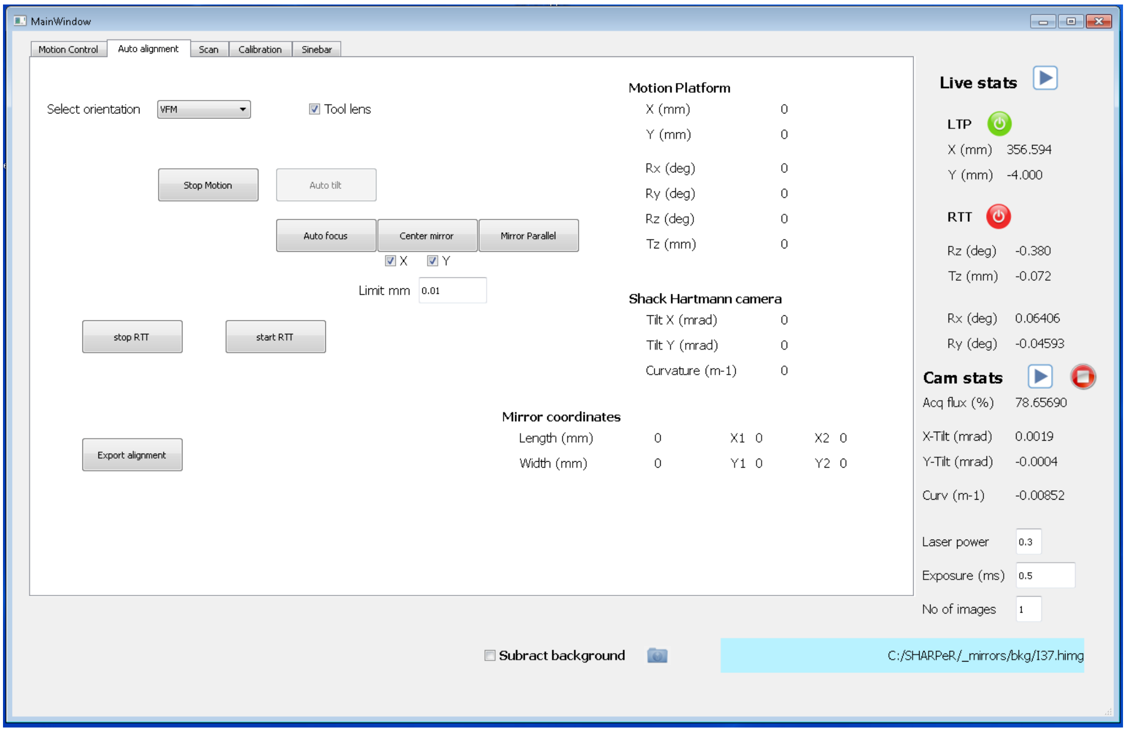

Select orientation VFM

☑ Tool lens

☑ X ☑ Y

Limit mm 0.01

Motion Platform
X (mm) 0
Y (mm) 0
Rx (deg) 0
Ry (deg) 0
Rz (deg) 0
Tz (mm) 0

Shack Hartmann camera
Tilt X (mrad) 0
Tilt Y (mrad) 0
Curvature (m-1) 0

Mirror coordinates
Length (mm) 0 X1 0 X2 0
Width (mm) 0 Y1 0 Y2 0

LTP
X (mm) 356.594
Y (mm) -4.000

RTT
Rz (deg) -0.380
Tz (mm) -0.072
Rx (deg) 0.06406
Ry (deg) -0.04593

Acq flux (%) 78.65690
X-Tilt (mrad) 0.0019
Y-Tilt (mrad) -0.0004
Curv (m-1) -0.00852

Laser power 0.3
Exposure (ms) 0.5
No of images 1

☐ Subract background

C:/SHARPeR/_mirrors/bkg/I37.himg

Figure 2.13 : PySHARPeR – auto alignment functions. The mirror is aligned parallel to the detector and at normal incidence where wavefront tilts are close to zero in X and Y directions. Mirror centering is also accurately adjusted through automated programs.

The Figure 2.14 shows the scan setup in PySHARPeR. A provision was provided to do AB and BA scans continuously without manual interventions in between which can minimize environmental disturbances. The mirror can be scanned multiple times in different modes such as normal incidence, multi incidence in addition to default scanning. Measurements can be performed step by step or in onfly. For normal incidence scans, an initial scan can be done to determine the tilts required at each subaperture position to be in normal incidence. The repeated scans can be performed by reusing the initial tilt axes positions as the tilt stages are highly repeatable (<10 µrad repeatability). The RTT tilt stage repeatability is in the same order as the pitch and roll errors of optical head translation axis.

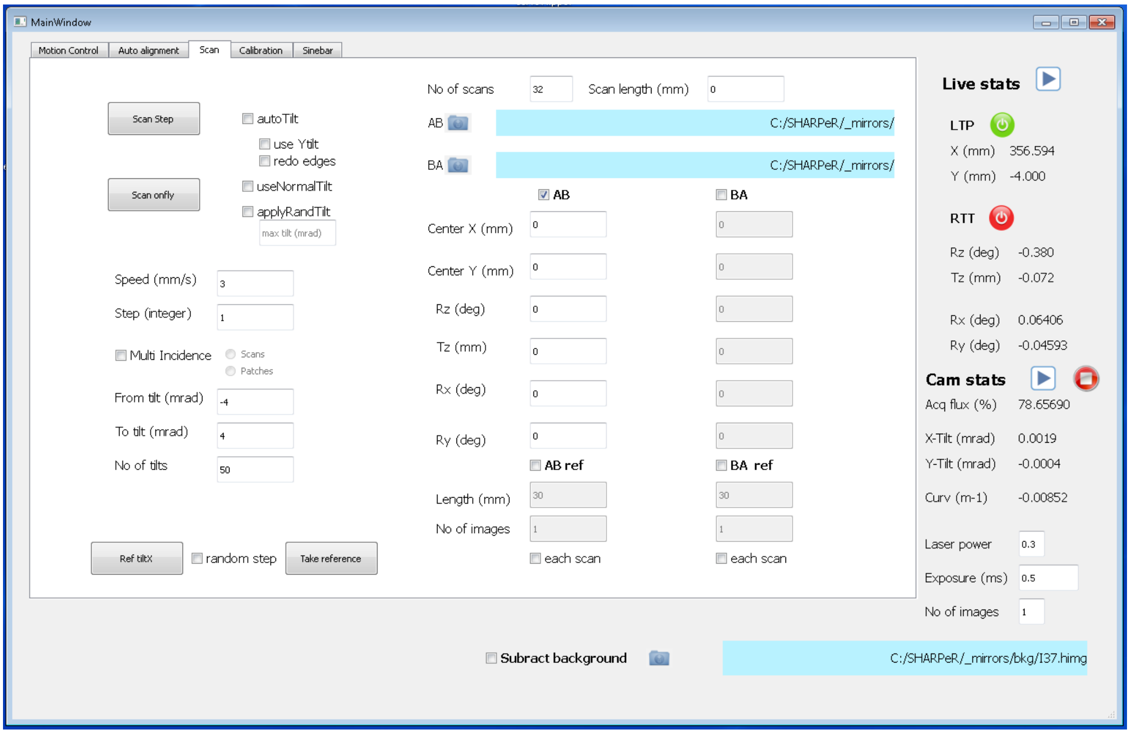

No of scans 32
Scan length (mm) 0
AB C:/SHARPeR/_mirrors/
BA C:/SHARPeR/_mirrors/
☐ autoTilt
☐ use Ytilt
☐ redo edges
☐ useNormalTilt
☐ applyRandTilt
max tilt (mrad)
Speed (mm/s) 3
Step (integer) 1
☐ Multi Incidence ○ Scans ○ Patches
From tilt (mrad) -4
To tilt (mrad) 4
No of tilts 50
☐ random step

	☑ AB	☐ BA
Center X (mm)	0	0
Center Y (mm)	0	0
Rz (deg)	0	0
Tz (mm)	0	0
Rx (deg)	0	0
Ry (deg)	0	0
	☐ AB ref	☐ BA ref
Length (mm)	30	30
No of images	1	1
	☐ each scan	☐ each scan

LTP
X (mm) 356.594
Y (mm) -4.000
RTT
Rz (deg) -0.380
Tz (mm) -0.072
Rx (deg) 0.06406
Ry (deg) -0.04593
Acq flux (%) 78.65690
X-Tilt (mrad) 0.0019
Y-Tilt (mrad) -0.0004
Curv (m-1) -0.00852
Laser power 0.3
Exposure (ms) 0.5
No of images 1
☐ Subract background C:/SHARPeR/_mirrors/bkg/I37.himg

Figure 2.14 : Scan setup with PySHARPeR. Scans can be done in step-by-step / onfly, in normal incidence and in multi incidence modes.

PySHARPeR has additional features compared to StitchWave such as auto alignment and scans in normal incidence and multi incidence. These new measurement methods have shown significant improvement in measurement quality as shown in sections 4.4 and 4.5, which would not have been possible without the ability to customize the scan controls.

2.3 Spatial resolution of SHARPeR

Spatial resolution is an important parameter for synchrotron mirror metrology and different metrology instruments operate over different spatial frequency domains [26]. In imaging instruments (e.g. microscopes, telescopes), the spatial resolution is limited ultimately by the diffraction limit of instrument. However, in slope measuring instruments like SHARPeR, spatial resolution is compromised to achieve high phase accuracy. The SHARPeR spatial resolution is limited by the size of the microlens of its wavefront sensor, however it can potentially be reduced using afocal with magnification larger than the current value of 1. New types of wavefront sensors are in development which offer improved spatial resolution [76]. The SHARPeR wavefront sensor micro lens size along with its focal length affects the range of measurable tilts and curvatures of the synchrotron mirrors. The microlens size of ~1.2 mm was chosen to operate in the low spatial frequency domain similar to LTPs and NOMs and to measure slopes with sensitivity smaller than 50 nrad. Simulations are shown in the current section to understand the spatial resolution limitations and minimum sampling required on instruments like SHARPeR. Measurements were performed on a real chirped mirror (with sinusoidal pattern of increasing spatial frequency from end to end) to understand spatial resolution limitations, and they are shown in chapter 4.4.2.2.

2.3.1 Simulations of spatial resolution of wavefront sensor with a chirped mirror profile

Following a similar approach to Yashchuk [39], in order to simulate the spatial resolution we assume a 1000 mm long mirror with chirped profile with spatial frequency varying from 0.1 to 1.9 mm^{-1} from end to end with constant slope amplitude as shown in Figure 2.15. The chirp slope profile ($s(x)$) with instantaneous frequency ($f_i(x)$) is simulated in 1D using the following equation.

$$s(x) = \sin[2\pi(ax + bx^2)]\,; \quad a = 0.1\,mm^{-1}, b = 9e-4\,mm^{-2}$$

$$f_i(x) = a + 2bx$$

A single ideal 1D microlens with a size of 1 mm is assumed and the mean of theoretical slopes within the microlens size is calculated to give the microlens measurement. The slope simulations are done over the full mirror length at a sampling step of 1 microlens size (i.e. 1 mm). The modulation transfer function (MTF) is calculated as the ratio of simulated microlens slopes to theoretical slopes [77]. The power spectral density (PSD) is calculated for both simulated and theoretical mirror slopes. MTF and PSD of simulations and theoretical slopes are presented in Figure 2.15. The MTF shows drop towards high frequencies and becomes negative above 1 mm^{-1} which implies antiphase in simulated slopes above 1 mm^{-1}. The PSD shows larger spectral power in simulated microlens slopes than theoretical slopes which may be from insufficient sampling, and the antiphase frequencies (>1 mm^{-1}) power is adding to lower frequencies in the PSD which is probably arising from aliasing. The PSD spatial frequencies are cutoff at 0.5 mm^{-1}, as the sampling is equivalent to microlens size of 1 mm.

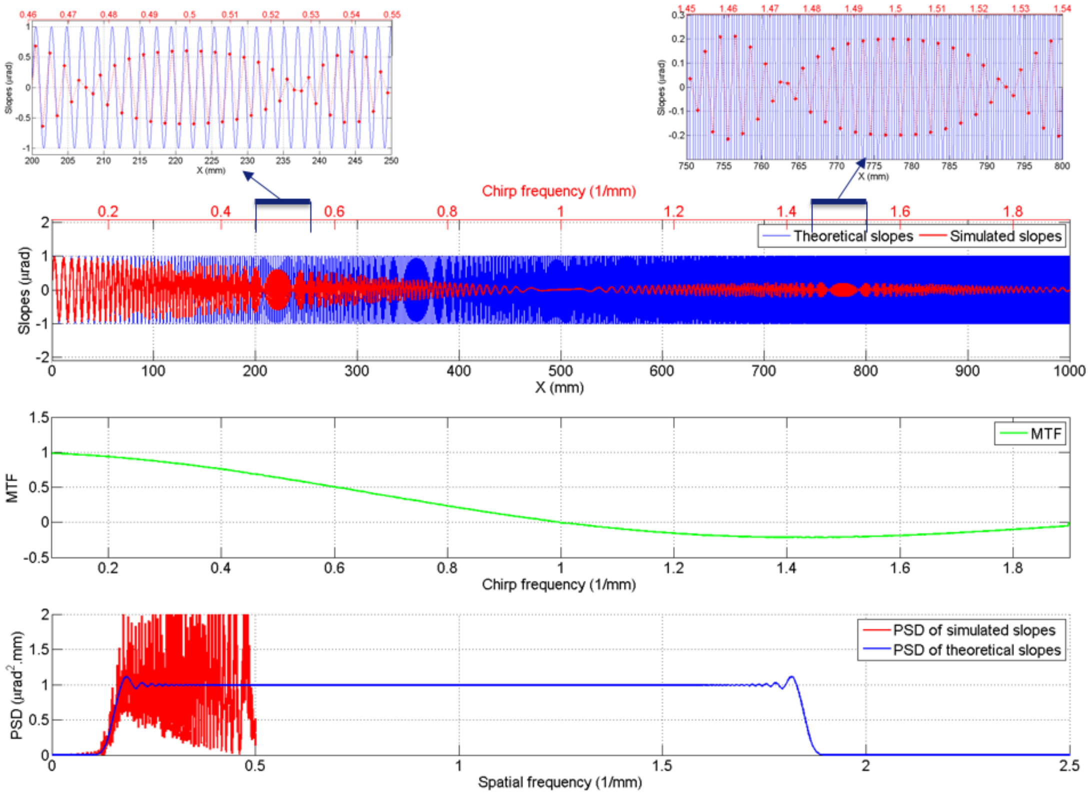

Figure 2.15 : Simulation of microlens slopes on 1 m long chirped mirror with chirp from 0.1 mm^{-1} to 1.9 mm^{-1} end to end. The microlens size and sampling is 1 mm.

Sampling period of signal is reduced to 0.5, 0.33, 0.1 mm^{-1}, and corresponding simulations for chirped slopes, MTF and PSD are shown in Figure 2.16, Figure 2.17 and Figure 2.18. The simulations shown in Figure 2.18 shows a cutoff in PSD at 1 mm^{-1} spatial frequency, which can also be seen in the MTF curve. The sampling size smaller than half the microlens size is needed to measure all spatial frequencies in the PSD, which is <0.5 mm for the simulations presented here. At higher samplings (Figure 2.17 and Figure 2.18), the PSD shows non-zero power at frequencies > 1 mm^{-1}, but it is measured in antiphase and it is problematic as it creates false low frequency signals. The MTF curve remains almost unchanged in all the simulations presented in this section, which implies the microlens slopes fall on the same curve irrespective of sampling (ideal curve is close to very high sampling as shown in Figure 2.18).

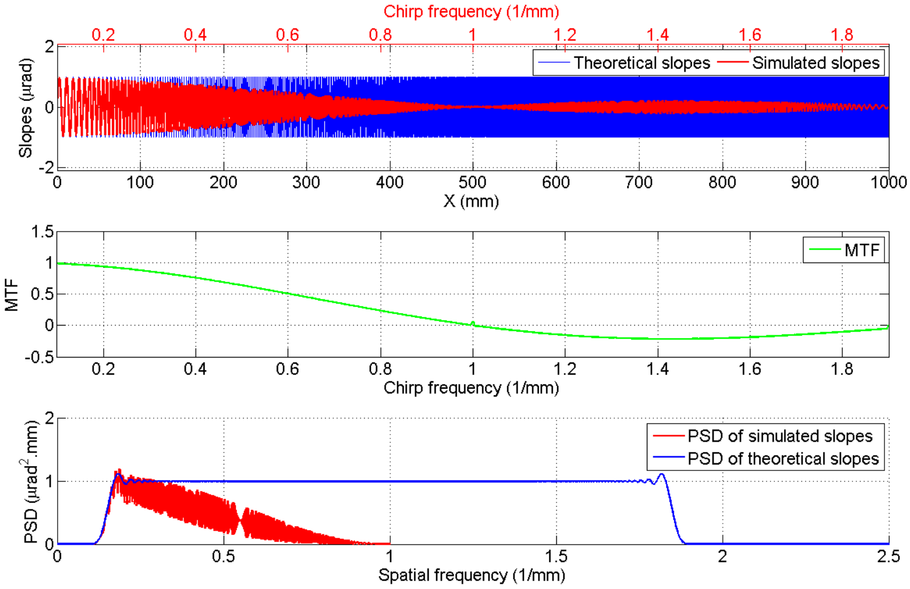

Figure 2.16 : Simulation with 1 mm microlens size and sampling of 0.5 mm.

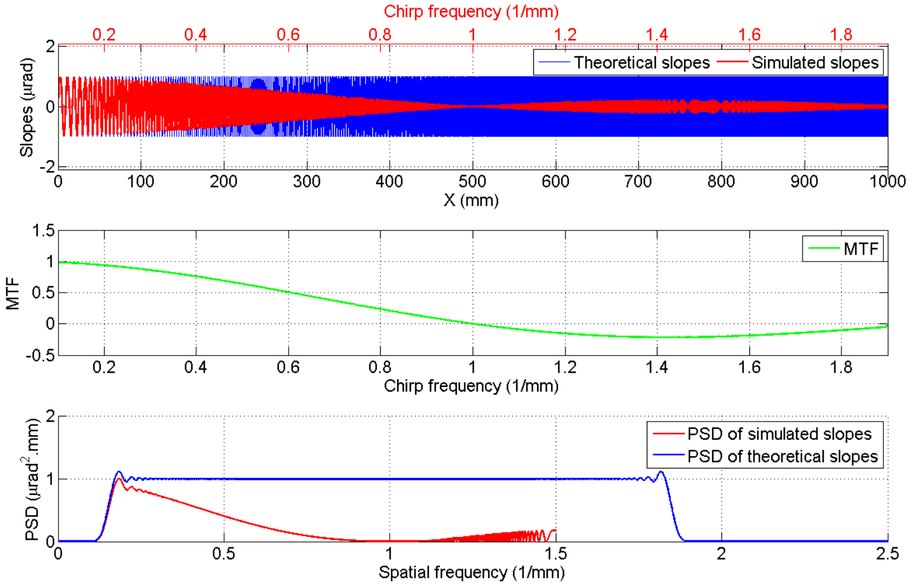

Figure 2.17 : Simulation with 1 mm microlens size and sampling of 0.33 mm.

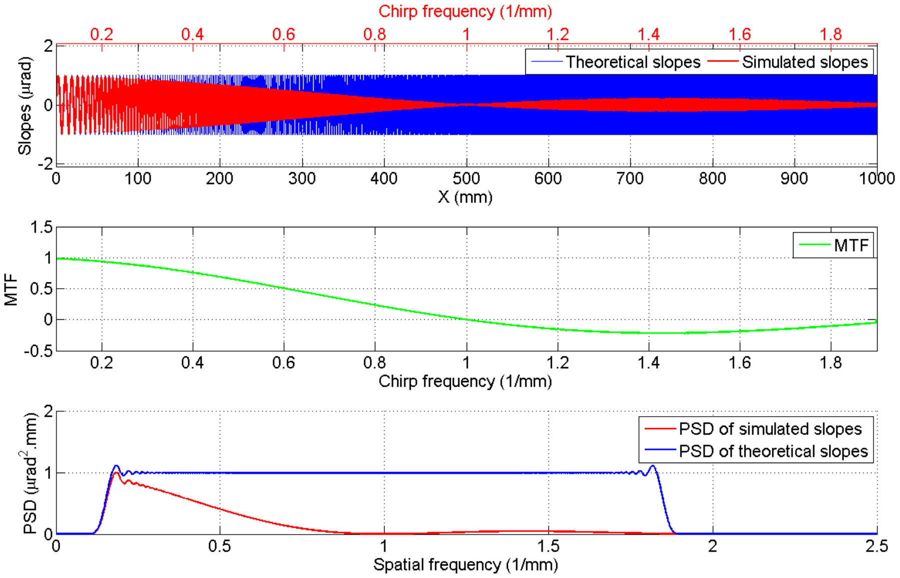

Figure 2.18 : Simulation with 1 mm microlens size and sampling of 0.1 mm.

2.4 Sources of measurement errors

The SHARPeR instrument is designed to measure the slope errors of synchrotron mirrors with sub-50 nrad accuracy. Consequently, characterization of error sources is critical for best performance. The measurement error is defined as ‘the measured quantity value minus a reference quantity value’ [79]. In the absence of a reference quantity value, which is the case for X-ray mirrors, methods such as accuracy with respect to measurements on the same test mirror by other instruments and measurement repeatability are often used to express measurement errors (see section 1.3). For a deeper understanding of measurement errors, we can identify systematic and random errors. Systematic error is defined as the component of measurement error that remains constant in repeated measurements or varies in a predictable manner, whereas the random error is the component which varies in an unpredictable manner [79]. Systematic errors for the SHARPeR instrument mostly arise from the optical head due to optical aberrations and misalignment of optical elements from design specifications etc. Random errors for the SHARPeR instrument are mostly from environmental fluctuations in airflows and temperature among others. Some of the systematic errors may also be generated by constant heat sources which cause static temperature gradients across the room. In this section and the subsections, the systematic and random errors from different sources within SHARPeR system are explored in detail.

The SHARPeR measurement error sources can be divided into two broad categories as shown in Figure 2.19, one section dealing with optical path and the other dealing mechanical and environmental errors. The latter category does not act in isolation but compounds with optical errors, for example thermal sources can cause shape changes of mirror during measurement as well as change the refractive index of air along optical path. Errors can appear also in the stitching data analysis from the choices of algorithms in addition to measurement errors. These will be studied separately in Chapter 3.

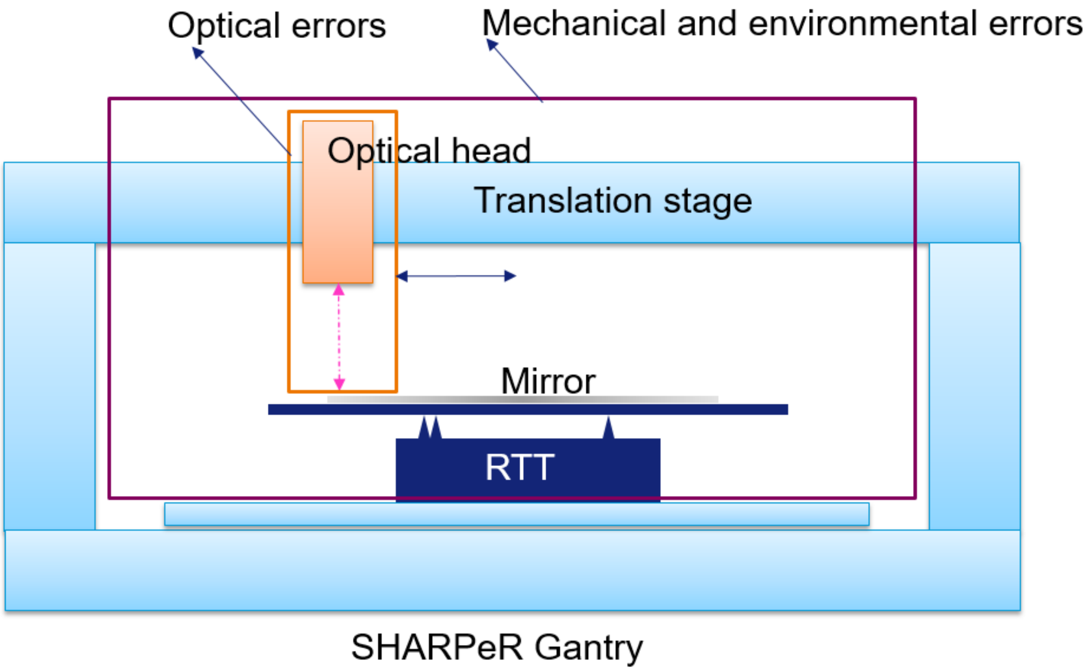

Figure 2.19 : Schematic of SHARPeR measurement processes for errors and noise characterization.

2.4.1 Optical and detector errors

Measurement errors originating from the optical head can be understood by considering different elements along the optical path and characterizing their behavior. The optical path starts with laser source and ends with detection by the CCD sensor in the wavefront sensor as shown in Figure 2.20. The laser beam exits from a fiber with a beam diameter of few µm and is collimated to ~25 mm size beam using the collimation lens. The collimated beam has a nearly flat wavefront (plane wave or constant phase) with a Gaussian intensity distribution (see section 2.1.2). The collimated beam is redirected by a polarizing beam splitter and passes through an afocal lens setup before impinging on the synchrotron test mirror. The afocal setup images the test mirror object plane onto the entrance pupil of the wavefront sensor, i.e. in the plane of microlens array. The incident beam passes through the afocal lens setup such that any phase deformation introduced by the afocal lens setup should be compensated in the reflected beam when it retraces the same path. As we shall see, in practice, this condition can only be satisfied for a perfectly flat mirror in normal incidence. The microlens array focusses the image wavefront (image of test mirror) onto the CCD sensor. The CCD intensity image is transferred to a PC and analyzed using proprietary Imagine Optic software algorithms to obtain slope arrays.

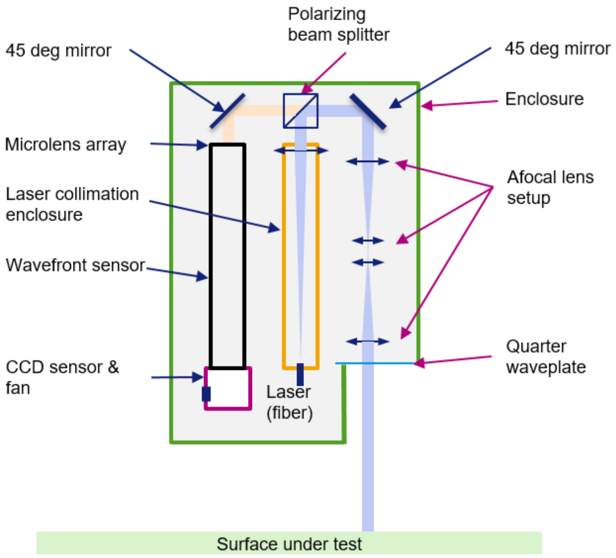

Figure 2.20 : Schematic of optical head.

2.4.1.1 Systematic errors from intensity variation across microlens array

The spatial resolution studies of SHARPeR are shown section 2.3, where the simulations are performed using an ideal microlens and assuming uniform intensity. The microlens slope calculation was also performed using a simple arithmetic mean. In this section, the measurement of wavefront by an ideal microlens is explained theoretically and possible systematic errors coming from variations in intensity across the microlenses are studied.

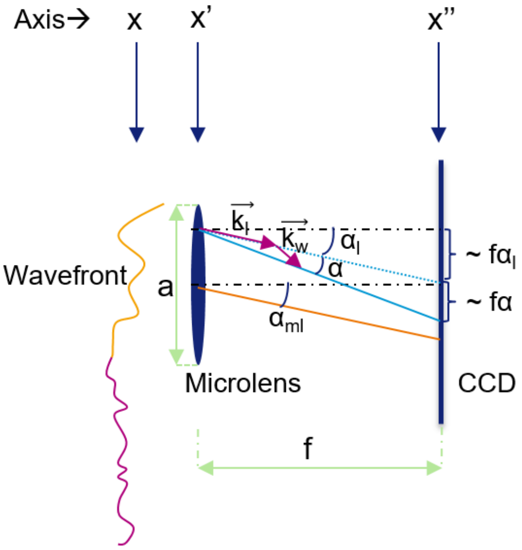

Figure 2.21 : Schematic of wavefront slope measurement by a single microlens.

The Figure 2.21 shows a schematic of a single ideal microlens measuring a deformed wavefront. The wavefront theoretical analysis is explained in detail in Appendix 1, which has been studied earlier by Bará, Salvador [78]. Assuming uniform intensity of wavefront, the microlens slopes can be described by eq.(2-1) measured at a mirror position x.

$$\alpha_{ml}(x) = \frac{\int_{x-a/2}^{x+a/2} \alpha(x')dx'}{\int_{x-a/2}^{x+a/2} dx'} = \frac{1}{a}\int_{-a/2}^{a/2} \alpha(x'-x)dx'$$

$$\alpha_{ml}(x) = \int_{-\infty}^{\infty} \frac{1}{a}\mathrm{rect}(\frac{x'}{a})\alpha(x'-x)dx'$$

$$\alpha_{ml}(x) = \frac{1}{a}\operatorname{rect}\left(\frac{x}{a}\right) * \alpha(x)$$

(2-1)

The eq.(2-1) shows the microlens slope (α_{ml}) as the mean of all the slopes of the wavefront (α) over the whole microlens aperture, which is equivalent to calculating the mean focal spot position in CCD plane. This approximation holds true at small angles and can be used for SHARPeR wavefront sensor whose microlenses operate in ±4 mrad slope range. In the equation, the size of microlens is represented by 'a', the lens aperture function '*1/a* rect*(x/a)*' represents the rectangular function of width 'a' and '*' stands for the convolution. The microlens may have aberrations which have to be calibrated with a flat wavefront and the calibrated microlens slope is subtracted as shown below.

$$\alpha_{ml,c}(x) = < \alpha(x) > - < \alpha_c(x) >$$

(2-2)

From eq.(2-1) it can be inferred that the simulated slopes shown in the section 2.3.1 are obtained by applying a filter of rectangular function over theoretical slopes. The rectangular function is the aperture function and the convolution of this with the theoretical slopes provides microlens slopes [39]. The theoretical microlens slopes (assuming this rectangular aperture) and the simulated slopes are shown in Figure 2.22, on a 100 mm long chirped mirror with chirp spatial frequency 0.1 mm^{-1} to 1.9 mm^{-1}. The chirp slope profile is simulated in 1D using the following equation.

$$s(x) = \sin[2\pi(ax + bx^2)]; \quad a = 0.1\ mm^{-1}, b = 9e-3\ mm^{-2}$$

The theoretical and simulated microlens slopes match very accurately in Figure 2.22. The microlens slopes on simulated mirror drop in amplitude at higher frequencies and are cut off at ~50 mm at spatial frequency 1 mm^{-1}. The microlens slopes between 50 mm and 100 mm are in antiphase to the theoretical slopes. The antiphase beyond resolution cutoff is a known phenomenon, published earlier by Yashchuk et al. [39]. The simulated curve with sampling of 0.1 mm almost completely resolves the theoretical microlens slopes obtained from convolution of theoretical mirror slopes with rectangular aperture. Whereas sampling of 1 mm could not completely resolve the theoretical microlens slopes.

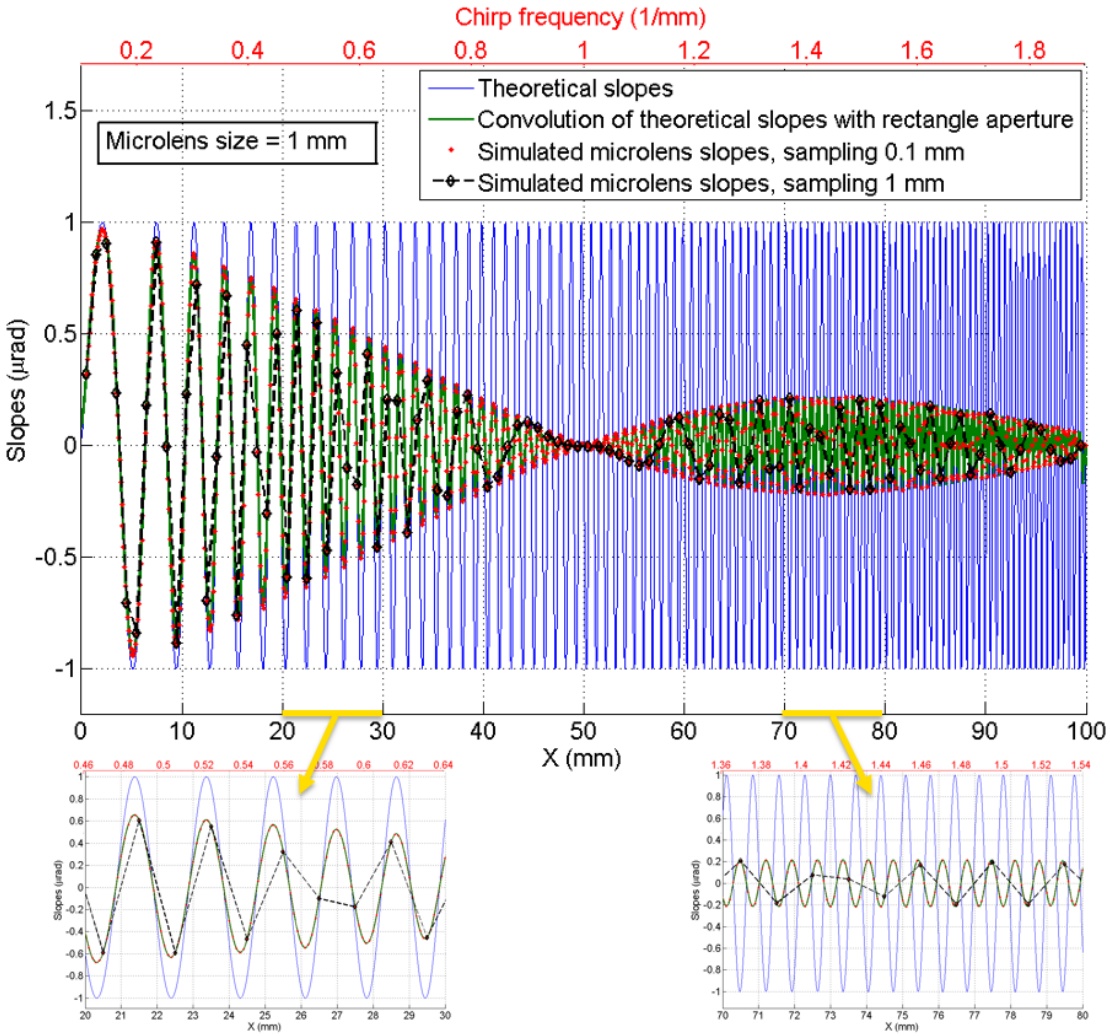

Figure 2.22 : Simulation of microlens slopes on 100 mm long chirped mirror with chirp frequency from 0.1 mm^{-1} to 1.9 mm^{-1} end to end. The microlens size is 1 mm and samplings of 1 mm and 0.1 mm are plotted (red & black curves). Theoretical microlens slopes with rectangular aperture function are also shown (green curve).

If the intensity is not uniform the microlens slopes can be expressed using eq.(2-3). The intensity over the microlens is given by $I(x')$ and sum of intensities over the microlens is given by the term I_{ml}.

$$\alpha_{ml}(x) = \frac{\int_{x-a/2}^{x+a/2} I(x')\,\alpha(x')\,dx'}{\int_{x-a/2}^{x+a/2} I(x')dx'} = \frac{1}{I_{ml}} \int_{-a/2}^{a/2} I(x'-x)\,\alpha(x'-x)dx'$$

$$\alpha_{ml}(x) = \frac{1}{I_{ml}} \int_{-a/2}^{a/2} I(x')\, \alpha(x'-x) dx'$$

$$\alpha_{ml}(x) = \int_{-\infty}^{\infty} \frac{1}{I_{ml}} rect(\frac{x'}{a}) I(x') \alpha(x'-x) dx'$$

$$\alpha_{ml}(x) = \frac{1}{I_{ml}} \mathrm{rect}\left(\frac{x}{a}\right) I(x) * \alpha(x)$$

(2-3)

Where it is assumed that $I(x'-x) = I(x') \quad \forall x \in \{\text{mirror positions}\}$, i.e. the intensity is constant over the mirror length and measurement time. Mirror reflectivity is usually uniform across the length and a stable laser ensures a uniform intensity profile over measurement time. The normalized intensity map of SHARPeR wavefront sensor is shown in Figure 2.23. The intensity is averaged over pixels in each microlens spot and the plot shows the intensity variations across the microlens array. The intensity variation is approximately Gaussian and has weak variation over an individual microlens aperture.

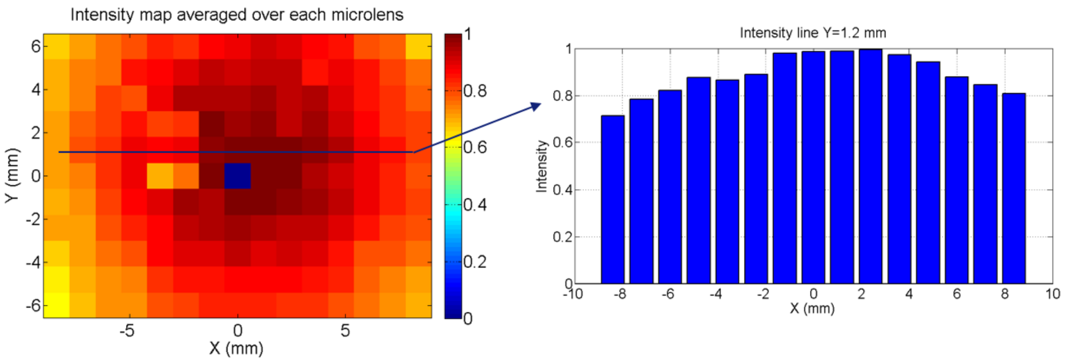

Figure 2.23 : The intensity map of SHARPeR wavefront sensor, with intensity of pixels within microlens spots averaged. The intensity is in Gaussian shape and it varies across microlenses and within microlens size.

The intensity variation is ~ 42 % from the maximum to the minimum over the microlens array but over a single microlens the variation is much smaller. The theoretical Gaussian shape with nearly sixty percent of maximum at the edges fits to the intensity profile of

SHARPeR as shown in Figure 2.23. The contrast ($[I_{max} - I_{min}] / I_{max}$) is 0.42 for the full Gaussian, however over the central microlens it is close to zero and at the corner microlens it is close to 0.13.

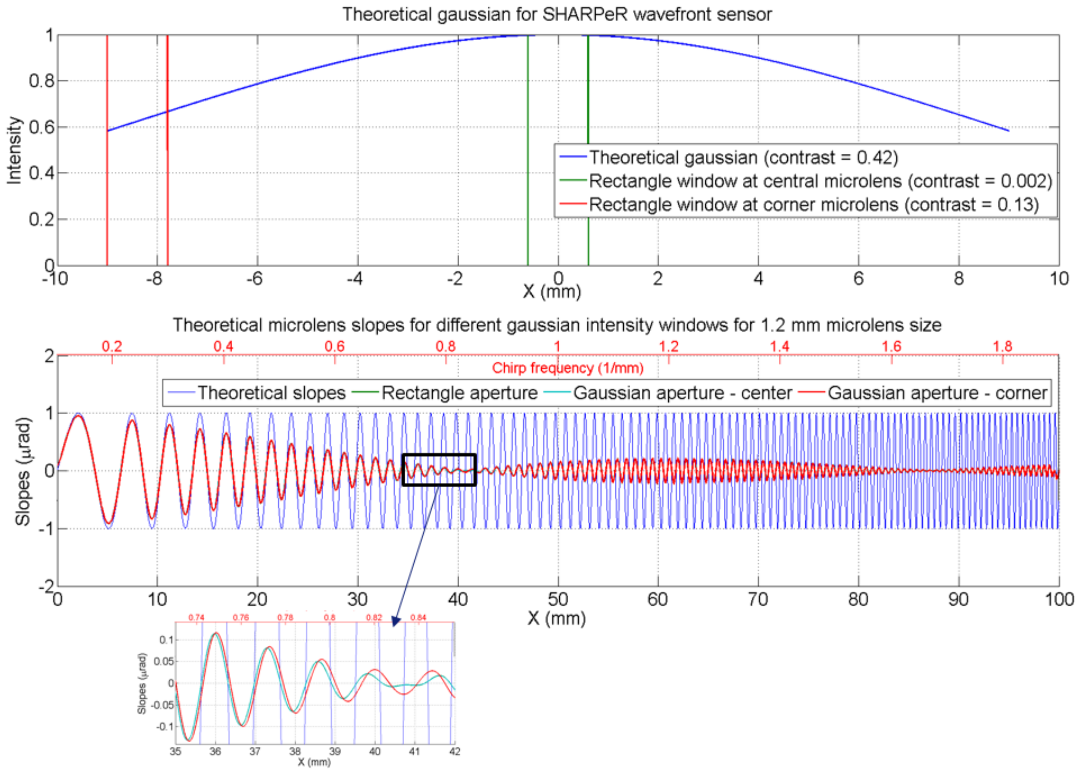

Figure 2.24 : Theoretical microlens slopes with three different intensity variations over the microlens aperture is shown in the bottom curve for (1) constant intensity (blue curve), (2) Gaussian intensity variation close to center of Gaussian (green curve) and (3) Gaussian intensity variation at corner microlens (red curve). The top curve shows intensity variation (blue curve) across wavefront sensor length (18 mm) and two windows of single microlens size at center and edge (green & red).

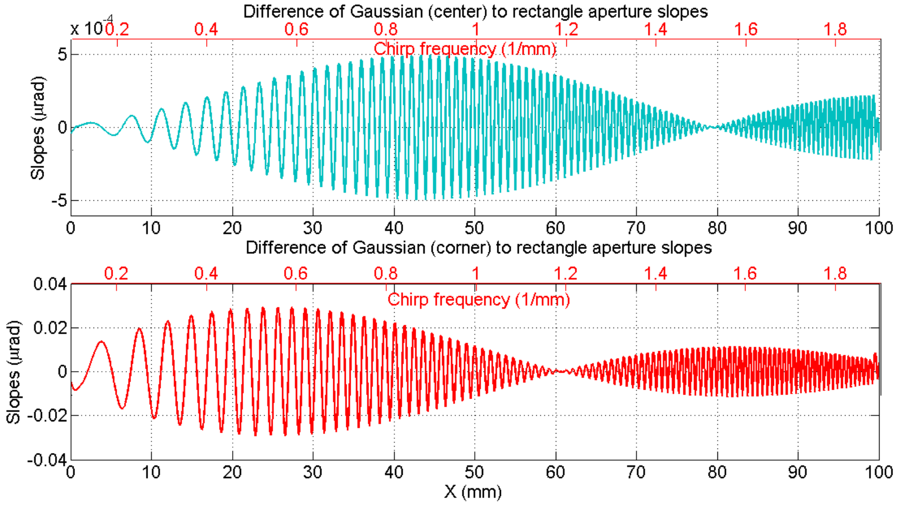

Figure 2.25 : Difference of microlens slopes calculated by convolution with (a) Gaussian (center) and rectangle and (b) Gaussian (corner) and rectangular aperture.

A theoretical 100 mm long chirped mirror (chirp 0.1 to 1.9 mm^{-1}) is convoluted with microlens of size 1.2 mm using three aperture functions corresponding to rectangular (uniform intensity), Gaussian center (very little intensity variation) and Gaussian corner is shown in Figure 2.24. The three functions produce little differences (<0.06 µrad or 3%) in the slope measured by the microlens as shown in Figure 2.25, and it can be neglected.

Most of the results presented here used sampling of microlens size (1.2 mm), as the oversampling methods has been analyzed at later stages of thesis and hence not implemented. But sampling at-least half of the microlens size is required to measure with the resolution limits of SHARPeR instrument.

2.4.1.2 CCD detector

The SHARPeR wavefront sensor uses a model VMV-8M camera manufactured by ‘Illunis’ which integrates a Kodak KAI – 08050 CCD image sensor. The characteristics of the CCD sensor such as dark current, readout noise, photon noise and sampling errors can give rise to measurement errors which may affect the centroid detection accuracy of the wavefront sensor [80]. The specified dark current for the CCD sensor (specifications in Appendix 3) is 140 electrons/s, the read-out noise is 12 electrons rms and the charge capacity of pixel is 20,000 electrons. The Appendix 3 contains different measurements to study the CCD performance at different exposures in a dark environment and in environment with background lighting. The Appendix 3 also estimates the contribution of different CCD noise sources to slope determination. Measurements with SHARPeR are usually made with ambient lighting in the enclosure. This background light contributes to the background noise signal in the CCD images. SHARPeR typically operates with exposures 0.5 ms to 100 ms, and even at 100 ms exposure the dark current noise is 14 electrons which is only 0.07 % of saturation level. The signal contribution from background light usually dominates (~1.4 % of saturation level at 100ms exposure) and is described in more detail in Appendix 3. The background noise contribution to centroid detection is minimized by usually applying a threshold on intensities, and only pixels with intensities above a threshold are used for centroid calculation. Some of the laser light reflected from optical surfaces in the SHARPeR head may also contribute to background noise in addition to the ambient lighting, even though the design has been optimized to minimize this (see section 2.1.2). The background intensity is measured at the operating laser level before measuring the test mirror and subtracted from each test image. The image noise after subtracting background is around 20 electrons rms for any exposure below 100 ms (see Appendix 3) which may be considered as the read noise, which is slightly larger than specified read noise for the sensor alone of 12 electrons rms. This slight increase may be attributed to either a contribution to the read-out noise from the camera electronics, fluctuations in background lighting, non-uniform response of sensor across pixels for background light and to dark current.

The noise in a single slope measurement has contributions from read noise of 28 nrad rms and from photon noise of 36 nrad rms (see Appendix 3), which are obtained using an image on flat test mirror with 0.5 ms exposure and laser power of 1.5 mW (giving typical peak intensities ~90% of the saturation values). The total noise in slopes for such an image is 45 nrad rms: This noise floor can be further reduced by averaging multiple images. The noise presented here is calculated for tangential slopes but it is equally valid for sagittal slopes.

2.4.1.2.1 Sampling errors

The CCD pixels discretely sample the microlens focal spot which can influence the centroid calculation. The sampling errors are dependent on the position of the spot itself, i.e. dependent on the wavefront slope and they are usually periodic with a period of one pixel. Such sampling errors can be severe for small spots of the size of one pixel or below but they reduce in amplitude for spots covering several pixels [81], [82]. Although the SHARPeR microlens spots are several pixels wide (rms width 6.6 pixels, FWHM of 15 pixels), the stringent accuracy conditions, which are in the order of thousandth of a pixel size (calculated for 50 nrad sensitivity, using CCD pixel size of ~ 5.5 µm and wavefront sensor focal length of ~0.3 m), require an analysis of these sampling errors.

The sampling errors are calculated using the formalism developed by Morgan et al [82]. The real microlens spot is shown in Figure 2.26, and it has a size of **217 pix x 217 pix**. The microlens focal spot is nearly sinc^2 shape in X and Y directions as the microlens is square shaped. The spot is averaged along sagittal pixels and the sampling errors are plotted for tangential centroid shift as shown in Figure 2.27. To determine the sampling errors, the spot (1D) is interpolated to subpixel positions with very high sampling of 1/1000th of pixel. The differences in the centroid positions calculated using the interpolated and the original focal spot curves (1D) are referred as the sampling errors. These are the sampling errors in tangential direction and similar procedure can be done to determine sagittal sampling errors. The sampling errors are calculated at different wavefront tilts within the range ~±90 µrad, which corresponds to microlens focal spot shift on the CCD over 10 pixels as shown in Figure 2.27.

The sampling errors are lowest when full spot is considered in centroiding calculation (<0.02 nrad PV). The read noise and background noise become larger when the full spot is considered for centroiding and limiting the spot size to ‘two side lobes’ or to ‘no side lobes’ increases the sampling errors only to <0.05 and <0.2 nrad PV respectively. Limiting the spot to cover half of the first side lobe increases sampling errors to <1.5 nrad PV which may be from steep edges of the spot at half side lobes.

Instead of determining the spot size based on side lobes, a global threshold excluding background and side lobe pixels can be applied. The maximum of first side lobe is 7.5 % of full spot maximum, for the spot profile shown in Figure 2.27. The sampling errors of the measured spot with a threshold of 10% is shown in Figure 2.28. The threshold avoids the side lobes as well as a small portion of main lobe, but the sampling errors increase to <25 nrad PV. The exact threshold used by Imagine Optic and corresponding calibration procedure is confidential information and so it is not presented here. Sampling errors are systematic errors and hence cannot be minimized through averaging like most of the other CCD based errors, however these errors are quite small compared to other errors sources and ignored at the current stage.

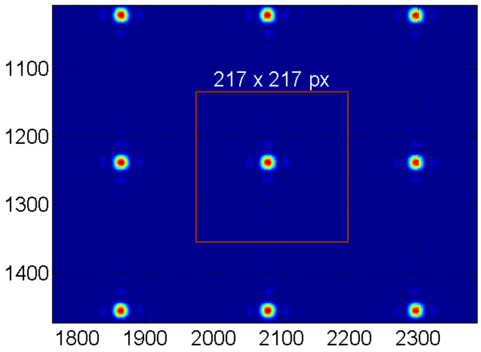

Figure 2.26 : Microlens spot full size.

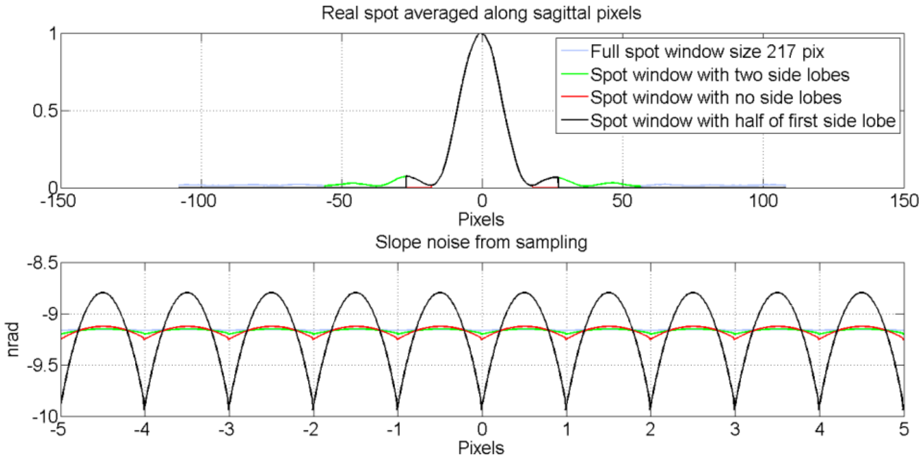

Figure 2.27 : The sampling errors from a measured microlens spot. The spot is averaged in sagittal direction (top image) and sampling errors calculated for different spot size limits (bottom image). The window is kept at 217 pixels for all

spot sizes. The spot size is varied to cover/uncover side lobes and intensities beyond spot size are set to zero (green, red and black curves in the top image).

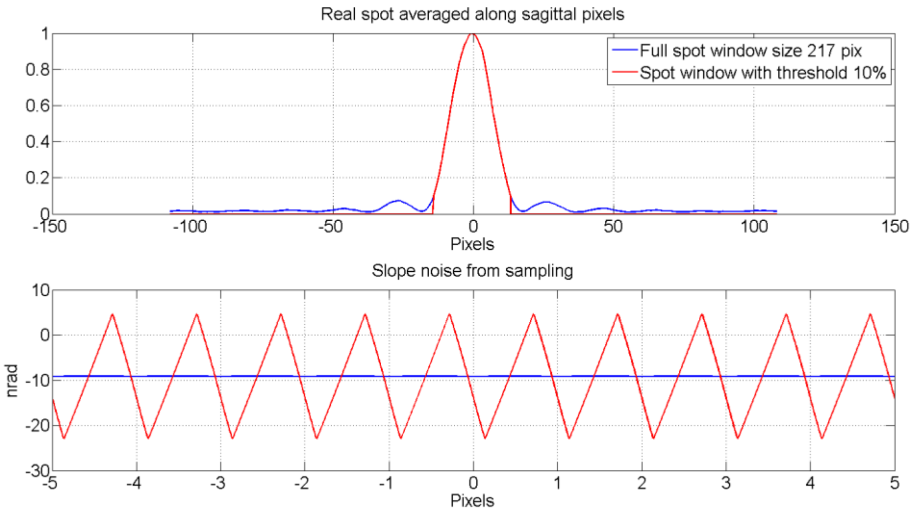

Figure 2.28 : The sampling errors from a measured microlens spot with a threshold of 10 % compared to full spot size. The 10% threshold completely ignores the side lobes and a small portion of main lobe (top image red curve).

2.4.1.3 Defocusing errors

The SHARPeR optical head by design is robust to the defocusing errors as it is a slope measuring instrument. Defocusing here refers to the test surface position being different to the focal distance defined by the tool lens (as explained in section 2.2.1, the tool lens is used to define test mirror focal position along optical axis where it is in conjugate plane with wavefront sensor microlens array), defocus errors refer to errors in measured slopes caused by defocusing. The defocusing can arise from (a) misalignment of the test surface, (b) piston errors from optical head translation, (c) on highly curved mirrors only small region may be in focus etc. The defocus primarily impacts the measured radius as explained in detail in Appendix 2. The appendix shows that on the theoretical basis the radius of curvature changes very little, nearly equivalent to the focal plane shift which does not exceed few mm in extreme cases, by only 0.1% for a mirror with radius 10 m even for a large defocus of 10 mm. The defocus does not change slope errors by design, except from position errors. The defocus errors also contribute to small position errors which can be neglected, e.g. for a defocus error of 1 mm at a random location on mirror, a slope of 1 mrad causes position errors of only 1 µm.

The defocus errors of the real SHARPeR instrument depend also on additional factors such as systematic instrument errors, environmental changes etc. The defocus errors were studied by placing a flat mirror below and the SHARPeR and moved using the RTT from -5 mm to 5 mm along optical axis (Z-axis). At various Z positions SHARPeR measured slopes in 20 repeated images with each image as an average of 30 camera exposures. The camera exposure time was 0.5 ms and a total of 30 exposures takes 7.5 s (including readout time). The mean and standard deviation of 20 images of wavefront tilt, slope rms without tilt and radius of curvature is shown in Figure 2.29, where std is shown as error bars.

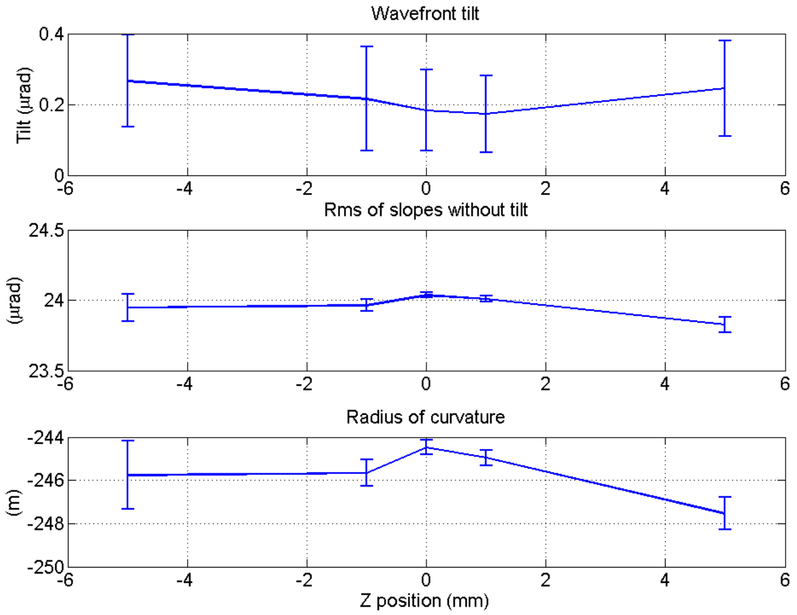

Figure 2.29 : The SHARPeR defocus errors from a shift of -5 to 5 mm in optical axis (Z-axis). The figure shows wavefront tilt, slope rms (without tilt) and curvature, with mean of 20 images at each Z location. (Note: reference not removed)

The measurements in Figure 2.29 were performed with minimization of the wavefront tilt as close to normal incidence as possible at each Z-position, but it still has large fluctuations even after averaging 30 images (<0.3 μrad) as seen in the standard deviation of the wavefront tilt in the figure. The rms slope and radius measurements show large discrepancies of ~1% change in mean values as well as increase in the standard deviation away from the focal position, which may be coming from systematic errors but are not readily explained.

2.4.1.4 Wavefront sensor calibration errors

The wavefront sensor module of the SHARPeR head is designed to operate with very high sensitivity and hence its design considers alignment and calibration with high accuracy. The wavefront sensor is very simple in terms of the number of components with just a microlens array and a CCD sensor as shown in Figure 2.30 [83]. Any misalignment between the microlens array and the CCD sensor can significantly affect the performance of instrument. The influence of any residual alignment errors has to be well calibrated. Alignment errors from lateral translations between the CCD and microlenses can be easily corrected by recalculating the center of wavefront on the CCD [83]. Misalignments in distance between microlenses and CCD needs to be calibrated as effective focal length. Other alignment errors such as tilt or rotation between the sensor and microlens array planes are calibrated using a reference wavefront as explained in section 2.1.4.

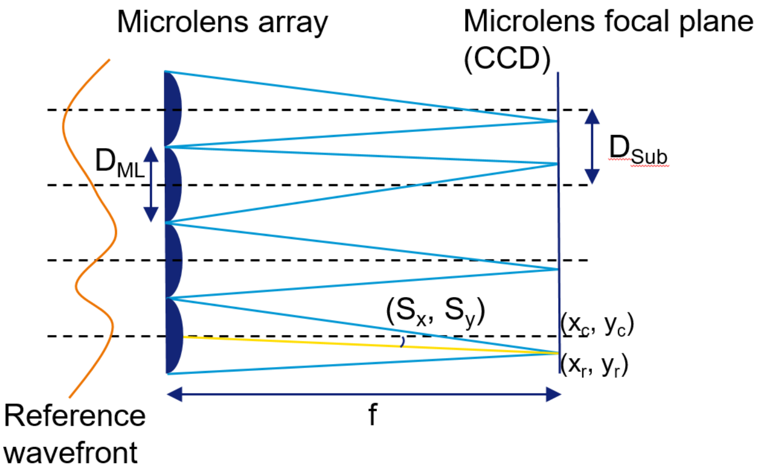

Figure 2.30 : Principle of Shack-Hartmann wavefront sensor.

The microlens are placed adjacently and the microlens size (D_{ML}) and their separation (D_{Sub}) is ~ 1.2 mm. The measured tangential (S_x) and sagittal (S_y) slopes can be expressed from test wavefront centroid positions (x_c, y_c), reference wavefront centroid positions (x_r, y_r) and focal length (f) as below.

$$\begin{pmatrix} S_x \\ S_y \end{pmatrix} = \frac{1}{f} \begin{pmatrix} x_c - x_r \\ y_c - y_r \end{pmatrix}$$

The measurement noises needs to take into account the noise from reference measurement as well, as shown below [84].

$$\begin{pmatrix} \sigma_{S_x}^2 \\ \sigma_{S_y}^2 \end{pmatrix} = \frac{1}{f} \begin{pmatrix} \sigma_{x_c}^2 + \sigma_{x_r}^2 \\ \sigma_{y_c}^2 + \sigma_{y_r}^2 \end{pmatrix}$$

The reference is taken with an ideal spherical wavefront usually with a laser point source placed far from wavefront sensor in a stable environment as explained in section 2.1.4, and averaged over more than 1000 images to minimize the statistical noise. The SHARPeR wavefront sensor can measure with λ/1000 rms accuracy and ~ λ/2000 rms repeatability, as specified by Imagine Optic. The reference mentioned here only corresponds to wavefront sensor, which may be insufficient to characterize errors originating from other sources such as other optical elements on the head. Another reference wavefront is usually measured with the full SHARPeR system prior to measurements on the test mirrors, which will be explained in the next chapters.

Another important factor to consider is the centroid computation algorithms of the wavefront sensor which can influence the noise in slope determination. The CCD based noises such as readout noise, sampling errors and their influence on centroid calculation is explained in section 2.4.1.2 using simple centroiding algorithm of ‘center of gravity’ approach. More complex algorithms such as thresholding, weighted centroid and correlation would have different influence on centroid determination errors [85]. The algorithms used by Imagine Optic for the SHARPeR wavefront sensor are proprietary knowledge and hence are not explored here.

2.4.1.5 Optical head errors

The SHARPeR optical head contributes to the measurement errors through imperfections in the optical elements and misalignments between the optics. The optical head errors are expected to be mostly systematic errors and can be calibrated using an external flat reference mirror as explained in detail in sections 2.2.3, 2.5.2 and 4.2.1. Nevertheless, pseudo-random errors due to temperature variations may also play a role, particularly for long acquisitions. The reference for optical head is different from wavefront sensor reference calibration mentioned in section 2.4.1.4, as it calibrates all the optical elements along the optical path including the wavefront sensor (except the test mirror).

2.4.1.6 Measurement surface shape based errors

The optical head errors strongly depend on the shape and alignment of test mirrors. The optical aberrations depend on the optical path traced by reflected beam. The reflected beam retraces the incidence beam path when reflected in normal incidence as can be observed in the optical head schematic in Figure 2.20. The beam incidence angles and reflected beam retrace path depend on the local slope of mirror, for curved mirrors the optic cannot be in normal incidence over the entire aperture. These systematic errors known as retrace errors are known to be a significant error source for other metrology instruments such as Fizeau interferometer [86]. The retrace errors are expected to be nonlinear and increase significantly on highly curved mirrors, which have strong slope variations across mirror length. Some of the ways to minimize retrace errors is (1) calibration of SHARPeR instrument for different angles, (2) adapted measurement techniques and (3) data analysis methods for retrace error correction. My thesis has investigated approaches (1) and (2) and explored a few data analysis methods.

The SHARPeR calibration with mirror tilt is presented in section 4.7 and different measurement techniques to minimize retrace errors are explained in section 2.5.4. One of the data analysis methods is proposed by Polack et al. [68], developed for stitching LTP to correct for instrument errors on strongly curved mirrors. This method has been explored only preliminarily for SHARPeR and will require further study, and no results are presented in the current document.

2.4.2 Motion errors

Optical errors are significant but not the only source of measurement errors. Motion and environmental errors may also influence the performance of SHARPeR. The SHARPeR optical head is fixed to a translation stage and the test mirror is placed below the optical head on a rotation and tip / tilt platform (RTT) as shown in Figure 2.31.

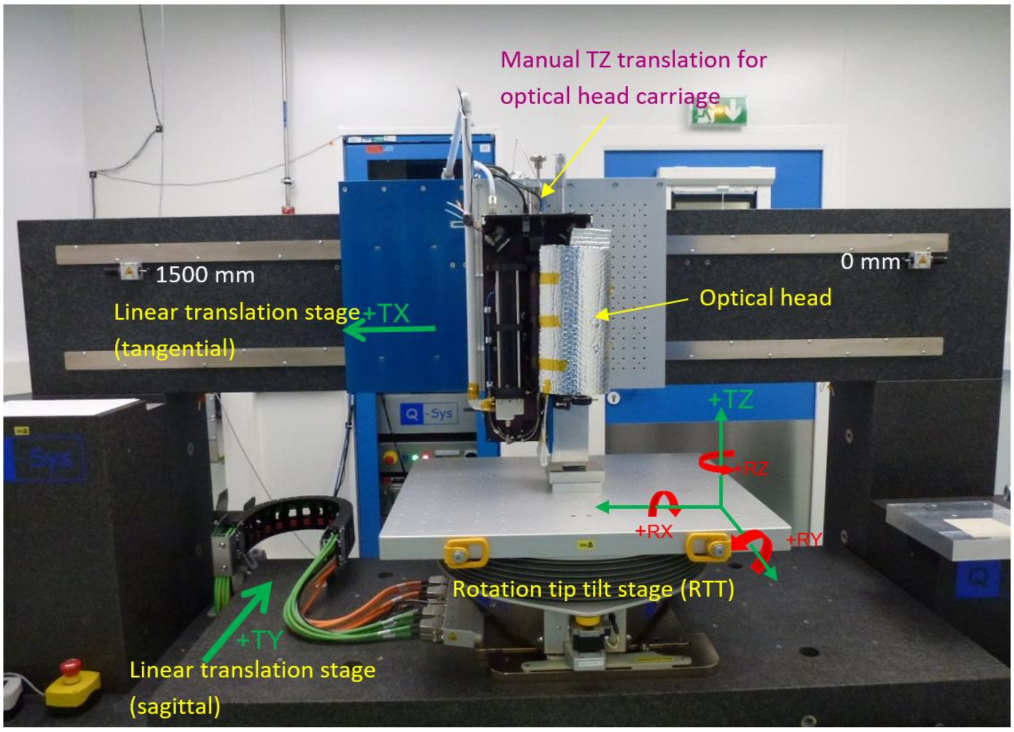

Figure 2.31 : SHARPeR instrument setup.

The SHARPeR system has six motorized motion axes, three linear axes (TX, TY, and TZ) and three rotational axes (RX, RY and RZ). The TX axis is used for scanning along the tangential direction, in which the optical head moves as a whole. The other five axes act upon the test mirror. In addition, a manual translation between the TX carriage and the optical head, permits a coarse adjustment of the distance (parallel to the TZ axis) between the mirror and optical head. The axes TX and TY, together termed as LTP axes, are permanently fixed to the SHARPeR gantry and they provide smooth linear translation using air bearing guides. The Rotation Tip Tilt (RTT) platform is an additional detachable mechanical platform placed on top of the TY translation stage. The RTT has rotation (RZ), tip-tilt (RX-RY) and Z translation (TZ) axes, where RX, RY and TZ movements are actuated by coordinated movements of three stepper motor driven linear translations in a tripod configuration. The RZ rotation uses an air bearing guided platine actuated by an asynchronous motor. All motorized movements of the system are equipped with optical encoders. The test mirror can be measured in vertical facing (VFM) or in sideways facing (HFM). The latter configuration requires introduction of a 90° deflecting mirror in to the optical path and has not been used in the scope of this work. The mirror is aligned using the five axes (except TX), and in the basic measurement mode the mirror is kept stationary, during scans by optical head along TX axis. New measurement methods were developed during the course of my thesis, which are explained in chapter 2.5.4, and they require tilting of the mirror during scanning.

The mirror tilt is adjusted using RX and RY axes when mirror is measured in vertical facing (VFM), and for sideways (HFM) using RZ and RX axes. As in any such system, the motions are not perfect and the motion errors along one axis can induce secondary errors along other axes which are shown in the following.

2.4.2.1 Translation and tilt errors

The primary scanning axis is TX which is the linear translation of optical head and this motion displays movement defects along all the six axes, either due to imperfections in the motors or in the moving stage or in the stage platform. From TX translation, the resultant errors along TX are termed as positioning errors, along TY/TZ as flatness/straightness and angular errors about Y/X/Z as pitch/roll/yaw. The errors are defined in terms of their accuracy which is the deviation from the expected value averaged over many scans, and the precision which is the repeatability of measured values over many scans in peak to valley.

The SHARPeR stages were characterized using a standard Michelson interferometer (HP model 5530 Dynamic Calibrator) from the ESRF Precision Engineering Laboratory (PEL) and the results are presented in detail in Appendix 4, and they are shown concisely in Table 2.5.

The specifications of different SHARPeR axis provided by Q-Sys are shown in Table 2.1 and Table 2.2, and they are smaller than measurements shown in Table 2.5. The specifications were measured over nearly same length for TX axis (1500 mm), but on much larger range for RX, RY axis (~±90 mrad) which could be the reason for larger accuracy specifications for RX & RY axis (30 µrad). The differences could be from (a)

ESRF characterization performed on the complete instrument (optical head installed) and (b) different environments, measuring instruments and measurement conditions.

Table 2.5 : Characterization results of different SHARPeR axes

Axis	**Calibration Range**	**Error type**	**Accuracy**	**Precision**
TX	1 - 1401 mm	Position errors	4 µm (direct) + 8.7 µm (pitch)*	1.3 µm
		Flatness (TXY)	4.5 µm (direct) + 16.5 µm (roll)*	4.2 µm
		Straightness (TXZ)	4.2 µm	3.8 µm
		Pitch	8.7 µrad	2.3 µrad
		Roll	16.5 µrad	1.9 µrad
		Yaw	4.3 µrad	2.8 µrad
RX	~±9 mrad	Position errors (angular)	14.8 µrad	9.0 µrad
RY	~±9 mrad	Position errors (angular)	19.7 µrad	8.5 µrad

*Assuming vertical facing orientation of mirror (VFM), the pitch/roll/yaw angular errors are projected on the mirror as is, whereas position error and flatness (TXY) on mirror also include pitch and roll projections. The center of rotation of the optical head is nearly 1 m distance from the mirror.

The positioning errors will only reduce the spatial resolution by a small fraction (<~1%) of theoretical resolution (given by microlens size of ~1.2 mm). The flatness acts similarly to the reduction of spatial resolution along sagittal direction (by <~2%). The straightness errors act as piston errors changing the focal length by very small amount (4.2 µm), which can be neglected as explained in the defocus analysis in chapter 2.4.1.3. The yaw errors cause negligible offsets in tangential and sagittal directions (by $y^*\theta_{yaw}$ in TX and $x^*\ \theta_{yaw}$ in TY which are in nanometers for the SHARPeR aperture of 18 mm x 13.2 mm).

The pitch and roll errors are however significant as they are much larger than the typical slope errors (<1 µrad) of synchrotron mirrors. These errors are usually corrected for within stitching algorithms using the redundancy in subaperture overlaps. The corrections are only approximate as these angular motion defects might introduce other errors like retrace errors and the direct measurement of pitch/roll errors during subaperture scanning may further improve the instrument performance [87].

New measurement schemes developed during my thesis like normal and multi incidence techniques (explained in chapter 2.5.4), use the RTT tilt axes RX and RY in conjunction with the TX translation. The RY axis is used for tangential tilt and RX for sagittal tilt on the mirror (with the mirror surface facing upwards). In this case the stitching algorithms should correct for the cumulative tilt errors of optical head pitch/roll errors, RY/RX angular positioning errors as well as applied tilt.

The RTT tilt induced position errors are dependent on the applied tilt in RX or RY, nearly equal to $z^*\theta$ where z is the distance between RTT center of rotation for RX and RY and the mirror optical surface (it was measured ~90 mm distance from RTT center of rotation to RTT top plane) and θ is the applied tilt. The RY tilt results in position error in tangential direction and for RX tilt sagittal position error. For a 10 mrad RY tilt and 100 mm z distance results in a 1 mm tangential position error which is significant and needs to be considered when measuring highly curved mirrors. The other major induced errors are piston errors which varies as $x^*\theta$ (for RY tilt) where x is the position of mirror measured from center of RTT. At an extreme case of 10 mrad RY tilt and at 1 m tangential TX position this gives a 10 mm piston error however due to the relative insensitivity to defocus errors, this only changes the measured radius by an equivalent value (see Appendix 2). Other induced errors (along other axes) from RTT tilts have not been studied.

2.4.3 Environmental errors

Environmental effects can be a significant source of errors for deflectometry based instruments like SHARPeR [88]–[90]. The environmental errors are very complex to characterize and they do not act in very deterministic fashion. The main environmental factors are temperature fluctuations, air turbulence and vibrations (and may also include humidity changes). The principal identified sources of such errors are shown in Figure 2.32, and include airflow from the roof and the heat generated by the wavefront sensor CCD and RTT stepper motors.

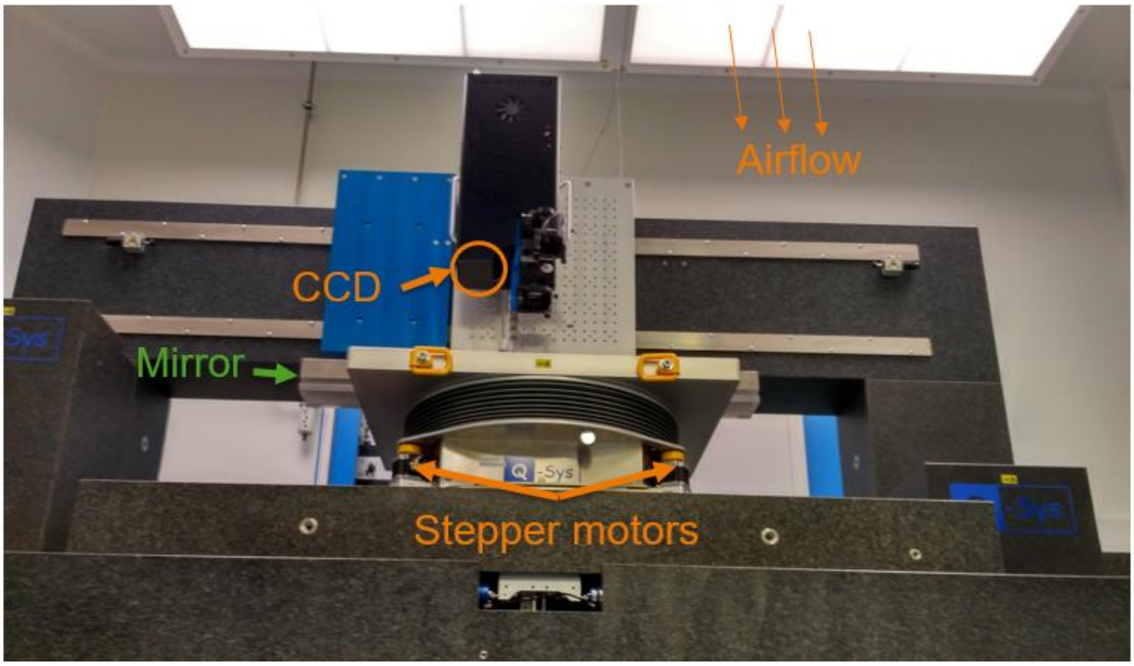

Figure 2.32 : Major environmental errors sources of airflow and heat sources.

The effects can appear in mechanical or optical components. The mechanical components of the SHARPeR (granite gantry, motion stages, air bearings etc.) are designed to be robust to thermal expansions or vibrations. The optical errors (from environment) can be divided into three sections (1) distortion of the optical head base plate due to thermal expansion leading to optical path length changes and alignment errors, (2) thermal expansions of optical elements and/or test mirror thus changing their surface shapes, thickness and (3) refractive index changes of air in the optical path from air turbulences, temperature and hygrometry fluctuations. Typically the humidity fluctuations have much smaller influences compared to temperature fluctuations on the air refractive index and can be neglected [91].

The temperature fluctuations need to be studied in different spatial and temporal domains. The CCD was operated with exposures in the range of 0.5 ms to 100 ms during my thesis and it has readout times near 250 ms, which gives the fastest frame rate of the camera of 4 Hz. At least 32 images are averaged per subaperture to reduce the statistical noise (the minimum image requirement is explained in detail in chapter 4.1), which implies time scales of few seconds spent at a single subaperture on the mirror. If the images are taken in quick succession, only high frequency environmental errors are of consequence to subaperture noise. However, the SHARPeR instrument usually scans the mirror multiple times taking a single image at a subaperture in each scan, which samples the images to be averaged over long time intervals often leading to few hours (total measurement times). In the case of repeated scans, subaperture noise can be affected by low frequency environmental errors over few hours. A single forward (or backward) scan takes a few minutes (typically 1 min to 30 min), and during a scan the optical head can travel typically from 10 mm to 1.5 m. The environmental fluctuations over time scales of ~1 – 30 min affect the scan noise which influences the stitched mirror profile. In addition, the spatial variations of environment noise along the scan length also contribute to noise within stitching. The spatial fluctuations in temperature can occur from thermal heat sources such as RTT stepper motors which can create a gradient of temperature along scan path through air convection. Heat generated by the CCD camera on the optical head can also lead to dynamic fluctuations as it moves along with optical head. The CCD comes with a heat extractor fan to cool the sensor, and the extracted hot air can contribute to convective air flow in the scan path. Heat dissipation by the camera is observed to vary depending upon the operating conditions with increased thermal power generated when the camera is in a read-out status compared to in standby. Such transient power can also affect the stability of the optical head due to the modification of temperature gradients within the optomechanics.

Globally in the SHARPeR enclosure, air flows from the ceiling with laminar flow through a large plenum to maintain temperature stability and (through filtering) maintain cleanliness of the measurement zone. Temperature variations over 72 hours of the ambient air were measured using a probe (temperature logger XR-420 from RBR) near the ceiling and locally with a probe near the CCD, as shown in Figure 2.33. The probes measure temperatures with accuracy specifications of ±2 mK. The temperature readings are performed after the room is closed and stabilized for a few hours and with no mechanical motions and the CCD in standby mode. The figure also shows power spectral densities of both the probes and the probe near the CCD shows large high frequency fluctuations. The ambient air probe PSD has a peak near 20 minutes and falls significantly at higher frequencies. The peak at 20 minute periods originates from perturbations due to the hygrometry control system. The fluctuations are only ~0.15℃ in peak to valley (PV) for both probes, however the probe near CCD is 0.7℃ hotter than the ambient air temperature. The readings of the probes during scans on 1.2 m long mirror are shown in Figure 2.34, while the camera is continuously reading out. The scan time for a single forward/backward scan cycle is nearly 50 minutes and is reflected in the periodicity of the temperature variations of the probe near the CCD. This is not observed in the ambient air probe and it indicates of spatial fluctuations in the temperature along the TX axis. The mean temperatures in Figure 2.34 are lower than Figure 2.33, as they were taken many months apart and in between temperature stabilization schema underwent some modifications. The effects of all these fluctuations on the actual scans are presented in detail in the chapter 4.1.

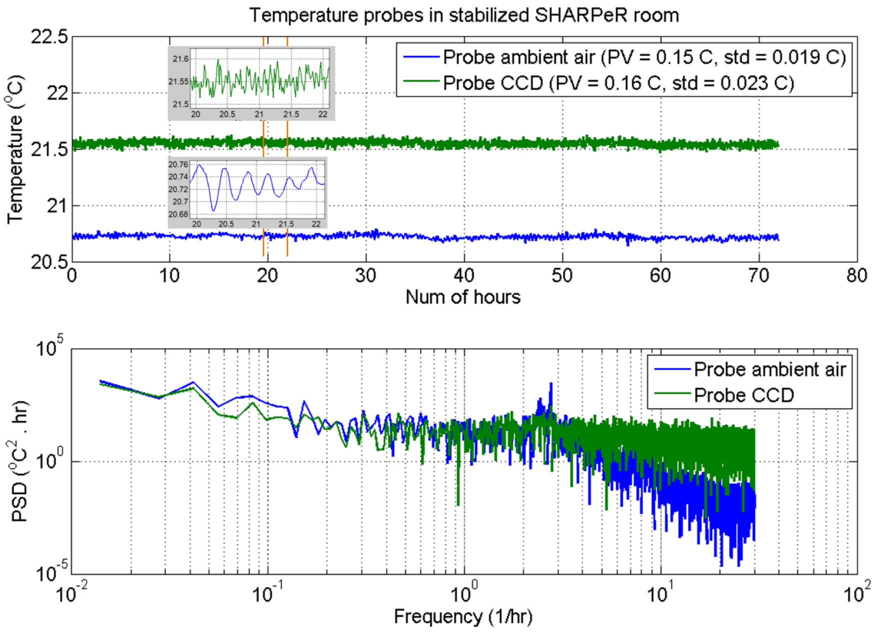

Figure 2.33 : Temperature probes one reading ambient air far from instrument (close to roof) and the other next to the CCD camera of wavefront sensor. The figure shows temperature readings over 72 hours and their power spectral density (PSD).

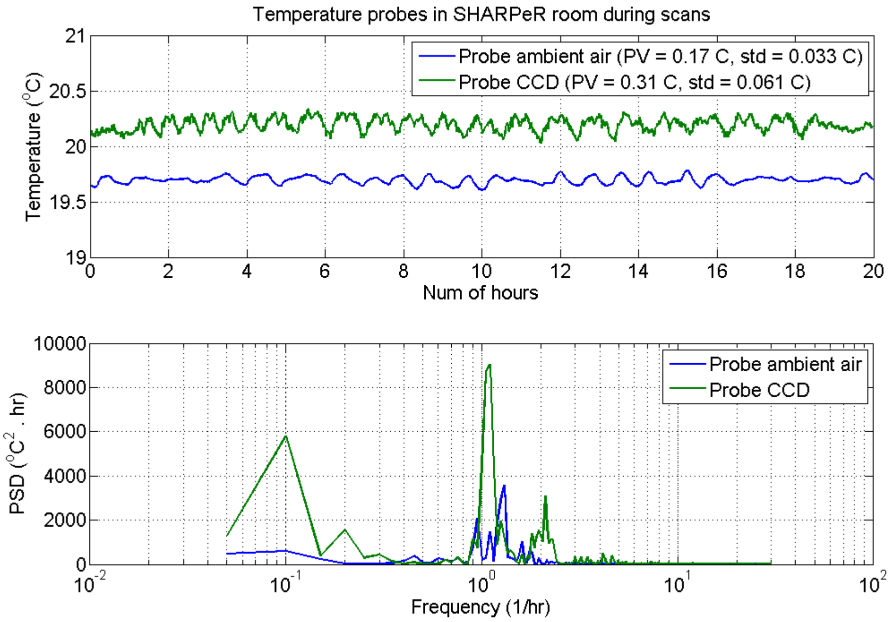

Figure 2.34 : Temperature probes for ambient air and near CCD while scanning a 1.2 m long mirror in 16 repeated forward-backward scans. A single forward/backward scan cycle takes nearly 50 minutes.

2.4.4 Errors from stitching algorithms

Different stitching algorithms may give different residual errors in the final result depending on the applied corrections, for example an algorithm correcting only motion errors (pitch/roll) is expected to leave higher residual errors in the final result than an algorithm correcting for both motion and systematic errors (e.g. reference errors). Apart from residual errors, the stitching algorithms themselves can generate errors such as from fitting errors [92], floating point errors etc. The stitching algorithms typically use plane fitting of subapertures in the overlapped regions, and errors in fitting add to stitching errors. Some of the errors like fitting errors can be minimized by normalization of data (e.g. rather than using SI units, scaling height data to nanometers and mirror lengths to millimeters typically results in better fitting of surface topographies for synchrotron mirrors, since the surface errors are in nanometer or sub-nanometer scales). If an algorithm utilizes optimization or recursive methods, its performance would also depend on initialization and the choice of optimization scheme as well. Another important feature of algorithms is customization based on the data, for example if the data has a lot of outliers (e.g. from polishing edges and dust particles on mirrors), filtering out bad data points may greatly improve performance, whereas on another dataset of small size (e.g. mirror with narrow clear aperture) using the whole data would improve performance. Different stitching algorithms were studied and implemented during the course of my thesis and are presented in chapter 3.2. The performance of these algorithms is presented in detail in chapter 3.5.

2.5 Techniques to minimize SHARPeR measurement errors

2.5.1 Inspirations from other instruments

The SHARPeR design was inspired from that of the Long Trace Profiler (LTP) and the initial prototype was developed by combining Shack-Hartmann techniques with an existing LTP motion platform as a collaboration between Imagine Optic and SOLEIL synchrotron [71]. SHARPeR uses stitching techniques similar to the methods increasingly used with stitching Fizeau interferometers and Micro interferometers [63],

[64]. Inspired by the on-the-fly measurements by the ESRF LTP to reduce measurement time and improve repeatability [36], the SHARPeR has also implemented on-the-fly scans. The ESRF LTP is enclosed in a thermally insulating chamber to minimize the thermal effects along the optical path. Different enclosures and few design changes were experimented for the SHARPeR to minimize thermal effects and air turbulences. Stitching interferometric techniques (using Fizeau or micro-interferometers) commonly measure the mirror in null fringe condition at each subaperture, and a similar normal incidence method was developed for SHARPeR. The SHARPeR normal incidence method was intended to minimize the retrace errors whereas the interferometric instruments apart from retrace errors also exhibit large fringe density at oblique incidences which quickly become unreadable [93]. Instruments such as the autocollimator-based NOMs are usually calibrated over their operating angular range, which are corrected from test mirror measurements [51]. A similar calibration was performed for SHARPeR over its slope measurement range. Although the calibration needs to be improved and performed on a finer scale, the current calibration has already greatly improved the radius of curvature measurements. The improvements strategies are presented in more detail in the next sections.

2.5.2 Reference measurement, forward – backward scans, AB and BA scans

The systematic errors of SHARPeR such as optical aberrations and misalignments, can be partially corrected by subtracting measurements of a flat reference mirror. In this approach any residual curvature from reference mirror is effectively subtracted from to the test mirror, and it becomes impossible to distinguish the curvature of test mirror from that of reference. The problem is not as severe on the slope error measurements as they are measured after subtraction of an idealized surface (sphere, cylinder, asphere), whereas the radius of curvature measurement requires accurate calibration SHARPeR head.

Reference error corrections:

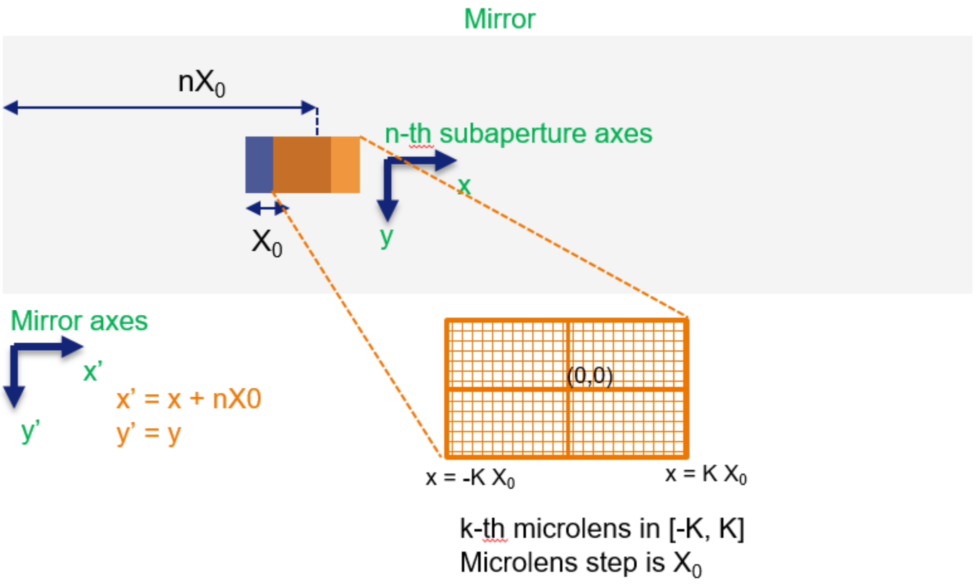

Figure 2.35 : SHARPeR subaperture coordinate system with stitching step same as microlens size.

In this section the reference errors and correcting them with flat reference mirror measurements are explained mathematically. The residual noise after reference correction in the stitched slopes is also explained. The SHARPeR stitching procedure on a test mirror with relationships between subaperture and global mirror coordinate systems is shown in Figure 2.35. The measured tangential slopes on n^{th} subaperture can be expressed as below.

$$m(x,y,n) = s(x+nX_0,y)+r(x,y)+e_s(nX_0)+ e_r[x,y,s(x+nX_0,y)]+e_n(\mathrm{x},\mathrm{y}) \tag{2-4}$$

Where the term $s(x',y') = s(x+nX_0,y)$ is the true tangential slope on the mirror, $r(x,y)$ is the systematic error contribution (from optical aberrations and misalignments etc.), e_s are the stage errors (pitch errors for tangential slopes), e_r are the retrace errors and e_n combine other noises like statistical and environmental errors. Sagittal slopes can be described in an equivalent formulation. The measurement on a flat reference mirror aligned in normal incidence (average slope of all microlenses < 2 µrad), can be expressed as below. The normal incidence threshold is limited by environmental fluctuations and a threshold below 2 µrad takes too long.

$$\boldsymbol{m_r(x,y) = s_r(x,y) + r(x,y)}$$

$$\begin{aligned}\boldsymbol{m(x,y,n) - m_r(x,y)} &\\ &\boldsymbol{= s(x+nX_0,y) - s_r(x,y) + e_s(nX_0) + e_r[x,y,s(x+nX_0,y)]} \\ &\boldsymbol{+ e_n(x,y)}\end{aligned}$$

(2-5)

Where the term $s_r(x,y)$ are the slopes of the reference mirror. The measurement errors from pitch/roll (e_s), retrace errors (e_r) and statistical/environmental errors (e_n) are explored in more details in next sections. The reference mirror slopes ($s_r(x,y)$) also contribute to systematic errors, and can be minimized by measuring different regions on the reference mirror and averaging. The reference errors are explored in more details in chapter 4.2.1.

Forward and backward scans:

The scans are done in forward and backward directions (FB) primarily to use the measurement time more economically. The FB scans are mechanically symmetrical and most of the motion errors (pitch / roll / position errors) are direction independent. However, the FB scans are not symmetrical in the environmental effects along scan path. The camera is placed on the bottom left corner of the optical head and the subaperture to be measured is under bottom right region of optical head as shown in Figure 2.36. In the forward scan beam path moves to the region heated by CCD and with fan exhaust air, whereas backward scans observe beam path moving ahead of hot regions. These temperature differences can lead to differences in forward and backward measurements.

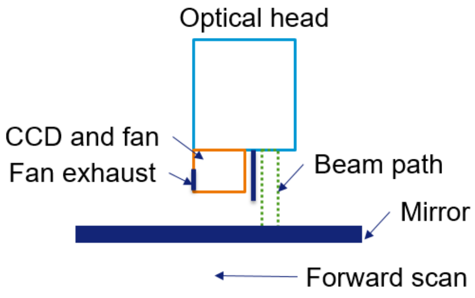

Figure 2.36 : Forward scan environmental effects.

AB and BA measurements:

A commonly used method to minimize some of the systematic errors is to measure the test mirror in AB and BA orientations [30], [94], as shown in Figure 2.37. The test mirror is either manually flipped or the RTT platform is rotated by 180 degrees to measure the mirror in BA configuration. The BA slope errors are averaged with those acquired in the AB orientation after flipping the data, as explained below:

$$m_{ab}(x,y) = s(x,y) + e(x,y)$$

$$m_{ba}(x,y) = -s(-x,-y) + e(x,y)$$

$$m_{abba}(x,y) = \frac{m_{ab}(x,y) - m_{ba}(-x,-y)}{2} = s(x,y) + \frac{e(x,y) - e(-x,-y)}{2}$$

(2-6)

Where $s(x,y)$ stands for tangential/sagittal slopes and $e(x,y)$ is the systematic error term. From eq.(2-6) it can be inferred that the ABBA averaging process removes the even ordered components of the systematic errors.

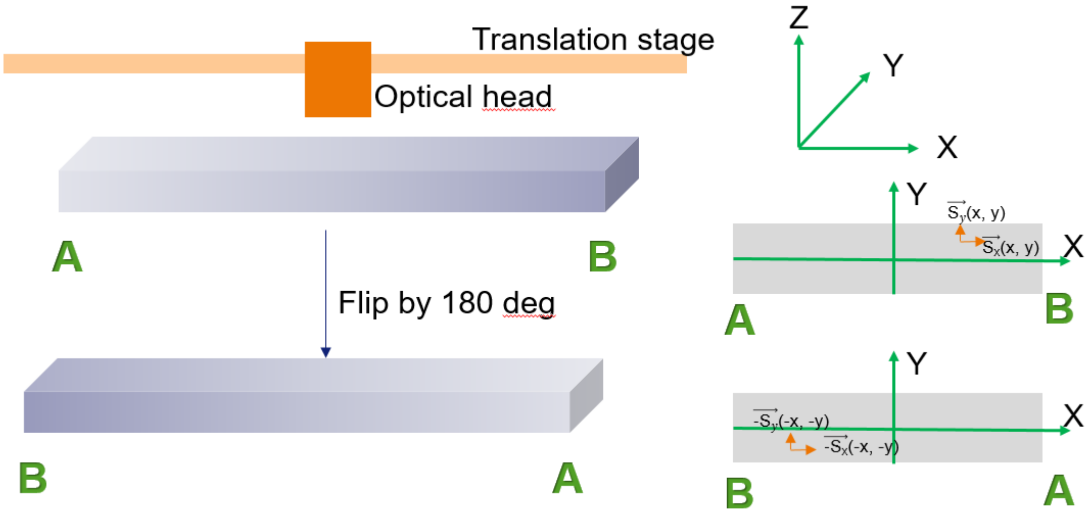

Figure 2.37 : AB and BA measurement schematic with SHARPeR.

2.5.3 Stitching methods

Stitching techniques may compensate for measurement errors by extracting relevant parameters from datasets with sufficient redundancy. Measured slopes as shown in eq. (2-4) have different error components along with true slopes and some of which like reference errors and pitch/roll errors can be measured externally. If such external measurements are not available, the stitching methods can correct for pitch/roll errors by measuring the mirror with overlapped subapertures. Within an overlap between i^{th} and j^{th} subaperture the differences can be assumed to originate from pitch/roll variations between the two subapertures. This assumption holds true as long as other errors are not significant. If the reference errors are not well calibrated by the external reference flat mirror, the stitching algorithms may need to be improved to extract the residual reference errors. If the retrace errors (errors from retracing different optical path) dominate the overlap differences additional data redundancy may be needed to extract both retrace errors and pitch/roll errors. One such method for characterizing systematic instrumental errors was proposed by Polack et al in the 'LEEP' data analysis procedure [68]. Different stitching algorithms are explored in more detail in chapter 3.

2.5.4 Normal incidence and multi incidence techniques

The systematic errors (from optical aberrations and misalignments) depend heavily on the optical path taken by the beam. The schematics of optical path for test mirror aligned in normal & oblique incidence is shown in Figure 2.38 and Figure 2.39. The optical path from the emergence of laser out of the fiber to incidence on surface under test (SUT) remains fixed (here we ignore possible modifications of the incident wavefront due to thermal expansions and misalignments and air turbulences). The Figure 2.38 and Figure 2.39 display expanded schematic of optical paths, in reality the beam reflected from the SUT in normal incidences retraces the incidence path until beam splitter and thereafter follows a different path into the wavefront sensor. Retracing the same path (afocal lenses, beam splitter corner) was intended to minimize optical aberrations of these elements.

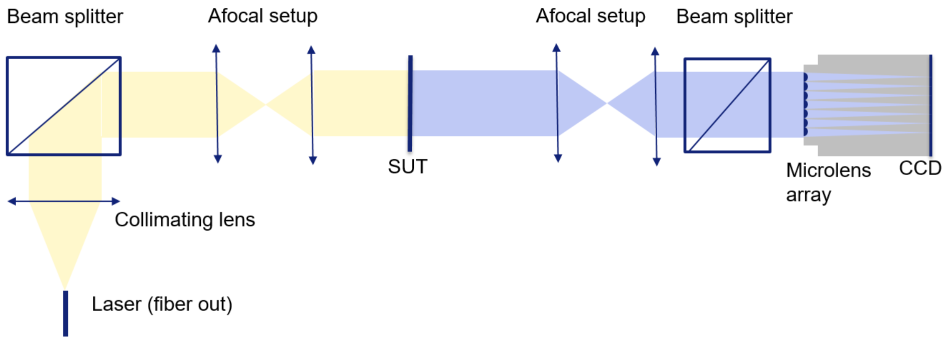

Figure 2.38 : Optical path schematic with test mirror (SUT) aligned in normal incidence. (The afocal setup is simplified. The real instrument has more lenses with a complex arrangement.)

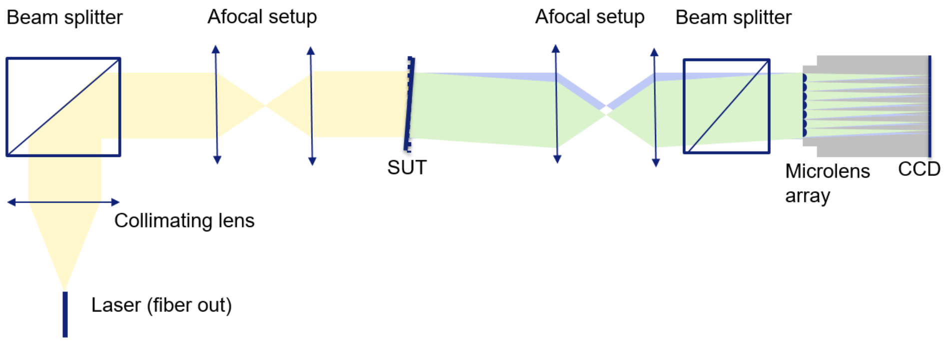

Figure 2.39 : Optical path schematic with test mirror (SUT) aligned at an angle to optical axis (oblique incidence).

The reference flat mirror is usually measured in normal incidence as shown in Figure 2.38. In this case if the reference mirror were perfectly flat the inward and outward optical paths would overlap and the effect of any optical aberrations would cancel. If the test mirror (SUT) is tilted, the inward and outward beams no longer follow identical optical paths and optical aberrations may not cancel. These 'retrace errors' are not corrected through reference measurement. For curved mirrors (spherical, tangential cylindrical, elliptical etc.), the mirror is aligned in normal incidence at the center of mirror. In the default measurement scheme the mirror is kept stationary and the optical head translates from end to end, in which case the incidence angle changes from one subaperture to another (since mirror is curved), and they all retrace different paths giving different retrace errors as shown in Figure 2.40. One way to reduce the influence of retrace errors on curved mirrors is to measure the mirror in normal incidence at each subaperture.

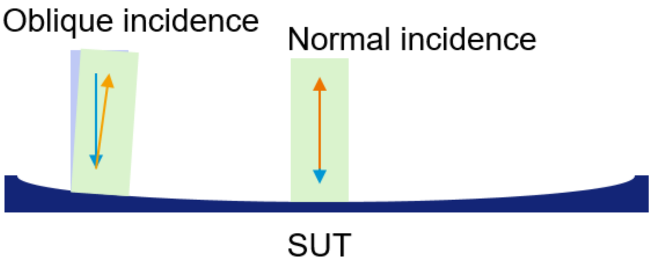

Figure 2.40 : Oblique incidence on curved mirrors at locations away from mirror center.

Even when measuring all subapertures in normal incidence on curved mirrors, the retrace errors may still be present, as not all the microlenses in a subaperture are in normal incidence. However normal incidence technique can still correct for some of these errors as explained mathematically in the following.

The measured slopes given by eq. (2-4) can be restated for normal incidence scans as follows.

$$\begin{aligned} m_{ni}(x,y,n) = {} & s(x+nX_0,y) + r(x,y) - s_m(nX_0) + e_s(nX_0) \\ & + e_r[x,y,s(x+nX_0,y) - s_m(nX_0)] + e_n(x,y) \end{aligned}$$

(2-7)

The above equation can be restated in terms of microlens position (k, l) instead of physical coordinates (x, y) as below.

$$x = kX_0\,;y = lX_0$$

$$\begin{aligned} m_{ni}(k,l,n) = {} & s(k+n,l) + r(k,l) - s_m(n) + e_s(n) \\ & + e_r[k,l,s(k+n,l) - s_m(n)] + e_n(k,l) \end{aligned}$$

(2-8)

The term $s_m(n)$ is the average measured slope at n^{th} subaperture, and it is obtained by optimizing the eq. (2-9). In practice the RTT platform is tilted iteratively until the measured tilt is below a given threshold.

$$\left|\sum_{k=-K}^{K}\sum_{l=-L}^{L} \boldsymbol{m(k,l,n)} - \boldsymbol{s_m(n)}\right| < \boldsymbol{t_n}$$

(2-9)

Where the normal incidence threshold t_n is set by default to 2 µrad in both tangential and sagittal directions, which is limited by environmental fluctuations and a threshold below 2 µrad takes too long. The number of microlenses are 2K+1 and 2L+1 in tangential and sagittal directions respectively.

The term $s_m(n)$ is the average of measured slopes (not true slopes) given by eq. (2-8), and can be expressed mathematically as below.

$$s_m(n) = \langle s(k+n,l) + e_s(n) + r(k,l) + e_r[k,l,s(k+n,l) - s_m(n)] + e_n(k,l)\rangle$$

$$s_m(n) = \langle s(k+n,l)\rangle + e_s(n) + E_m(n)$$

(2-10)

The notation < > represents averaging over all microlenses (k, l). The term $E_m(n)$ represents the mean errors over all microlenses of systematic errors (reference errors

$r(k,l)$ and retrace errors e_r), and pseudo-random environmental errors ($e_n(k,l)$). The term $s_m(n)$ measures the average departure of the measured surface from the normal incidence condition. Substituting $s_m(n)$ in eq. (2-8) gives the following.

$$\begin{aligned} m_{ni}(k,l,n) = {} & s(k+n,l) - \langle s(k+n,l)\rangle + r(k,l) \\ & + e_r[k,l,s(k+n,l) - \langle s(k+n,l)\rangle] + e_n(k,l) - E_m(n) \end{aligned}$$

(2-11)

The systematic static reference errors $r(k,l)$ are corrected typically using flat reference mirror measurement (see eq.(2-5)). The stitching corrects for tilts between subapertures induced by the normal incidence acquisition condition, mostly the term $\langle s(k+n,l)\rangle$ but it also has contribution from other noise terms if they are significant. The stitching also averages over all the microlenses along tangential direction (for a stitching step of one microlens). The final stitched slopes can be expressed as following.

$$\begin{aligned} s_f(\mathrm{x}',\mathrm{y}') = {} & s(x',y') - E_{ns}(x',y') - \frac{\sum_{k=-\mathrm{K}}^{K} s_r(k,l)}{2\mathrm{K}+1} \\ & + \frac{\sum_{k=-\mathrm{K}}^{K} e_r[k,l,s(k+n,l) - \langle s(k+n,l)\rangle]}{2\mathrm{K}+1} \end{aligned}$$

(2-12)

The term $E_{ns}(x',y')$ refers to the stitched environmental noise and $s_r(k,l)$ refers to the residual errors from flat reference mirror. For the special case of tangential cylinder mirrors the retrace error e_r average in eq. (2-12) becomes approximately constant for all x' positions on the mirror. SHARPeR measurements on spherical mirrors using normal incidence technique are presented in chapter 4.4.

Multi incidence scans:

The simplification used for cylindrical mirror does not hold true for more complex mirror shapes. For cylinders the slopes in each subaperture are nearly same in the peak to valley and have nearly same curvature, which is not the case for ellipses or more complex shaped aspheric surfaces. Retrace errors, although reduced for aspheres in the normal incidence method, are no longer independent of the mirror tangential positions. The multi incidence method extends the normal incidence technique, with each subaperture measured not just in normal incidence but in a predefined set of incidences (*i*), as shown in Figure 2.41. The figure shows ray tracing of two subapertures with different curvatures (Low, High) in normal incidence and multi incidence scans. Afocal lens setup is approximated to two identical lenses separated by 340 mm, with mirror plane at 170 mm before first lens and mirror image plane (microlens plane) at 170 mm away from second lens. Multi-incidence scans apply a virtual aperture stop at the two lenses and rays beyond these are ignored for final slope calculations.

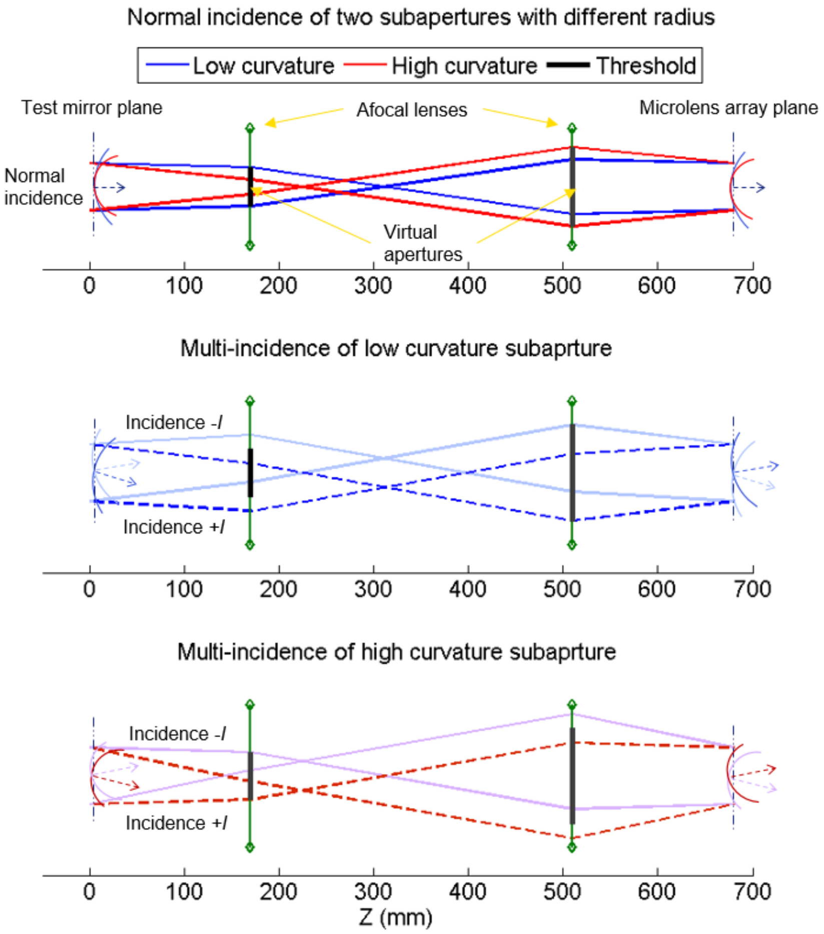
Normal incidence of two subapertures with different radius

Multi-incidence of low curvature subaprture

Multi-incidence of high curvature subaprture

Figure 2.41 : Schematic of multi-incidence method on two subapertures with different curvatures. The schematic shows a simplified afocal lens setup using two lenses, with mirror plane at Z=0 mm and its image plane at Z=670 mm. Three different incidence angles (normal, +I, -I) are shown in the three subfigures. The threshold region is outlined in dark black over the lenses, and in all cases light rays

with retrace paths beyond the threshold are filtered from subaperture images before stitching.

Multi incidence method aims to correct retrace errors on aspherical mirrors. The retrace errors of SHARPeR instrument depend on two factors (a) slope on test mirror and (b) location of the microlens measuring the slope. In order to solve these problems each pixel on the test mirror (corresponding to microlens size) may be measured, (1) by all microlenses and (2) for each microlens at a specific list of incidences common to all mirror positions. Stitching with a step of one microlens can partially solve retrace error problems, as it averages over all the microlenses in tangential direction to get final slopes at each mirror position. 2D stitching with scanning in both tangential and sagittal directions can further improve as it utilizes all microlenses of the SHARPeR to evaluate slope at each mirror position, however it has yet to be implemented and not used here. Multi incidence method measures each subaperture in a list of incidences around normal incidence ([-I, I] mrad, including normal incidence). In this process each microlens (in tangential direction) effectively measures a position on mirror in a wide span of tilts. In the preliminary implementation of this method, the aim is to achieve a uniform tilt span across the mirror length by all (tangential) microlenses, although they are not exactly same tilts. Uniform tilt span is achieved by applying a fixed threshold on slopes before stitching which is explained mathematically in more details in the following.

The analysis extends the normal incidence analysis presented earlier in this section. The subapertures slopes measured in multi-incidence method for nth subaperture at an incidence (i) can be expressed as below, by extending the normal incidence formalism given by eq. (2-8).

$$\begin{aligned} m_{mi}(k,l,n,i) = \; & s(k+n,l) + r(k,l) - s_m(n) + i + e_s(n) \\ & + \; e_r[k,l,s(k+n,l) - s_m(n) + i] + e_n(k,l) \end{aligned}$$

(2-13)

The term $s_m(n)$ is the normalization tilt applied to each subaperture, and i is the incidence tilt applied in a range [-I, I] afterwards for each subaperture. A threshold is applied to exclude all microlens slopes beyond the range of slopes in the normal incidence scan.

$$m_{mi}(x,y,n,i) = NaN, \qquad \forall\, |m_{mi}(x,y,n,i)| > s_{th}$$

$$s_{th} = \max(m_{mi}(x,y,n,0))$$

(2-14)

The subapertures at an incidence (i) are stitched after applying the threshold. The stitching is very similar to normal incidence stitching given by eq. (2-12), except for the incidence angle i, which can be expressed as follows.

$$s_f(\mathrm{x}',\mathrm{y}',i) = i + s(x',y') - E_{ns}(x',y') - \frac{\sum_{k=-\mathrm{K}}^{K} s_r(\mathrm{k},\mathrm{l})}{2\mathrm{K}+1} + \frac{\sum_{k=-\mathrm{K}}^{K} e_r[k,l,s(k+n,l) - s_m(n) + i]}{2\mathrm{K}+1}$$

(2-15)

Averaging the stitched slopes over incidences i = -I to I gives

$$s_f(\mathrm{x}',\mathrm{y}') = s(x',y') - E_{ns}(x',y') - \frac{\sum_{k=-\mathrm{K}}^{K} s_r(\mathrm{k},\mathrm{l})}{2\mathrm{K}+1} + E_{rKI}$$

The term E_{rKI} represents the averaged retrace error contribution to the final stitched slopes after averaging all incidences in the multi-incidence measurement, and is given by the following.

$$E_{rKI} = \frac{\sum_{i=-I}^{I} \sum_{k=-\mathrm{K}}^{K} e_r[k,l,s(k+n,l) - s_m(n) + i]}{(2\mathrm{K}+1)(2\mathrm{I}+1)}$$

(2-16)

The threshold on slopes given by eq.(2-14) makes sure $|s(k+n,l) - s_m(n) + i| < S_{th}$ for all mirror tangential positions. If very high number of tilts with very fine steps are used the eq. (2-16) can be rewritten as below, which makes it independent of mirror tangential position.

$$E_{rKI} = \frac{\int_{-\boldsymbol{s_{th}}}^{\boldsymbol{s_{th}}} \sum_{k=-\mathrm{K}}^{K} e_r[k, l, s]\ ds}{(2\mathrm{K}+1)\int_{-\boldsymbol{s_{th}}}^{\boldsymbol{s_{th}}} ds}$$

(2-17)

Both the normal incidence and multi incidence can correct for retrace errors in tangential direction. Extending scanning in sagittal direction (2D scanning) can potentially correct for sagittal retrace errors. The SHARPeR measurements using multi incidence technique are presented in chapter 4.5.

2.5.5 On the fly scanning techniques

Measuring the test mirrors in on the fly (or onfly) mode is usually much faster than measuring in step by step mode, which allows either to measure more repeated scans in the same measurement time and potentially reducing the statistical errors or using the measurement times more efficiently. The onfly scans primarily help reduce measurement time, but may also be helpful in reducing environmental noise such as low frequency drift errors due to temperature variations. The SHARPeR motors are controlled by a commercial Delta Tau PowerPMAC controller, which in turn is controlled by a Windows 7 PC. The SHARPeR camera is directly controlled by the PC to take and read images, and to save the image slopes data. To implement the onfly scans a new trigger cable is added between the Delta Tau controller and the SHARPeR camera, which triggers the camera to start exposure (for a pre-configured exposure time) based on the list of TX carriage positions supplied to the Delta Tau program at the beginning of the scan. Reading the camera images is still done by PC, which has to continuously monitor the Delta Tau program so that after the trigger is generated the PC requests the transfer of the image from the camera. The camera readout and saving of the slopes by the PC must finish before the next trigger occurs, which in practice is the limiting factor determining the maximum speed of onfly scans. The camera cannot read beyond 4 Hz frequency, which limits the onfly speed to <4.8 mm/s when triggers are generated with one microlens size (~1.2 mm) spacing. With the typical exposure time of 10 ms the maximum head movement during the exposure (which blurs the spatial resolution accordingly) is 48 µm (4 % of the microlens aperture).

The exposure time can be easily reduced with higher laser powers and currently exposures of 0.5 ms are used which blurs spatial resolution by a maximum of 2.4 µm or 0.2 % of the microlens aperture. Blur in spatial resolution happens also from synchronization delays between forward and backward scans. The onfly and stepwise scan communication scheme is explained in more detail in Appendix 5. The synchronization delays are studied with measurements on a fiducialized mirror in step-by-step and onfly scans which are presented in section 4.6. The onfly scans have also been implemented with normal incidence techniques described in the previous section. In this case the time interval from end of camera exposure to next trigger is also used to tilt the RTT axes (RX, RY) to normal incidence for the next subaperture.

2.5.6 SHARPeR design optimization

The SHARPeR as it was installed at ESRF is shown in Figure 2.42. The SHARPeR was modified in different stages over the course of my thesis (additional details in Appendix 6), to minimize the environmental errors that were discussed in chapter 2.4.3. The most recent design of the optical head is shown in Figure 2.43.

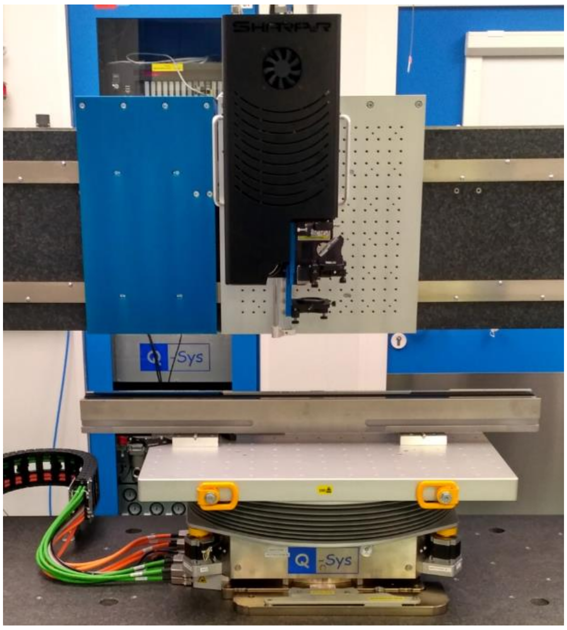

Figure 2.42 : SHARPeR optical head after installation at ESRF in May 2017.

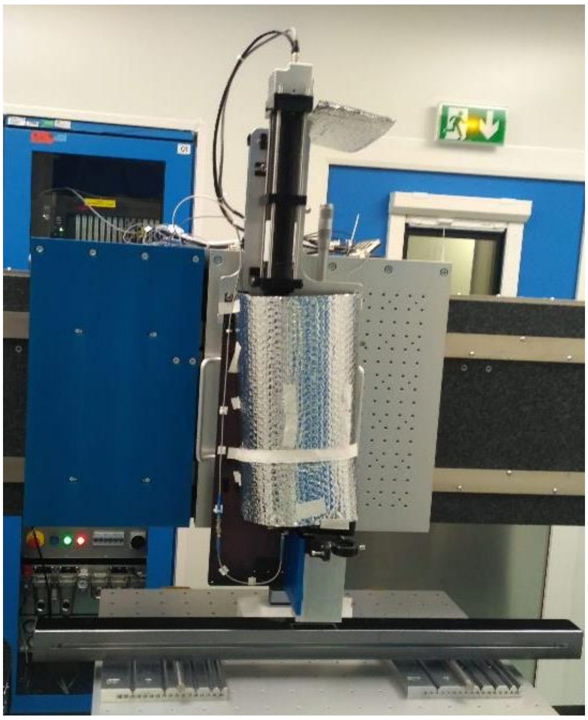

Figure 2.43 : SHARPeR optical head after many design changes in October 2019.

The latest design has modifications only on the optical head and the rest of the SHARPeR remains the same. The main changes are (1) shifting the wavefront sensor to the top, (2) partially isolating the optical path from surroundings, nearly from ~10 mm above the test mirror to the entrance pupil of wavefront sensor and (3) redirecting hot exhaust air from CCD fan (which is pushed down by downward airflow from roof), away from the optical path and test mirror. The modifications are shown schematically in Figure 2.44. The aim of the changes is to shift the CCD and its cooling fans, which is acting as dynamic heat source, away from optics and scan path. The other aim is to enclose the full optical path without any heat sources inside it.

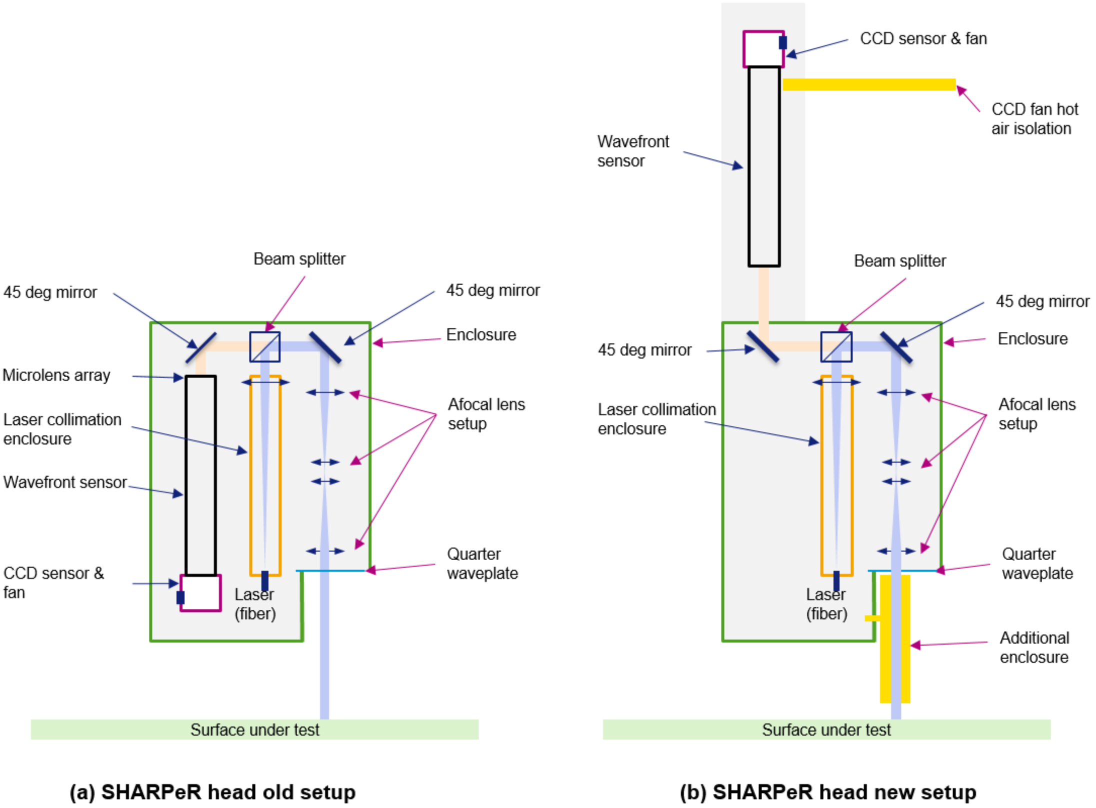

(a) SHARPeR head old setup

(b) SHARPeR head new setup

Figure 2.44 : Schematic of SHARPeR optical head modifications between old and new setups.

The SHARPeR measurements on long mirrors with old and new designs are presented in chapter 4.3.

3 STITCHING ALGORITHMS

Software stitching of subapertures is a common technique used by many optical metrology instruments [38], [64], [95], [96] to measure optics larger than the aperture size of the instrument. The SHARPeR instrument is provided with a stitching software, StitchWave, by Imagine Optic. This chapter provides an overview of StitchWave and some other stitching softwares in section 3.1. Such commercial stitching software are generally black boxes and the stitching algorithms applied are proprietary knowledge. To overcome this shortcoming, a few stitching algorithms were developed as open source during my thesis and they are presented in section 3.2. An open source and general stitching software (PyLOSt) for different synchrotron mirror metrology instruments developed during my thesis is presented in sections 3.3 and 3.4. PyLOSt implements the algorithms presented in section 3.2. The performance of different algorithm implementations is studied in section 3.5.

3.1 StitchWave and other commercial stitching software

StitchWave is the software developed by Imagine Optic to both control the data acquisition and stitch subapertures measured by the SHARPeR instrument on X-ray mirrors. The StitchWave software measures and stitches the mirror during the scanning and has no option to stitch subapertures offline. All the code for stitching is stored inside proprietary ‘dll’ files (for windows) and is not accessible to users. Imagine Optic also provides interface files in MATLAB to access the functions inside the ‘dll’ files to custom implement stitching, which can be used offline. However, the modifications that can be made to the StitchWave stitching are minimal and the software remains to a large extent a ‘black box’.

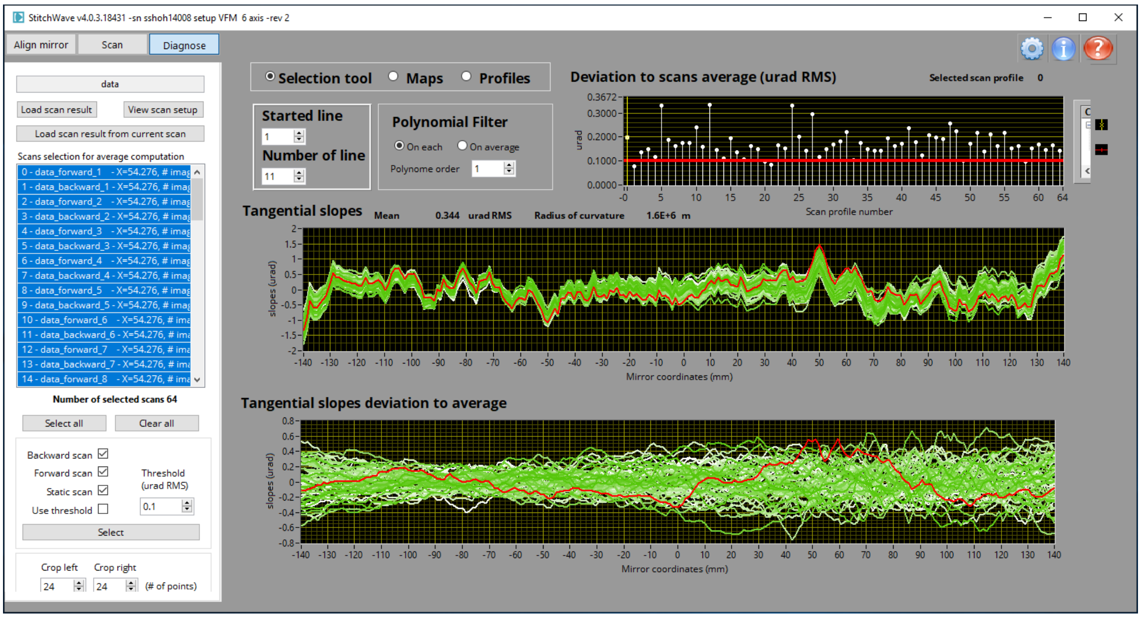

StitchWave v4.0.3.18431 -sn sshoh14008 setup VFM 6 axis -rev 2

Scans selection for average computation
0 - data_forward_1 - X=54.276, # imag
1 - data_backward_1 - X=54.276, # imag
2 - data_forward_2 - X=54.276, # imag
3 - data_backward_2 - X=54.276, # imag
4 - data_forward_3 - X=54.276, # imag
5 - data_backward_3 - X=54.276, # imag
6 - data_forward_4 - X=54.276, # imag
7 - data_backward_4 - X=54.276, # imag
8 - data_forward_5 - X=54.276, # imag
9 - data_backward_5 - X=54.276, # imag
10 - data_forward_6 - X=54.276, # ima
11 - data_backward_6 - X=54.276, # ima
12 - data_forward_7 - X=54.276, # ima
13 - data_backward_7 - X=54.276, # ima
14 - data_forward_8 - X=54.276, # ima

Number of selected scans 64

Backward scan ☑
Forward scan ☑
Static scan ☑
Use threshold ☐
Threshold (urad RMS) 0.1

Crop left 24
Crop right 24
(# of points)

● Selection tool ○ Maps ○ Profiles

Started line 1
Number of line 11

Polynomial Filter
● On each ○ On average
Polynome order 1

Selected scan profile 0

Tangential slopes Mean 0.344 urad RMS Radius of curvature 1.6E+6 m

Figure 3.1 : StitchWave stitched slope line profiles on a 300 mm long flat mirror. The mirror was measured in 32 forward and 32 backward repeated scans. The line profiles shown in the figure are obtained by averaging stitched 2D tangential slopes along sagittal direction.

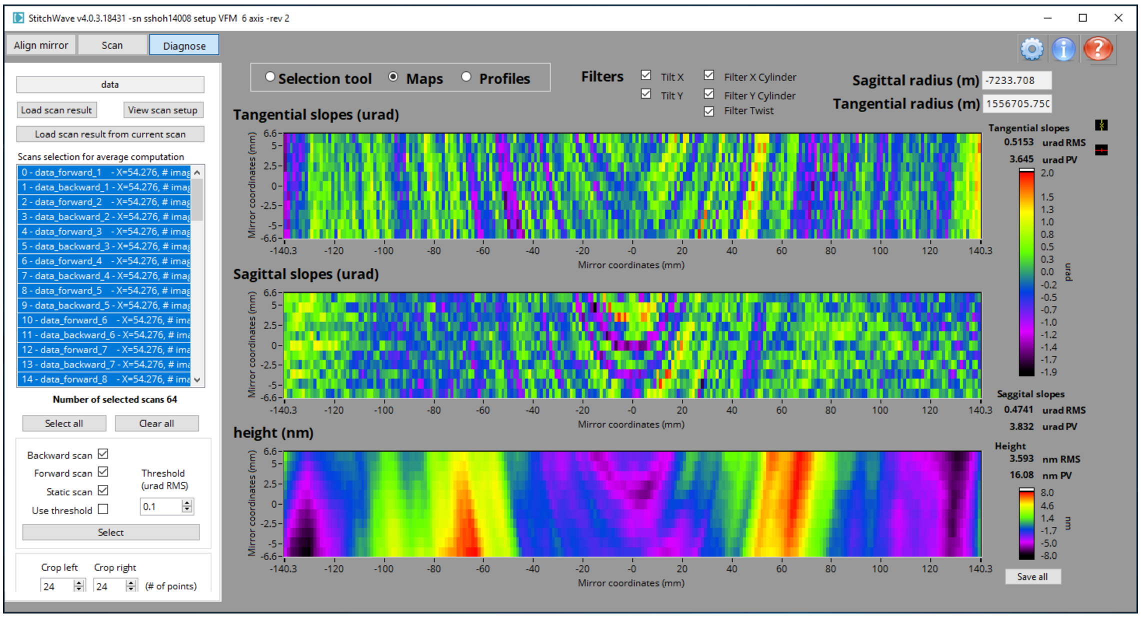

StitchWave v4.0.3.18431 -sn sshoh14008 setup VFM 6 axis -rev 2

Scans selection for average computation
0 - data_forward_1 - X=54.276, # imag
1 - data_backward_1 - X=54.276, # imag
2 - data_forward_2 - X=54.276, # imag
3 - data_backward_2 - X=54.276, # imag
4 - data_forward_3 - X=54.276, # imag
5 - data_backward_3 - X=54.276, # imag
6 - data_forward_4 - X=54.276, # imag
7 - data_backward_4 - X=54.276, # imag
8 - data_forward_5 - X=54.276, # imag
9 - data_backward_5 - X=54.276, # imag
10 - data_forward_6 - X=54.276, # ima
11 - data_backward_6 - X=54.276, # ima
12 - data_forward_7 - X=54.276, # ima
13 - data_backward_7 - X=54.276, # ima
14 - data_forward_8 - X=54.276, # ima

Number of selected scans 64

Backward scan ☑
Forward scan ☑
Static scan ☑
Use threshold ☐
Threshold (urad RMS) 0.1

Crop left 24
Crop right 24
(# of points)

○ Selection tool ● Maps ○ Profiles

Filters
☑ Tilt X
☑ Tilt Y
☑ Filter X Cylinder
☑ Filter Y Cylinder
☑ Filter Twist

Sagittal radius (m) -7233.708
Tangential radius (m) 1556705.750

Tangential slopes 0.5153 urad RMS 3.645 urad PV
Saggital slopes 0.4741 urad RMS 3.832 urad PV
Height 3.593 nm RMS 16.08 nm PV

Figure 3.2: StitchWave slopes and height profiles in 2D measured on 300 mm flat mirror and average of 64 scans. Height profile is obtained by integrating the tangential and sagittal slopes.

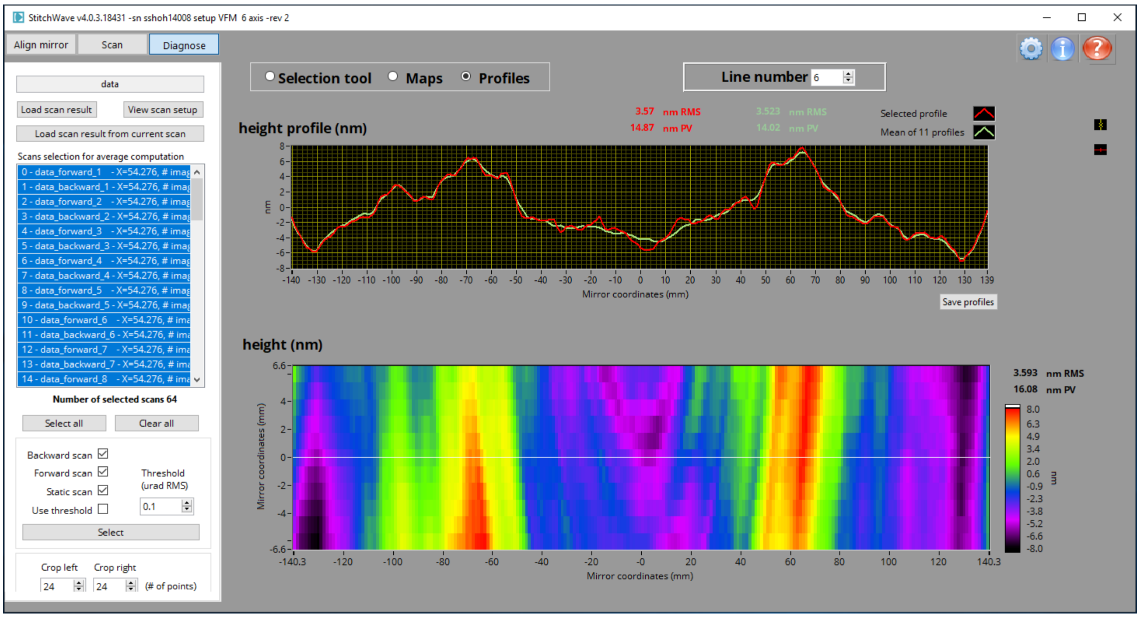

StitchWave v4.0.3.18431 -sn sshoh14008 setup VFM 6 axis -rev 2

Scans selection for average computation

0 - data_forward_1 - X=54.276, # imag
1 - data_backward_1 - X=54.276, # imag
2 - data_forward_2 - X=54.276, # imag
3 - data_backward_2 - X=54.276, # imag
4 - data_forward_3 - X=54.276, # imag
5 - data_backward_3 - X=54.276, # imag
6 - data_forward_4 - X=54.276, # imag
7 - data_backward_4 - X=54.276, # imag
8 - data_forward_5 - X=54.276, # imag
9 - data_backward_5 - X=54.276, # imag
10 - data_forward_6 - X=54.276, # ima
11 - data_backward_6 - X=54.276, # ima
12 - data_forward_7 - X=54.276, # ima
13 - data_backward_7 - X=54.276, # ima
14 - data_forward_8 - X=54.276, # ima

Number of selected scans 64

Backward scan ☑
Forward scan ☑
Static scan ☑
Use threshold ☐
Threshold (urad RMS) 0.1

Crop left 24
Crop right 24 (# of points)

○ Selection tool ○ Maps ● Profiles

Line number 6

3.57 nm RMS
14.87 nm PV
3.523 nm RMS
14.02 nm PV

3.593 nm RMS
16.08 nm PV

Figure 3.3: StitchWave stitched height 2D profile and a selectable line profile for measurements on 300 mm flat mirror and averaged over 64 scans.

3.1.1 StitchWave features

StitchWave includes functions to assist with the X-ray mirror alignment and acquisition setup, to controlling motion stages, for setting up different types of scans and stitching subapertures when the measurements are finished. 2D slope subapertures in tangential and sagittal directions are stitched separately and integrated using the Southwell integration algorithm [97] to get mirror height information. Stitching results can be visualized as shown in Figure 3.1, Figure 3.2 and Figure 3.3 for measurements on a 300 mm long flat mirror measured in 32 forward and 32 backward scans. Averaged 2D slopes and heights can be visualized along with repeatability on tangential slope line profiles. Basic algorithms allowing removal of residual tilts, fitting/subtraction of best fit cylindrical surfaces and twist can be applied to slope and height data and the final post-processed results can be exported to ASCII text files.

3.1.2 Stitching with Zygo MetroPro software

MetroPro [98] is a software package developed by Zygo Corporation [99] for control and data analysis with their instruments and has different modules available for different instruments. Newer instruments from Zygo use Mx software, which essentially offers the same basic functionalities as MetroPro but with a richer scripting environment based upon the Python language. Mx is the primary software in all new Zygo instruments. The older Zygo Fizeau interferometer installed at the ESRF uses MetroPro software delivered with modules to control the acquisition, stitching module, filters module and analysis tools. Functions for measuring long X-ray mirrors using stitching methods such as controlling stage translations and acquisitions were developed in house using LabVIEW, and MetroPro interferometer configuration modules can be called from LabVIEW [66]. MetroPro allows interfacing with external programs to call its modules with simple commands, as well as to develop custom user modules within MetroPro itself. MetroPro also includes an internal module intended primarily for stitching data acquired from micro-interferometers. As for StitchWave, this module is a black box based on undisclosed algorithms and cannot be modified.

3.1.3 Stitching with Bruker Vision software

Vision64 is the software provided by Bruker (formerly Veeco) [100] with their micro-interferometers. Due to their high spatial resolution (down to ~1µm) such instruments have a rather restricted field of view (~1-5 mm) and consequently they are often used in a stitching mode to provide information of surface topography over larger fields. Such measurements are commonly termed Micro-Stitching Interferometry (MSI). Micro-interferometers are commonly used for assessing the micro roughness of X-ray mirrors but MSI can extend the applicability of such instruments to the measurement of surface figure of even quite long optics [38], [64]. Vision64 is a general-purpose software package which controls different Bruker instruments (not just micro-interferometers). It includes the stage controls, MSI acquisition controls and stitching software as well as other analysis and visualization tools. The stitching component is not available by default and has to be purchased separately. The Vision64 software and stitching procedure can also be interfaced with other platforms like LabVIEW or Python, but only in very limited fashion. Only a limited set of stitching options can be modified within or from external program. Unlike MetroPro, no continuous communication channel is possible between Vision and external software. External programs can be only used to launch the Vision stitching process and can only modify the initial parameters. Vision stitching is also a black box with no information regarding the algorithms which are implemented.

3.2 Stitching methods

Stitching subaperture methods for optical metrology have been in development long before they were applied to the measurement of synchrotron mirrors [62]. However the problems faced by stitching algorithms of synchrotron mirrors are different from other applications such as panoramic photo stitching which generally use feature matching techniques like SIFT (Scale Invariant Feature Transform) [101]. The synchrotron mirrors are highly polished and usually do not have specific features with large contrast to be useful for subaperture stitching. Most of the stitching algorithms for synchrotron mirrors corrects for orientation mismatch between subapertures. Stitching based 2D profile measuring instruments like SHARPeR and MSI take subaperture images at translation steps with enough overlap region between successive images. The maximum overlap required may vary from mirror to mirror. Stitching techniques in general exploit data redundancy within overlapped regions, to correct some of the mechanical translation and systematic errors. Simpler stitching methods try to correct the piston, pitch and roll errors from the overlap regions. Advanced algorithms may correct for systematic errors such as reference errors.

In this work we have investigated the application of various stitching algorithms. Most commonly stitching algorithms correct for orientation errors between subapertures such as piston, pitch and roll, as described by Bray [102]. Stitching subaperture based metrology has been adapted by many laboratories [56], [64], [68], [72], [103]. Assoufid et al. presented the main problems faced for accurate metrology using stitching subapertures [104], which continues to be the case even today. Some of the main problems are propagation of different errors over stitching resulting in large noise in stitched measurements, even if the starting subaperture errors are small in scale. The errors can be static systematic errors (e.g. reference errors) and dynamic thermal and mechanical errors. Mimura et al. [65] presented a different approach with RADSI (relative angle determinable stitching interferometry) to measure highly curved mirrors, where the tilt angles of different subapertures (pitch/roll) are not determined numerically but directly measured with an additional flat mirror. Huang et al. [105] also presented a 2D stitching interferometry method based on external tilt angle measurements for each subaperture. Nicolas et al. [106] showed some additional problems with stitching algorithms such as periodic errors and curvature errors arising from ambiguities between test mirror and reference profiles, and proposed solutions like using two or more variable stitching steps. Polack et al. [107], [108] showcased algorithms to retrieve and correct for instrumental errors using redundant information within subaperture overlaps. Huang et al. [109] later published a similar self-calibration approach stitching algorithms using the redundancy in subaperture overlaps, and provided different algorithms (a) to estimate reference directly along with stitched height, (b) to separate evaluation of reference for faster computation and (c) to iteratively stitch and estimate the reference/systematic errors. Many of these concepts have been utilized to develop our stitching algorithms which are presented in this section.

Measurement schematic: The notation adopted to describe the stitching process is shown in Figure 3.4, and it will be used in the following sections to understand the stitching algorithms.

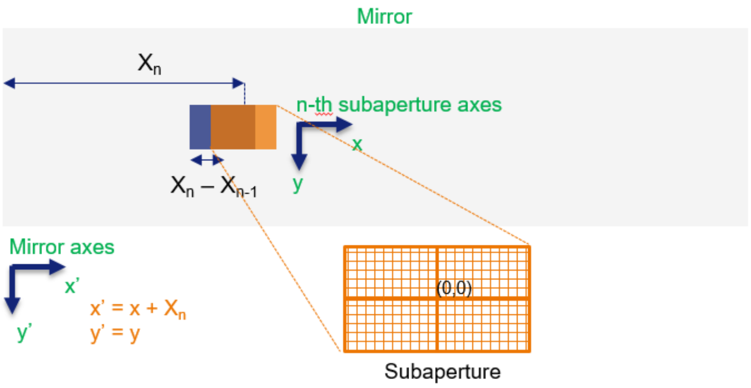

Figure 3.4 : Schematic of mirror and subaperture measurement setup.

Imperfections of the translation stages and/or the intentional reorientation of the mirror to minimize optical aberrations induce (primarily) piston, pitch and roll errors between measurements of adjacent sub-apertures. The stitching procedure should minimize these errors. In one of the simplest approaches these alignment corrections are minimized by introducing one or more of the errors as free parameters in a least squares optimization of the pixel wise errors in the overlapped region. Measured subaperture data can be represented by eq.(3-1).

$$m(x,y,n) \;=\; s(x+X_n,y) + \; e_s(n) \;\; + \; e_r[x,\; y,\; s(x+X_n,y)] + \; e_{oth}(x,y,n)$$

(3-1)

The measurement setup for eq.(3-1) is shown in Figure 3.4, where x & y represent the subaperture coordinate system and X_n is the offset of nth subaperture ($X_n = nX_0$ if the translation step is constant). Measured data is represented in subaperture coordinates, and the subaperture is centered on (X_n, 0) where the scan translation is only along the longitudinal mirror axis X. In eq.(3-1), $s(x+X_n,y)$ represents the true height / slope profile of the mirror combined with different errors to give the measured data. The error term $e_s(n)$ represents the stage translation (or mirror reorientation) errors such as pitch, roll, and piston. The term e_r encompasses the systematic errors, which are dependent not only on the position in the instrument aperture but also on the shape and orientation of the mirror. The error term e_{oth} represents the remaining errors such as statistical noise, drift errors, and noise from environmental effects.

3.2.1 Simple average

The simple averaging algorithm corrects only for piston for sub-aperture height data using a pixel wise least squares approach which minimizes the following cost-function.

$$f(x',y',C) = \sum_j \sum_k [oe(x',y',j,k) - c(j) + c(k)]^2$$

Where the term $oe(x',y',j,k)$ is the overlap error between jth and kth subaperture, $c(j)$ is the piston correction for jth subaperture, C is the full array of piston correctors and $f(x',y',C)$ is the cost function.

For slope data, no correction is applied. The algorithm then applies a simple arithmetic averaging to join the subapertures. This algorithm is useful to join sub-apertures where pitch and roll errors due to translation between sub-apertures are not very significant (<0.1 µrad). In practice with high quality synchrotron mirrors and translation stages which exhibit angular motion defects which are typically ~1-10 µrad this type of algorithm is little used.

3.2.2 Progressive stitching (PROG)

The progressive stitching algorithm (PROG) applies correction of piston, pitch, and roll errors and stitches in a sequential approach as shown in Figure 3.5. Beginning from one of the mirror ends, the first and second subaperture are stitched and to this result the third subaperture is joined. The intermediate stitched image gradually grows until all the subapertures are stitched and a (k+1)th subaperture image is stitched to kth intermediate stitched images. The progressive stitching algorithm was developed based on discussions with Francois Polack from SOLEIL synchrotron.

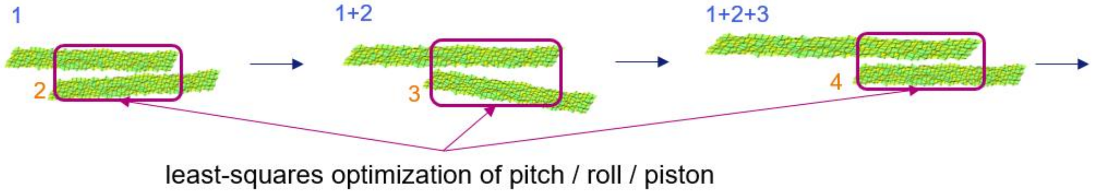

Figure 3.5 : Sequential stitching of subapertures using progressive stitching algorithm.

The algorithm can be expressed by eq.(3-2). The measurement notation and various terms used follow those presented in Figure 3.4 and eq.(3-1).

$$s_{\mathrm{k}}(\mathrm{x}',\mathrm{y}',\mathrm{k}) = \frac{\sum_{i=1}^{k}\{m(x'-X_i,y',i)-c(i)\} * w(i)}{k}$$

$$c(k) = least\_square\_optimize\big(m(x'-X_k\,,y',k)-s_{k-1}(\mathrm{x}',\mathrm{y}',k-1)-c(k)\big)$$

(3-2)

The term *c(k)* represents the corrections for pitch, roll and piston errors and *w(i)* stands for weight function. The correctors are obtained by optimizing the cost function, s_k of eq.(3-2) using a least squares minimization. By default, all the pixels in the overlap are used in the optimization function. The weight function is by default one, which means using simple arithmetic mean to join corrected subapertures. The weight function can be adjusted to represent the confidence level of measurement accuracy within the instrument aperture pixels. In general, optical systems perform most accurately close to the optical axis, however for each instrument a weight function can be derived from its optical transfer function. After all the subapertures are stitched to yield reconstructed mirror heights / slopes, $s_r(x', y')$¸ the algorithm can continue stitching iteratively *n* times from the first subaperture. From the second iteration onwards, each subaperture is compared to the reconstructed result from previous iteration to determine pitch, roll and piston corrections. Such iteration is optional, however as the algorithm does not use any initializations and uses localized optimizations, iteration of the stitching can help minimize the errors more effectively. Also, as the algorithm is directional (i.e. stitching may be different if started from mirror left end compared to starting from right end), bidirectional iteration might help minimize some of these errors (e.g. stitch in the iteration sequence (1) left to right, (2) right to left, (3) left to right etc.).

3.2.3 Global methods

Stitching algorithms performed offline after the scans are finished can use the data from all subapertures to find the best corrections globally. The progressive stitching algorithm which was discussed in section 3.2.2, could only apply stage error corrections locally. Two stitching algorithms, one matrix based (MO) and other optimization based (GO) are discussed in the following subsections.

3.2.3.1 Matrix approach for solving linear equations of overlap errors (MO)

The matrix overlap error (MO) method is based upon an algorithm implemented by Josep Nicolas from ALBA synchrotron [106]. Imagine Optic developed its stitching algorithm based on similar approach independently to the work of Josep Nicolas. It uses overlap regions not just between successive subapertures, but all possible overlaps between all subapertures above a minimum overlap threshold as shown in Figure 3.6.

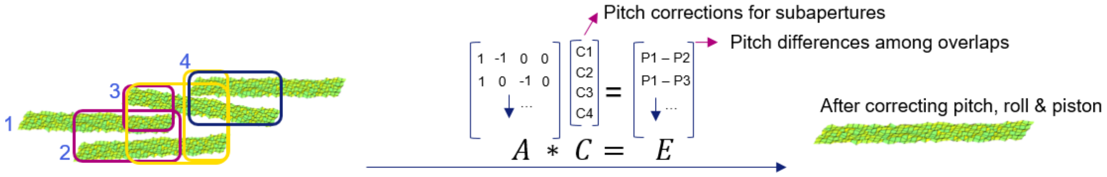

Figure 3.6 : Schematic of stitching with matrix overlap error (MO) method.

The algorithm evaluates pitch, roll and piston differences between subapertures j and k from the overlap region. If the subaperture data is in heights, plane fitting is used within overlap to determine pitch, roll and piston differences. In the case of slope stitching, tangential and sagittal subaperture slopes are stitched separately. Averaging over all pixels within overlap region provides the pitch error difference from tangential slopes and roll error difference from sagittal slopes. Piston errors are absent in slope stitching.

$$oe(x', y', j, k) = m(x' - X_j, y', j) - m(x' - X_k, y', k)$$

(3-3)

The overlap error between subapertures j and k is shown in eq.(3-3). X_j and X_k are the relative positions of subapertures on the mirror. Only the overlaps larger than minimum threshold are considered i.e. $|X_k - X_j| < (1 - \text{threshold})*L$, where L is the subaperture length along X. If the data is in heights, the overlap error (*oe*) is fit to a plane $P_{jk}\,x' + R_{jk}\,y' + T_{jk}$, and if the data is in slopes, P_{jk} is the mean of tangential slope overlap error, Q_{jk} is the mean of sagittal slope overlap error.

$$c_p(j) - c_p(k) = P_{jk}$$

$$c_q(j) - c_q(k) = Q_{jk}$$

$$c_t(j) - c_t(k) = T_{jk}$$

$$A * C = E$$
$$C = A^{-1} * E$$

(3-4)

P_{jk}, Q_{jk}, T_{jk} stand for pitch, roll and piston differences between subapertures j and k, and correspondingly c_p, c_q, c_t represent the pitch, roll and piston correctors. The linear equations for all the valid overlaps (which have larger than minimum overlap) are solved using the matrix notation as seen in eq.(3-4), where A is the index matrix, C is the array of correctors and E is the array of pitch, roll and piston differences. The inverse of index matrix (A) is determined using Python (Moore-Penrose) pseudo inverse which is based on Singular Value Decomposition (SVD). The Python function *numpy.linalg.pinv* has been used to calculate pseudo inverse of matrix [110]. The Moore-Penrose pseudo inverse (MPP) is one of the most commonly used algorithms to solve overdetermined linear inverse problems, however it may not be as efficient in case of sparse matrix inversions [111]. MPP is also processor intensive and can slowdown or fail with very large matrices. To improve the overall performance, a fast version of the algorithm was implemented using sparse matrices for A, C & E. For the case of a sparse square matrix A, the inverse has been implemented using python function *scipy.sparse.linalg.spsolve* [112]. The non-square matrix inversion still utilizes MPP and alternatives may need to be explored in the future.

The corrector array (C) is determined from eq. (3-4) and finally the stitched mirror profile can be obtained as shown in eq.(3-5).

$$s_{\mathrm{r}}(\mathrm{x}', \mathrm{y}') = \frac{\sum_{k=1}^{N} \{ m(x' - X_k, y', k) - c(k) \} * w(k)}{N}$$

(3-5)

Where *w(k)* is the weight function and N is the total number of subapertures and *c(k)* is $C_p(k)$ x’ + $C_q(k)$ y’ + $C_t(k)$ for heights and $C_p(k)$ / $C_q(k)$ for tangential / sagittal slopes. Weights are set to one in the current work and more complex weight functions could be investigated in the future.

3.2.3.2 Global optimization of total overlap error cost function (GO)

Global optimization (GO) follows same principles as the *matrix overlap error* method in defining the problem, however the algorithm solves the pitch/roll/piston corrector determination through optimization instead of matrix techniques and it has been implemented by myself. The main difference of optimization methods, compared to linear matrix inversion methods, are the flexibility in defining the total error function (eq.(3-6)), as linear/non-linear functions. In case of data with large outliers some of the optimization methods may work better than simple linear matrix inversion methods. The GO algorithm implementation uses the python least squares optimization of any general error function *scipy.optimize.least_squares* [113]. The optimization is an iterative process which is done internally with default tolerance limit. The loss function used for optimization is *arctan*, which is used to estimate increments to optimizing parameters in each iteration. The loss function *arctan* is expected to perform well in case of outliers. Many other customization options are available within optimization which need to be further explored.

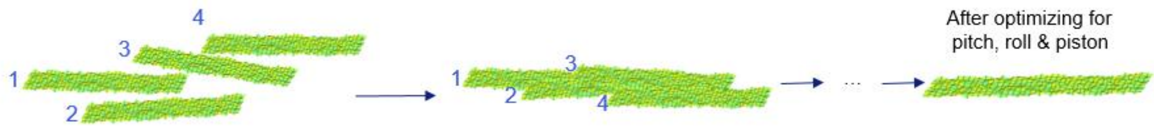

Figure 3.7 : Schematic of stitching with global optimization (GO) method.

The schematic of global optimization approach is shown in Figure 3.7. A total error function of all overlap errors above a minimum overlap threshold, for all pixels in the overlap is defined as shown in eq.(3-6).

$$f_e(x',y',C) = \sum_j \sum_k [oe(x',y',j,k) - c(j) + c(k)]^2$$

(3-6)

The total error function is solved by least square optimization to get the best corrector array *C* which minimizes the error function. Finally, the subapertures are corrected and joined in the same way as for the *matrix overlap error* method as shown in eq.(3-5).

Global optimization (GO) may be performed for all pixels in all overlaps (GO-FULL) or with averaging over pixels in each overlap (GO-SIMPLE). The method GO-SIMPLE is not useful for height stitching, but for slope stitching approximating overlap errors to their mean can greatly improve speed and is also sufficient in general. The MO algorithm (section 3.2.3.1) uses similar approximation as well, where the mean overlap error is equated to the pitch/roll differences between subapertures.

3.3 PyLOSt stitching software for X-ray mirrors

In response to the commercial ‘black-box’ stitching software solutions which also present certain limitations with regard to pre-processing of data and the use of proprietary data formats it was decided to develop an alternative software suite capable of incorporating different algorithms flexibly. PyLOSt (Python Large Optic Stitching) is a software package developed in Python for stitching of sub-aperture topography measurements of X-ray mirrors measured with different instruments. The PyLOSt software is being developed to satisfy objectives from my thesis as well as another project namely ‘Metrology On One-Nanometer-Precise Optics’ (MooNpics [69]). MooNpics is a work package of the CALIPSOplus European project, aimed to push mirror metrology and mirror fabrication to single-nanometer figure errors and 20 nrad rms slope error precision and make the metrology know-how available to several user facilities and mirror producing companies.

My thesis aims to develop new algorithms to improve upon the existing StitchWave stitching for the SHARPeR instrument. MooNpics requires development of an open source stitching software framework that can be used by multiple instruments from different synchrotron and mirror manufacture facilities across Europe. The stitching methods which are explained in section 3.2 have been implemented in the PyLOSt software.

Table 3.1 : Stitching software PyLOSt specifications

Data dimensions (subaperture)	**0D**	**1D**	**2D**
Instruments (examples)	LTP / NOM	LTP stitching	SHARPeR, Fizeau Interferometer, Micro-stitching Interferometer
Stitching	- (May be combined to other 1D/2D data)	1D	1D, (2D)
Type	Slopes / height	Slopes / height	Slopes / height
Stitch algorithms	Y	Y	Y
Stitch different data sizes	-	Y	Y
Other functions (Filters/ masks/ fitting)	Y	Y	Y

Table 3.1 shows specifications for the PyLOSt stitching software. It should be able to process and visualize data from different instruments. The table shows commonly available data dimensions, where instruments like LTP and NOM measure slopes in 0D at a single position at each subaperture on the mirror (a mirror subaperture corresponds to instrument aperture). LTP stitching is an example of 1D data stitching, which is usually applied to stitching curved mirrors [45], [68]. The most frequently stitched data is 2D subapertures obtained from instruments such as SHARPeR, Fizeau interferometers and Micro-interferometers. Stitching can be performed with data from scanning along one axis (tangential) or along two axes (tangential & sagittal). The most commonly stitched

data types are slopes and heights. In some rare cases, curvature data is also used to reconstruct mirror topographies [114]. Stitching can be done with different algorithms. PyLOSt stitching algorithms are discussed in more detail in section 3.2. Stitching can be performed with different data sizes, and the algorithms should able to cope with larger datasets. Some additional functions are needed such as filtering, masking, and fitting data, in order to perform stitching and post-stitching analysis.

3.3.1 PyLOSt tools and schematic

PyLOSt is developed using Python 3 [115], PyQt5 [116], [117], HDF5 [118], Nexus [119], and silx [120] tools. PyQt is used for graphical user interface (GUI) development. Silx is an ESRF library in Python for data visualization and processing (fitting, masking etc.). HDF5 and Nexus are discussed in more detail in the following section.

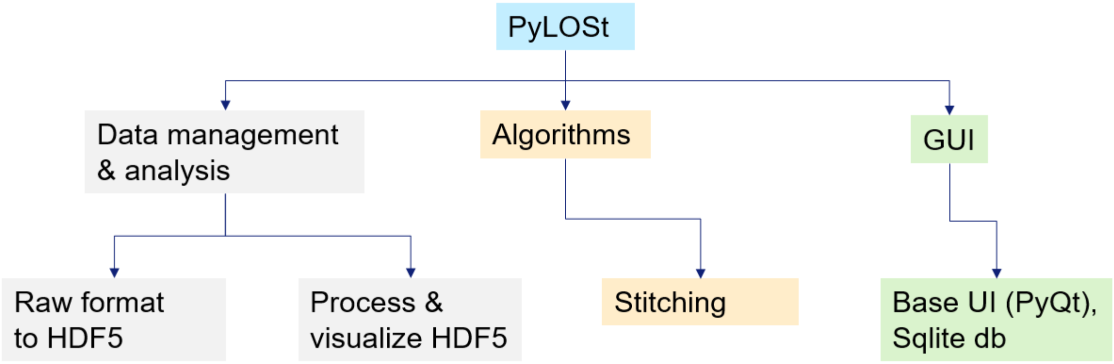

Figure 3.8 : Schematic of PyLOSt software.

Figure 3.8 shows the basic structure of the PyLOSt software. It has three principal components: 1) data management and analysis tools, 2) stitching algorithms and 3) graphical user interface (GUI). Measurement data is stored, processed and the processed results are stored within HDF5 file format. Proprietary instrument file formats such as ‘*.has’ for SHARPeR and ‘*.dat’, ‘*.datx’ for Zygo Fizeau interferometer are converted to a standardized HDF5 file format. This standard format is discussed in section 3.3.2. Much of the data visualization (e.g. plotting) and processing (e.g. masking) is done using silx toolbox but some specific processes have been developed for PyLOSt (e.g. fitting ellipse). Different stitching methods are the primary algorithms in development, however additional functions such as binning, filtering are being developed independently of stitching algorithms. PyLOSt aims to be flexible for users to integrate their stitching and non-stitching algorithms as plugins. The GUIs unrelated to manipulation of HDF5 measurement files (which rely on silx), such as raw data conversion, are developed using PyQt. Any PyLOSt software related data is stored to a local SQLite database file, such as instrument list, algorithm options and instrument options.

3.3.2 Standard data format using HDF5 & Nexus

HDF5 [118, p. 5] is a flexible tool to manage and process large data sets. It was originally developed for supercomputing applications and gradually it is being used by large facilities such as synchrotrons. The ESRF is shifting to use HDF5 for all its data management. To improve interoperability and collaboration a standardized file format using HDF5 is being defined by the MooNpics community to store data from different instruments. The standard HDF5 file format allows easy exchange of measurements between users, and use of such a format simplifies stitching implementation with PyLOSt. The Nexus format [119] is a convention on top of HDF5 designed to define a more structured common data exchange format between different X-ray and neutron facilities (although Nexus may be used without HDF5 as well). HDF5 files are primarily comprised of three elements - groups, datasets, and attributes. Groups are akin to folders on a hard disk drive, whereas datasets are similar to files and attributes allows the recording of additional metadata along with groups and datasets. Apart from these, HDF5 is very flexible and does not create any structuring or cataloguing. Nexus allows structuring with a set of design principles and class attributes. Some of the defined Nexus base classes are NXentry, NXsample, NXdata, and NXinstrument. NXentry class is required by all the groups at the top level in a HDF5 file and it typically contains all the data and meta information of a single experiment. NXsample class is used for group containing information about sample, NXinstrument for instrument information and NXdata for measured data. In addition to the Nexus base classes, additional custom classes may be defined for specific applications. Group and dataset naming is flexible, and Nexus class is required for all groups in HDF5 file but not for any datasets. Discussions are ongoing within the MooNpics community to having a comprehensive list of guidelines for standard HDF5 file format. They include coordinate systems, units, shape of raw subaperture data and the use of Nexus conventions.

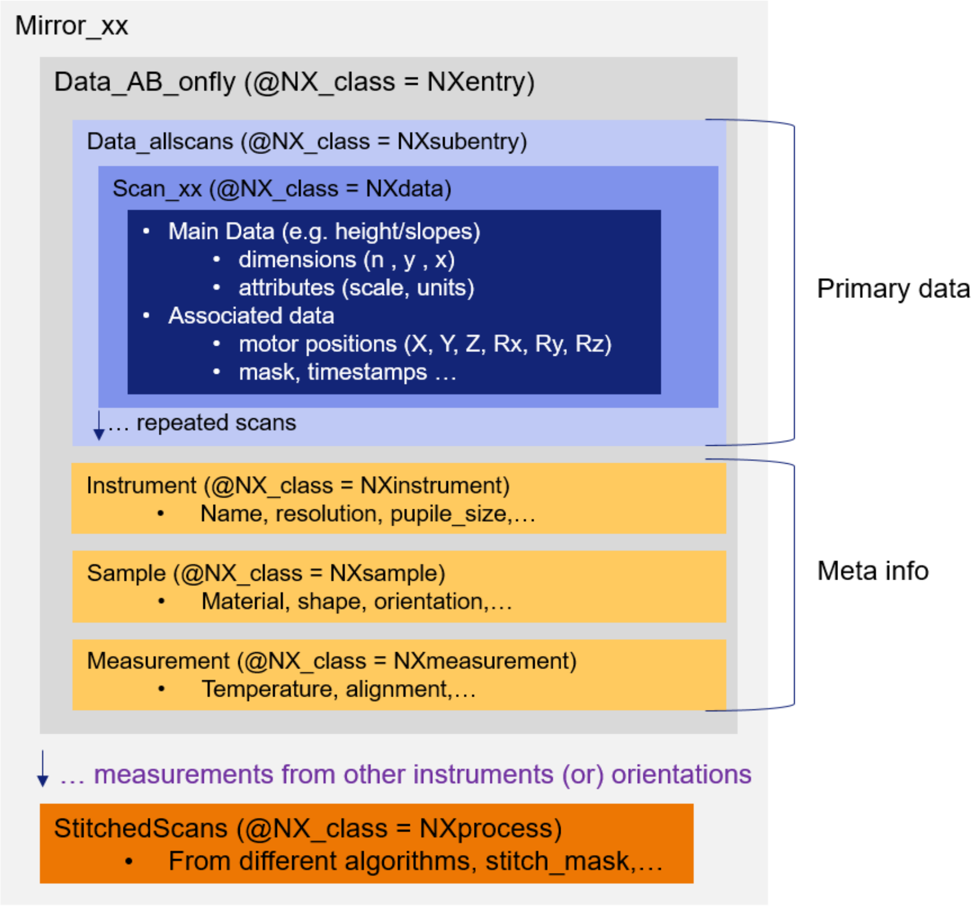

Figure 3.9 : Example data format in HDF5 for X-ray mirror metrology.

Figure 3.9 shows an example data format in HDF5 that we are currently using at the ESRF to structure data to be stitched with PyLOSt. Measurements of a single mirror are envisaged to be stored in a single file. Raw data from different measurements on a mirror with different instruments or with the same instrument in different orientations are stacked in a single file. Scans may be repeated many times to minimize the statistical noise, and with SHARPeR, scans are stitched and later averaged. In contrast, the ESRF Zygo Fizeau and Veeco micro-interferometer instruments usually measure many subaperture images at each mirror position and average the height maps before stitching and only the averaged subapertures are stored. It is therefore difficult to define raw data;

instruments such as Fizeau interferometers generate fringe data in a subaperture, which has to be processed to obtain height information. Such fringes can be considered raw data instead of heights, or heights from average of many images may be considered raw data. Instruments such as LTP, which do not use stitching in normal circumstances, may have raw data synonymous to stitched data from SHARPeR. The MooNpics HDF5 format and PyLOSt software aim to create an expandable framework for X-ray mirror metrology. For simplicity, sub-aperture heights and slopes are currently considered as raw data. Any pre-processing before converting to an HDF5 file, such as averaging many images, can be recorded in metadata in the HDF5 file. The raw data conversions for different ESRF instruments LTP, SHARPeR, Zygo Fizeau, and Veeco MSI are implemented in PyLOSt software as shown in Figure 3.10. Users can modify or develop new conversion programs to work with their instruments using PyLOSt.

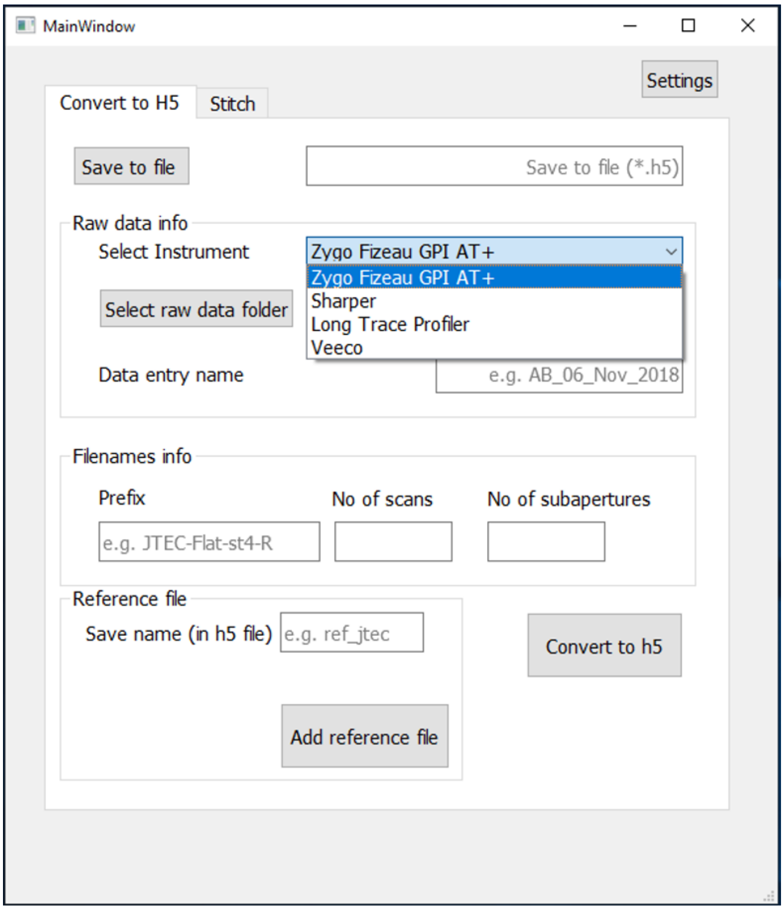
Select Instrument: Zygo Fizeau GPI AT+

Figure 3.10 : PyLOSt raw data conversion module. Data is converted from instrument raw format to standardized hdf5 format.

3.3.3 Stitching using PyLOSt software

Currently, PyLOSt can stitch 2D slopes and heights using different algorithms. They were tested with data from ESRF instruments. The performance of different stitching algorithms for different instruments are explored in section 3.4. An overview of the HDF5 file structure and data visualization with the PyLOSt software is shown in Figure 3.11. The figure shows an HDF5 file with measurements on a 100 mm long JTEC flat mirror with LTP, SHARPeR, Zygo Fizeau and Veeco MSI at the ESRF, with each measurement as an NXentry class. All the fields in an NXentry are not mandatory, however to do stitching some of the datasets such as height / slope data and instrument pixel size are required.

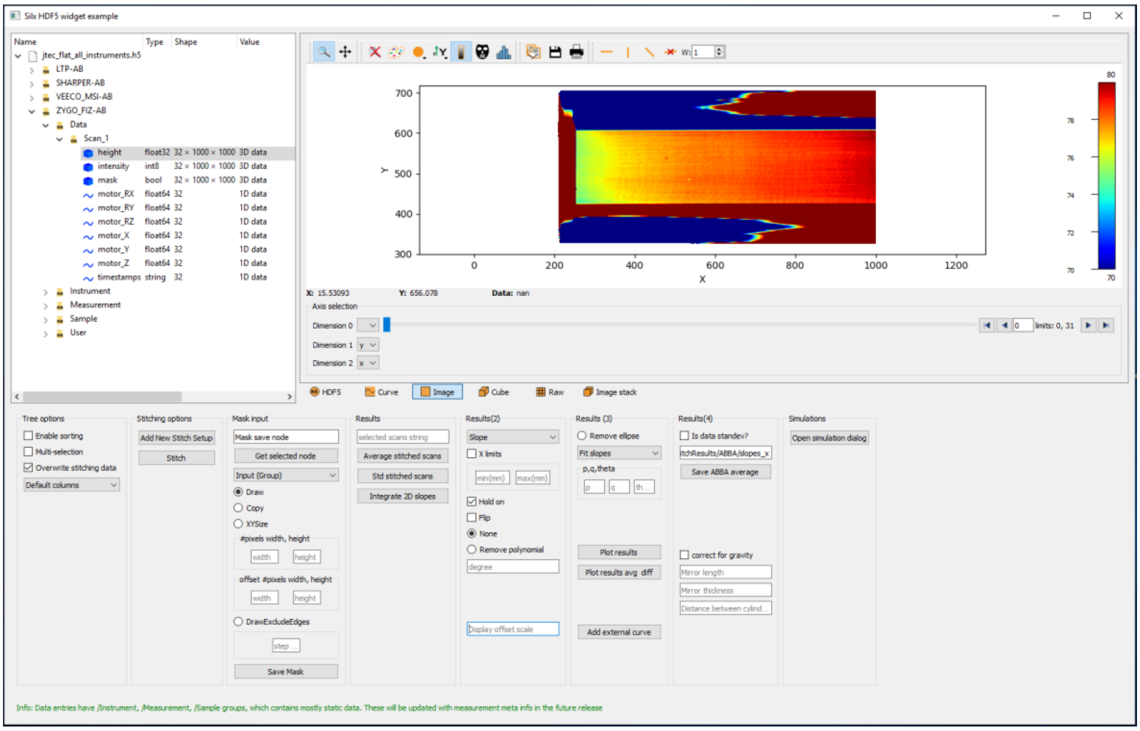

Name	Type	Shape	Value
jtec_flat_all_instruments.h5			
LTP-AB			
SHARPER-AB			
VEECO_MSI-AB			
ZYGO_FIZ-AB			
Data			
Scan_1			
height	float32	32 × 1000 × 1000	3D data
intensity	int8	32 × 1000 × 1000	3D data
mask	bool	32 × 1000 × 1000	3D data
motor_RX	float64	32	1D data
motor_RY	float64	32	1D data
motor_RZ	float64	32	1D data
motor_X	float64	32	1D data
motor_Y	float64	32	1D data
motor_Z	float64	32	1D data
timestamps	string	32	1D data
Instrument			
Measurement			
Sample			
User			

X: 15.53093 Y: 656.078 Data: nan

Info: Data entries have /Instrument, /Measurement, /Sample groups, which contains mostly static data. These will be updated with measurement meta info in the future release

Figure 3.11 : PyLOSt software visualization of data and the tree structure of HDF5 file. The figure shows a subaperture image of a 100 mm long JTEC flat measured by Zygo Fizeau.

A stitching setup is created for each NXentry that needs to be stitched, as shown in Figure 3.12. This stitching setup allows configuration of different parameters such as stitch step (currently constant) and type of stitching algorithm. Stitching algorithm options can also be customized for measurements from different instruments or from the same instrument with different setups (such as different magnifications for micro-interferometry data). Additional pre-stitching steps such as masking subaperture data can be done within the stitching setup before the stitching procedure. PyLOSt can also be used post-stitching to plot and compare different results, filtering global shapes such as sphere and ellipse, and more.

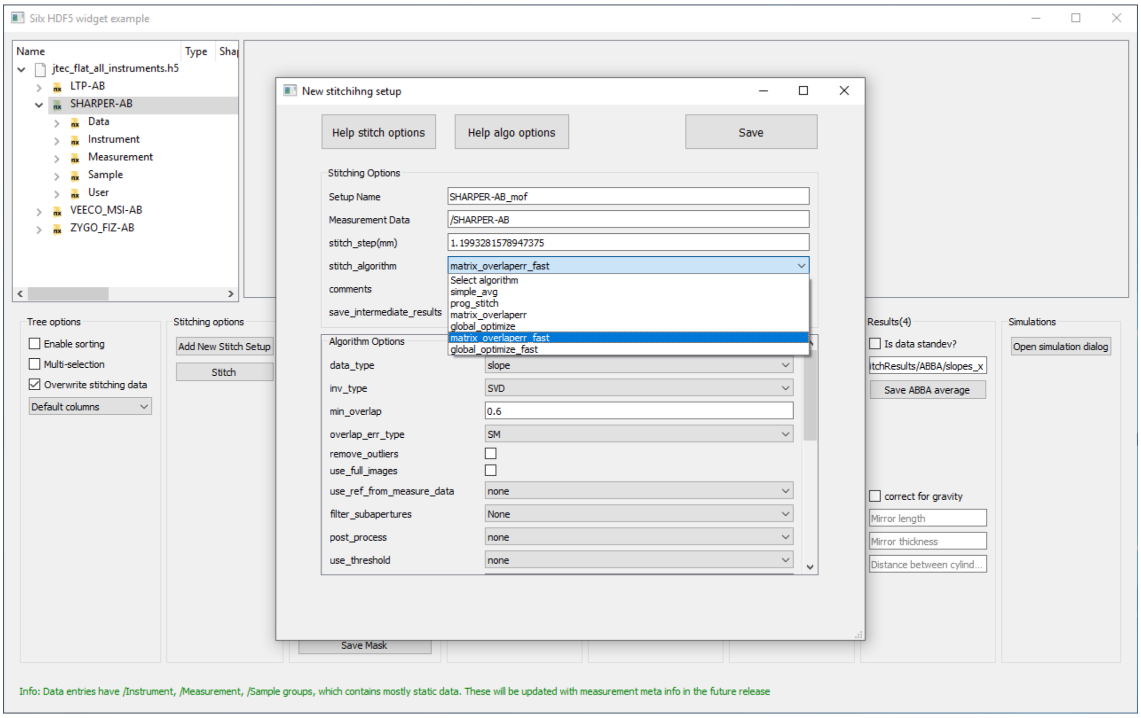

☐ Enable sorting
☐ Multi-selection
☑ Overwrite stitching data
Default columns

☐ Is data standev?
itchResults/ABBA/slopes_x
☐ correct for gravity

Setup Name: SHARPER-AB_mof
Measurement Data: /SHARPER-AB
stitch_step(mm): 1.1993281578947375
stitch_algorithm: matrix_overlaperr_fast
comments
save_intermediate_results

data_type: slope
inv_type: SVD
min_overlap: 0.6
overlap_err_type: SM
remove_outliers: ☐
use_full_images: ☐
use_ref_from_measure_data: none
filter_subapertures: None
post_process: none
use_threshold: none

Info: Data entries have /Instrument, /Measurement, /Sample groups, which contains mostly static data. These will be updated with measurement meta info in the future release

Figure 3.12 : Stitching setup with PyLOSt. Stitching parameters such as stich step, type of stitching algorithms are saved to stitching setup within the same file. Algorithms options such as minimum overlap size can also be changed in the stitch setup. Stitch setup can be created only for groups with NXentry class. However, multiple setups (with different algorithms) for single entry can be created.

3.4 Additional functionalities in PyLOSt

3.4.1 Reference error corrections

A reference measurement is usually performed on a separate flat mirror with good quality to provide an initial estimate of the instrument errors originating mostly from the optical aberrations of the instrument. The reference measurement is subtracted from subapertures prior to stitching. Typically to minimize the reference mirror wavefront error contribution, several images are taken at different regions on the reference mirror and averaged. Averaging can minimize high frequency reference errors, but the low frequency errors such as reference radius of curvature still remains. Even with a good reference mirror, as the X-ray mirrors can be of comparable or even higher quality than reference, it becomes a significant challenge to calibrate the reference errors.

PyLOSt stitching algorithms also include the option to extract this reference data from the average of measured test surface itself. Within this reference second order polynomial is subtracted, so as to avoid correcting the mirror curvature. PyLOSt also implements algorithms which extract this reference during stitching. Thus, the matrix overlap error or global optimization approach can be extended to extract a repeated reference image along with pitch, roll and piston errors. The correction term can be generally represented (for height data) as shown in eq.(3-7).

$$C(\mathrm{k,x,y}) = C_p(\mathrm{k})\,\mathrm{x'} + C_q(\mathrm{k})\,\mathrm{y'} + C_t(\mathrm{k}) + \sum_{i=i_0}^{N_i} C_r(\mathrm{i}) * B_i(\mathrm{i,x,y}) \tag{3-7}$$

Where the reference is expressed as a sum of base functions. C_r represents the reference correction terms and B_i is the base function to represent the reference, by default polynomial base functions are used to extract the reference in PyLOSt. Usually shape is ignored for reference extraction and hence the starting base function order is larger than two. The terms $C_p(\mathrm{k}), C_q(\mathrm{k}), C_t(\mathrm{k})$ represent the pitch, roll and piston errors respectively for k$^{\mathrm{th}}$ subaperture. The reference is assumed to be a static surface repeated over all subapertures, and hence is independent of k. The number of terms given in eq.(3-7) for reference base functions (N_i) are limited by performance of the algorithm. The eq.(3-4) is extended to include the reference base functions with matrix A for all pixels in all overlaps, as given by eq.(3-8).

$$A_{N_p \times N_c} * C_{N_c \times 1} = E_{N_p \times 1}$$

(3-8)

Where N_p equals to total number of pixels from all overlaps, N_c equals to total corrector terms equivalent to $3 * N_k + (N_i - i_0)$, with the term N_k is the total number of subapertures. Once the correctors are calculated through matrix inversion or optimization (section 3.2.3), a 2D map given in eq.(3-7) is evaluated and corrected for each subaperture.

3.5 Measuring the performance of stitching algorithms

Different stitching methods mentioned in section 3.2 have been implemented with PyLOSt, and in this section, the performance of these algorithms is explained. The performance is studied using synthetic datasets generated to mimic (a) slope data based on the SHARPeR instrument, (b) height data for Zygo Fizeau instrument. The synthetic data considers various errors, which can be characteristic of the respective instruments.

3.5.1 Slope stitching with synthetic SHARPeR data

An ideal flat mirror with parameters given below is simulated and stitched after adding different errors typical of the SHARPeR instrument.

- Mirror aperture dimensions 100 x 13.2 mm^2
- Stitching step of 1.2 mm
- Subaperture size 18 x 13.2 mm^2
- No. of subapertures : 68
- No. of scans: 64 (32 FW, 32 BW)
- Random noise (PV) : 2 µrad - applied to each microlens independently in a box distribution. The random noise value was determined with SHARPeR taking

static images (without motion, over ~ 2 minutes and 300 images), and measuring PV of noise (i.e. peak to valley of slopes minus slope average over 300 images).

- Pitch / roll error (PV) - systematic : 2.2 / 0.5 µrad – Pitch and roll were obtained for each subaperture from stage calibration (see Appendix 4) over 100 mm near the center of translation stage (~ 700 to 800 mm).
- Pitch / roll repeatability (PV) - random : 1.8 / 0.5 µrad – Using box distribution to determine the random repeatability error for each subaperture.
- Instrument systematic errors as measured on flat JTEC mirror (of <50 nrad / ~0.1 nm rms specification) as shown in Figure 3.13. The systematic (refernce) errors measured with JTEC flat mirror are added to simulation data. Additional reference measured on a flat SiC mirror (~0.7 nm rms specification), is used before stitching for reference correction.

The random noise levels were determined from SHARPeR static images. The pitch & roll errors were determined from the calibration of SHARPeR scanning axis over 100 mm length near the center of stages.

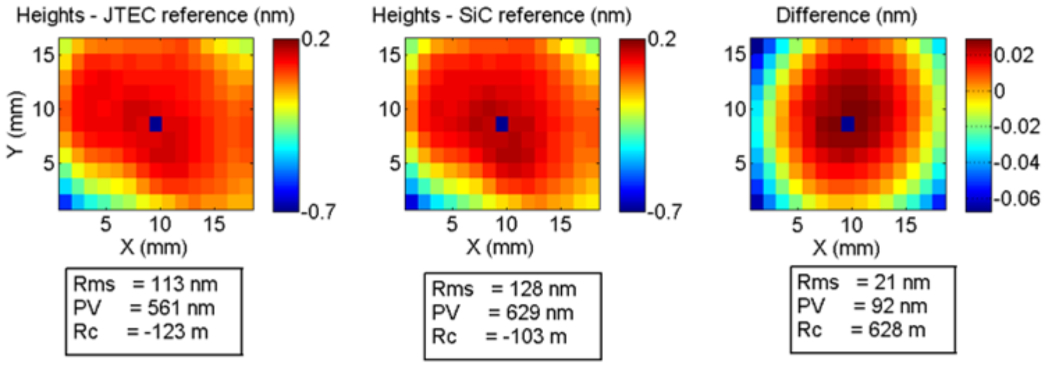

Figure 3.13 : SHARPeR reference heights with two different flat mirrors (JTEC flat & SiC flat) and their difference.

The simulated subapertures are stitched using different PyLOSt algorithms and the results are presented in Table 3.2 and Figure 3.14. The JTEC flat reference is added to the subapertures in all simulations, assuming JTEC flat reference is very accurate representation of systematic errors. The same JTEC reference is corrected from all subapertures in simulation 1, and it results in very flat reconstructed mirror (Rc ~5700 km), with slope error rms ~13.4 nrad. It implies simulation 1 is the stitched noise if the reference is well calibrated. If a different reference (e.g. measured with SiC mirror) is corrected from subapertures and stitced, the results as shown in simulation 2 give a radius of curvature ~-1.25 km (nearly double the radius of the SiC-JTEC difference as shown in Figure 3.13), also a large slope error rms of ~0.3 µrad. Simulations 3 to 7 use the following sequence of two references corected from each subartures; (a) correct for reference obtained on SiC mirror and (b) correct for a second reference obtained from average of subapertures. The second reference is generated from the average of subapertures without the spherical/cylindrical component (by removing a plane fit from slopes). Removing the first coarse reference with SiC mirror helps in better fitting of plane to the residual subaperture, and thus avoids any mirror true curvature being subtracted with the second reference correction. Simulations 3 to 7 still has same curvature as simulation 2, and the curvature may have to be well calibrated for the reference mirror being used (e.g. using another standard metrology instrument). Simulations 3 to 7 differ in the algorithm used for stitching (MOF, PROG, GOF) or in algorithm options, but they all converge to nearly same slope errors rms (~13 nrad) and they have similar 2D slope error maps, but they differ in stitch time. Simulation 4 is the fastest as it uses scan average option in MOF algorithm, which averages subapertures from all repeated scans and then stitches the avarages. However drift errors are not included in these simulations, in which case averaging subapertures may be less efficient. The convergence to ~13 nrad for all simulations except simulation 2, may imply systematic errors are welll corrected and remaining noise is the statistical average of random noise in all algorithms.

Table 3.2 : Stitching simulated SHARPeR data with different PyLOSt algorithms

Simu no	Algorithms *	Algorithm options **	Reference ***	Tangential Slope err rms (nrad)	Radius (km)	Time (s)
1	MOF		JTEC	13.4	5718	5.9
2	MOF		SiC	306.2	-1.25	5.5
3	MOF		SiC + m_avg	13.3	-1.26	4.2
4	MOF	Scan avg	SiC + m_avg	13.3	-1.26	0.4
5	PROG		SiC + m_avg	13.6	-1.26	12.9
6	GOF	SIMPLE	SiC + m_avg	13.6	-1.26	19.7
7	GOF	FULL	SiC + m_avg	13.6	-1.26	55.8

* Algorithms:
MOF – Matrix Overlap error method
PROG – Progressive stitching
GOF – Global Optimization method

** Algorithm Options:
Scan avg – Average images at a subaperture location from all scans before stitching
SIMPLE (GOF) – Overlap differences are averaged over pixels, which are optimized
FULL (GOF) – All pixel differences in overlap are optimized (see section 3.2.3.2)

*** Reference: Subapertures generated by adding JTEC flat reference.
Later subapertures are corrected with (a) same JTEC flat mirror reference, (b) SiC flat mirror reference (or)
(c) SiC + m_avg – where m_avg is the subaperture average without shape (plane fit is removed)

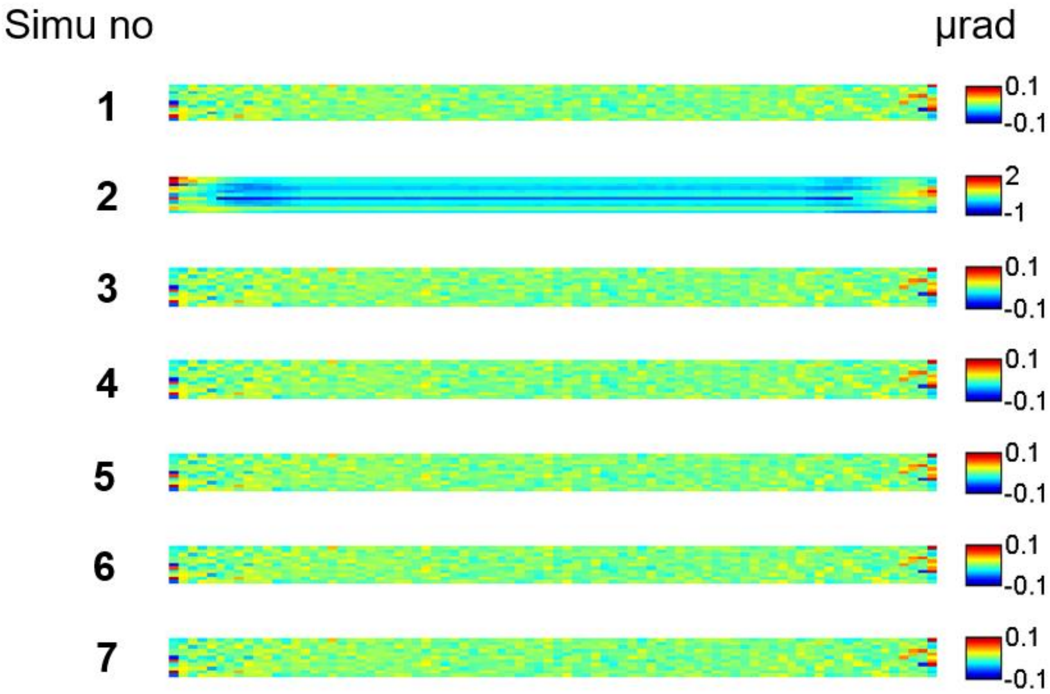

Figure 3.14 : Simulated tangential slope errors of size 100 x 13.2 mm^2, stitched with different PyLOSt algorithms.

The simulations were continued with different noise levels with algorithms MOF/PROG/GOF as shown in Table 3.3 and Figure 3.15. The systematic errors were multiplied by 10 times in simulation (a) and similarly pitch/roll errors and random noise were multiplied 10 times in simulations (b) & (c) respectively. The algorithms used default options (GOF used SIMPLE option), and the reference correction with SiC mirror reference and subaperture average similar to simulations 3 to 7. The slope error rms in simulations (a) & (b) is very close to simulations 1 to 7 (~ 13 nrad), whereas simulation (c) has nearly 10 times the slope error rms for all algorithms, further validating that the remaining stitching errors are from the statistical random noise.

Table 3.3: Simulations with different noise levels

Algorithm->	**MOF**	**PROG**	**GOF**
Slope error rms (µrad)			
(a) 10x systematic errors	13.1	13.1	13.1
(b) 10x pitch/roll errors	12.2	12.2	12.2
(c) 10x random noise	125.1	125.0	125.0
Reference used: SiC + m_avg **Radius: -1.26 km for all simulations in this table**			

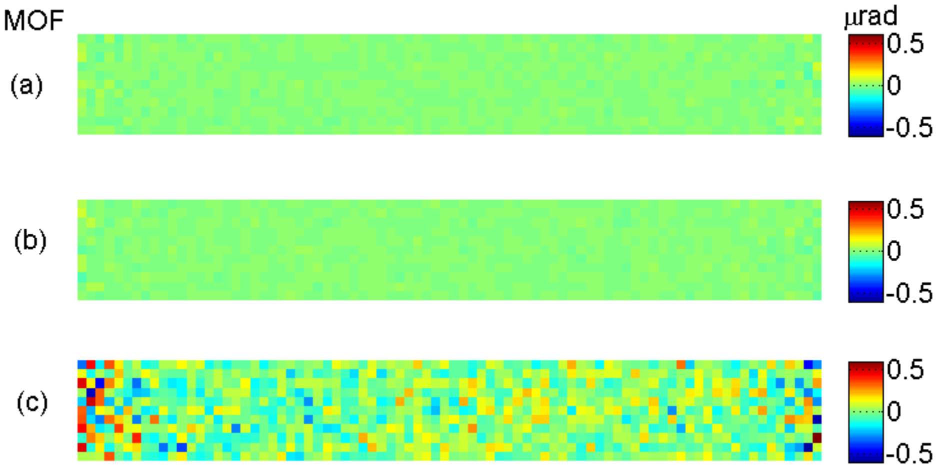

Figure 3.15 : Simulated tangential slope errors of size 100 x 13.2 mm^2, stitched with MOF algorithm with different noise levels; (a) 10x systematic errors, (b) 10x pitch/roll errors and (c) 10x random noise with respect to simulations 1 to 7 as shown in Table 3.2.

3.5.2 Height stitching with synthetic Fizeau data

An ideal flat mirror is simulated and stitched after adding different errors from ESRF Zygo Fizeau instrument, with parameters given below.

- Mirror aperture dimensions 80 x 4 mm^2
- Stitching step of 1.4 mm
- No. of subapertures : 47, subaperture size: 16 x 4 mm^2
- No. of scans: 1
- Random noise (PV) : 0.1 nm - applied to each pixel independently in a box distribution
- Piston / Pitch / roll error (PV) : 250 nm / 0.5 µrad/ 0.7 µrad – used errors calculated from stitching real measurements on the JTEC flat mirror
- Instrument systematic errors measured on flat JTEC mirror (of <50 nrad / ~0.1 nm rms quality), as shown in Figure 3.16. The reference was measured by averaging many images taken on JTEC flat mirror at various locations. The reference is added to each subaperture prior to stitching in order to simulate the influence of the figure errors of the transmission flat.

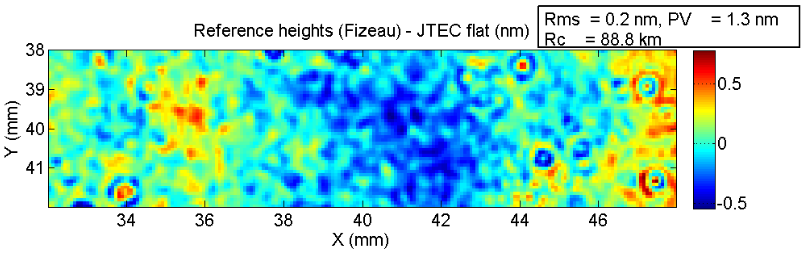

Figure 3.16 : Fizeau reference topography calculated on 16 x 4 mm^2 aperture from averaging of multiple sub-apertures distributed across a JTEC flat mirror.

The parameters used for stitching the simulated Fizeau data with different PyLOSt algorithms and the key stitched topography results are shown in Table 3.4. The stitched images of different simulations are shown in Figure 3.17. Stitching the subapertures using MOF algorithm without any reference correction (simulation 1) results in large height errors (0.06 nm rms, 1.2 nm PV) and a large curvature with radius ~11 km compared to reference radius of 98 km as shown in Figure 3.16. The stitching topography from simulation 1 in Figure 3.17 shows periodic stitching artifacts most likely from the uncorrected reference errors. The algorithms MOF, PROG and GOF perform well using references generated by averaging subapertures (simulations 2, 5, 6), with almost same height error rms and radius.

In simulation 3, reference extraction method using subaperture overlaps is used (explained in section 3.4.1). In simulation 4, two references are corrected from all subapertures, first one from average of subapertures without shape (by removing 2nd order polynomial) and subsequently a second reference extracted using subaperture overlaps. The second reference is calculated within stitching along with other errors like pitch/roll errors as explained in section 3.4.1. The two extracted references from simulations 3 & 4 are compared to the reference from simulations 2/5/6 in Figure 3.18. The reference extraction was able to extract low frequency reference errors (in Figure 3.18), with very little reference errors extracted in simulation 4 (bottom plot in Figure 3.18) as most of the errors were corrected with the first reference. The stitched image for simulation 3 (in Figure 3.17) also shows periodic stitching artefacts, but compared to simulation 1 some of the low frequency errors are absent. Reference extraction algorithms (used in simulation 3) need to be further improved to extract may be the high frequency reference errors as well.

Table 3.4 : Stitching simulated Fizeau data with different PyLOSt algorithms

Simu no	**Algorithms ***	**Reference ****	**Height err rms (nm)**	**Difference reference rms (nm) *****	**Radius (km)**	**Time (s)**
1	MOF	None	0.061	-	10.8	22
2	MOF	m-avg	0.011	0.49	88.8	23
3	MOF	extract-ref	0.066	0.94	-27.9 R_{ref}=21.7 R_{diff}=89.4 ****	70
4	MOF	m-avg + extract-ref	0.011	0.49	90.0	71
5	PROG	m-avg	0.011	0.49	88.8	23
6	GOF	m-avg	0.011	0.49	88.9	716

*Algorithms:
MOF – Matrix Overlap error method
PROG – Progressive stitching
GOF – Global Optimization method

** Reference:

m-avg – the subaperture average without shape (2nd order polynomial removed)

extract-ref – extract reference from subaperture differences within overlaps

m-avg + extract-ref – reference from subaperture averages is removed and later additional reference is extracted from overlap differences

*** Difference reference rms: Rms of difference in extracted reference from stitching and simulation reference

**** R_{ref} : Radius of curvature of extracted reference,
R_{diff} : Radius difference between stitched result and extracted reference

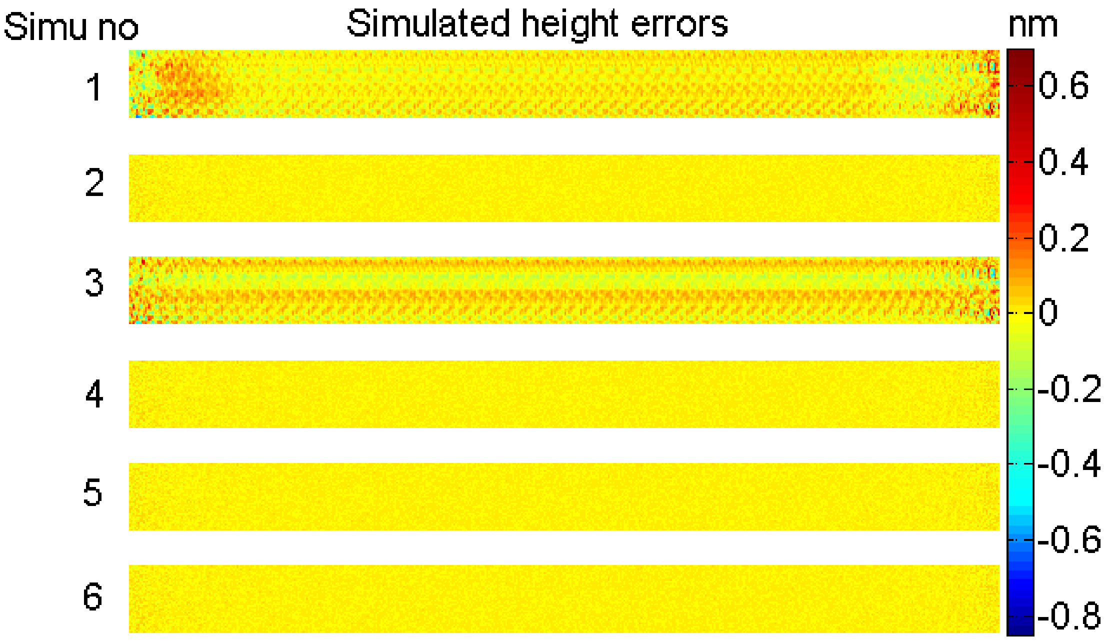

Figure 3.17 : Simulated Fizeau height errors of size 80 x 4 mm^2, stitched with different PyLOSt algorithms.

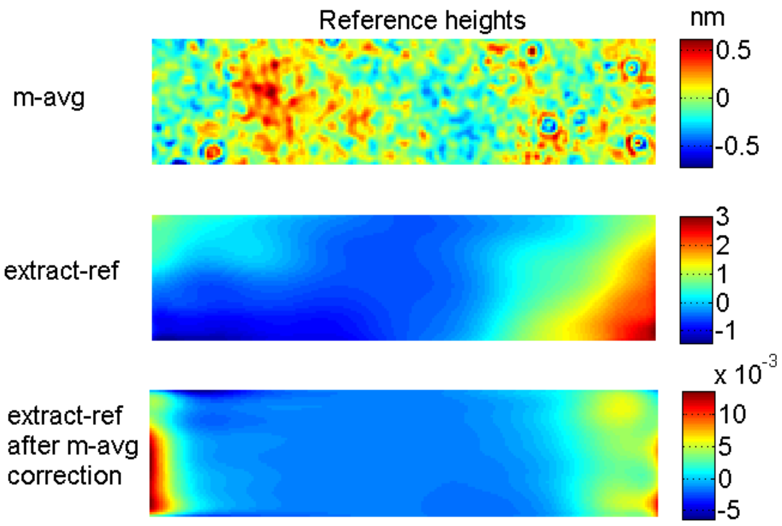

Figure 3.18 : Extracted Fizeau references of size 16 x 4 mm^2 from different PyLOSt algorithms shown in Table 3.4.

The simulations were continued with different noise levels with algorithms MOF/PROG/GOF as shown in Table 3.5 and Figure 3.19. The systematic errors were multiplied by 10 times in simulation (a) and similarly pitch/roll errors and random noise were multiplied 10 times in simulations (b) & (c) respectively. The reference of subaperture average (m-avg) was used for all algorithms. In simulation (a), the radius increased by 10 times but had no effect on slope error rms of stitched result. In simulation (c) slope error rms increased by 10 times. Hence the stitched slope noise are largely dependent on the random errors in the system, whereas large systematic errors needs well calibration for radius but has minimal effect on stitched slope errors.

Table 3.5 : Simulations with different noise levels

Algorithm->	**MOF**	**PROG**	**GOF**
Slope error rms (nm) | Radius of curvature (km)			
(a) 10x systematic errors	0.01 | 8.876	0.01 | 8.875	0.01 | 8.876
(b) 10x pitch/roll errors	0.01 | 88.772	0.01 | 88.778	0.01 | 88.772
(c) 10x random noise	0.11 | 88.945	0.11 | 88.931	0.11 | 88.890
Reference used: m-avg			

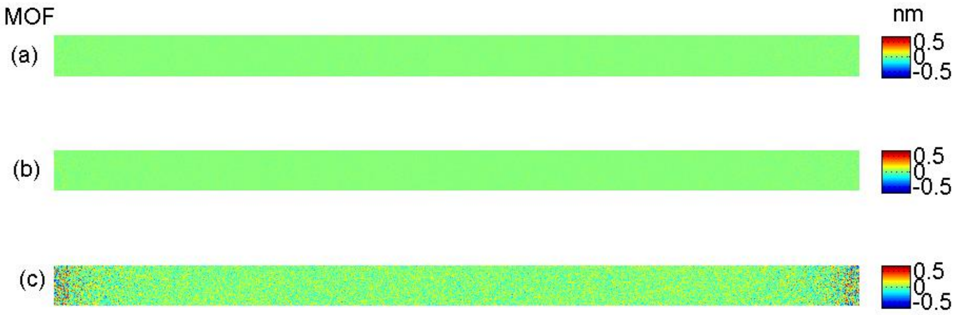

Figure 3.19 : Simulated Fizeau height errors of size 80 x 4 mm^2, stitched with MOF algorithm with different noise levels; (a) 10x systematic errors, (b) 10x pitch/roll errors and (c) 10x random noise.

All the different algorithms (MOF, GOF and PROG) showed similar performance and can be utilized for stitching. But it was observed that in most cases (not presented here) MOF performed well, and it has been commonly used to stitch measurements presented within this thesis (chapter 4). The algorithms still have much potential for improvements. PyLOSt has overall helped to pool different algorithms and cross compare their performances. It also has helped simplify cross comparison between different instruments, especially for a round robin where single standard mirror is measured by different instruments and cross compared. The round robin helps understand the limitations among different metrology instruments; PyLOSt not only helps manage measurement data of various instruments, it also helps for discounting stitching algorithm differences between cross comparison of metrology instruments.

4 SHARPeR RESULTS

The ESRF SHARPeR instrument was used to measure different X-ray mirrors of different shapes and sizes. It can measure mirrors with lengths in between 20 mm-1400 mm and radius of curvatures larger than 1m. The measurement errors strongly depend upon the type of mirror under test. For example, on longer mirrors, extended measurement times and/or the thermal fluctuations over the total measurement path could lead to significant measurement errors, whereas for short mirrors these errors are reduced due to shorter measurement times and path lengths. SHARPeR was used to study the contribution of different sources of errors by measuring different mirrors e.g. short flat (<100 mm), long flat (~1 m), spherical mirrors with medium to high curvatures (200 m to 10 m), aspherical mirrors (ellipses) etc., and they are presented in this section.

4.1 Static scans

Random noise sources of SHARPeR are analyzed using different techniques mentioned below. The random noise contributes to measurement errors which cannot be calibrated. These primarily originate from environmental influences such as fluctuations in temperature, humidity, air flows, vibrations etc. These errors are usually minimized through statistical averaging of many images. Analysis of the random noise also helps in optimizing instrument designs and implementing proper isolation around the measurement path.

4.1.1 Noise analysis with stationary optical head

The random noise in SHARPeR measurements was analyzed using many images taken with optical head in a stationary position above a test mirror with <1 nm height errors and >30 km radius of curvature. The test mirror was placed on the RTT stage whose motors and air flow to air bearings are switched off for stability. The translation stage of the optical head is still active with power to motors and air to air pads, although the head is not moving during measurements. Over the course of my thesis (May.2017-Mar.2020), the SHARPeR has been modified many times and the random noise contribution to SHARPeR evolved accordingly. The random noise analysis presented in this section was measured in Jan.2020 (unless specified), and corresponds to the latest design as shown in section 2.5.6. In the following the measurement noise is analyzed statistically over short durations, drifts over long durations and contribution to final stitched slopes.

Static images:

Individual images are taken continuously with SHARPeR over a period of time and their analysis is shown in Figure 4.1. 256 images were taken over ~106 s (~2.5 Hz sampling rate), with exposure time of 0.5 ms each. Figure 4.1 shows the measured wavefront tilt (mean slope of all microlenses), rms of slopes without tilt, and radius of curvature for each image and also as a cumulative average over the images. Here the tilt, slope rms and radius are referring for the total wavefront, by combining tangential and sagittal components. Rms of tangential and sagittal values are used for wavefront tilt and wavefront slope rms, and total curvature is obtained by fitting sphere to combined wavefront.

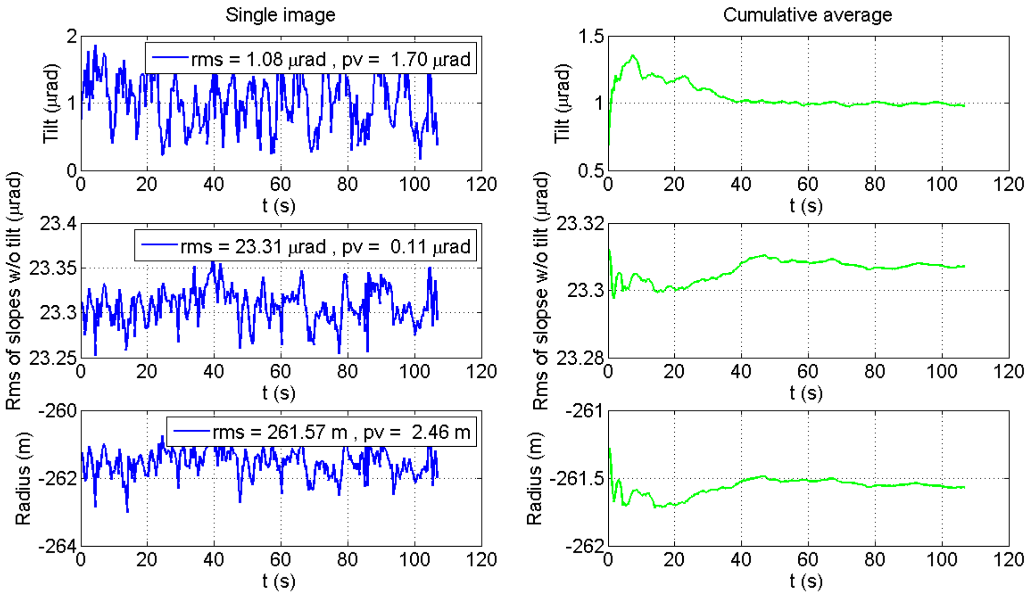

Figure 4.1 : SHARPeR statistical noise analysis with 256 images over 105 sec (~2.5 Hz sampling rate). The wavefront tilt, slope error rms and radius of curvature are shown with individual images (left column) and cumulative average (right column).

The tilt PV is large (~2 µrad) without averaging, but stabilizes with cumulative average of >40 seconds (changes < 50 nrad for >40 second average), corresponding to 100 images. The slope rms is quite large (~23 µrad rms), which originates from large systematic errors from optical aberrations (also called reference errors). However, the PV of slope rms over time is quite small without averaging (0.11 µrad), and drops to <50 nrad for cumulative acquisition times of >40 seconds. Similarly, the wavefront has significant curvature due to these systematic errors (radius ~262 m), and significant curvature changes from random noise (radius PV ~2.46 m), averaging for more than 40 seconds reduces radius variation to <0.1 m.

Drift with static images:

The noise analysis shown above is for acquisitions within a short time frame (<2 minutes); for longer times, over many hours, drift errors also play a vital role. SHARPeR measured the same test mirror repeatedly at 2.5 Hz without movement of the TX carriage over 35 hours. Out of all images, a set of 256 images sampled at ~8 min period were selected for analysis as shown in Figure 4.2. Cumulative averaging images reduces all wavefront parameters (tilt, slope rms without tilt, radius) initially, but increases continuously above 15 hours, with PV of 0.25 µrad in tilt, 0.1 µrad in slope rms and 2.5 m in radius of curvature. The drift errors may be reduced using faster measurement strategies such as on the fly scans.

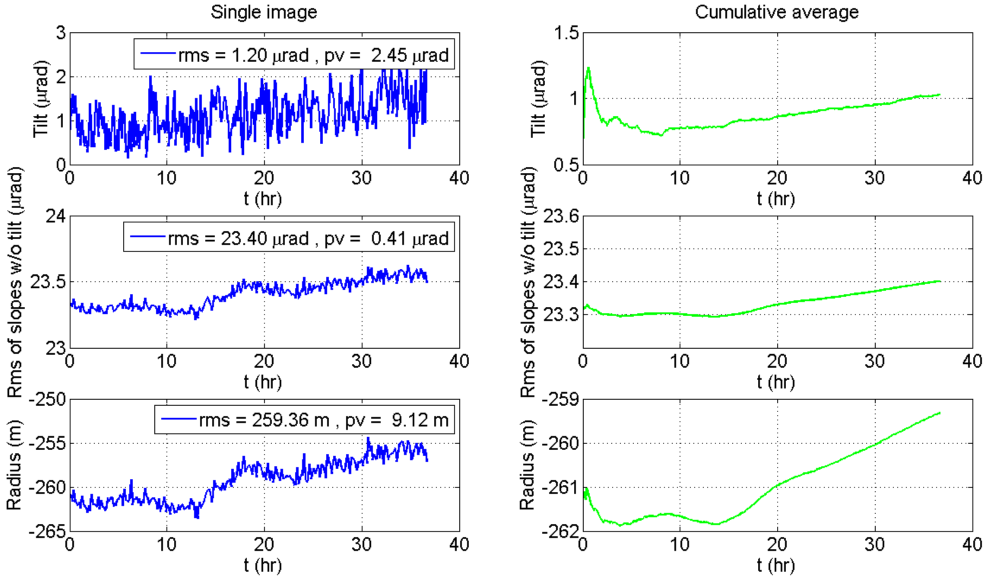

Figure 4.2 : SHARPeR drift analysis with 256 static images over ~35 hours (~0.002 Hz sampling rate). The wavefront tilt, slope error rms and radius of curvature are shown with individual images (left column) and cumulative average (right column).

Stitching of static images:

Stitching subapertures offers some reduction in random noise as the process averages subapertures within the overlapped region. The SHARPeR measured a 1.4 m long ‘artificial’ mirror (i.e. static without motion), for 128 repeated scans which are stitched with StitchWave software. This method has been used as a quick noise analysis with StitchWave at the beginning of thesis, and it provides an estimation of environmental noise within the final stitched scans. Averaging many stitched scans can reduce the statistically random environmental noises, and this procedure has been used to determine the minimum number of scans required to reduce statistical noise below a threshold (e.g. <50 nrad) over mirrors up to 1.4 m length. In these measurements, each of the scans has 1161 subaperture images (~ 8 minutes per scan) taken without moving the optical head. Before stitching, a reference image taken on the same mirror at the same location is subtracted from all the static images, so that only the random noise is stitched.

The stitched noise wavefront tilt, slope rms and curvature are shown in Figure 4.3, for the 128 stitched scans and for cumulative average. The measurements with recent setup (Jan.2020) are compared to similar scans with initial SHARPeR setup (June.2017) in the Figure 4.3.

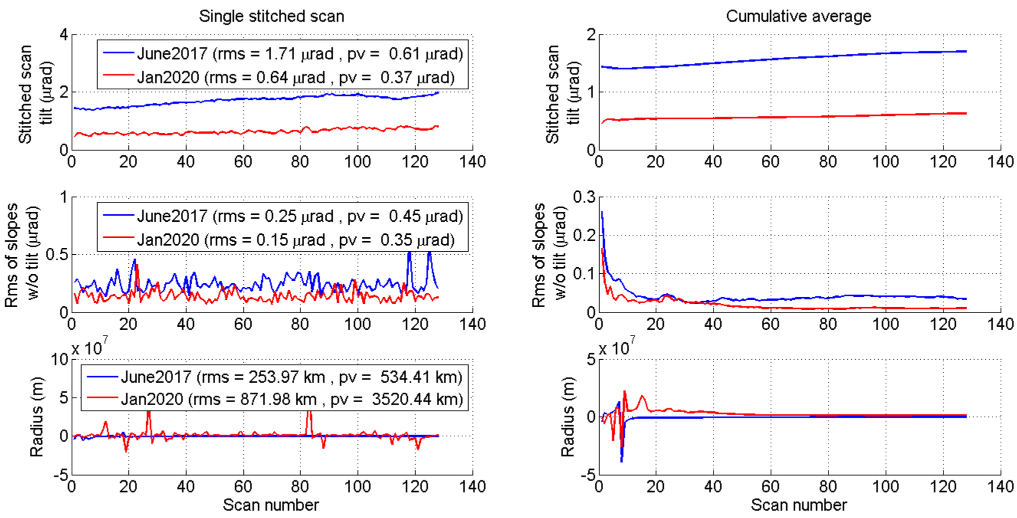

Figure 4.3 : SHARPeR random noise influence in stitching with recent measurements (Jan.2020) compared to with initial SHARPeR design (June.2017). The images over 'artificial' 1.4 m long mirror are stitched. The stitched surface tilt, slope error rms and radius of curvature are shown with individual scans (left column) and cumulative average (right column).

The stitched noise tilt, slope rms without tilt, and radius of curvature are shown in Figure 4.3, without averaging scans and with cumulative average over scans. The new setup performed better than the old setup in all respects, it has less drift in stitched scan tilts, lower slope rms and larger mean radius i.e. flatter stitched noise wavefront. Slope rms saturates after averaging above 30 scans in old setup around ~30 nrad, but it reduces to much smaller value in new setup for over 60 scans of ~10 nrad.

4.1.2 Noise analysis with a mirror fixed to the moving optical head

Noise analysis shown in previous section is done with optical head in static position. However, in real measurements as the head moves, it can dynamically modify the surrounding environment which can completely modify measurement noise contribution. This is especially significant as there are heat sources near the test mirror such as the camera. To estimate the measurement noise within the dynamic forward and backward scans, measurements were done with a mirror attached to optical head as explained in the following.

A small flat mirror with 25 mm diameter was attached to the optical head as shown in Figure 4.4. The mirror was glued to its holder which was screwed tightly to optical head. No cover was present surrounding the optics in the head. An extraction pipe made up of PVC was installed to extract the hot air from camera and move it away from the instrument. A bubble wrap was installed above the SHARPeR gantry, to prevent the vibrations from the direct airflow from the roof hitting the test mirrors. The mirror was placed near the focal distance of the head (with <1 mm accuracy). The head scanned in forward (FW) and backward (BW) direction over 1400 mm length for 24 scans (24 FW/24 BW), simulating scans of a long mirror without the contribution of the mirror itself towards the slope/height errors. The laser power is adjusted for acquisition by CCD to ~80% saturation limit. The exposure time is 100 ms and measurements performed in step by step mode.

As the camera is on the moving optical head and is close to the surface under test, it could create thermal gradients locally. To minimize these noises, the optical setup and the SHARPeR gantry were modified as shown in Figure 4.5. The bubble wrap blocking the direct roof airflow was removed. The optics on the head was covered using aluminium foil to prevent the thermal convection and radiation from camera from reaching the afocal optics and the optical path. The laser collimation setup has already a tube covering the optical path from fiber output to the collimating lens. The optical path from the attached mirror to the entrance of optical head was also covered using a plastic tube. Forward and backward scans were repeated with the new setup over 1400 mm length for 24 scans.

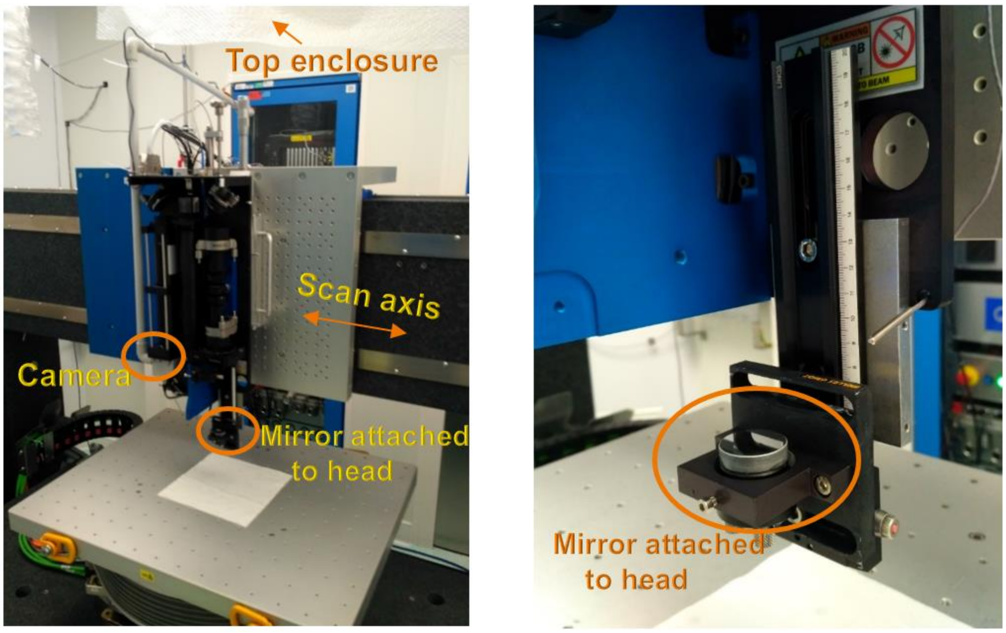

Figure 4.4 : SHARPeR measurement setup on 09-Nov-2018 for forward and backward scans with a mirror attached to optical head. The mirror was close to focal position of the head. The camera is the primary source of thermal perturbations in this setup.

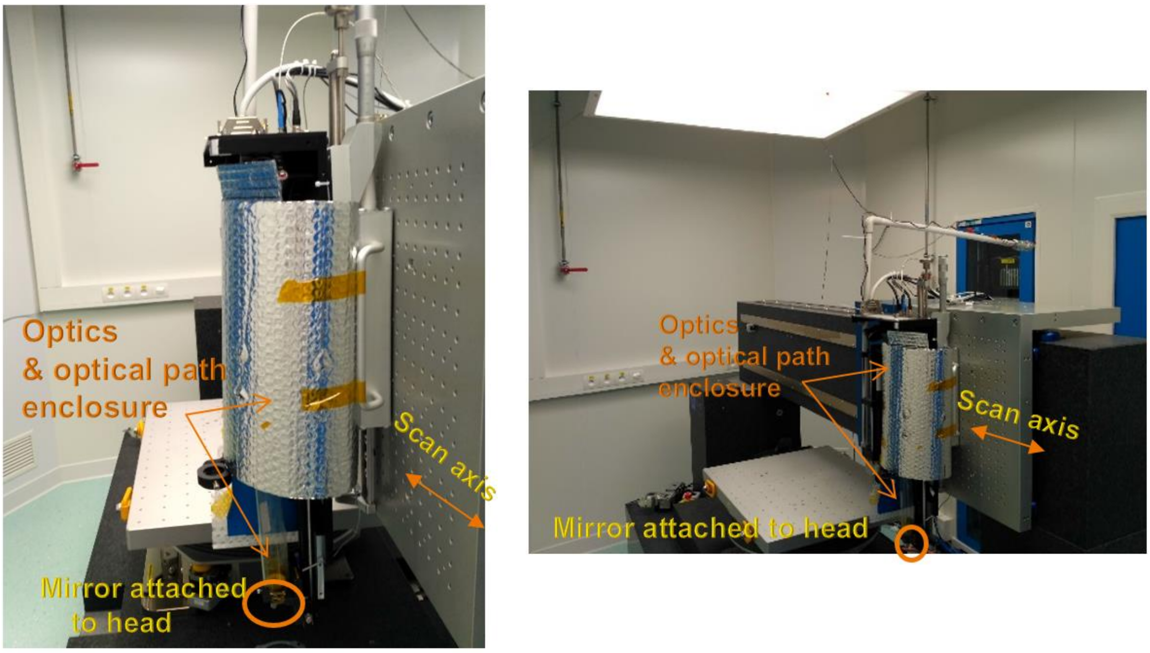

Figure 4.5 : SHARPeR measurement setup on 27-Nov-2018 for forward and backward scans with a mirror attached to optical head. Optical path is enclosed to isolate thermal effects.

The measured mirror subapertures in these two configurations (Figure 4.4 and Figure 4.5) were stitched using PyLOSt software matrix overlap error method (see sections 3.2 and 3.3). The tangential and sagittal slope errors on a line passing through center of mirror is compared between the two setups, as shown in Figure 4.6. A significant drop in the rms and peak to valley (PV) values can be observed for the tangential slope errors with the new setup on 27-Nov-2018. Also, a small improvement in sagittal slope error rms and PV values can be seen.

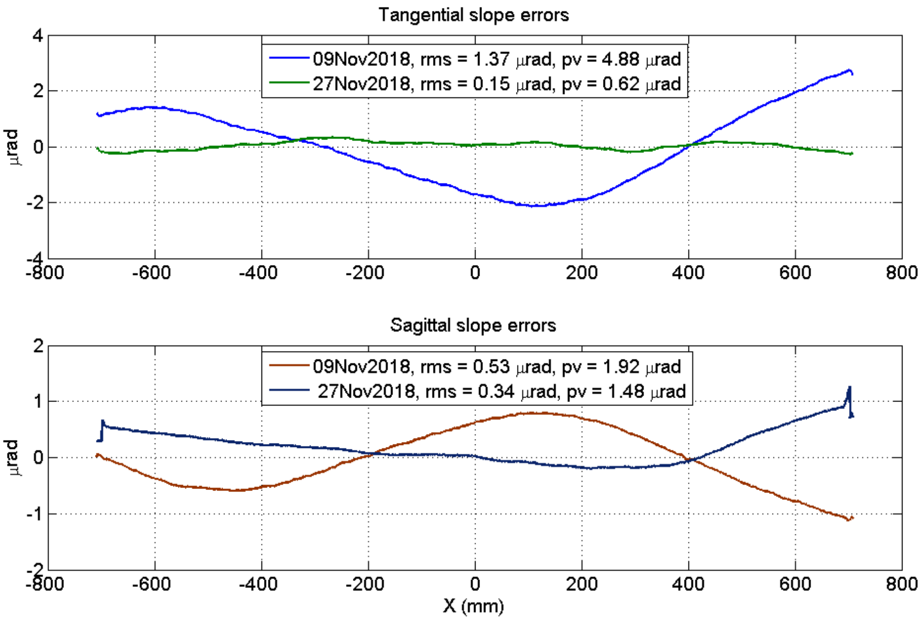

Figure 4.6 : Comparison of environmental errors in different SHARPeR setups, using stitched tangential & sagittal slope errors (average of 24 scans) of a mirror fixed to moving optical head.

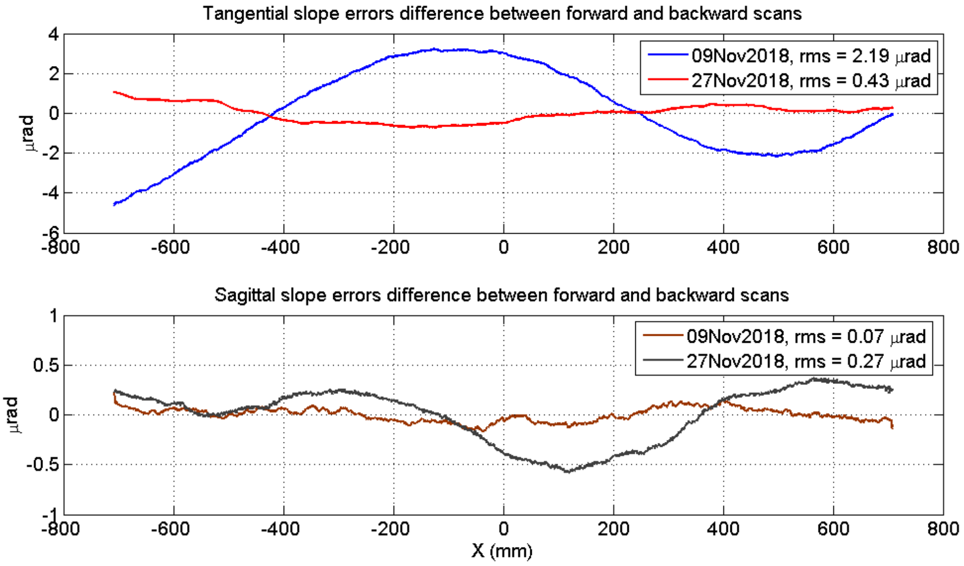

Figure 4.7 : Differences in environmental error contributions to stitched slope errors (tangential & sagittal) between forward and backward scans. The differences are shown for two different SHARPeR setups on 09th and 27th Nov 2018.

Difference between forward and backward scan averages of slope errors are plotted in Figure 4.7. Tangential slope errors showed lower difference between forward and backward scans with the new setup (27 Nov 2018). As the mirror is firmly attached to the head, any pitch and roll errors during translation should not affect measurements since the whole head including the test mirror tilts. The optics and the base plate could experience expansions and contractions depending on the position of the head along the scan path, which would in turn change the instrument errors. Even during static conditions with no mechanical motions, the size and alignment of optics could change due to thermal load from camera or from other heat sources. These effects to a large extent can be minimized by subtracting a reference taken on the same test mirror, after few hours of stabilization of the SHARPeR room, before starting the scans. Dynamic effects of refractive index changes in the optical path from air currents, which arise from airflows in the room or from the convection currents from moving camera, may be a more significant factor compared to conduction based effects such as expansions of base plate / optics / test mirror. Conduction effects are usually slower and would not lead to major differences for scanning in forward or backward directions. Insulating the optical path which minimizes air currents in the optical path may have reduced the tangential slope errors difference between forward and backward directions as seen in Figure 4.7. However, the sagittal slope error differences between forward and backward scans have increased with the new setup. This may be an unwanted side-effect of the enclosure preventing better cooling of the optics, and if thermal gradients are formed normal to the base plate within the enclosure they might increase the environmental noise in sagittal slopes. Due to time constraints similar experiments were not performed with the latest design with the wavefront sensor at the top (see section 2.5.6), and with this new architecture the results are probably even better.

4.2 Measurements on short flat mirrors

A short flat mirror manufactured by JTEC Corporation [121] was measured by SHARPeR and other metrology instruments at the ESRF including the LTP and Fizeau interferometer. The mirror (Figure 4.8) has physical dimensions 110 x 30 x 35 mm^3 (with an optical aperture of 95 x 10 mm^2). The mirror was manufactured from single crystal silicon and the reflecting surface was coated with a multilayer coating $C/[W/B_4C]_{100}/Cr$. In the following this mirror is referred to as the 'JTEC flat'. The total mirror length is measured in 77 subapertures with a stitching step of 1.2 mm corresponding to the microlens separation. The laser power is adjusted for acquisition by CCD to ~80% saturation limit. The exposure time is 100 ms and measurements performed in step by step mode.

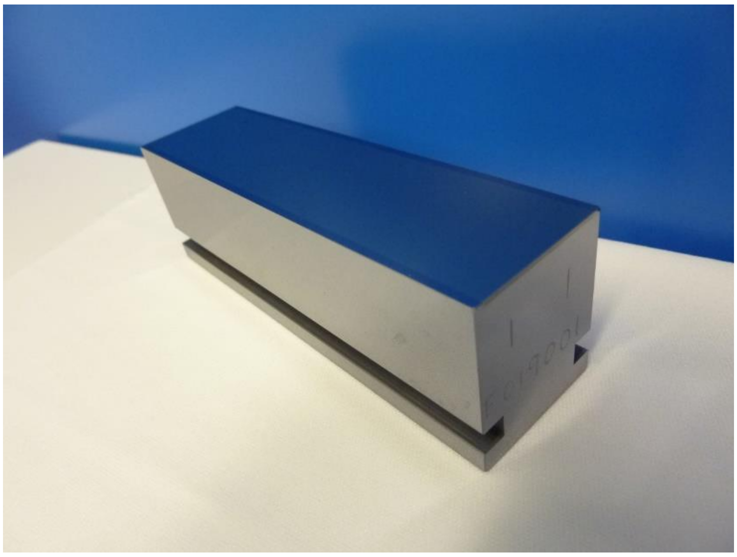

Figure 4.8: JTEC flat mirror.

4.2.1 Reference measurement

Prior to SUT characterization as described in sections 2.2.3 and 2.5.2, a measurement on a reference flat mirror by the SHARPeR instrument is used to capture the systematic errors of the whole optical head. Figure 4.9 shows the average of subapertures on the

JTEC flat, which have rms values of 40 µrad for tangential slopes, 54 µrad for sagittal slopes and 0.1 µm in height. The rms height error measured by manufacturer (JTEC) and other ESRF instruments is known to be approximately 0.1 nm, which means almost 99.9% of the wavefront distortion measured by SHARPeR is due to residual reference errors coming from the instrument. The reference mirror is measured regularly (ideally before every measurement of sample mirror), to account for any slight variations of alignment or expansion of optical elements due to environmental changes. The reference, taken on a good flat mirror (with <0.25 µrad rms slope errors) is subtracted from every sample mirror sub-aperture measurement. StitchWave software combines the reference mirror measurement with the average of test mirror subapertures and generates a more comprehensive reference. The StitchWave reference method tries to exclude any specific features on the reference mirror being added to stitching result, and as the method is proprietary knowledge of Imagine Optic it is not presented here.

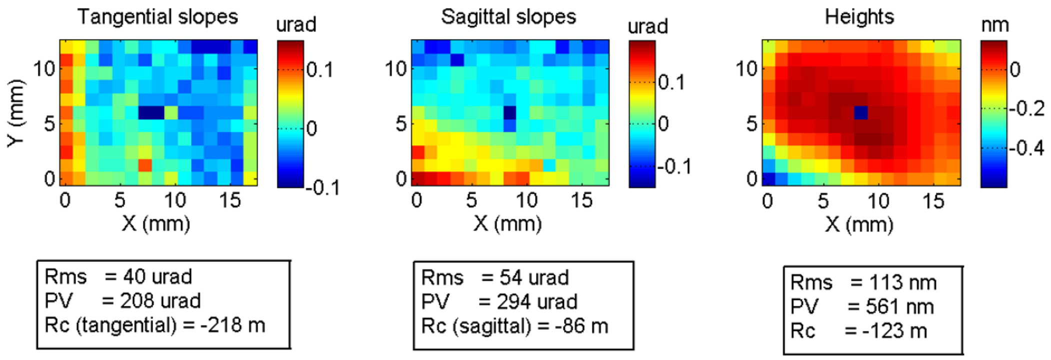

Figure 4.9 : Reference wavefront tangential & sagittal slopes and heights measured on JTEC flat mirror.

4.2.2 Stitching subapertures

The mirror is measured 32 times in the forward (fwd) and 32 times in the backward (bwd) direction. A minimum of 32 scans are required to sufficiently minimize the statistical random noise contribution from the measurements. The process of optimizing the number of scans for the SHARPeR is explained in Section 4.1. The mirror is physically flipped along stitch direction (AB → BA, as explained in section 2.5.2) and 32 fwd/32 bwd scans are repeated in BA direction. The reference is obtained by averaging images of the same JTEC flat mirror in a single forward scan excluding the images containing edges, and this reference is subtracted from subapertures before stitching. This procedure helps avoid performing a reference measurement on another flat mirror, which if it is not as good as the JTEC flat can add additional noise. This process also has the disadvantage that it removes any global curvature of mirror, unless a radius term was removed from calculated reference from subaperture average. Subapertures of the JTEC flat were stitched using PyLOSt software matrix overlap error method (see sections 3.2 and 3.3).

AB and BA measurements are stitched separately and the stitched results are averaged as shown in Figure 4.10. Stitched tangential and sagittal slopes are integrated to get mirror heights using the Frankot and Chellappa algorithm [122], also shown in Figure 4.10.

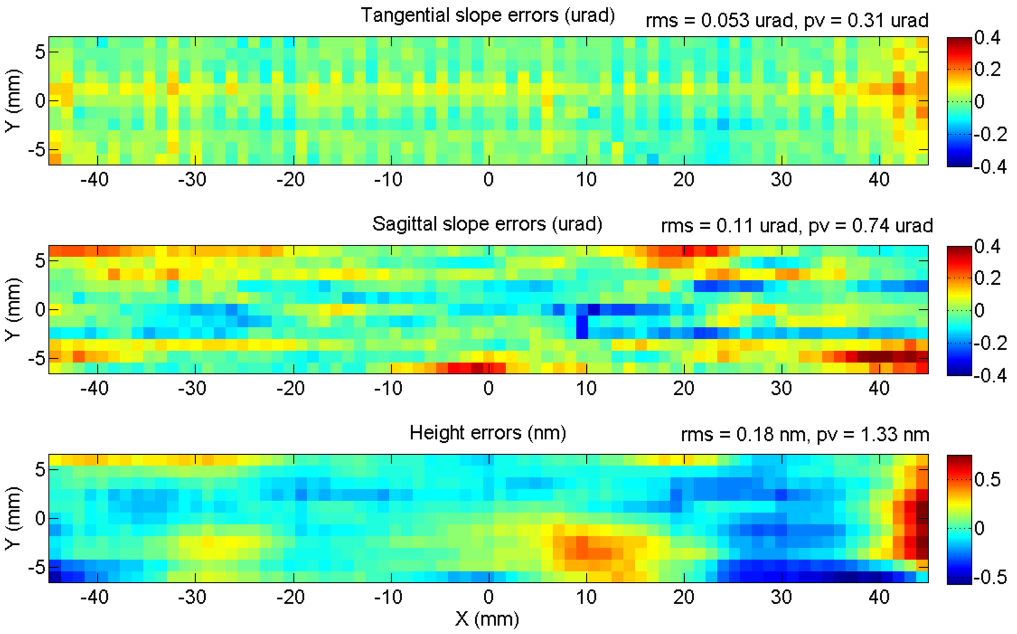

Figure 4.10: JTEC flat slope and height error 2D maps, stitched using the PyLOSt stitching software.

4.2.3 Repeatability of stitched scans

The Repeatability of n stitched scans is obtained by calculating standard deviation (STD) of the mean which is given as below. The noise is assumed to be uncorrelated between all scans, i.e. no systematic errors or long-term drifts.

$$\sigma_m = \frac{\sigma}{\sqrt{n}}$$

The term $\boldsymbol{\sigma}$ represents the repeatability of a single scan, and $\boldsymbol{\sigma_m}$ represents the repeatability of average. The repeatability on the JTEC flat mirror is shown in Figure 4.11, for 128 scans with AB and BA measurements having 64 total scans each (fwd+bwd).

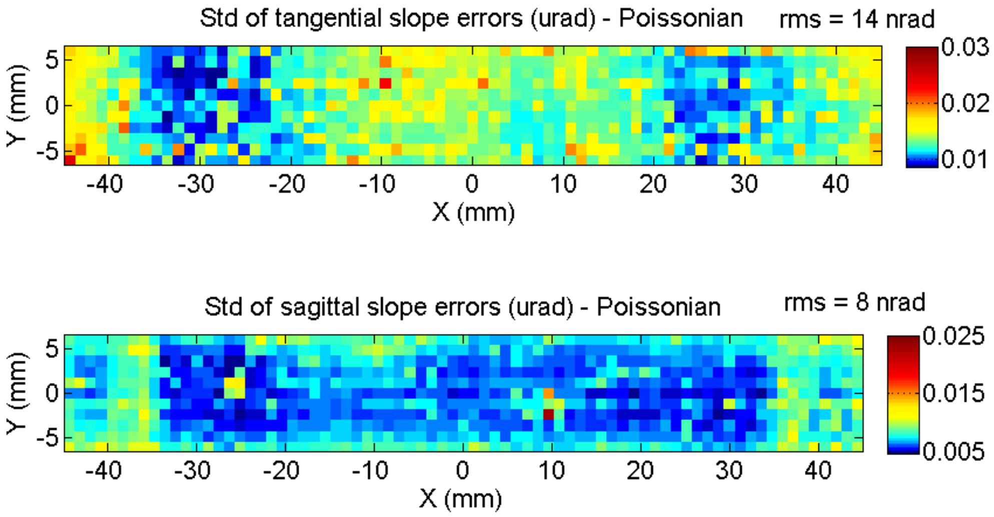

Figure 4.11: Repeatability of slope errors of 128 scans including AB and BA orientations on the JTEC flat mirror.

The AB and BA measurements are repeated five times, each containing 128 scans, to verify if the theoretical repeatability of mean calculated above holds true. The 128 scans are averaged and a line on the tangential slope errors through the center of mirror is shown in Figure 4.12 for the five repeated measurements.

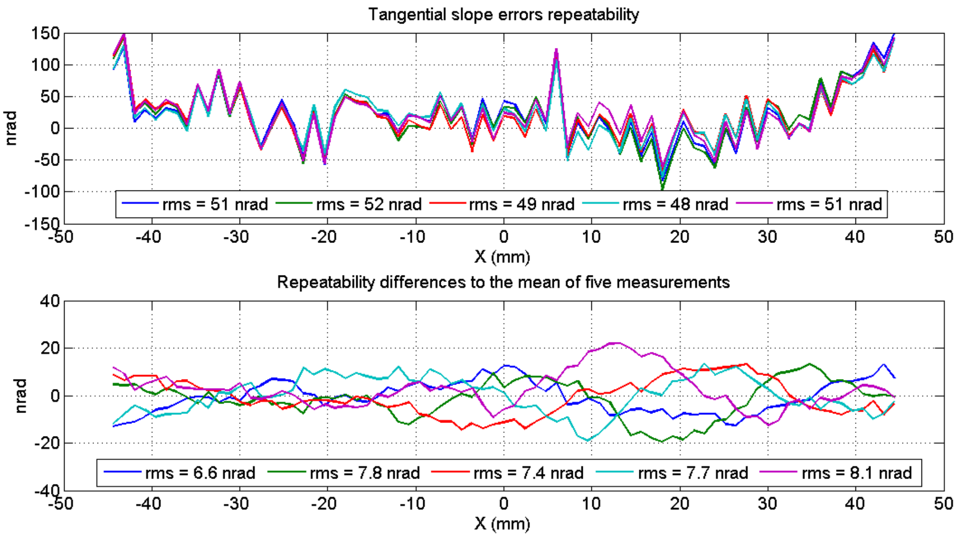

Figure 4.12: Repeatability of tangential slope errors on a line through mirror center, with five ABBA scan averages each with a total of 128 scans.

Table 4.1: Results from repeated measurements on JTEC flat

Measurements→	**M1**	**M2**	**M3**	**M4**	**M5**
Rms tangential slope error on 2D profile (nrad)	53	54	52	52	54
Rms tangential slope error on line through center (nrad)	51	52	49	48	51
Rms tangential slope error (line) difference to average of M1 to M5 (nrad)	6.6	7.8	7.4	7.7	8.1
Tangential radius (km)	-50	-79	32	12	19

The Table 4.1 shows the complete results from the five repeated measurements. Repeatability calculated on the first ABBA averaged tangential slope error measurement is 14 nrad as shown in Figure 4.11, and on a line through center rms is 13.5 nrad. The rms of tangential slope error differences shown in the Table 4.1 are less than 9 nrad, which are better than repeatability calculated theoretically. One of the reasons could be initial measurements are noisier compared to later measurements. The tangential radius of curvature of the five averaged ABBA measurements differ quite significantly, which may be dependent on the evolution of environment within each AB & BA measurement. More results on this are presented in the Appendix 8.

4.2.4 Comparison of SHARPeR results with other metrology instruments

The SHARPeR height error measurements, obtained using Southwell 2D integration of slopes, are compared to measurements from the mirror manufacturer (JTEC) and from other ESRF metrology instruments: The Long Trace Profiler (LTP), Zygo Fizeau interferometer, Veeco micro-interferometer. The comparisons are shown in Figure 4.13 and Table 4.2, the results were published by Vivo et al.[38]. The SHARPeR results are in good agreement with other instruments except JTEC measurements. Here the JTEC measurements were done prior to coating the mirror. Fizeau and micro-interferometry measurements also used stitching techniques to extend the field of view. Additional results can be found in Appendix 8.

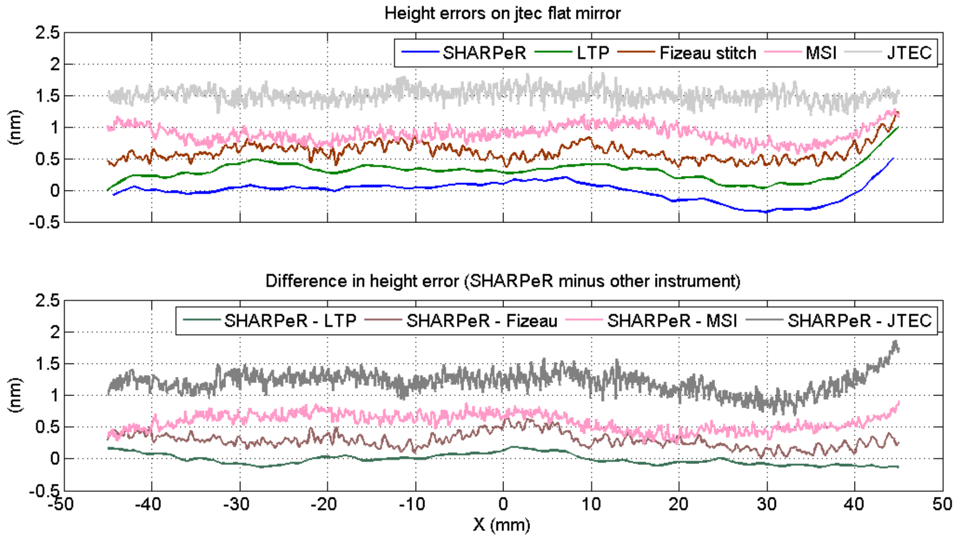

Figure 4.13: SHARPeR height error measurements on JTEC flat mirror compared to measurements from other instruments (curves are offset in height to aid visibility).

Table 4.2: SHARPeR measurement results in comparison to other instruments

Instruments	**Spatial resolution**	**height error (nm)**		**Difference in height error (nm)**		**Measurement time (h|m)**
	(µm)	Rms	pv	rms	pv	
SHARPeR	1200	0.16	0.85	-	-	3h15
LTP	2000	0.15	1.00	0.09	0.32	45 min
JTEC	50	0.11	0.69	0.17	1.18	-
Fizeau	80	0.13	0.87	0.12	0.63	3h30
MSI	40	0.13	0.71	0.13	0.68	2h30

4.3 Measurements on long mirrors

Measuring long mirrors (>500 mm length) has been a significant problem with instruments like SHARPeR [124], mainly due to errors from environmental factors such as drift errors as discussed in section 4.1.1. Different modifications were tested for the SHARPeR instrument to improve the long mirror measurements, related to insulation of the measurement path and to design change to reduce camera influence (see section 2.5.6). A 950 mm-long, flat, uncoated, Silicon mirror supplied by E-XFEL was measured by SHARPeR with different configurations of the optical head as shown in Figure 4.14. The mirror dimensions are 950 x 52 x 52 mm^3, and it has clear aperture 900 x 20 mm^2. The mirror has slope errors in the order of ~0.2 µrad rms as measured by E-XFEL. In all the measurements presented here, the laser power is adjusted for acquisition by CCD to ~80% saturation limit and the exposure time is 2 ms and measurements performed in onfly mode.

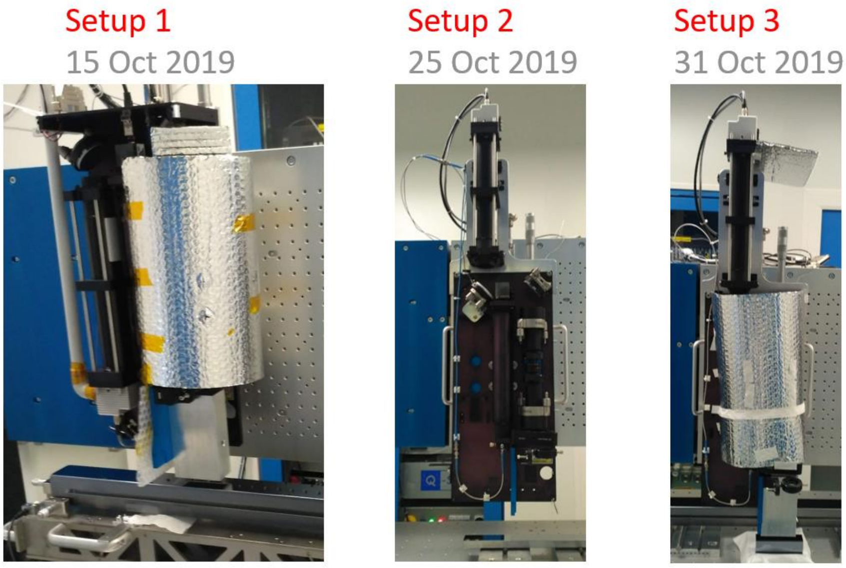

Setup 1
15 Oct 2019

Setup 2
25 Oct 2019

Setup 3
31 Oct 2019

Figure 4.14 : A 950 mm long XFEL flat mirror tested with different SHARPeR designs.

The mirror was measured in October 2019, before and after a major modification involving shifting the wavefront sensor away from test mirror and measurement path. Each measurement was done in AB and BA orientations with 32 forward & 32 backward scans. The three setups in Figure 4.14 show (a) camera at bottom and optical path enclosure, (b) camera at top and (c) camera at top and optical path enclosure.

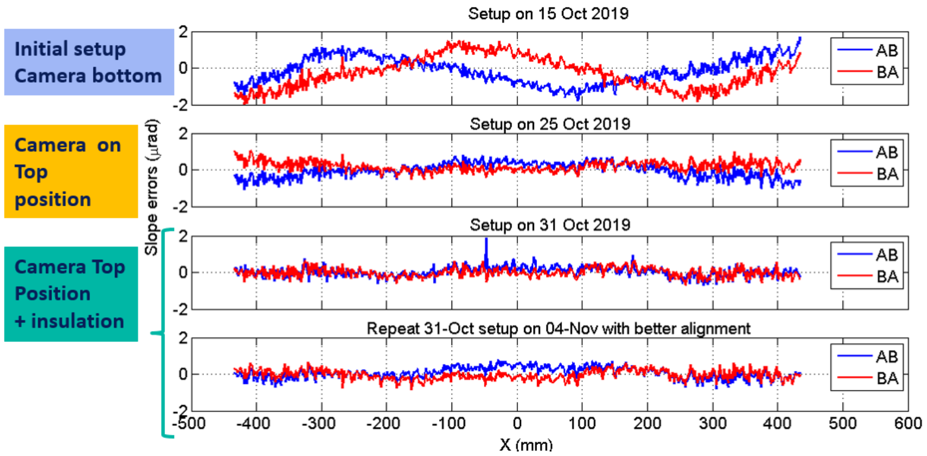

Figure 4.15 : Tangential slope errors in AB and BA on the long flat mirror with different SHARPeR setups.

The tangential slope errors measured by different SHARPeR designs are shown in Figure 4.15. The mirror is better aligned in AB and BA on 04-Nov-2019 using fiducial marks on the optical surface as shown for AB minus BA difference plots in Figure 4.16. All other measurements used alignment with markings on mirror edges. The AB, BA difference also reduced with the latest design.

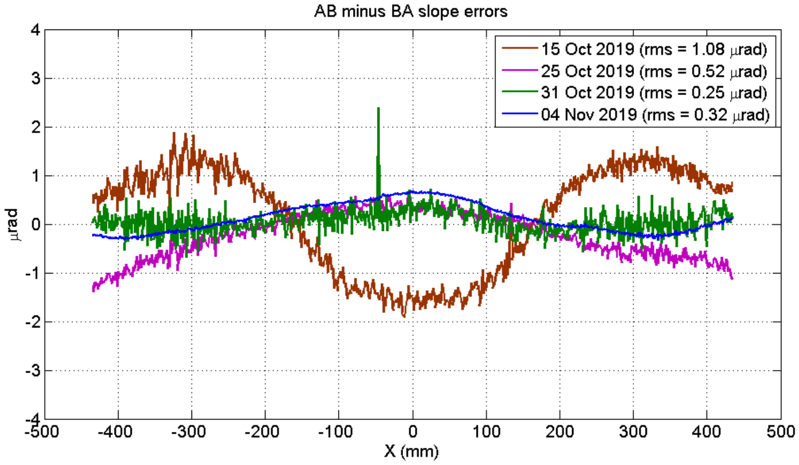

Figure 4.16 : Difference between AB and BA slope errors with different setups.

The slope errors are compared between SHARPeR and LTP measurements in Figure 4.17. The LTP measured with markings on the edges, but the same line measured by SHARPeR using edge markings (31-Oct-2019) has significant discrepancies in high frequencies of slope errors. The LTP matches more closely with SHARPeR measurement on the line aligned with fiducials (04-Nov-2019).

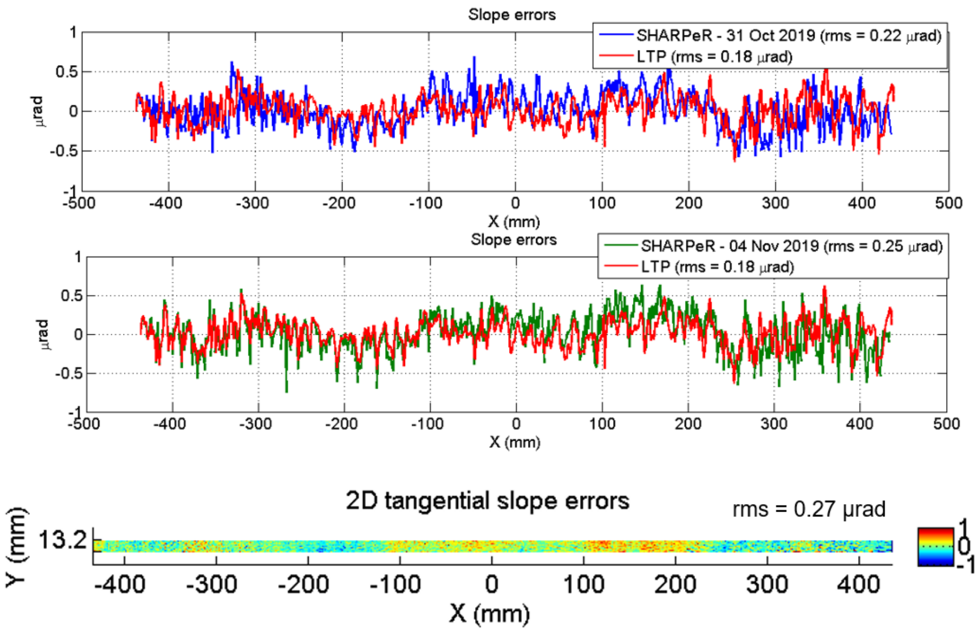

Figure 4.17 : Comparison of SHARPeR tangential slope errors to LTP (ABBA average), measured with the latest design (Setup 3 in Figure 4.14). The figure also highlights mirror misalignment errors when comparing two instruments. The SHARPeR 2D slope errors are also shown.

The fiducials were observed to be not in line with edge markings from the measurement by the ESRF Zygo Fizeau instrument, and LTP had problems aligning using fiducials. Even when using the same type of alignment such as using edge markings by LTP and SHARPeR, ambiguities in lateral position are severe as the alignment relies upon visual adjustment of the measurement beam with the markings.

4.4 Normal incidence scans on spherical surfaces

4.4.1 Measurements on a moderate sphere (radius ~120 m)

SHARPeR instrument was used to measure a spherical mirror (SG4) manufactured by Carl Zeiss SMT [125]. The mirror has physical dimensions 220 x 40 x 30 mm^3 with an optical/clear aperture of 200 x 30 mm^2 and a nominal radius of curvature ~120 m. The mirror was placed under the optical head in fixed position (on RTT) and scanned in forward and backward directions 32 times. The mirror was then flipped along the scan direction (AB→BA) and scans were repeated 32 times in forward and backward directions. The subapertures were stitched using StitchWave for each scan and the stitched scans are averaged. The laser power is adjusted for acquisition by CCD to ~80% saturation limit. The exposure time is 100 ms and measurements performed in step by step mode.

Stitched 2D tangential and sagittal slopes, measured by the SHARPeR instrument on the spherical mirror in the AB direction over an area of 200 mm x 11 mm centered on the mirror, are plotted in Figure 4.18. The mirror was not moved during the scans and hence adjusted in normal incidence only for the central subaperture; even for this subaperture only microlenses close to the center of image can truly be in normal incidence. We consider normal incidence when the nominal tilt of subaperture, which is the average tangential and sagittal slopes of all microlenses, is close to zero (<2 µrad tilt). The spherical component is subtracted from slopes of the central line trace and the residual slope errors plotted in Figure 4.19, for AB & BA and their averages. AB and BA measurements show a large second order component of opposing sign indicating a systematic error between the two measurements (ideally the AB and BA curves should match). The difference between AB, BA probably originate primarily from retrace errors. Some of these errors, can be corrected by averaging AB and BA, as explained in section 2.5.2.

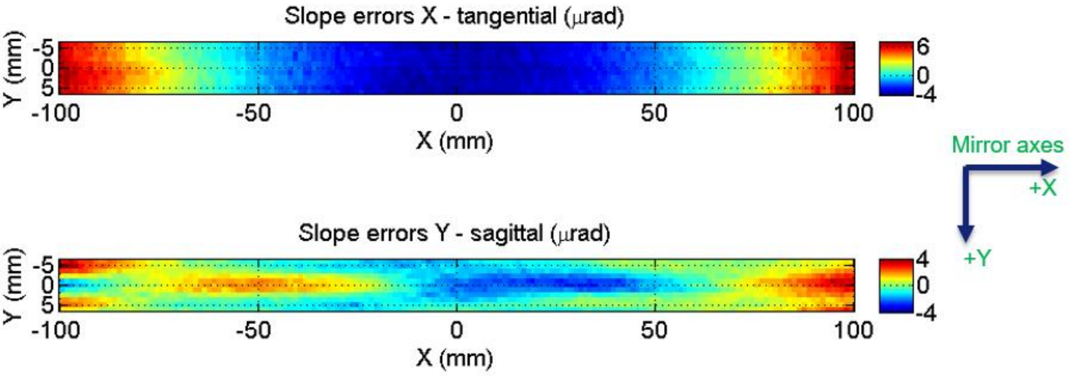

Measured values:
- radii = 118.12 m (tangential), 117.06 m (sagittal)
- rms = 3.15 μrad (tangential), 1.26 μrad (sagittal)
- pv = 11.72 μrad (tangential), 7.08 μrad (sagittal)

Figure 4.18: SHARPeR 2D slope error maps of the SG4 spherical mirror measured in AB orientation. Here the sphere and tilt terms in X and Y are subtracted from stitched slopes.

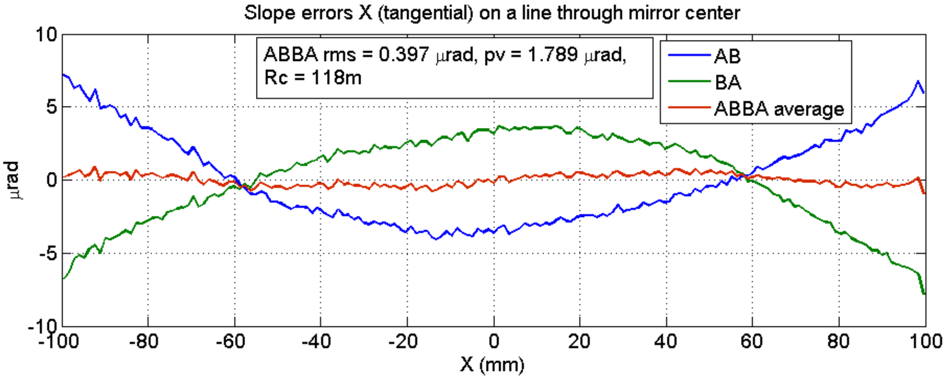

Figure 4.19: Slope errors of the SG4 spherical mirror for AB and BA measurements on a line through center.

4.4.1.1 Measurements with Normal incidence technique

ABBA averaging could not completely remove the systematic errors as shown in the comparison between LTP and SHARPeR measurements in Figure 4.21. In order to minimize the systematic retrace errors, the SG4 spherical mirror was measured for 100 forward and backward scans in AB and BA with SHARPeR using a normal incidence technique: The mirror was placed in normal incidence at each subaperture by tilting the mirror. The technique has been explained in detail in section 2.5.4. The tangential slopes measured by the microlenses of the line through center of the sensor array is shown for all subapertures of a single scan in Figure 4.20(a). The central microlens is blackened and therefore does not provide any value. AB and BA stitched slope errors in Figure 4.20 match more closely compared to measurements without acquisition in normal incidence as shown in Figure 4.19. SHARPeR measurements are also compared to LTP measurements in Figure 4.21. The normal incidence technique significantly improves the accuracy of measurements by minimizing the error contribution from retrace errors.

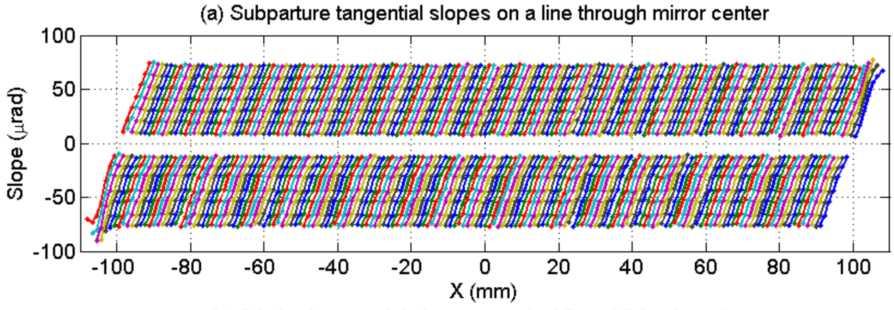

(b) Stitched tangential slope errors in AB and BA orientations

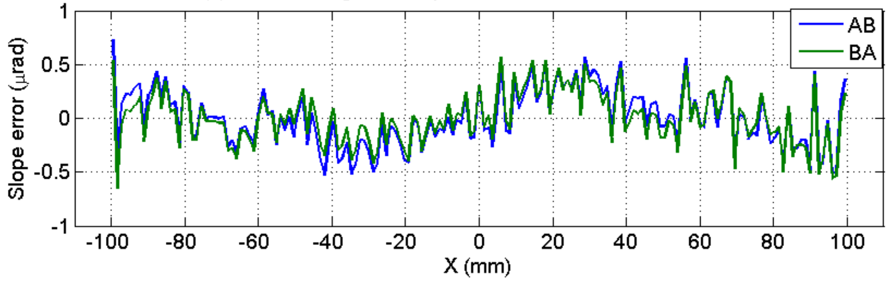

Figure 4.20: SHARPeR measurements of the SG4 sphere in normal incidence. Plot (a) each oblique colored line shows the tangential slopes measured by each of the 14 active microlenses along the central line of the SHARPeR sensor where this line is aligned with the central tangential mirror trace. The 'missing' data point at zero slope corresponds to the blackened central microlens which gives no data. Successive lines correspond to the measured slopes after the sensor has been moved along Tx by one microlens spacing (1.2mm) and the mirror tilted around Ry to place the center of the mirror in normal incidence. Plot (b) is the stitched tangential slopes along the mirror central line derived from such datasets in AB and BA orientations.

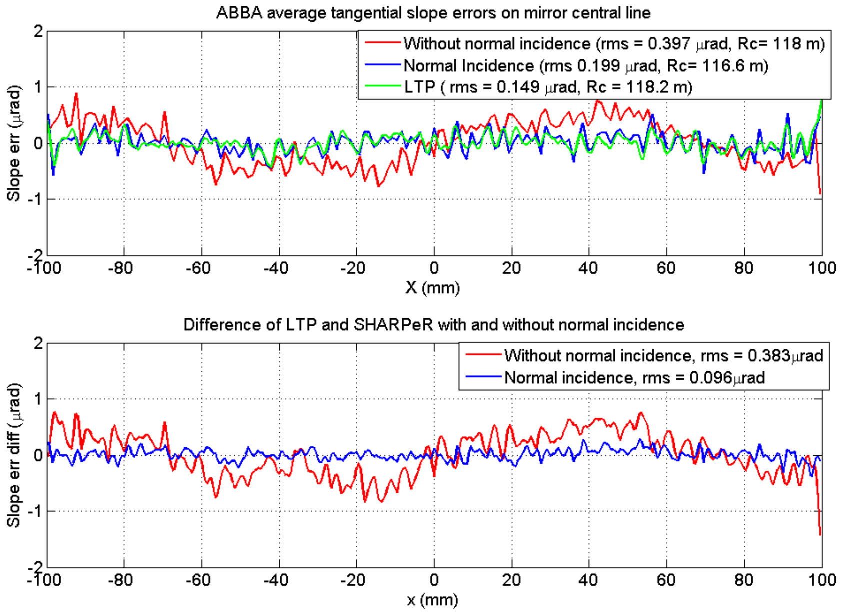
ABBA average tangential slope errors on mirror central line

Difference of LTP and SHARPeR with and without normal incidence

Figure 4.21: SHARPeR measurements on the SG4 sphere compared to ESRF LTP. All the measurements are tangential slopes on the mirror central line. Top plot shows the comparison between LTP and SHARPeR with and without normal incidence. Bottom plot is the difference between SHARPeR and LTP slope errors.

4.4.2 Measurements on a highly curved spherical mirror (radius ~9.3 m)

A spherical mirror with nominal radius ~9.3 m from ‘Helmholtz - Zentrum Berlin für Materialien und Energie’ (HZB) was measured using SHARPeR using the normal incidence acquisition mode. The mirror has physical dimensions 145 x 45 x 45 mm^3, and is made of uncoated silicon substrate. The mirror has two clear apertures, one is a spherical profile and other is a chirped profile overlaid on top of the spherical profile. The chirped region is centered on the mirror and spherical region is offset by ~10 mm from center in sagittal direction. The laser power is adjusted for acquisition by CCD to ~80% saturation limit. The exposure time is 10 ms and measurements performed in onfly mode at speed 3 mm/s.

4.4.2.1 Spherical profile

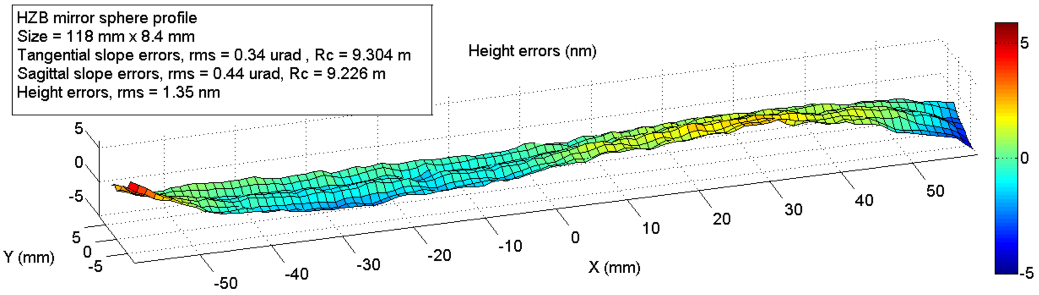

Figure 4.22 : Height errors on the spherical profile region on the mirror measured with SHARPeR in normal incidence.

The mirror is measured using the normal incidence technique for 32 forward and 32 backward scans in AB and BA orientations. The total measurement time for AB & BA measurements is nearly 2 hours. The mirror is measured on both the regions of interest (chirp and sphere) in separate scans. The stitched height errors from the spherical region on the mirror are shown in Figure 4.22.

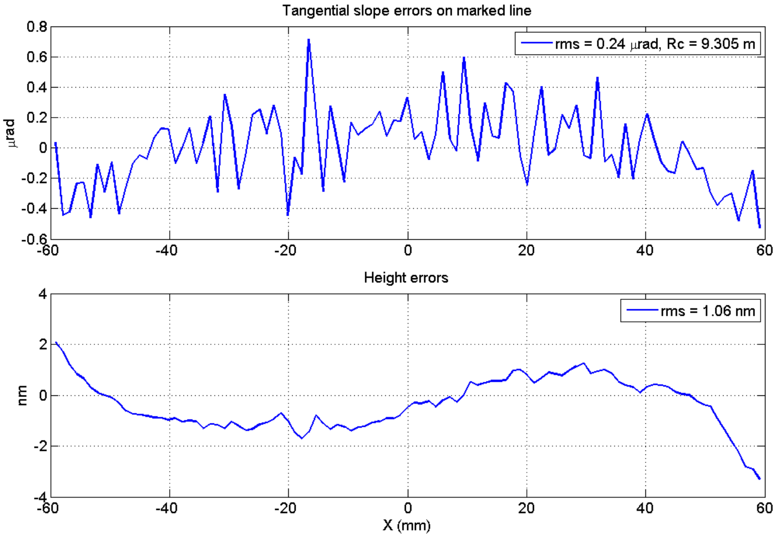

Figure 4.23 : Tangential slope and height errors (ABBA average), on a line physically marked on spherical profile region, measured by SHARPeR in normal incidence.

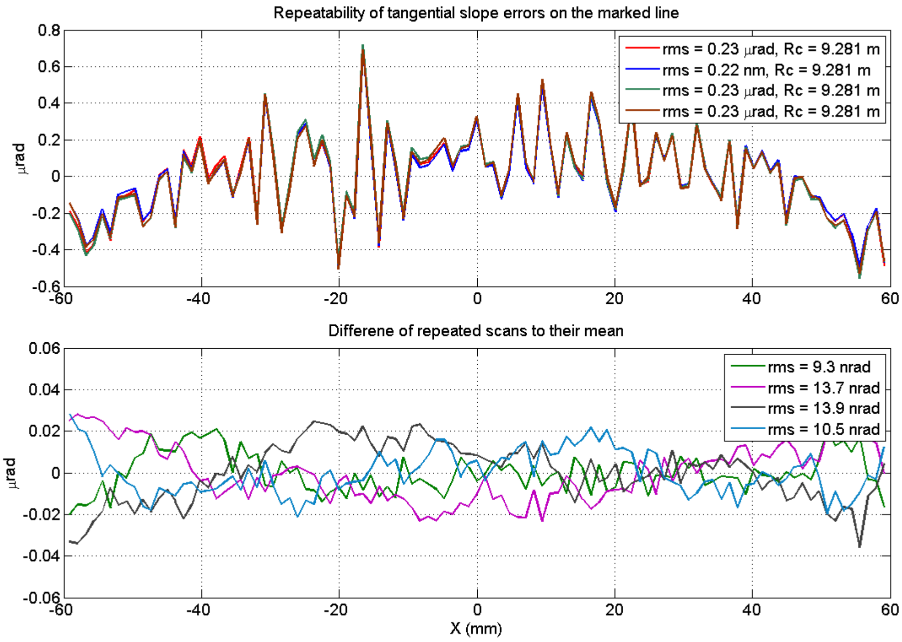

Figure 4.24 : Repeatability of tangential slope errors with measurements done by SHARPeR in AB and BA orientations. A measurement (AB & BA) has 32 forward and 32 backward scans in each orientation, and they are averaged (ABBA average). The measurement is repeated four times and the ABBA averages are compared.

A line profile marked physically on the mirror edges, is chosen for primary comparison between different instruments. The tangential slope errors and height errors on the marked profile are shown in Figure 4.23. The full measurements of the spherical region are repeated four times and the repeatability of slope errors are shown in Figure 4.24. The difference of slope errors between the each of the repeated scans and the mean values from the four separate measurements each give a rms value below 15 nrad.

4.4.2.1.1 Accuracy comparison with other instruments

SHARPeR height errors on the spherical region are compared to measurements made using the ESRF instruments Zygo Fizeau, Veeco MSI and LTP, in Figure 4.25 and Figure 4.26.

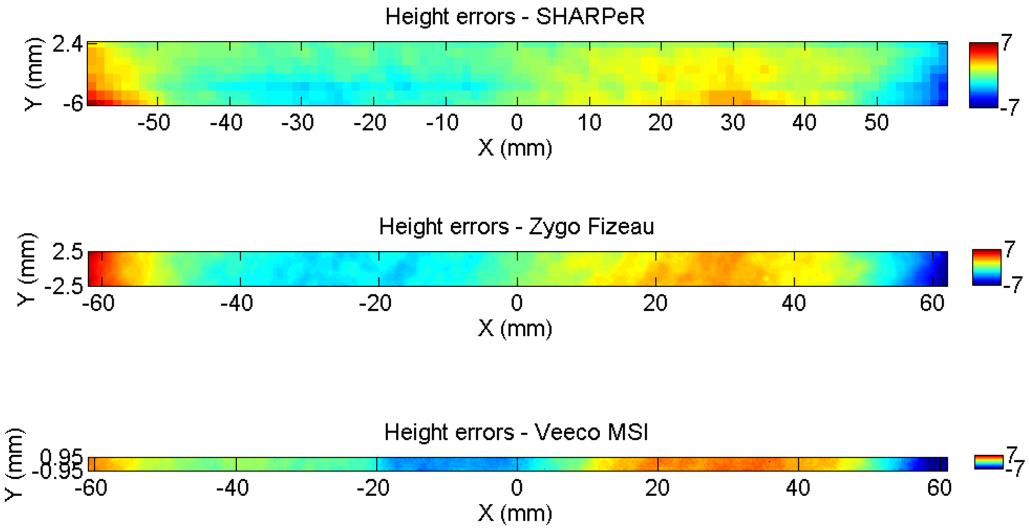

Figure 4.25 : SHARPeR 2D height errors on HZB sphere compared to ESRF Fizeau and MSI.

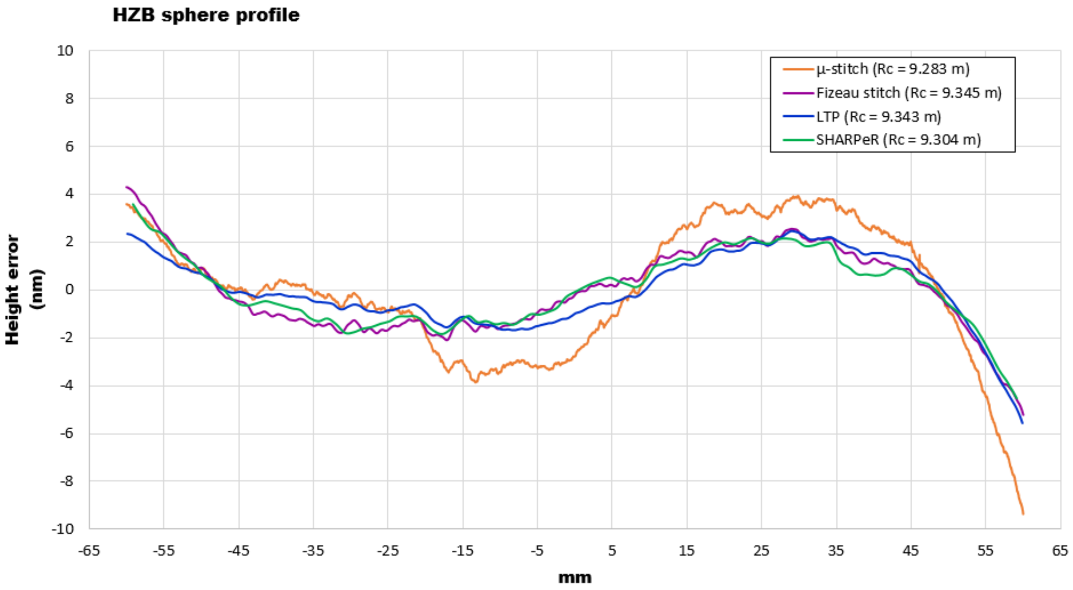

Figure 4.26 : SHARPeR (line) height errors on HZB sphere compared to ESRF Fizeau, MSI and LTP.

Table 4.3 : Comparison of SHARPeR measurement parameters on HZB sphere to ESRF Fizeau, MSI and LTP

	Height error rms (nm)	**Height error pv (nm)**	**Radius of curvature (m) ***
SHARPeR 2D	1.43	11.77	9.304
Fizeau 2D	2.24	14.24	9.345
MSI 2D	2.78	138.09	9.283
SHARPeR 1D	1.53	8.11	-
Fizeau 1D	1.74	9.51	-
MSI 1D	2.71	13.29	-
LTP 1D	1.52	8.02	9.343

* Radius of SHARPeR obtained with tilt calibration correction (explained in chapter 4.7)

The comparison of different measurement parameters is shown in Table 4.3. SHARPeR results are close to Fizeau and LTP whereas MSI showed some discrepancies. The MSI has significant high frequency errors perhaps originating from dust particles on the mirror leading to very large PV values. The height error rms and PV measured by SHARPeR are much closer to the LTP compared to other instruments which may be explained by similar resolution between LTP and SHARPeR (1-2 mm). The radius values agree to <0.7% between the instruments.

4.4.2.2 Chirped profile

SHARPeR was also used to measure the chirped region in normal incidence for 32 forward and 32 backward scans in AB and BA directions. The measurements were performed using a step size ~1.2 mm between the subapertures, equivalent to single microlens size of the wavefront sensor. Effectively the stitching of these subapertures create discrete surface profile measurements with a sampling period 1.2 mm. The chirp spatial period was changing from 2 mm to 7 mm from left to right. The step of 1.2 mm is used commonly to simplify stitching process, but in order to verify if the chirped surface can be better resolved with SHARPeR, oversampling was used as explained in the following. To increase the sampling in tangential direction, the mirror was measured again with offsets step/3 and 2*step/3 in tangential direction. Usually the mirror center is used to define the subaperture positions in a scan, and the offset was added to the mirror central position, and with these offsets the AB and BA scans were repeated. The three measurements are stitched and averaged (ABBA) separately and their datasets, tangential/sagittal slope errors and height errors, are merged directly without any interpolation. As a result, an oversampled surface with tangential period of 0.4 mm was obtained. The slope and height errors are presented in Figure 4.27 and Figure 4.28.

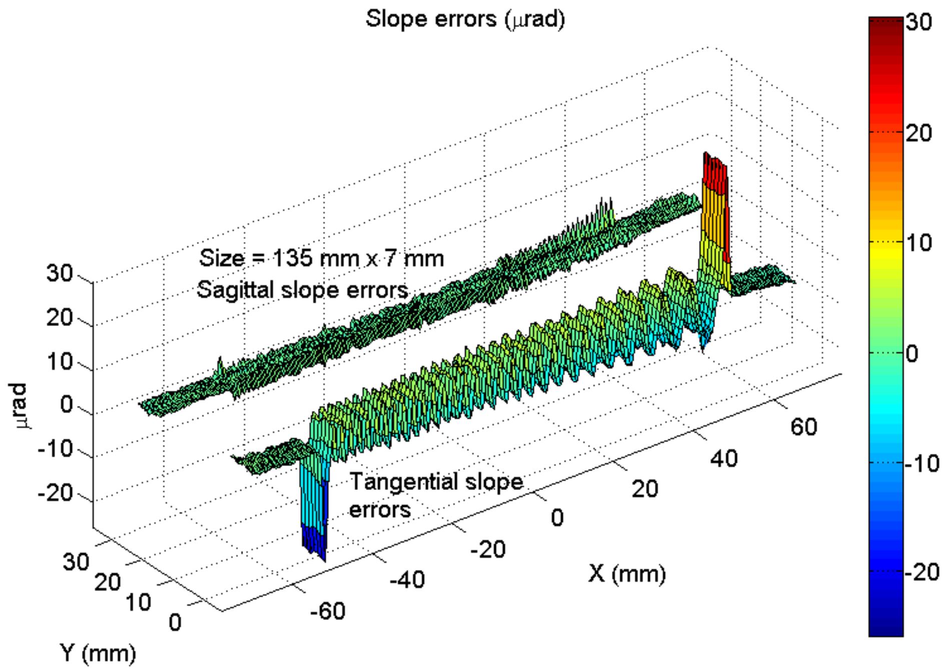

Figure 4.27 : SHARPeR stitched slope errors (tangential & sagittal) on the chirped region on HZB sphere with sampling of 0.4 mm.

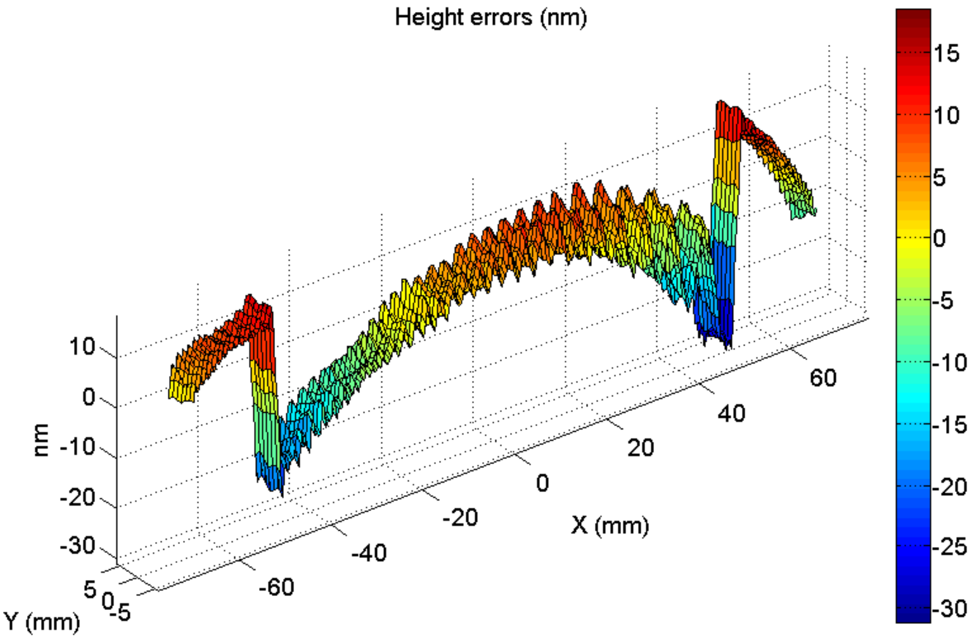

Figure 4.28 : SHARPeR stitched height errors on the chirped region on HZB sphere with sampling of 0.4 mm.

4.4.2.2.1 Advantages with oversampling

The tangential slope and height errors of SHARPeR measurements on a line through the mirror center, with and without oversampling are shown in Figure 4.29, along with slope and height errors from Zygo Fizeau instrument at ESRF. The Fizeau measures heights and the slope profile was obtained through differentiation of the height profile. Oversampling clearly shows an improvement in resolving chirped features of high spatial frequency, although the amplitude of high frequency features drop. The spatial resolution of SHARPeR is ~-1.2 mm (see section 2.3), whereas the spatial resolution is ~0.44 mm for Fizeau measurement (after filtering high frequencies, original resolution was 0.032 mm), which explains the drop in the amplitude of chirp frequencies above 1.2 mm. Increasing the sampling frequency to 0.4 mm for SHARPeR shows improvement in the measured surface profile, as expected by Nyquist-Shannon sampling theorem which necessitates a minimum sampling of 0.6 mm (half the resolution period).

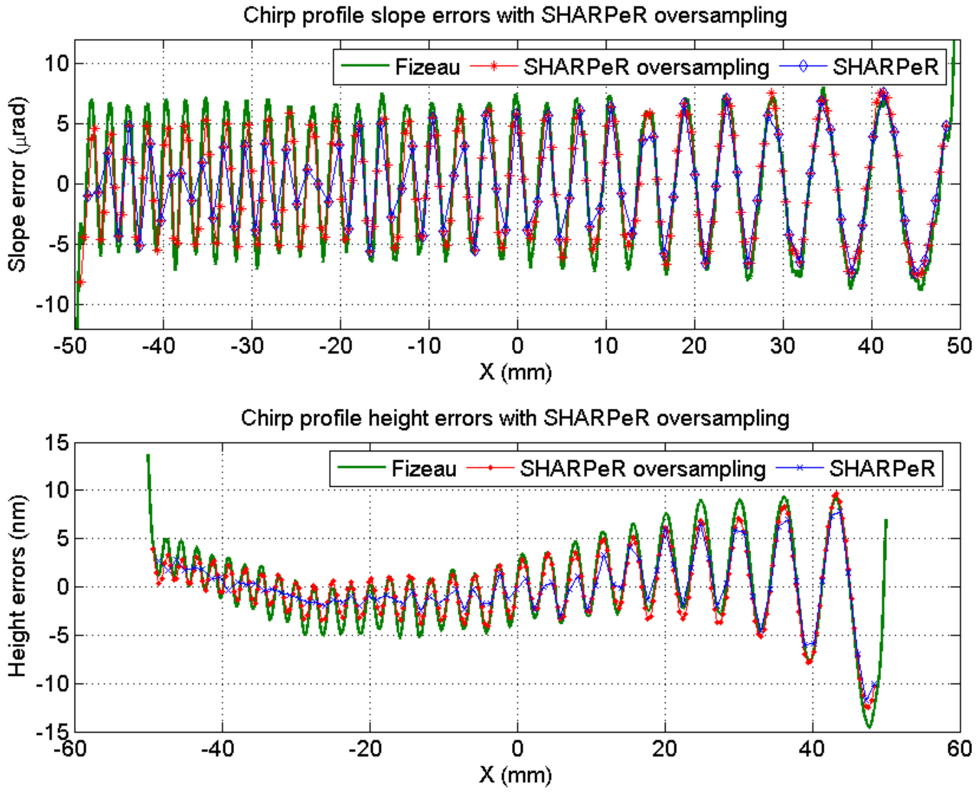

Figure 4.29 : Comparison of SHARPeR slope and height errors in tangential direction with and without oversampling and to the Fizeau slope and height errors on chirped region. Fizeau slope errors are obtained from partial derivative of its height errors in tangential direction. Fizeau has a sampling of 0.44 mm and SHARPeR has 1.2 mm sampling in default and 0.4 mm while using oversampling.

4.4.2.2.2 Simulations using Fizeau height profile on chirped region

Due to the higher spatial resolution of the instrument the height profile measured by the Fizeau interferometer is assumed to provide a more accurate evaluation of the chirped profile. In order to understand the effects of the oversampling on the measurements of the chirped profile, the height errors measured by the Fizeau interferometer on the chirped region are used to simulate SHARPeR behavior with and without oversampling. The Fizeau height error profile as shown in Figure 4.30, is subdivided into multiple regions of size 1.2 mm (SHARPeR microlens size) and each sub-region is fit to a line. Also, each sub-region was centered on the mirror X-axis positions measured with SHARPeR. The slope of the fitted lines is shown in the bottom plot of Figure 4.30. These slopes are compared to slope errors measured by SHARPeR in Figure 4.31. The Simulated slopes follow very closely the actual slope errors measured by SHARPeR.

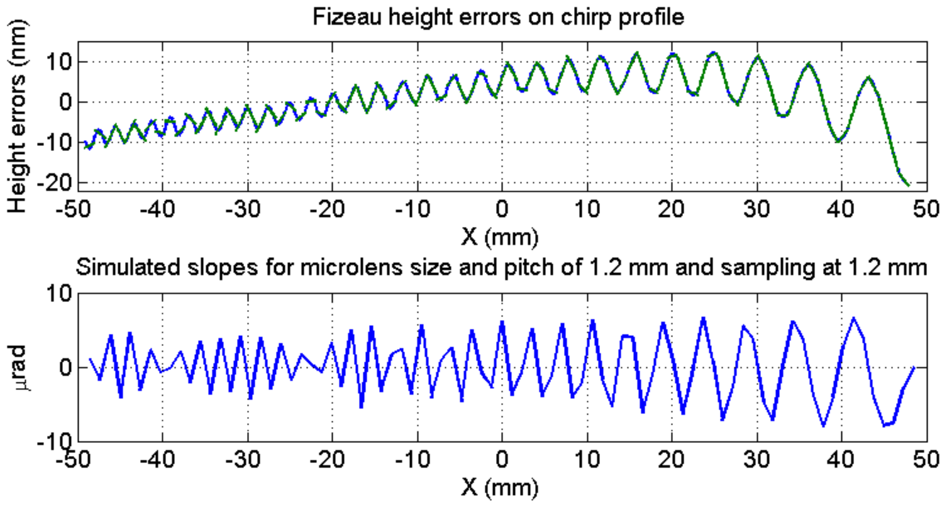

Figure 4.30: Simulation of SHARPeR behavior using Fizeau height error profile. Fizeau data is subdivided into many regions of a microlens size (1.2 mm) and each one is fitted to a line. The slope of line is shown in the bottom plot.

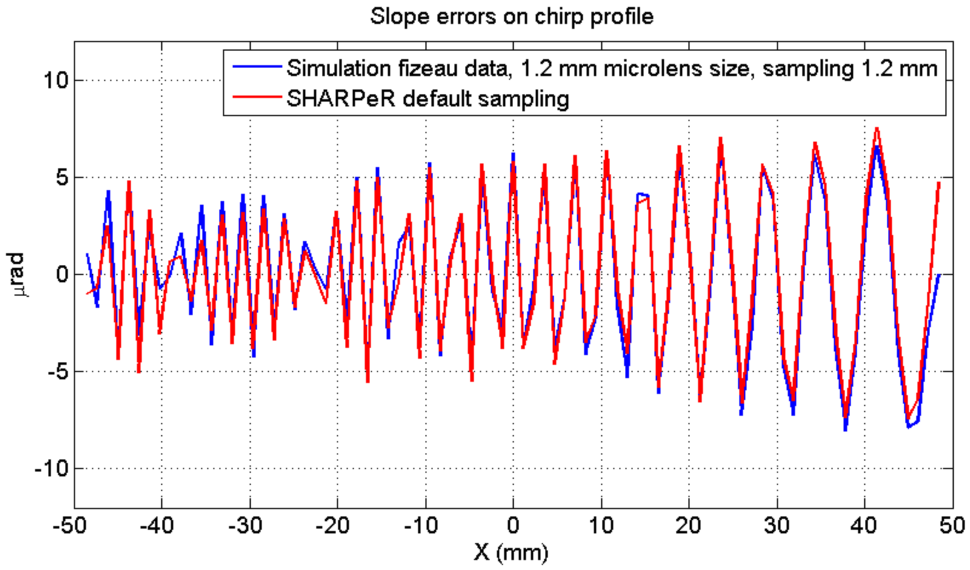

Figure 4.31: Simulation of SHARPeR slopes from Fizeau data as shown in Figure 4.30 is compared to the actual SHARPeR measurement.

Fizeau simulations are extended to simulate SHARPeR oversampling method. Sub-regions on the Fizeau height error profile were shifted by -0.4 mm and -0.8 mm and the slopes were obtained in each case with the line fitting. The slopes are joined and the oversampled simulated slopes are compared to SHARPeR oversampling in Figure 4.32. The simulations and SHARPeR measurements match very well, and the simulations clearly imply improved resolution of chirp profile with oversampled SHARPeR measurements.

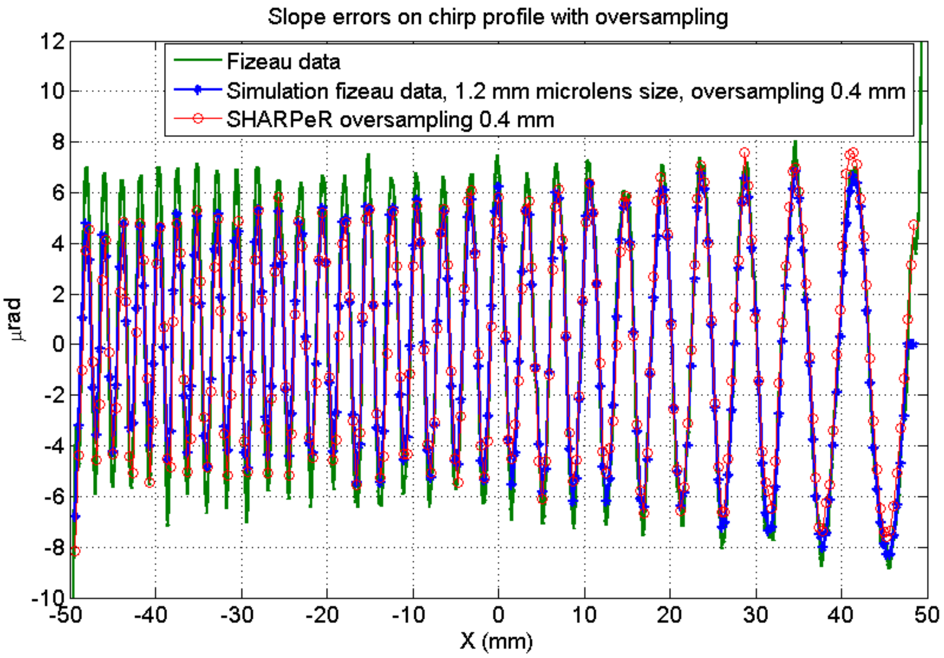

Figure 4.32: Simulation of SHARPeR oversampling using Fizeau height errors compared to SHARPeR measurement with oversampling.

4.5 Multi incidence scans on aspheric surfaces

As shown in section 3.4 the normal incidence technique significantly improves measurement quality on moderately to strongly curved mirrors. However, on highly curved mirrors (radius < 20 m) with strong asphericity (i.e. with large variations in radius of curvature along the mirror length), significant residual instrument errors are observed even when using the normal incidence method. An elliptical mirror with mean radius of curvature of ~13 m was measured using SHARPeR in normal incidence as shown in Figure 4.33. The mirror made with silicon has dimensions of 70 x 20 x 20 mm^3 with an uncoated clear aperture of dimensions 60 x 4 mm^2. The radius of curvature varies from ~8 m at one end to ~16 m at the other. The laser power was adjusted for acquisition by CCD to ~80% saturation limit. The exposure time was 100 ms and measurements performed in step by step mode.

Figure 4.33a show different the slopes measured by the microlenses corresponding to the central line of the sensor along mirror length for a sequence of subaperture measurements along the ellipse. The mirror has higher curvature close to the left edge with a gradual decrease in curvature towards the right edge, which results in larger range of slopes measured by subapertures on the left. The subapertures are stitched using PyLOSt software matrix overlap error algorithm (see sections 3.2 and 3.3). The stitched profile on a line through the mirror center is compared to the profile measured by ESRF LTP (also produced by applying a stitching procedure) in Figure 4.33b, and shows very poor agreement.

The ellipse was later measured using a 'multi-incidence' method as shown in Figure 4.34. The 'multi-incidence' method has been explained in detail in section 2.5.4. In this method each subaperture was first aligned with normal incidence and then tilted around Ry axis over 50 points in the range -1 mrad to 1 mrad, and measured at each tilt position. The whole of mirror was measured in this manner for 20 forward and 20 backward scans, giving rise to 2000 images at a subaperture. An example of three tilts of -0.45, 0, 0.45 mrad are shown in Figure 4.34a. A threshold is applied before stitching the subapertures with microlenses presenting slopes outside the threshold range (e.g. -1 mrad < slopes < 1 mrad) being excluded from the stitching process, and stitched slopes are averaged. The stitched slope errors with best ellipse removed are shown in Figure 4.34b. Multi-incidence method shows much better agreement with the LTP measurement compared to normal incidence.

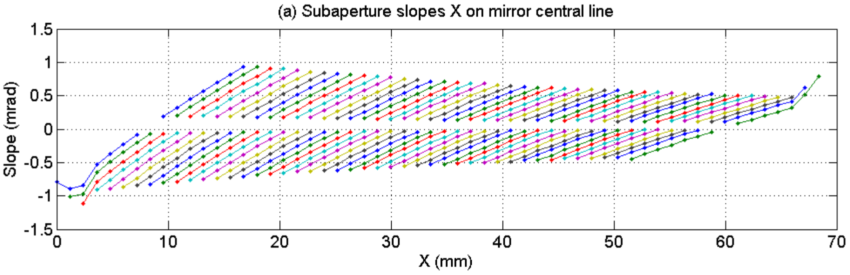
(a) Subaperture slopes X on mirror central line

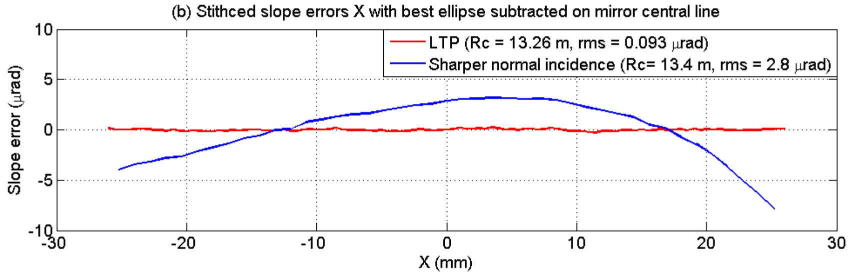
(b) Stithced slope errors X with best ellipse subtracted on mirror central line

Figure 4.33 : SHARPeR normal incidence measurements on the ellipse. Plot (a) shows many lines each from SHARPeR tangential slopes of a single subaperture on the mirror central line. Plot (b) is the stitched tangential slopes on mirror central line from SHARPeR normal incidence compared to stitched LTP scan.

(a) Subaperture slopes X on mirror central line at different incidences

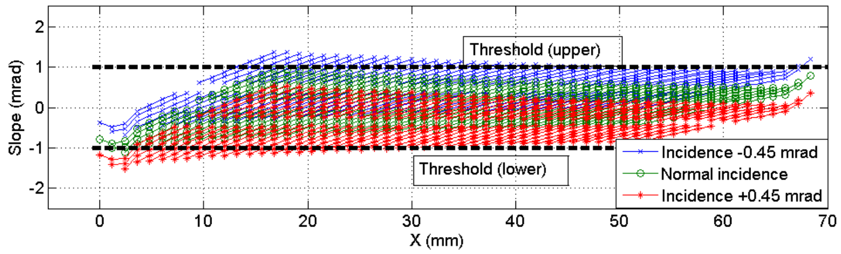

(b) Stithced slope errors X with best ellipse subtracted on mirror central line

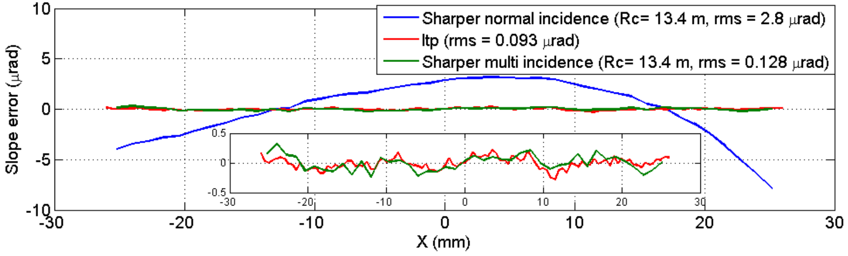

Figure 4.34 : SHARPeR multi-incidence measurements on the ellipse. Plot (a) shows many lines each from tangential slopes of a single subaperture on the mirror central line, and each subaperture is measured in normal, ± 0.45 mrad incidences. This measurement corresponds to a single forward scan, showing only three incidence angles, the actual measurement has 50 incidence angles. Plot (b) is the stitched tangential slopes on mirror central line from SHARPeR in normal and multi incidence scans compared to stitched LTP scan.

4.6 On the fly scans

SHARPeR instrument used to be operated in step by step mode, where the optical head moves to a position on top of the mirror, stops and images the subaperture before moving to next position. An alternative way of measuring the mirror in on the fly (or onfly) mode was implemented as explained in section 2.5.5. In the onfly mode the optical head moves at a constant speed over the whole mirror length and images subapertures at specific positions. The average speed for the step by step mode was 0.8 mm/s. The onfly scans are commonly measured at 3 mm/s speed which is nearly four times faster than the step by step mode.

4.6.1 Onfly vs stepwise measurements on a long mirror

A 950 mm-long, flat, uncoated, Silicon mirror supplied by E-XFEL was measured by SHARPeR in stepwise and onfly modes, to compare the performance of the two acquisition modes. Measurements on this mirror with various SHARPeR designs has already been presented in section 4.3. In this current section, both stepwise and onfly measurements were performed on 25-Oct-2019, one after other without changing the mirror setup. The laser power is adjusted for acquisition by CCD to ~80% saturation limit, and the exposure time is 2 ms for both onfly and stepwise modes. The mirror was measured in AB and BA orientations in both modes. The number of repeated scans in each orientation are 32 forward-backward (FB) scans (i.e. 32 forward, 32 backward) in stepwise mode and 96 forward-backward scans in onfly mode. The onfly scans were performed at 3 mm/s continuous speed, whereas for stepwise scans the average speed is nearly 0.8 mm/s.

The ABBA average tangential slope errors on a line passing through mirror center is shown in Figure 4.35, for onfly and stepwise modes. Many of the high frequencies were matching between the two modes with visible differences in the low frequencies. The difference between the two modes is also shown in the same figure, which shows only low frequencies dominated by a third order polynomial. The difference in AB and BA slope errors is also shown in the same figure, and it shows nearly second order polynomial differences. The AB minus BA difference is much smaller for onfly scans (rms = 0.46 µrad) compared to stepwise scans (rms = 1.12 µrad), i.e. onfly scans are better. Another significant difference is the radius of curvature in ABBA averages, with higher curvature for onfly scans (radius -16.4 km) than for stepwise scans (radius +75.5 km). One of the reasons for differences in radius may be the drift errors as shown in Figure 4.36, as the measurements were taking very long time. The radius of curvature differences could be further investigated.

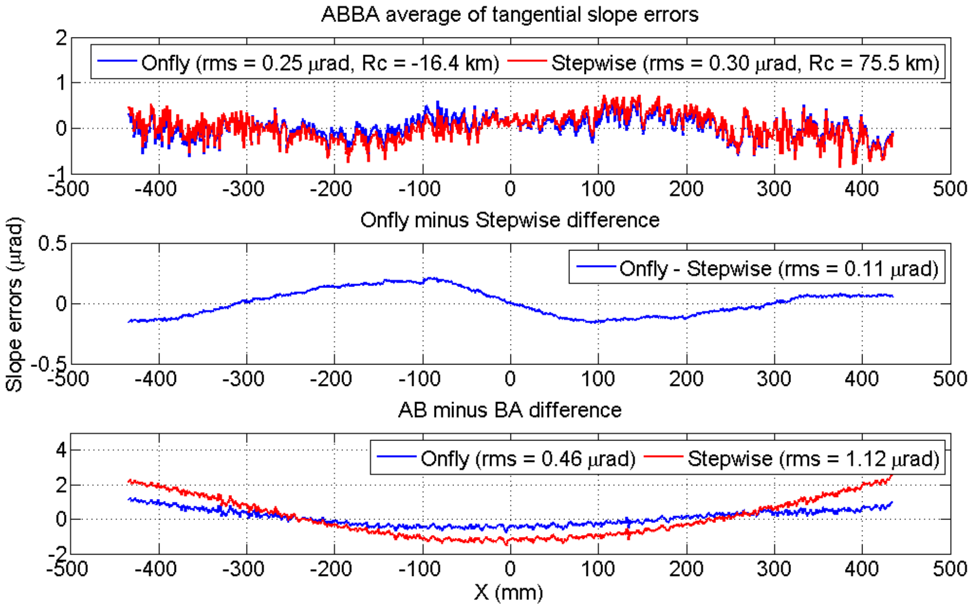

Figure 4.35 : Comparison of ABBA tangential slope errors on a line through mirror center, in stepwise and onfly modes (top). The difference between ABBA stepwise and onfly is also shown (middle). In both modes difference between AB and BA slope errors is also shown (bottom).

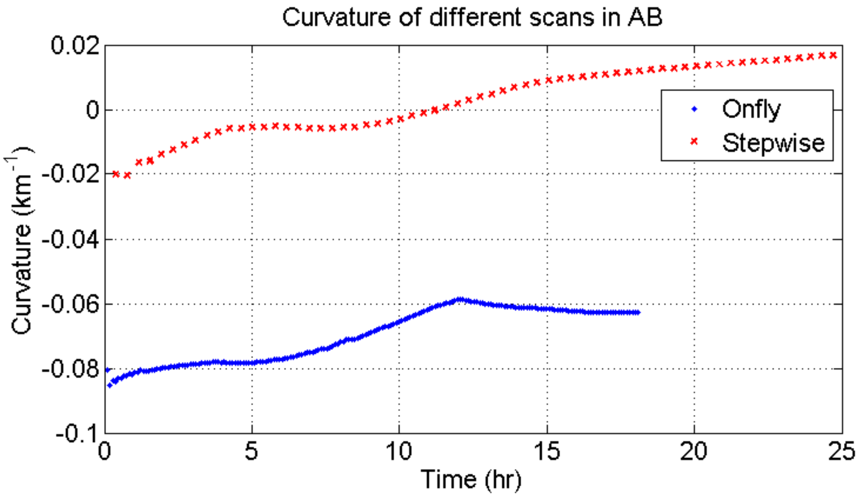

Figure 4.36 : Curvature of different stitched scans measured in AB orientation, in onfly (96 FB scans) and stepwise (32 FB scans).

Following a similar approach to Nicolas et al. [52], onfly scans were statistically analyzed for noise reduction over many scans as shown in Figure 4.37. The measurement noise as statistical random noise is calculated using the equation below, and presented in the figure as Onfly (stat) & Stepwise (stat) curves.

$$\sigma = \frac{\sigma_0}{\sqrt{N}}$$

Where σ_0 is the standard deviation of individual scans over N scans. The measurement noise is calculated cumulatively over 96 FB scans in onfly and 32 FB scans in stepwise, measured in the AB orientation. Total scan time is ~24 hours in stepwise and ~18 hours in onfly scans, uniformly distributed over each scan. The standard deviation (σ_0) is calculated for each position on mirror (on the line through center), and then rms over all positions is taken. Onfly scans can clearly reach a much lower noise level within a similar time frame as it allows more scans to be taken. Onfly scans can reach below 40 nrad noise within 50 minutes whereas stepwise scans require nearly 20 hours to reach similar noise level.

The measurement noise may not be completely random in repeated scans as there are drift errors and pseudo random errors such as those explained in section 4.1.2. The measurement noise calculated as difference between cumulative scan average and total scan average, is shown as dotted Onfly & Stepwise curves in Figure 4.37. The difference is taken for tangential slope errors on the line passing through center of mirror, and rms of this difference over positions is shown. The stepwise curve nearly follows the statistical random noise curve, whereas onfly curves deviate significantly. For the 40 nrad noise level using this procedure, onfly scans takes nearly over 2 hours, whereas stepwise scans takes nearly 15 hours. As the cumulative scans reach close to total scans the difference converges to zero very quickly, which is the reason for steep turn at the right end of the stepwise and onfly curves.

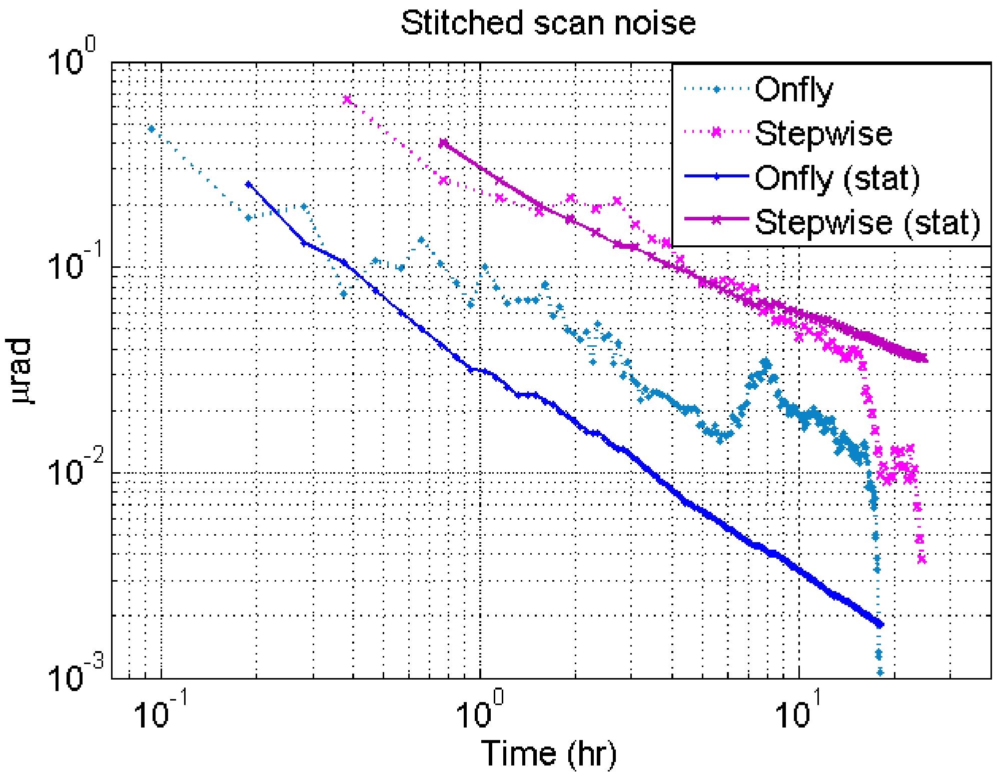

Figure 4.37 : Noise reduction as a function of time over many stitched scans in onfly and stepwise modes (AB orientation).

4.6.2 On the fly scans on a test mirror with fiducials

In order to evaluate the quality of the data acquisition synchronization in the onfly mode, a flat mirror with fiducial markers at specific positions was measured by SHARPeR in stepwise and onfly modes. The mirror dimensions are 245 x 50 x 50 mm^3 and is made of uncoated Zerodur. The mirror has fiducials on two tangential lines at nearly -10 mm, +10 mm away from center. The laser power was adjusted for acquisition by CCD to ~80% saturation limit. The exposure time was 100 ms in step by step mode and 10 ms in onfly mode. Each line was measured for 32 FB scans in AB orientation, and the resulting subapertures are stitched using PyLOSt software.

The stitched slope and height errors from SHARPeR stepwise measurement is shown in Figure 4.38. Line 1 corresponding to measurement positioned at a -10 mm offset from the mirror center has five fiducials spaced by 50 mm each, and line 2 measurement positioned at a +10 mm offset from the center has three fiducials separated by nearly 100 mm each. A line profile for stitched tangential slope errors through center of fiducials on line 1 is shown in Figure 4.39 for stepwise and onfly measurements. The onfly measurements were performed at 3 mm/s speed. In the Figure 4.39a, forward scans average and backward scans average are shown each for onfly and stepwise, and difference between forward and backward are shown in Figure 4.39b & c. Onfly scans show much smaller difference between forward and backward scans, of peak to valley (pv) ~3 µrad, which is much smaller than the stepwise difference of pv ~60 µrad.

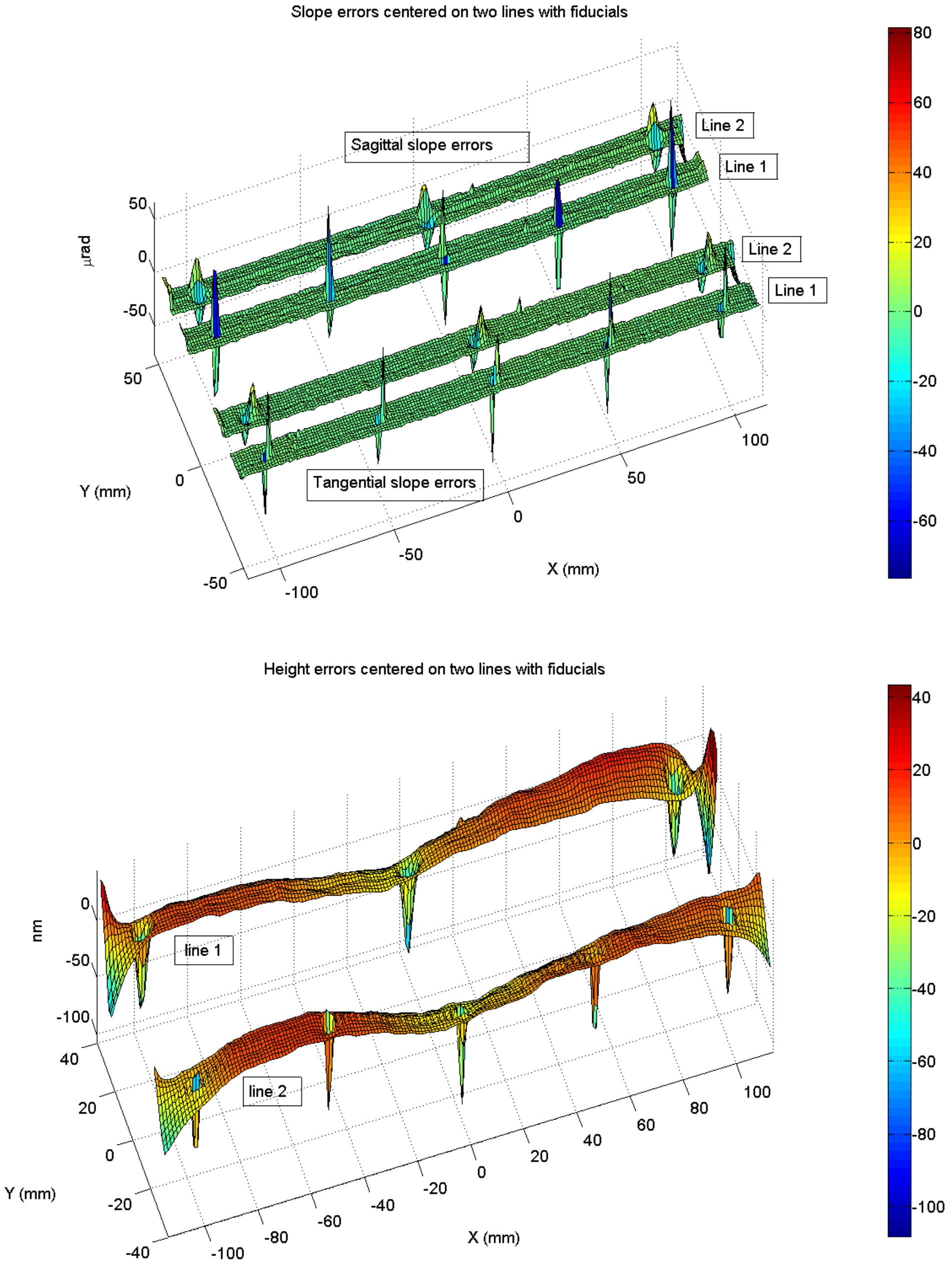

Figure 4.38 : SHARPeR 2D slope and height errors on a fiducialized flat mirror measured in step-by-step mode. Fiducials are present along two tangential lines on mirror with five and three fiducials on lines 1 & 2.

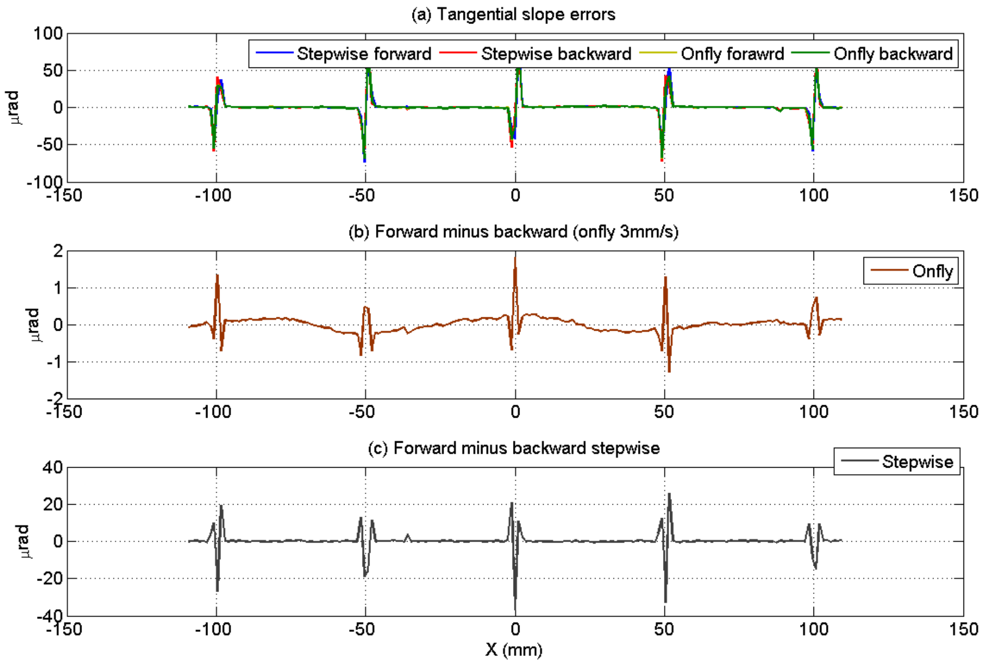

Figure 4.39 : Tangential slope errors on line 1 passing through center of fiducials, measured in stepwise and onfly 3mm/s and in forward and backward scans are shown in top figure. Middle and bottom figures show the difference between forward & backward scans, for onfly and stepwise modes respectively.

The fiducial spot at the center of line 1 is approximated to Gaussian shape and the difference between forward and backward scans in Figure 4.39 b & c is fit to an offset in Gaussian spots. The offset is obtained as ~10 µm or a delay of 3.3 ms for onfly scans, which may be arising from software delays or signal transmission delays in the cable connecting camera and motion control system. The offset was approximately -200 µm for stepwise scans. However, the X-positions recorded by encoders placed on motors had a mean value of and 0.3 µm between forward and backward directions in step by step scans. The discrepancy is quite large in step by step scans and it needs to be further investigated.

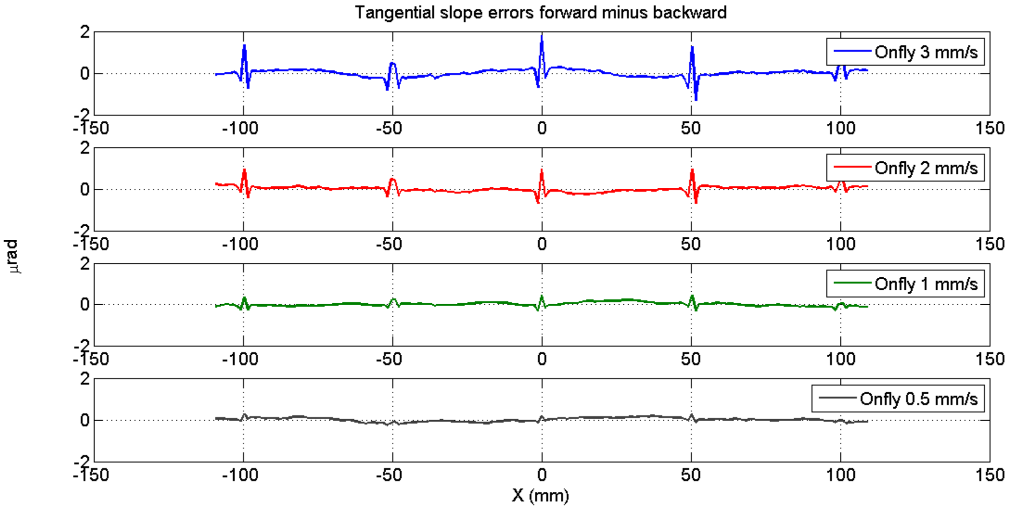

Figure 4.40 : Tangential slope errors (line 1) forward minus backward in onfly measurements at different translation speeds.

If the delay of 3.3 ms is from external factors such as software or signal transmission, it may be assumed to be constant and should result in smaller offsets in distance, for onfly measurements at slower speeds. The Figure 4.40 shows forward and backward scan differences in onfly mode at different speeds, and shows a reduction in the amplitude of the difference peaks at fiducials towards the lower speeds. The magnitude of difference peaks matches to the Gaussian spot model for a constant delay time of 3.3 ms, between trigger and image capture. The delay can be visualized using the schematic of camera exposures as shown in Figure 4.41.

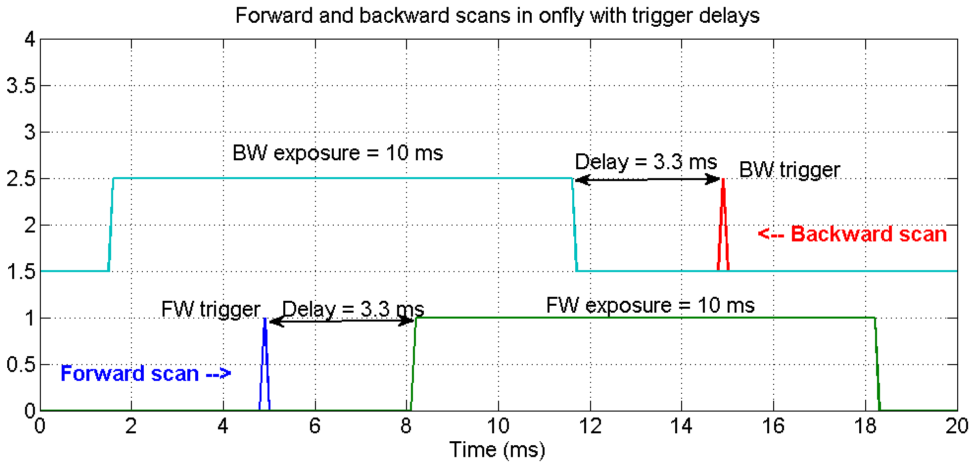

Figure 4.41 : Delays in trigger pulse generation in Q-Sys controller software and camera image exposure pulse. This delay causes measurement position offsets between forward and backward scans.

4.7 Calibration of SHARPeR optical head with test surface tilt

The SHARPeR instrument motion stages were characterized using a standard Michelson interferometer (model HP 5530 Dynamic Calibrator); the results are presented in Appendix 4. The SHARPeR optical head was calibrated for tangential tilt using the same interferometer simultaneously with the RTT RY tilt axis characterization, as shown in Figure 4.42. The interferometer zero position was set to the zero angle of the RY axis. At this position the optical head measured a tangential tilt of 0.82 mrad. In the sagittal direction RX was set to 1 mrad to align the mirror below optical head close to the normal incidence position. In summary, the mirror below optical head measured 0.82 mrad in tangential tilt and 0.003 mrad in sagittal tilt at the start of calibration scans, and the RTT RY measured ~0 mrad and RX measured 1 mrad, and the interferometer is set to 0 mrad in tangential tilt (sagittal tilt is not measured with interferometer).

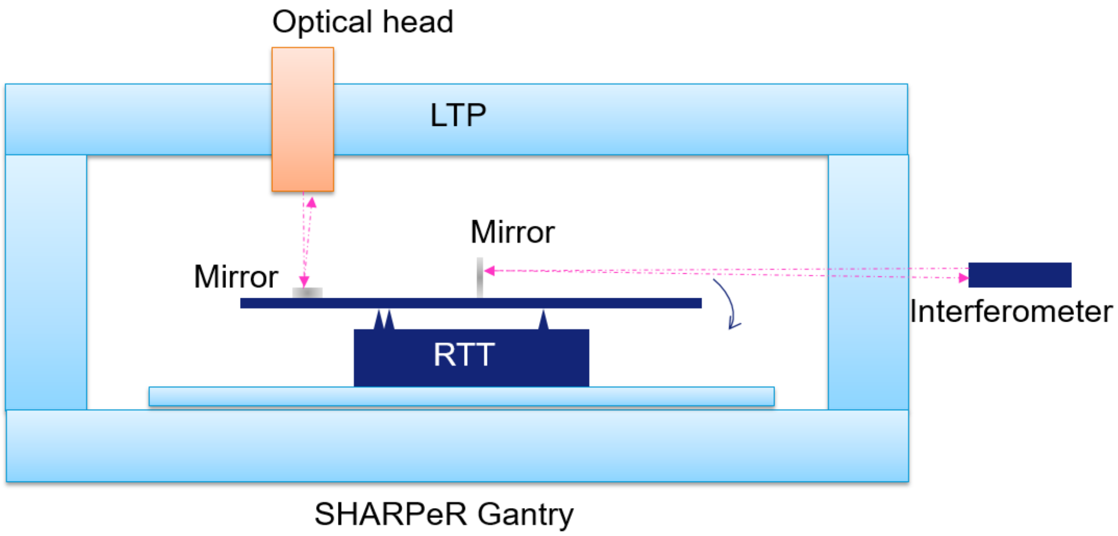

Figure 4.42 : Measurement schematic of SHARPeR optical head calibration for tangential tilt using the interferometer. A double corner cube mirror was placed at the center of RTT as shown in Figure 7.16, and another mirror was placed below optical head as shown here.

The RY axis (tangential) is tilted from -8.7 mrad to 8.7 mrad (-0.5 to 0.5 deg) in steps of 17.45 µrad for 1001 points in three bidirectional scans (forward/backward). The three bidirectional scans are averaged and each microlens tilt is calibrated against the interferometer measured tilt. The Figure 4.43 shows the microlens calibration errors in tangential and sagittal directions for the measured tangential tilt by SHARPeR wavefront sensor. The wavefront sensor has 165 microlenses in total, with the central microlens blackened, to resolve the ambiguities in correlating microlenses to their respective focal spots measured with CCD. Instrument errors such as optical aberrations might be responsible for the large calibration errors shown in Figure 4.43. The linear trend in Figure 4.43 relates to scaling errors, and non-linear errors are from optical aberrations. In Figure 4.43, accuracy refers to peak to valley of calibration errors of all microlenses over the full measurement range, and dispersion refers to peak to valley of deviation of microlens calibration errors from their mean over the full measurement range. HP interferometer has angular accuracy of ± 0.2 % measured value. The errors of SHARPeR optical head are much larger than the RY axis angular errors as shown in Figure 7.17 in Appendix 4.

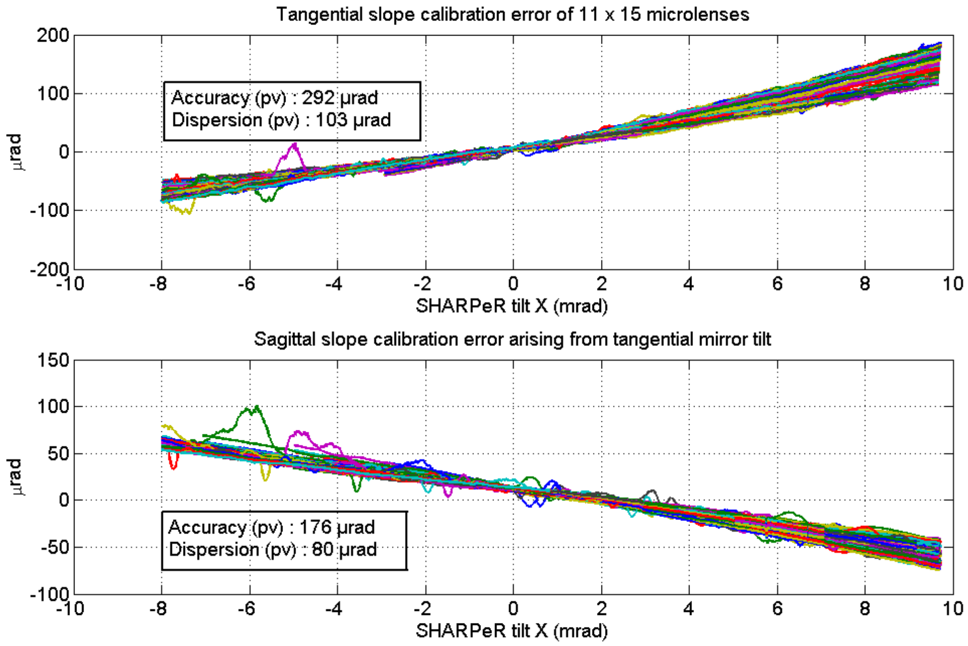

Figure 4.43 : SHARPeR optical head calibration for tangential mirror tilt. SHARPeR wavefront sensor has calibration errors in tangential and sagittal directions. The mirror was tilted from ~ -8 mrad to 9.5 mrad in steps of 17.45 µrad with 1001 points in three bidirectional scans. The error is SHARPeR value minus Interferometer value in tangential direction, and SHARPeR value in sagittal direction.

The accuracy of SHARPeR optical head is 292 µrad in tangential direction and 176 µrad in sagittal direction in peak to valley (sagittal tilt is induced within SHARPeR optical head by tangential RTT tilt). Not all the microlenses measure the same error and the dispersion between them is 103 µrad in tangential direction and 80 µrad in sagittal direction in peak to valley.

4.7.1 Radius of curvature improvements with calibration corrections

The SHARPeR instrument calibration errors, with external interferometer, for different tangential tilts is corrected from the measurement on the spherical mirror presented in section 4.4.2 (radius ~9.3 m). The radius of curvature agrees more closely with other ESRF instrument measurements after applying the calibration correction as shown in

Figure 4.44. The sagittal radius was measured almost same as tangential for the other ESRF instruments (MSI, Fizeau) but SHARPeR measured 9.226 m, which indicates a need to correct with a similar calibration procedure for the sagittal tilts. Only radius of curvature correction is shown here, but SHARPeR tilt calibration can potentially be used for correction of retrace errors in slope error measurements.

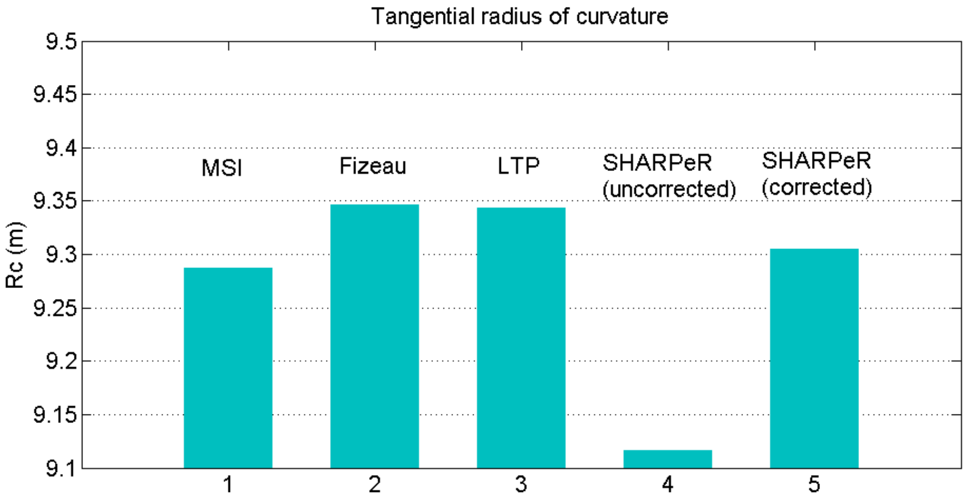

Figure 4.44 : SHARPeR tangential radius of curvature of HZB spherical mirror. The SHARPeR calibration (tangential) is corrected, and compared to uncorrected radius and with other ESRF instruments.

5 CONCLUSIONS

The SHARPeR instrument was designed for the metrology of synchrotron x-ray mirrors to provide a highly accurate 2D surface profiles. It was designed using some of the principles from existing mirror metrology instruments such as LTP, stitching Fizeau interferometry combined to Shack-Hartmann wavefront sensing technology. As such SHARPeR faced some similar problems faced by other instruments like the long-term drifts, reference errors, retrace errors etc. My thesis aimed to characterize, and where possible, solve some of these problems for the SHARPeR instrument. Different solutions were attempted for many of these problems during the three phases: pre-measurement, measurement and post measurement.

Pre-measurement solutions such as retrace error calibration, instrument design optimizations have been developed. In the simplest case instrument systematic errors from optical aberrations are calibrated using a very flat reference mirror, which are by default measured in normal incidence. This method has been extended to calibrate the SHARPeR systematic errors at various incidence angles, which includes retrace errors, on the flat reference mirror. The mirror ‘real’ tilt was measured by a standard Michelson interferometer (model HP 5530 Dynamic Calibrator). It provided a calibration map of SHARPeR systematic errors for all microlenses as a function of tilt, which have been successfully used to improve the accuracy of SHARPER measurements, and a better agreement of radius of curvature (<0.7%) has been observed on spherical mirrors when compared to other instruments. The calibration map was obtained at a tilt step of ~18 µrad which may need to be improved with a finer step. Calibration correction for mirror slope/shape errors also need to be demonstrated, which are usually much smaller typically in sub-micro radian scale and are much more sensitive to calibration inaccuracies. Calibration correction assumes measured slope values have only systematic errors from optical aberrations, and may perform poorly if applied before correcting for other noises such as pseudo random errors from environment.

The SHARPeR instrument has been modified during my thesis to test various environmental noise insulation and isolation schema. In the latest design the optical head has been reconfigured, with the wavefront sensor reoriented (from upward facing to downward facing), to distance the wavefront sensor CCD away from the test mirror and measurement path. The CCD sensor has been a large contributor to thermal fluctuations and air convections, which were influencing test mirror measurements. The new design has shown clear improvement in the measurement accuracy of slope errors with respect to earlier designs on a 1 m long flat mirror. The new design has not completely eliminated environmental noises and may require further interventions such as CCDs with low power consumption; or a better cooling for CCD, which currently uses an extraction fan for cooling. The RTT platform has been another critical component in heat generation and air convections, and current standard measurement schemes disable RTT unless needed, by switching off its motors and rotary air bearings. RTT may need to be improved to minimize heat generation using low power consuming stepper motors, and implementation of cooling mechanisms. The optical head core design has not been modified so far (i.e. the optical elements and relative distances between them are same), and this might be explored further. There is scope for upgrading optical components as the wavefront errors from optical aberrations are quite large (rms ~113 nm) when compared to synchrotron test mirrors of sub nanometer rms shape errors. Retrace errors have been a significant component in the SHARPeR measurement errors on curved mirrors and new designs which can compensate or avoid these errors could be explored (e.g. by Wu et al. [76]).

New measurement techniques such as normal incidence and multi-incidence methods have been developed to address the problem of retrace errors on curved mirrors. Normal incidence methods measure all the mirror subapertures in normal incidence with tilt (tangential & sagittal) applied using RTT, and stitching corrects for the applied tilt between subaperture overlaps. Normal incidence was able to correct retrace errors on highly curved spherical mirrors with very accurate slope/shape errors in comparison to other instruments. Normal incidence methods cannot completely correct for retrace errors on aspheric mirrors where the subapertures are not uniform, and multi-incidence methods have been developed extending from normal incidence methods. Multi-incidence methods measure mirror subapertures in a list of incidences, and ignores all microlens slopes beyond a threshold across all subapertures, which effectively creates uniform subapertures across the mirror. Multi-incidence methods have shown good slope error accuracy on highly curved elliptical mirrors in comparison to other instruments. An advantage with new measurement methods is they use the same mirror for retrace error correction unlike a flat mirror used for creating tilt calibration map. Calibration also ignores the pseudo random errors from environmental changes which can become significant especially if the optical system changes over time (e.g. optics and alignment changes slightly from thermal fluctuations), which gives more credence to retrace error correction with measurement methods. Normal and multi-incidence methods have been implemented only for tangential direction and hence sagittal retrace errors are not corrected, which provides the scope for extending the methods to 2D in future.

Post measurement of test mirror the subaperture images are stitched, and different stitching algorithms (PROG, MO, GO etc.) have been implemented in a new software (PyLOSt). Part or whole of the stitching algorithms have been developed based on the contributions from Francois Polack (SOLEIL), Josep Nicolas (ALBA) and Lei Huang (BNL). The algorithms have been implemented to stitch slope or height data from different instruments (SHARPeR, Zygo Fizeau, Veeco MSI), which can be extended to include more. The stitching algorithms have been studied using synthetic data, which provided the performance as well as limitations of the algorithms. The algorithms are still basic implementation of widely used methods and have scope for development of advanced algorithms especially the reference error retrieval methods.

The thesis has implemented most of the objectives envisioned at the inception however few things still remain, such as development of 2D stitching and analysis of toroidal mirrors which could not be focused on due to limitations of time, and may need to be implemented in the future SHARPeR developments.

Overall SHARPeR is a good instrument to consider by synchrotrons and mirror manufacturers, as one of the very few commercial alternatives to LTPs and NOMs. However, caution may be applied especially by mirror manufacturers as the instrument is still in research and development. In the near future with the integration of research within this thesis and further research, Imagine Optic may make available the production ready SHARPeR for mirror manufacturers. SHARPeR can also be considered as a complementary if not alternative to instruments such as micro stitching interferometers, as they frequently face problems measuring low spatial frequencies where SHARPeR can perform better.

CONCLUSIONS (FRENCH)

L'instrument SHARPeR a été developpé pour fournir des cartographies de surface 2D très précises des miroirs rayons X synchrotron. Cet instrument allie sa technologie de détection de front d'onde Shack-Hartmann à certains principes d’autres instruments de métrologie existants tels que le LTP ou la technique de recollement de vues obtenues par interférométrie Fizeau. Comme eux il est donc confronté à des problèmes tels que les dérives long terme, les erreurs de référence, les erreurs de retour de faisceau (connues sous le terme « retrace error » en anglais), etc... Ma thèse avait pour objectif de caractériser et, si possible, résoudre certains de ces problèmes pour l'instrument SHARPeR. Les solutions proposées et testées interviennent à différents moments des trois étapes qui composent la mesure : avant, pendant et après l’acquisition.

Les solutions pré-acquisition développées incluent une calibration des erreurs de retour de faisceau ou encore une optimisation du design mécanique du système. Une approche simple de l’évaluation des erreurs systématiques dues aux aberrations optiques consiste à mesurer en incidence normale un miroir de référence plan de très haute qualité. Cette méthode a été étendue pour calibrer les erreurs de retour de faisceau du SHARPeR à différents angles d'incidence. L'inclinaison « réelle » du miroir mesurée simultanément par le SHARPeR et par un interféromètre Michelson standard (modèle HP 5530 Dynamic Calibrator) permet d’obtenir un étalonnage des erreurs systématiques pour chacune des microlentilles en fonction de l'angle. Cette calibration a permis d’améliorer la précision des mesures SHARPER et d’obtenir pour les miroirs sphériques un meilleur accord du rayon de courbure (<0,7%) avec celui fourni par d’autres instruments. La procédure pourrait encore être affinée en choisissant un pas angulaire plus petit que les ~ 18 µrad utilisés. Cependant l’efficacité de cet étalonnage sur la précision des erreurs de pente ou de hauteur reste à démontrer. En effet pour les miroirs rayons X, les ordres de grandeur de ces erreurs résiduelles étant inférieurs au microradian ou nanomètre, les résultats peuvent être affectés par la précision de la calibration. Par ailleurs cette correction suppose que les valeurs de pente mesurées ne présentent que des erreurs systématiques dues aux aberrations optiques et peut mal fonctionner si elle est appliquée avant de corriger d'autres sources de bruit telles que les erreurs pseudo-aléatoires de l'environnement.

L'instrument SHARPeR a été modifié au cours de ma thèse pour tester différents schémas d'isolation thermique et de bruit environnemental. Dans le dernier design mécanique de la tête optique, le capteur de front d’onde (CDD) qui contribue largement aux fluctuations d’air par convection thermique, a été éloigné du miroir à mesurer. Cela a permis d’améliorer de façon significative la précision de mesure des erreurs de pente d’un miroir plan de 1m de long comparée au design initial. Malgré sa réduction, le bruit environnemental subsiste et il serait judicieux d’envisager des solutions visant à réduire la dissipation thermique du capteur comme l’utilisation d’un CCD à faible consommation d’énergie ou une amélioration de son système de refroidissement actuellement assuré par un ventilateur d’extraction.

La plateforme RTT a été identifiée comme une autre source de chaleur critique, générant de la convection dans l’environnement de mesure. C’est pourquoi la procédure de mesure standard prévoit d’éteindre quand cela reste possible l’ensemble de ses moteurs ainsi que la rotation sur paliers à air. La dissipation thermique de cette plateforme pourrait également être diminuée en utilisant des moteurs pas à pas à faible consommation d'énergie ou par la mise en œuvre de mécanismes de refroidissement.

La conception optique du SHARPeR inchangée jusqu’à présent (les composants optiques ainsi que leurs distances relatives sont restés identiques au schéma initial) mériterait d’être davantage étudiée. Compte tenu que les erreurs de front d’onde dues aux aberrations optiques sont assez importantes (rms ~ 113 nm) par rapport aux valeurs cibles à mesurer qui sont de l’ordre du nanomètre pour les miroirs rayons X, un remplacement des éléments optiques du système par des composants de meilleure qualité pourrait être envisagé. Par ailleurs les erreurs de retour de faisceau qui sont une composante importante dans le budget des erreurs lors de la mesure de miroirs courbés avec le SHARPeR, pourraient être soit compensées soit évitées par de nouvelles approches conceptuelles (par exemple par Wu et al. [76]).

De nouvelles techniques de mesure telles que les méthodes dites d'incidence normale ou de multi-incidence ont été développées afin de répondre au problème d’erreurs de retour de faisceau inhérent aux mesures de miroirs courbés. Les méthodes d'incidence normale mesurent chaque sous-pupille du miroir en incidence normale, le miroir étant alors incliné dans les 2 directions (tangentielle et sagittale) grâce à la plateforme RTT. Les valeurs d'inclinaison sont alors transmises à l'algorithme de recollement de vue qui applique ces corrections angulaires dans les zones de recouvrement. Cette méthode a permis de minimiser efficacement les erreurs de retour de faisceau et d'améliorer ainsi la précision de mesure pour des miroirs fortement courbés, permettant d'obtenir des profils d'erreur de pente/forme plus proches de ceux obtenus avec d'autres instruments. Cependant cette technique de mesure étant insuffisante pour des miroirs asphériques pour lesquels l'ensemble des sous-pupilles ne présente pas une courbure uniforme, la méthode dite multi-incidence a été développée. Cette technique consiste à mesurer chaque sous-pupille sous différentes inclinaisons dans le sens de la mesure afin de garantir au final pour chacune d'elle une variation angulaire constante. La mesure de miroirs elliptiques fortement courbés par la méthode multi-incidence a donné des résultats d'erreur de pente en bon accord avec les autres instruments. Un des avantages de ces deux méthodes réside dans le fait que les erreurs de retour de faisceau sont corrigées en utilisant le miroir à mesurer et cela pendant la mesure, contrairement à la méthode de calibration qui utilise un miroir de référence plan. De fait la calibration ne prend pas en compte les erreurs pseudo-aléatoires liées à l'environnement qui peuvent être prépondérantes si le système optique évolue au cours du temps (i.e. l'alignement des optiques varie avec les fluctuations thermiques) ce qui rend plus fiable également les méthodes développées. Ces deux méthodes implémentées à ce jour pour corriger les erreurs introduites dans la direction de mesure (tangentielle) pourrait dans le futur être étendues pour minimiser les erreurs dans la direction sagittale dans le cadre d'une mesure par recouvrement dans les 2 directions destinée à fournir une cartographie de surface 2D élargie.

Afin de reconstruire la surface du miroir à partir des images 2D collectées au cours de la phase d'acquisition, différents algorithmes (PROG, MO, GO, etc...) ont été intégrés dans un nouveau logiciel (PyLOst). La plupart de ces codes ont été développés sur la base de contributions de François Polack (SOLEIL), Josep Nicolas (ALBA) et Lei Huang (BNL). Ils permettent de réaliser une reconstruction 2D à partir de données de pente ou de hauteur issues de divers instruments (SHARPeR, Zygo Fizeau, Veeco MSI) dont la liste pourra être étendue. Les différents algorithmes ont été étudiés en traitant des données simulées afin de déterminer leurs performances et limitations respectives. Leur version reste une implémentation basique de méthodes largement utilisées et laisse entrevoir la possibilité de développement plus avancés permettant en particulier d’extraire les erreurs de la référence.

La plupart des objectifs initiaux de la thèse ont été atteints, cependant certains points qui n’ont pu être abordés par manque de temps, comme le développement de la mesure SHARPeR suivant deux directions ou la mesure de surfaces toroïdales, pourront être étudiés dans les futurs développements de l’instrument.

Globalement, le SHARPeR est un bon instrument pouvant être considéré par les synchrotrons et les fabricants de miroirs comme l'une des très rares alternatives commerciales aux LTP et NOM. Cependant, la prudence doit pourtant rester de mise en particulier pour les fabricants de miroirs car l'instrument est toujours en phase de recherche et développement. Dans un future proche, grâce aux travaux réalisés dans le cadre de cette thèse et à des recherches complémentaires, Imagine Optic pourrait fournir une version du SHARPeR pouvant satisfaire les besoins de production des fabricants de miroirs. Le SHARPeR peut également être considéré comme un complément, voire une alternative, aux instruments tels que les micro-interféromètres utilisant la technique du recollement de vues, car ces derniers peuvent rencontrer des problèmes de mesure dans le domaine des basses fréquences spatiales, là où le SHARPeR peut être plus performant.

6 REFERENCES

[1] A. L. Robinson, "History of Synchrotron Radiation," *Synchrotron Radiation News*, vol. 28, no. 4, pp. 4–9, Jul. 2015, doi: 10.1080/08940886.2015.1059228.

[2] R. Talman, *Accelerator X-Ray Sources*. John Wiley & Sons, 2007.

[3] A. Hofmann, "Quasi-monochromatic synchrotron radiation from undulators," *Nuclear Instruments and Methods*, vol. 152, no. 1, pp. 17–21, Jun. 1978, doi: 10.1016/0029-554X(78)90231-8.

[4] D. Attwood, Soft X-Rays and Extreme Ultraviolet Radiation: Principles and Applications, 1st ed. Cambridge University Press, 1999.

[5] "European Synchrotron Radiation Facility (ESRF)." http://www.esrf.fr/ (accessed Feb. 20, 2020).

[6] M. Altarelli, "The European Synchrotron Radiation Facility in Grenoble: A Progress Report," *Physica Scripta*, vol. T34, pp. 73–76, Jan. 1991, doi: 10.1088/0031-8949/1991/T34/010.

[7] A. G. Michette and C. J. Buckley, *X-Ray Science and Technology,*. Taylor & Francis, 1993.

[8] B. L. Henke, E. M. Gullikson, and J. C. Davis, "X-Ray Interactions: Photoabsorption, Scattering, Transmission and Reflection," p. 174.

[9] D. H. Bilderback, "Reflectance Of X-Ray Mirrors From 3.8 To 50 keV (3.3 To 0.25 Å)," in *Reflecting Optics for Synchrotron Radiation*, May 1982, vol. 0315, pp. 90–102, doi: 10.1117/12.932994.

[10] M. S. del Río and R. J. Dejus, "XOP v2.4: recent developments of the x-ray optics software toolkit," in *Advances in Computational Methods for X-Ray Optics II*, Sep. 2011, vol. 8141, p. 814115, doi: 10.1117/12.893911.

[11] J. Susini, "Design parameters for hard x-ray mirrors: the European Synchroton Radiation Facility case," *OE*, vol. 34, no. 2, pp. 361–377, Feb. 1995, doi: 10.1117/12.194835.

[12] T. W. Barbee Jr, "Multilayers for x-ray optics," in *Applications of Thin Film Multilayered Structures to Figured X-Ray Optics*, May 1985, vol. 0563, pp. 2–29, doi: 10.1117/12.949647.

[13] A. Snigirev, V. Kohn, I. Snigireva, and B. Lengeler, "A compound refractive lens for focusing high-energy X-rays," *Nature*, vol. 384, no. 6604, pp. 49–51, Nov. 1996, doi: 10.1038/384049a0.

[14] P. Willmott, An Introduction to Synchrotron Radiation: Techniques and Applications. John Wiley & Sons, 2019.

[15] A. K. Freund *et al.*, “X-ray mirrors for the European Synchrotron Radiation Facility,” *OE*, vol. 29, no. 8, pp. 928–942, Aug. 1990, doi: 10.1117/12.55678.

[16] K. W. Jones, P. Z. Takacs, J. B. Hastings, J. M. Casstevens, and C. D. Pionke, “Fabrication Of An 8:1 Ellipsoidal Mirror For A Synchrotron X-Ray Microprobe,” in *Metrology: Figure and Finish*, Apr. 1987, vol. 0749, pp. 37–45, doi: 10.1117/12.939839.

[17] A. Elliott, “The use of toroidal reflecting surfaces in x-ray diffraction cameras,” *J. Sci. Instrum.*, vol. 42, no. 5, pp. 312–316, May 1965, doi: 10.1088/0950-7671/42/5/302.

[18] P. Kirkpatrick and A. V. Baez, “Formation of Optical Images by X-Rays,” *Journal of the Optical Society of America*, vol. 38, no. 9, p. 766, Sep. 1948, doi: 10.1364/JOSA.38.000766.

[19] H. Wolter, “Spiegelsysteme streifenden Einfalls als abbildende Optiken für Röntgenstrahlen,” *Annalen der Physik*, vol. 445, no. 1–2, pp. 94–114, 1952, doi: 10.1002/andp.19524450108.

[20] J. Susini, D. Labergerie, and L. Zhang, “Compact active/adaptive x-ray mirror: Bimorph piezoelectric flexible mirror,” *Review of Scientific Instruments*, vol. 66, no. 2, pp. 2229–2231, Feb. 1995, doi: 10.1063/1.1145715.

[21] D. Cocco, M. Idir, D. Morton, L. Raimondi, and M. Zangrando, “Advances in X-ray optics: From metrology characterization to wavefront sensing-based optimization of active optics,” *Nuclear Instruments and Methods in Physics Research Section A: Accelerators, Spectrometers, Detectors and Associated Equipment*, Mar. 2018, doi: 10.1016/j.nima.2018.03.026.

[22] J. M. Bennett, “Recent developments in surface roughness characterization,” *Meas. Sci. Technol.*, vol. 3, no. 12, p. 1119, 1992, doi: 10.1088/0957-0233/3/12/001.

[23] K. Becker and E. Heynacher, “M400 - A Coordinate Measuring Machine With 10 nm Resolution,” in *In-Process Optical Metrology for Precision Machining*, Jan. 1987, vol. 0802, pp. 209–216, doi: 10.1117/12.967123.

[24] G. Binnig and H. Rohrer, “Scanning tunneling microscopy—from birth to adolescence,” *Reviews of Modern Physics*, vol. 59, no. 3, pp. 615–625, Jul. 1987, doi: 10.1103/RevModPhys.59.615.

[25] G. Binnig, C. F. Quate, and Ch. Gerber, “Atomic Force Microscope,” *Physical Review Letters*, vol. 56, no. 9, pp. 930–933, Mar. 1986, doi: 10.1103/PhysRevLett.56.930.

[26] V. V. Yashchuk *et al.*, “Cross-check of different techniques for two-dimensional power spectral density measurements of x-ray optics,” in *Advances in Metrology for X-Ray and EUV Optics*, Sep. 2005, vol. 5921, p. 59210G, doi: 10.1117/12.619892.

[27] D. A. Content, P. Arsenovic, I. G. Kuznetsov, and T. Hadjimichael, “Grating groove metrology and efficiency predictions from the soft x-ray to the far infrared,” in *Optical Spectroscopic Techniques, Remote Sensing, and Instrumentation for Atmospheric and Space Research IV*, Jan. 2002, vol. 4485, pp. 405–416, doi: 10.1117/12.454276.

[28] J. M. Elson and J. M. Bennett, “Calculation of the power spectral density from surface profile data,” *Appl. Opt., AO*, vol. 34, no. 1, pp. 201–208, Jan. 1995, doi: 10.1364/AO.34.000201.

[29] F. Siewert, “Slope Error and Surface Roughness,” in *Modern Developments in X-Ray and Neutron Optics*, A. Erko, D. M. Idir, D. T. Krist, and P. A. G. Michette, Eds. Springer Berlin Heidelberg, 2008, pp. 175–179.

[30] L. Assoufid *et al.*, “Results of x-ray mirror round-robin metrology measurements at the APS, ESRF, and SPring-8 optical metrology laboratories,” in *Proceedings of SPIE*, San Diego, CA, USA, 2005, vol. 5921, pp. 59210J-59210J–12, doi: 10.1117/12.623209.

[31] A. Rommeveaux, M. Thomasset, D. Cocco, and F. Siewert, “First report on a European round robin for slope measuring profilers,” in *Advances in Metrology for X-Ray and EUV Optics*, Sep. 2005, vol. 5921, p. 59210I, doi: 10.1117/12.621087.

[32] I. BiPM, I. IFCC, I. IUPAC, and O. ISO, “The international vocabulary of metrology—basic and general concepts and associated terms (VIM),” *JCGM*, vol. 200, 2012, [Online]. Available: https://www.bipm.org/utils/common/documents/jcgm/JCGM_200_2012.pdf.

[33] B. Davies, “Precision and accuracy in glacial geology,” *AntarcticGlaciers.org*. http://www.antarcticglaciers.org/glacial-geology/dating-glacial-sediments-2/precision-and-accuracy-glacial-geology/ (accessed Feb. 25, 2020).

[34] A. Rommeveaux, M. Thomasset, and D. Cocco, “The Long Trace Profilers,” in *Modern Developments in X-Ray and Neutron Optics*, A. Erko, M. Idir, T. Krist, and A. G. Michette, Eds. Berlin, Heidelberg: Springer Berlin Heidelberg, 2008, pp. 181–191.

[35] K. von Bieren, “Pencil Beam Interferometer For Aspherical Optical Surfaces,” in *Laser Diagnostics*, Nov. 1982, vol. 0343, pp. 101–108, doi: 10.1117/12.933743.

[36] A. Rommeveaux, O. Hignette, and C. Morawe, “Mirror metrology and bender characterization at ESRF,” presented at the Advances in Metrology for X-Ray and EUV Optics, Sep. 2005, vol. 5921, p. 59210N, doi: 10.1117/12.621379.

[37] A. Erko, M. Idir, T. Krist, and A. G. Michette, Eds., *Modern developments in X-ray and neutron optics*. Berlin: Springer, 2008.

[38] A. Vivo, R. Barrett, and F. Perrin, “Stitching techniques for measuring X-ray synchrotron mirror topography,” *Review of Scientific Instruments*, vol. 90, no. 2, p. 021710, Feb. 2019, doi: 10.1063/1.5063339.

[39] V. V. Yashchuk *et al.*, “Investigation on lateral resolution of surface slope profilers,” in *Advances in Metrology for X-Ray and EUV Optics VIII*, Sep. 2019, vol. 11109, p. 111090M, doi: 10.1117/12.2539527.

[40] V. V. Yashchuk et al., “Sub-microradian surface slope metrology with the ALS Developmental Long Trace Profiler,” Nuclear Instruments and Methods in Physics Research Section A: Accelerators, Spectrometers, Detectors and Associated Equipment, vol. 616, no. 2, pp. 212–223, May 2010, doi: 10.1016/j.nima.2009.10.175.

[41] M. Thomasset and F. Polack, “Characterization of optical surfaces for the present generations of synchrotron sources,” in *Ninth International Symposium on Laser Metrology*, Oct. 2008, vol. 7155, p. 715506, doi: 10.1117/12.814695.

[42] Y. Senba, H. Kishimoto, T. Miura, and H. Ohashi, “Development of a long trace profiler at SPring-8 using a newly developed slope sensor,” in *Advances in Metrology for X-Ray and EUV Optics VI*, Sep. 2016, vol. 9962, p. 996204, doi: 10.1117/12.2239394.

[43] M. L. Ng, J. Nicolas, D. Spiga, C. L. Hardin, D. S. Morton, and D. Cocco, “Development of the new long trace profilometer at LCLS for bendable x-ray mirror metrology,” in *Adaptive X-Ray Optics V*, Oct. 2018, vol. 10761, p. 1076106, doi: 10.1117/12.2323293.

[44] S. M. Nikitin, G. S. Gevorkyan, W. R. McKinney, I. Lacey, P. Z. Takacs, and V. V. Yashchuk, “New twist in the optical schematic of surface slope measuring long trace profiler,” in *Advances in Metrology for X-Ray and EUV Optics VII*, Sep. 2017, vol. 10385, p. 103850I, doi: 10.1117/12.2274400.

[45] A. V. Rommeveaux, B. Lantelme, and R. Barrett, “ESRF metrology laboratory: overview of instrumentation, measurement techniques, and data analysis,” in *Advances in Metrology for X-Ray and EUV Optics III*, Aug. 2010, vol. 7801, p. 780107, doi: 10.1117/12.864141.

[46] V. V. Yashchuk, N. A. Artemiev, I. Lacey, W. R. McKinney, and H. A. Padmore, “Advanced environmental control as a key component in the development of ultrahigh accuracy ex situ metrology for x-ray optics,” *OE*, vol. 54, no. 10, p. 104104, Oct. 2015, doi: 10.1117/1.OE.54.10.104104.

[47] F. Siewert, T. Noll, T. Schlegel, T. Zeschke, and H. Lammert, “The Nanometer Optical Component Measuring Machine: a new Sub-nm Topography Measuring Device for X-ray Optics at BESSY,” *AIP Conference Proceedings*, vol. 705, no. 1, pp. 847–850, May 2004, doi: 10.1063/1.1757928.

[48] F. Siewert, J. Buchheim, T. Höft, T. Zeschke, A. Schindler, and T. Arnold, “Investigations on the spatial resolution of autocollimator-based slope measuring profilers,” *Nuclear Instruments and Methods in Physics Research Section A: Accelerators, Spectrometers, Detectors and Associated Equipment*, vol. 710, pp. 42–47, May 2013, doi: 10.1016/j.nima.2012.10.130.

[49] F. Siewert, J. Buchheim, G. Gwalt, R. Bean, and A. P. Mancuso, “On the characterization of a 1 m long, ultra-precise KB-focusing mirror pair for European XFEL by means of slope measuring deflectometry,” *Review of Scientific Instruments*, vol. IWXM2019, no. 1, p. 021713, Feb. 2019, doi: 10.1063/1.5065473@rsi.2019.IWXM2019.issue-1.

[50] S. G. Alcock, I. Nistea, and K. Sawhney, “Nano-metrology: The art of measuring X-ray mirrors with slope errors <100 nrad,” *Review of Scientific Instruments*, vol. 87, no. 5, p. 051902, May 2016, doi: 10.1063/1.4949272.

[51] F. Siewert, J. Buchheim, and T. Zeschke, “Characterization and calibration of 2nd generation slope measuring profiler,” *Nuclear Instruments and Methods in Physics Research Section A: Accelerators, Spectrometers, Detectors and Associated*

Equipment, vol. 616, no. 2, pp. 119–127, May 2010, doi: 10.1016/j.nima.2009.12.033.

[52] J. Nicolas, P. Pedreira, I. Šics, C. Ramírez, and J. Campos, “Nanometer accuracy with continuous scans at the ALBA-NOM,” in *Advances in Metrology for X-Ray and EUV Optics VI*, Sep. 2016, vol. 9962, p. 996203, doi: 10.1117/12.2238128.

[53] S. D. Jacobs, “International innovations in optical finishing,” in *Current Developments in Lens Design and Optical Engineering V*, Oct. 2004, vol. 5523, pp. 264–272, doi: 10.1117/12.557274.

[54] S. G. Alcock *et al.*, “The Diamond-NOM: A non-contact profiler capable of characterizing optical figure error with sub-nanometre repeatability,” *Nuclear Instruments and Methods in Physics Research Section A: Accelerators, Spectrometers, Detectors and Associated Equipment*, vol. 616, no. 2, pp. 224–228, May 2010, doi: 10.1016/j.nima.2009.10.137.

[55] D. Malacara, *Optical Shop Testing*. John Wiley & Sons, 2007.

[56] G. D. Ludbrook, S. G. Alcock, and K. J. S. Sawhney, “A Fizeau interferometer system with double-pass and stitching for characterizing the figure error of large (>1m) synchrotron optics,” in *Optical Measurement Systems for Industrial Inspection VI*, Jun. 2009, vol. 7389, p. 738939, doi: 10.1117/12.827865.

[57] M. Vannoni and I. F. Martín, “Metrological characterization of a large aperture Fizeau for x-ray mirrors measurement,” in *Modeling Aspects in Optical Metrology V*, Jun. 2015, vol. 9526, p. 95260A, doi: 10.1117/12.2184748.

[58] M. Vannoni and I. F. Martìn, “Surface measurements in ‘grazing incidence’ interferometry for long x-ray mirrors: theoretical limits and practical implementations,” in *Advances in Metrology for X-Ray and EUV Optics VI*, Sep. 2016, vol. 9962, p. 996207, doi: 10.1117/12.2238623.

[59] H. Yumoto, S. Matsuyama, H. Mimura, K. Yamauchi, and H. Ohashi, “Absolute calibration of optical flats using the three-flat test by considering the relative humidity change,” *Nuclear Instruments and Methods in Physics Research Section A: Accelerators, Spectrometers, Detectors and Associated Equipment*, vol. 710, pp. 2–6, May 2013, doi: 10.1016/j.nima.2012.10.126.

[60] “Interferometer System - Verifire^{TM} HDX.” https://www.zygo.com/?/met/interferometers/verifire/hdx/ (accessed Apr. 06, 2020).

[61] “The Wyko Surface Optical Profiler Heritage of Bruker’s 3D Optical Microscopes,” *Bruker.com*. https://www.bruker.com/products/surface-and-dimensional-analysis/3d-optical-microscopes/wyko-veeco-history.html (accessed Apr. 06, 2020).

[62] Y. J. Fan, “Stitching interferometry: principles and algorithms,” in *17th Congress of the International Commission for Optics: Optics for Science and New Technology*, Sep. 1996, vol. 2778, p. 2778ED, doi: 10.1117/12.2316206.

[63] M. Bray, “Stitching interferometry: how and why it works,” in *Optical Fabrication and Testing*, Sep. 1999, vol. 3739, pp. 259–274, doi: 10.1117/12.360153.

[64] K. Yamauchi *et al.*, “Microstitching interferometry for x-ray reflective optics,” *Review of Scientific Instruments*, vol. 74, no. 5, pp. 2894–2898, Apr. 2003, doi: 10.1063/1.1569405.

[65] H. Mimura *et al.*, “Relative angle determinable stitching interferometry for hard x-ray reflective optics,” *Review of Scientific Instruments*, vol. 76, no. 4, p. 045102, Mar. 2005, doi: 10.1063/1.1868472.

[66] A. Vivo and R. Barrett, “Fizeau stitching at the European Synchrotron Radiation Facility (ESRF),” presented at the Advances in Metrology for X-Ray and EUV Optics VII, Sep. 2017, vol. 10385, p. 103850N, doi: 10.1117/12.2274745.

[67] A. Rommeveaux and R. Barrett, “Micro-stitching interferometry at the ESRF,” *Nuclear Instruments and Methods in Physics Research Section A: Accelerators, Spectrometers, Detectors and Associated Equipment*, vol. 616, no. 2, pp. 183–187, May 2010, doi: 10.1016/j.nima.2009.11.020.

[68] F. Polack, M. Thomasset, S. Brochet, and A. Rommeveaux, “An LTP stitching procedure with compensation of instrument errors: Comparison of SOLEIL and ESRF results on strongly curved mirrors,” *Nuclear Instruments and Methods in Physics Research Section A: Accelerators, Spectrometers, Detectors and Associated Equipment*, vol. 616, no. 2, pp. 207–211, May 2010, doi: 10.1016/j.nima.2009.10.166.

[69] B. Schramm, “JRA1 - Metrology On One-Nanometer-Precise Optics (MooNpics),” *CALIPSOplus*. http://www.calipsoplus.eu/joint-research-activities-jra/jra1-moonpics/ (accessed Feb. 19, 2020).

[70] I.-T. Nistea, S. G. Alcock, M. B. da Silva, and K. Sawhney, “The Optical Metrology Laboratory at Diamond: pushing the limits of nano-metrology,” in *Advances in Metrology for X-Ray and EUV Optics VIII*, Sep. 2019, vol. 11109, p. 1110906, doi: 10.1117/12.2529401.

[71] J. Floriot *et al.*, “Surface metrology with a stitching Shack-Hartmann profilometric head,” in *Optical Measurement Systems for Industrial Inspection V*, Jun. 2007, vol. 6616, p. 66162A, doi: 10.1117/12.726058.

[72] M. Idir, K. Kaznatcheev, G. Dovillaire, J. Legrand, and R. Rungsawang, “A 2 D high accuracy slope measuring system based on a Stitching Shack Hartmann Optical Head,” *Opt. Express, OE*, vol. 22, no. 3, pp. 2770–2781, Feb. 2014, doi: 10.1364/OE.22.002770.

[73] A. Vivo, “Personal communication with Amparo Vivo.”

[74] M. R. Howells and D. L. Lunt, “Design considerations for adjustable-curvature, high-power, x-ray mirrors based on elastic bending,” *OE*, vol. 32, no. 8, pp. 1981–1989, Aug. 1993, doi: 10.1117/12.146391.

[75] R. Leach and C. Giusca, “Calibration of Optical Surface Topography Measuring Instruments,” in *Optical Measurement of Surface Topography*, R. Leach, Ed. Berlin, Heidelberg: Springer, 2011, pp. 49–70.

[76] Y. Wu, M. K. Sharma, and A. Veeraraghavan, “WISH: wavefront imaging sensor with high resolution,” *Light: Science & Applications*, vol. 8, no. 1, pp. 1–10, May 2019, doi: 10.1038/s41377-019-0154-x.

[77] T. Su, A. Maldonado, P. Su, and J. H. Burge, “Instrument transfer function of slope measuring deflectometry systems,” *Applied Optics*, vol. 54, no. 10, p. 2981, Apr. 2015, doi: 10.1364/AO.54.002981.

[78] S. Bará, “Measuring eye aberrations with Hartmann–Shack wave-front sensors: Should the irradiance distribution across the eye pupil be taken into account?,” *Journal of the Optical Society of America A*, vol. 20, no. 12, p. 2237, Dec. 2003, doi: 10.1364/JOSAA.20.002237.

[79] BiPM, I. E. C., I. IFCC, I. IUPAC, and O. ISO, “The international vocabulary of metrology—basic and general concepts and associated terms (VIM).” JCGM 200:2012, Accessed: Aug. 07, 2019. [Online]. Available: https://www.bipm.org/en/publications/guides/vim.html.

[80] W. Jiang, H. Xian, and F. Shen, “Detection error of Shack-Hartmann wavefront sensor,” in *Adaptive Optics and Applications*, Oct. 1997, vol. 3126, pp. 534–544, doi: 10.1117/12.279060.

[81] G. Cao and X. Yu, “Accuracy analysis of a Hartmann-Shack wavefront sensor operated with a faint object,” *OE*, vol. 33, no. 7, pp. 2331–2336, Jul. 1994, doi: 10.1117/12.169716.

[82] J. S. Morgan, D. C. Slater, J. G. Timothy, and E. B. Jenkins, “Centroid position measurements and subpixel sensitivity variations with the MAMA detector,” *Appl. Opt., AO*, vol. 28, no. 6, pp. 1178–1192, Mar. 1989, doi: 10.1364/AO.28.001178.

[83] J. Pfund, N. Lindlein, and J. Schwider, “Misalignment effects of the Shack–Hartmann sensor,” *Appl. Opt., AO*, vol. 37, no. 1, pp. 22–27, Jan. 1998, doi: 10.1364/AO.37.000022.

[84] D. R. Neal, J. Copland, and D. A. Neal, “Shack-Hartmann wavefront sensor precision and accuracy,” in *Advanced Characterization Techniques for Optical, Semiconductor, and Data Storage Components*, Nov. 2002, vol. 4779, pp. 148–161, doi: 10.1117/12.450850.

[85] S. Thomas, T. Fusco, A. Tokovinin, M. Nicolle, V. Michau, and G. Rousset, “Comparison of centroid computation algorithms in a Shack–Hartmann sensor,” *Mon Not R Astron Soc*, vol. 371, no. 1, pp. 323–336, Sep. 2006, doi: 10.1111/j.1365-2966.2006.10661.x.

[86] C. B. Kreischer, “Retrace error: interferometry’s dark little secret,” in *Optifab 2013*, Oct. 2013, vol. 8884, p. 88840X, doi: 10.1117/12.2029324.

[87] I. Lacey *et al.*, “The ALS OSMS: Optical Surface Measuring System for high accuracy two-dimensional slope metrology with state-of-the-art x-ray mirrors,” in *Advances in X-Ray/EUV Optics and Components XIII*, Sep. 2018, vol. 10760, p. 1076002, doi: 10.1117/12.2321347.

[88] L. Assoufid, O. Hignette, M. Howells, S. Irick, H. Lammert, and P. Takacs, “Future metrology needs for synchrotron radiation grazing-incidence optics,” *Nuclear Instruments and Methods in Physics Research Section A: Accelerators, Spectrometers, Detectors and Associated Equipment*, vol. 467–468, pp. 267–270, Jul. 2001, doi: 10.1016/S0168-9002(01)00296-0.

[89] P. Z. Takacs, E. L. Church, C. J. Bresloff, and L. Assoufid, “Improvements in the accuracy and the repeatability of long trace profiler measurements,” *Applied Optics*, vol. 38, no. 25, p. 5468, Sep. 1999, doi: 10.1364/AO.38.005468.

[90] R. D. Geckeler *et al.*, “Environmental influences on autocollimator-based angle and form metrology,” *Review of Scientific Instruments*, vol. 90, no. 2, p. 021705, Feb. 2019, doi: 10.1063/1.5057402.

[91] M. L. Wesely, “The Combined Effect of Temperature and Humidity Fluctuations on Refractive Index,” *J. Appl. Meteor.*, vol. 15, no. 1, pp. 43–49, Jan. 1976, doi: 10.1175/1520-0450(1976)015<0043:TCEOTA>2.0.CO;2.

[92] P. H. Richter, “Estimating errors in least-squares fitting,” *The Telecommunications and Data Acquisition Report*, p. p 107-137, Aug. 1995.

[93] P. Murphy, J. Fleig, G. Forbes, D. Miladinovic, G. DeVries, and S. O’Donohue, “Subaperture stitching interferometry for testing mild aspheres,” in *Interferometry XIII: Applications*, Aug. 2006, vol. 6293, p. 62930J, doi: 10.1117/12.680473.

[94] S. C. Irick, “Error reduction techniques for measuring long synchrotron mirrors,” presented at the SPIE’s International Symposium on Optical Science, Engineering, and Instrumentation, San Diego, CA, Nov. 1998, pp. 101–108, doi: 10.1117/12.331122.

[95] L. Huang *et al.*, “Stitching interferometry for synchrotron mirror metrology at National Synchrotron Light Source II (NSLS-II),” *Optics and Lasers in Engineering*, vol. 124, p. 105795, Jan. 2020, doi: 10.1016/j.optlaseng.2019.105795.

[96] C. Zhao, R. A. Sprowl, M. Bray, and J. H. Burge, “Figure measurement of a large optical flat with a Fizeau interferometer and stitching technique,” in *Interferometry XIII: Applications*, Aug. 2006, vol. 6293, p. 62930K, doi: 10.1117/12.681234.

[97] W. H. Southwell, “Wave-front estimation from wave-front slope measurements,” *J. Opt. Soc. Am., JOSA*, vol. 70, no. 8, pp. 998–1006, Aug. 1980, doi: 10.1364/JOSA.70.000998.

[98] Zygo corporation, MetroPro Reference Guide version 9.0. 2011.

[99] “Zygo Corporation.” https://www.zygo.com/ (accessed Mar. 23, 2020).

[100] “Vision64 Map Software,” *Bruker.com*. https://www.bruker.com/products/surface-and-dimensional-analysis/3d-optical-microscopes/surface-optical-metrology-accessories/vision64-map-software.html (accessed Mar. 23, 2020).

[101] J.-H. Mun and Y.-S. Ho, “Panorama Image Stitching based on ‘SIFT’ Feature Points,” p. 2.

[102] M. Bray, “Stitching interferometer for large plano optics using a standard interferometer,” *Proc. SPIE*, vol. 3134, no. 1, pp. 39–50, Nov. 1997, doi: doi:10.1117/12.295153.

[103] A. Vivo, B. Lantelme, R. Baker, and R. Barrett, “Stitching methods at the European Synchrotron Radiation Facility (ESRF),” *Rev. Sci. Instrum.*, vol. 87, no. 5, p. 051908, May 2016, doi: 10.1063/1.4950745.

[104] L. Assoufid, M. Bray, J. Qian, and D. Shu, “3D surface profile measurements of large x-ray synchrotron radiation mirrors using stitching interferometry,” presented at the International Symposium on Optical Science and Technology, Seattle, WA, Dec. 2002, p. 21, doi: 10.1117/12.454816.

[105] L. Huang, M. Idir, C. Zuo, T. Wang, K. Tayabaly, and E. Lippmann, “Two-dimensional stitching interferometry based on tilt measurement,” *Optics Express*, vol. 26, no. 18, p. 23278, Sep. 2018, doi: 10.1364/OE.26.023278.

[106] J. Nicolas, M. L. Ng, P. Pedreira, J. Campos, and D. Cocco, “Completeness condition for unambiguous profile reconstruction by sub-aperture stitching,” *Opt. Express, OE*, vol. 26, no. 21, pp. 27212–27220, Oct. 2018, doi: 10.1364/OE.26.027212.

[107] F. Polack and M. Thomasset, “Determination and compensation of the ‘reference surface’ from redundant sets of surface measurements,” *Nuclear Instruments and Methods in Physics Research Section A: Accelerators, Spectrometers, Detectors and Associated Equipment*, vol. 710, pp. 67–71, May 2013, doi: 10.1016/j.nima.2012.10.134.

[108] F. Polack, M. Thomasset, S. Brochet, and D. Dennetiere, “Surface shape determination with a stitching Michelson interferometer and accuracy evaluation,” *Review of Scientific Instruments*, vol. 90, no. 2, p. 021708, Feb. 2019, doi: 10.1063/1.5061930.

[109] L. Huang *et al.*, “Two-dimensional stitching interferometry for self-calibration of high-order additive systematic errors,” *Opt. Express*, vol. 27, no. 19, pp. 26940–26956, Sep. 2019, doi: 10.1364/OE.27.026940.

[110] “numpy.linalg.pinv — NumPy v1.18 Manual.” https://numpy.org/doc/stable/reference/generated/numpy.linalg.pinv.html?highlight=pinv#numpy.linalg.pinv (accessed Apr. 22, 2020).

[111] I. Dokmanić and R. Gribonval, “Beyond Moore-Penrose Part I: Generalized Inverses that Minimize Matrix Norms,” p. 43.

[112] “scipy.sparse.linalg.spsolve — SciPy v0.14.0 Reference Guide.” https://docs.scipy.org/doc/scipy-0.14.0/reference/generated/scipy.sparse.linalg.spsolve.html (accessed Apr. 22, 2020).

[113] “scipy.optimize.least_squares — SciPy v1.4.1 Reference Guide.” https://docs.scipy.org/doc/scipy/reference/generated/scipy.optimize.least_squares.html (accessed Apr. 22, 2020).

[114] G. S. Gevorkyan, G. Centers, K. S. Polonska, S. M. Nikitin, I. Lacey, and V. V. Yashchuk, “Surface slope metrology of highly curved x-ray optics with an interferometric microscope,” in *Advances in Metrology for X-Ray and EUV Optics VII*, Sep. 2017, vol. 10385, p. 103850H, doi: 10.1117/12.2274220.

[115] “Python 3.0 Release,” *Python.org*. https://www.python.org/download/releases/3.0/ (accessed Apr. 22, 2020).

[116] “PyQt5 Reference Guide — PyQt v5.14.0 Reference Guide.” https://www.riverbankcomputing.com/static/Docs/PyQt5/ (accessed Apr. 22, 2020).

[117] “PyQt5 tutorial 2020: Create a GUI with Python and Qt.” https://build-system.fman.io/pyqt5-tutorial (accessed Apr. 22, 2020).

[118] “The HDF Group - ensuring long-term access and usability of HDF data and supporting users of HDF technologies,” *The HDF Group*. https://www.hdfgroup.org/ (accessed Feb. 11, 2020).

[119] M. Könnecke *et al.*, “The NeXus data format,” *J Appl Crystallogr*, vol. 48, no. 1, pp. 301–305, Feb. 2015, doi: 10.1107/S1600576714027575.

[120] “Overview — silx 0.12.0 documentation.” http://www.silx.org/doc/silx/latest/overview.html (accessed Apr. 22, 2020).

[121] “High-precision X-ray mirror | J-tec corporation.” https://www.j-tec.co.jp/english/optical/high-precision-x-ray-mirror/ (accessed Feb. 20, 2020).

[122] R. T. Frankot and R. Chellappa, “A Method for Enforcing Integrability in Shape from Shading Algorithms,” *IEEE Trans. Pattern Anal. Mach. Intell.*, vol. 10, pp. 439–451, 1988, doi: 10.1109/34.3909.

[123] I. BIPM, I. IFCC, I. ISO, and O. IUPAP, “Evaluation of measurement data—guide to the expression of uncertainty in measurement, JCGM 100: 2008 GUM 1995 with minor corrections,” *Joint Committee for Guides in Metrology*, 2008, [Online]. Available: https://www.bipm.org/utils/common/documents/jcgm/JCGM_100_2008_E.pdf.

[124] G. Sostero, D. Cocco, and S. Qian, “Metrological challenges of synchrotron radiation optics,” in *Optical Fabrication and Testing*, Sep. 1999, vol. 3739, pp. 310–316, doi: 10.1117/12.360158.

[125] “Synchrotron Optics.” https://www.zeiss.com/semiconductor-manufacturing-technology/products-solutions/semiconductor-manufacturing-optics/synchrotron-optics.html (accessed Feb. 20, 2020).

[126] J. W. Goodman, *Introduction to Fourier Optics*. Roberts and Company Publishers, 2005.

[127] V. N. Mahajan, Optical Imaging and Aberrations: Ray geometrical optics. SPIE Press, 1998.

[128] “KODAK KAI-08050 image sensor performance specification.” Kodak Image Sensor Solutions, Oct. 12, 2009.

7 APPENDICES

APPENDIX 1: MICROLENS THEORETICAL FRAMEWORK

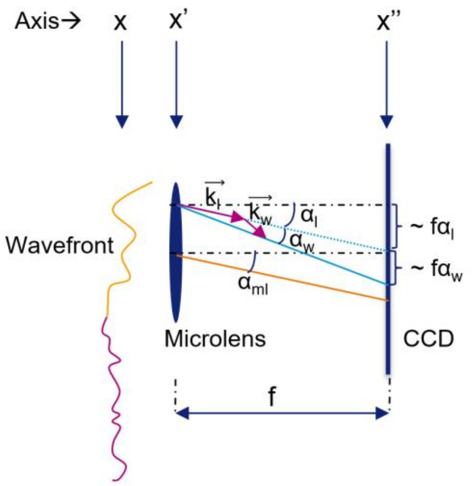

Figure 7.1 : The schematic of microlens wavefront measurement.

In this section, microlens theoretical framework is used to express the centroiding method of the CCD plane within the microlens plane, such that microlens measured wavefront slope may be explained in its relation to the instantaneous slopes of the wavefront. A schematic diagram of an ideal microlens as presented in Figure 7.1, which is used to demonstrate the theoretical framework of wavefront sensing. The wavefront incident on the microlens array contains the mirror height information in its phase (neglecting any phase perturbations due to instrumental or environmental effects). The microlens field function (u_l) together with the incident wavefront field (u_w) contribute to image shape at the focal plane measured by the CCD, with field given by u_f. The image formation can be described by Fresnel propagation with thin lens approximation as explained in equations below. The Fresnel diffraction equation and lens field equation are taken from 'Introduction to Fourier Optics' by Joseph W. Goodman in chapters 4.2 and 6.1 [126]. The coordinates in the microlens plane are represented by the x' axis and the focal plane by the x'' axis. The field amplitude is represented by A and the phase by ϕ in general. The wavenumber is k, the wave vector at a position x' is $\vec{k}(x')$ and corresponding angles in ray tracing formalism as $\alpha(x')$ as shown in Figure 7.1, where the total wavevector is sum of lens and mirror wavefront wavevectors.

The field functions of incoming wavefront (u_w) and microlens (u_l) are expressed in general as follows.

$$u_l(x') = A_l(x')\exp\left(-i\varphi_l(x')\right)$$

$$u_w(x') = A_w(x')\exp\left(-i\varphi_w(x')\right)$$

(7-1)

The microlens phase is quadratic term given as below, with f representing the focal length of microlens.

$$\varphi_l(x') = \frac{k}{2f}x'^2$$

(7-2)

The wavevectors for lens phase ($\overrightarrow{k_l}(x')$) and input wavefront phase ($\overrightarrow{k_w}(x')$) can be expressed as below.

$$\overrightarrow{k_l}(x') = \frac{d\varphi_l(x')}{dx'} = k\frac{x'}{f} = k\ \alpha_l(x')$$

$$\overrightarrow{k_w}(x') = \frac{d\varphi_w(x')}{dx'} = k\ \alpha_w(x')$$

(7-3)

The field at CCD ($u_f(x'')$) can be expressed as a Fresnel propagation of field after microlens ($u_l(x')u_w(x')$) as shown below.

$$u_f(x'') = \frac{\exp(ikf)}{ikf} \int_{-\infty}^{\infty} u_l(x')u_w(x') \exp\left(\frac{ik}{2f}(x'' - x')^2\right) dx'$$

$$u_f(x'') = \frac{\exp(ikf)}{ikf} \int_{-\infty}^{\infty} w(x') \exp\left(-i\varphi_l(x') + \frac{ik}{2f}(x'' - x')^2\right) dx'$$

(7-4)

Where the function $w(x')$ is given by,

$$w(x') = A_l(x')A_w(x') \exp(-i\varphi_w(x'))$$

Substituting lens phase from eq.7-2 and ignoring the constant phase term $\exp(ikf)$,

$$u_f(x'') = \frac{\exp(ikf)}{ikf} \int_{-\infty}^{\infty} w(x') \exp\left(-\frac{ik}{2f}x'^2 + \frac{ik}{2f}(x''^2 + x'^2 - 2x'x'')\right) dx'$$

$$u_f(x'') = \frac{\exp\left(\frac{ik}{2f}x''^2\right)}{ikf} \int_{-\infty}^{\infty} w(x') \exp\left(-\frac{ik}{f}x'x''\right) dx'$$

(7-5)

The equation above is a Fourier transform of *w(x')* in focal plane, with a phase factor as given below.

$$u_f(x'') = \frac{\exp\left(\frac{ik}{2f}x''^2\right)}{ikf} W(x'')$$

(7-6)

The phase of wavefront just before microlens contains the height information of mirror and its derivative contains the mirror slopes. In the SHARPeR instrument, in addition to mirror heights, the phase also has errors from the optical aberrations. The eq.7-3 shows the relation between the mirror slopes and angular deviations *α(x')* after the microlens.

The centroiding of x-position in the CCD image is given by,

$$x''_{ml} = \frac{\int_{-\infty}^{\infty} x'' I_f(x'')dx''}{\int_{-\infty}^{\infty} I_f(x'')dx''}$$

(7-7)

The intensity can be represented by field function ($W(x'')$) multiplied by its complex conjugate from eq.7-6 (quadratic phase $\exp\left(\frac{ik}{2f}x''^2\right)$ is cancelled by complex conjugate multiplication). The denominator in eq. (7-7) can be expressed as follows.

$$\int_{-\infty}^{\infty} I_f(x'')dx'' = \int_{-\infty}^{\infty} W(x'')W^*(x'')\, dx'' = \int_{-\infty}^{\infty} w(x')w^*(x')dx'$$

$$\int_{-\infty}^{\infty} I_f(x'')dx'' = \int_{-\infty}^{\infty} I_f(x')dx'$$

(7-8)

The above equation implies total intensity is same in the microlens plane and CCD plane, which is a restatement of Parseval's identity. The numerator in eq.7-7 can be expressed as follows, using the Fourier transform relation $x''W(x'') \leftrightarrow -\frac{if}{k}\frac{dw(x')}{dx'}$.

$$\int_{-\infty}^{\infty} x'' I_f(x'')dx'' = \int_{-\infty}^{\infty} x'' W(x'')W^*(x'')\, dx'' = -\frac{if}{k}\int_{-\infty}^{\infty} \frac{dw(x')}{dx'} w^*(x')dx'$$

(7-9)

$$\frac{dw(x')}{dx'} = \frac{d\big(A_l(x')A_w(x')\big)}{dx'} \exp\big(-i\varphi_w(x')\big) - i\frac{d\varphi_w(x')}{dx'}\, w(x')$$

(7-10)

If the intensity variation is low the first term in in eq.7-10 can be ignored. Using equations 7-3 and 7-10 in eq.(7-9),

$$\int_{-\infty}^{\infty} x'' I_f(x'')dx'' = -\frac{if}{k}\int_{-\infty}^{\infty} -ik\alpha_w(x')\, w(x')w^*(x')dx'$$

$$\int_{-\infty}^{\infty} x'' I_f(x'')dx'' = -f\int_{-\infty}^{\infty} \alpha_w(x')\, I(x')dx'$$

$$x''_{ml} = < x'' > = -f < \alpha_w(x') > = -f\alpha_{ml}$$

(7-11)

Thus, the centroid determination by the CCD intensity images can be reinterpreted at the microlens plane, in terms weighted intensity average of mirror wavefront slopes, within the microlens size.

APPENDIX 2: DEFOCUS ERRORS

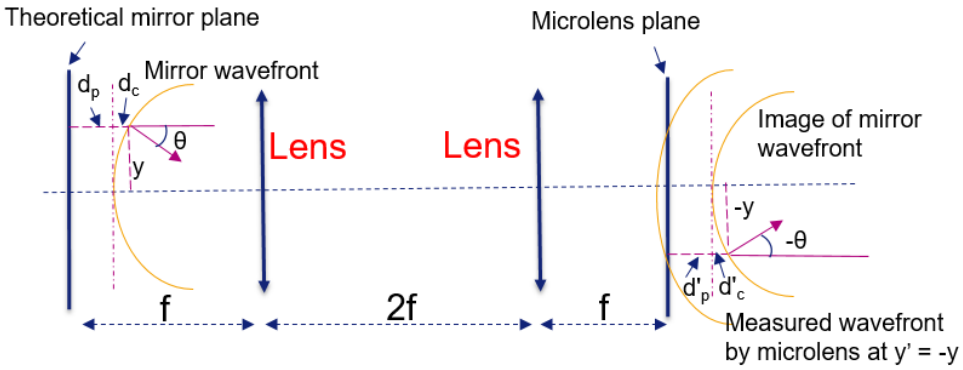

$$d(y) = d_p + d_c(y)$$
$$d'(y') = d'_p + d'_c(y')$$

Figure 7.2: Schematic of SHARPeR afocal system with defocus. (Afocal setup is simplified to two lenses for representation. Real instrument has more lenses with complex arrangement.)

In this section the effects of defocusing errors (mirror not placed in the focal plane), on the measured wavefront curvature are explained. The SHARPeR optical system is approximated to afocal system (ignoring the phase errors of all optical elements), as shown in Figure 7.2, with lenses separated by $2f$ and the mirror and microlens array are placed at distances f from lenses. The SHARPeR afocal system has 1:1 magnification. From the raytracing it can be observed that a point (y, θ) - at mirror position y with slope θ, is imaged at (-y, -θ) in microlens plane. The distance to microlens array is fixed but the test mirror may be placed slightly away from focal plane (by distance d). The offset of the mirror plane from focal plane could be from misalignments in mirror placement below optical head or piston errors from optical head stage translation. The defocus shift can be divided into two components, a constant shift d_p and a shift arising from mirror itself ($d_c(y)$). If the mirror is highly curved only few microlenses (e.g. microlens at the center of aperture) can be in focus, other microlenses measure slightly different curvature as shown in Figure 7.2. Assume the radius of the mirror R_o and the measured radius as R_m.

The afocal system theoretical framework developed by Mahajan in the book 'Optical Imaging and Aberrations: Ray geometrical optics' [127], in chapter 1.3.6 is used in the following discussion. The defocus shift in the image plane (d') is equivalent to the shift in mirror plane (d) for an afocal system with magnification of 1, which is equivalent to the difference in measured and actual radius of mirror as shown in eq.(7-13).

$$\Delta R = R_m - R_o = d'(y') = d(y)$$

$$\Delta R = d_p + d_c(y)$$

$$\Delta R = d_p + \frac{R_o \theta^2}{2}$$

(7-12)

The SHARPeR is designed to measure synchrotron mirrors with radius (R_o) above 1 m. Typically, radius values below 10 m are considered highly curved. The defocus errors (or piston errors) can be at worst a few millimeters and the slopes of the mirror usually do not reach larger than few milliradians. The SHARPeR instrument itself is limited to slope range ±4 mrad.

$$\frac{\theta^2}{2} \ll \frac{d_p}{R_o} \ll 1$$

(7-13)

For example, a mirror of 10 m radius and length 200 mm and a piston error of 10 mm has radius measurement errors (in ideal afocal system with no optical aberrations), as shown below

$$\frac{d_p}{R_o} = 1e - 3$$

$$\max(\theta) = \frac{0.1}{10} rad = 10\, mrad$$

$$\frac{\max(\theta)^2}{2} = 5e - 5$$

The defocus error from mirror curvature can be neglected, and assuming constant defocus error of 10 mm contributes a change in the measured radius of ~0.1 percent. The test mirror can be aligned to <1 µm accuracy using tool lens with <2 µm repeatability with RTT TZ axis. The optical head stage translation can generate piston errors <5 µm. In extreme case a 1.4 m mirror misaligned at 1 mrad tilt can create only 0.7 mm defocus at the edges (provided it is aligned to focal plane at the center). For most practical purposes the defocus errors can be considered much less than 10 mm value that was considered above.

APPENDIX 3: CCD DETECTOR

In this section, different errors from CCD such as readout noise, photon noise and their contribution to wavefront sensor slope measurement noise are presented. The CCD image sensor Kodak KAI -08050 specifications are shown in Figure 7.3.

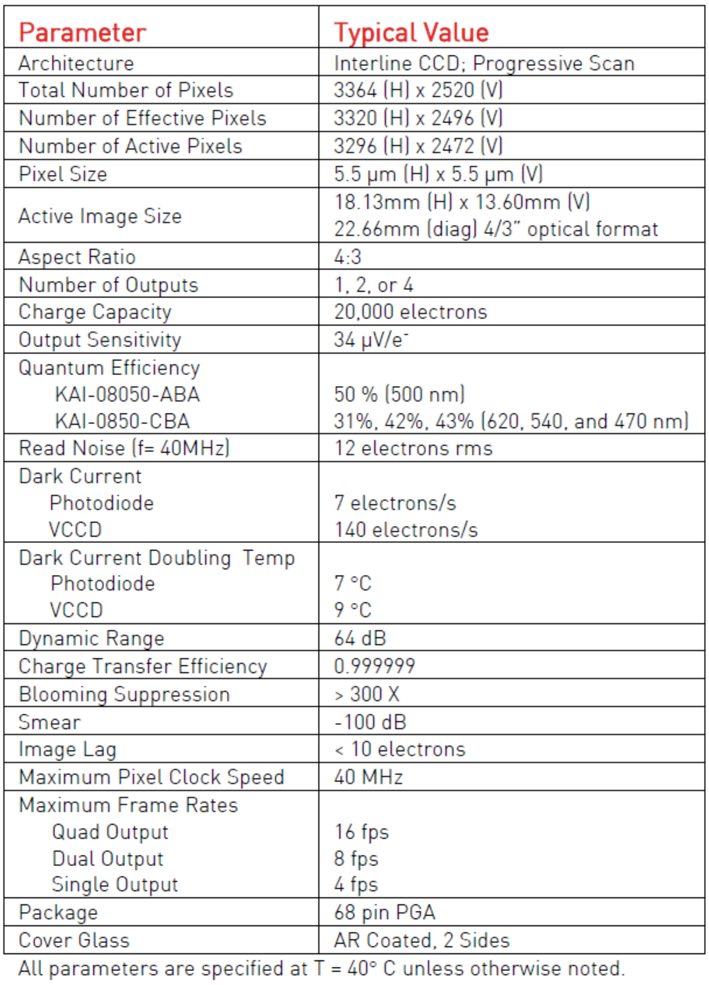

Parameter	Typical Value
Architecture	Interline CCD; Progressive Scan
Total Number of Pixels	3364 (H) x 2520 (V)
Number of Effective Pixels	3320 (H) x 2496 (V)
Number of Active Pixels	3296 (H) x 2472 (V)
Pixel Size	5.5 μm (H) x 5.5 μm (V)
Active Image Size	18.13mm (H) x 13.60mm (V) 22.66mm (diag) 4/3" optical format
Aspect Ratio	4:3
Number of Outputs	1, 2, or 4
Charge Capacity	20,000 electrons
Output Sensitivity	34 μV/e$^-$
Quantum Efficiency	
KAI-08050-ABA	50 % (500 nm)
KAI-0850-CBA	31%, 42%, 43% (620, 540, and 470 nm)
Read Noise (f= 40MHz)	12 electrons rms
Dark Current	
Photodiode	7 electrons/s
VCCD	140 electrons/s
Dark Current Doubling Temp	
Photodiode	7 °C
VCCD	9 °C
Dynamic Range	64 dB
Charge Transfer Efficiency	0.999999
Blooming Suppression	> 300 X
Smear	-100 dB
Image Lag	< 10 electrons
Maximum Pixel Clock Speed	40 MHz
Maximum Frame Rates	
Quad Output	16 fps
Dual Output	8 fps
Single Output	4 fps
Package	68 pin PGA
Cover Glass	AR Coated, 2 Sides

All parameters are specified at T = 40° C unless otherwise noted.

Figure 7.3 : Specifications of Kodak KAI – 08050 [128].

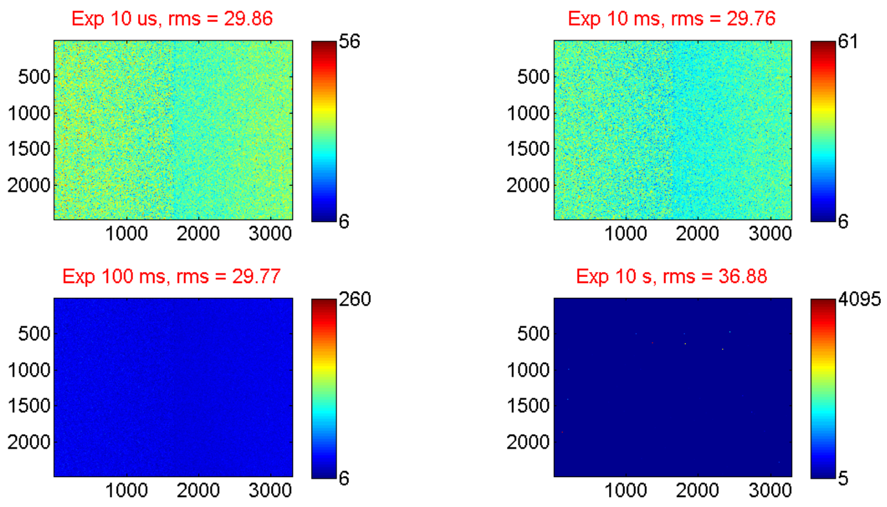

Figure 7.4 : CCD images in dark environment at exposures (a) 10 µs, (b) 10 ms, (c) 100 ms and (d) 10 s. Rms values shown in the plots refer to rms mean intensities of all pixels.

The saturation level of a pixel is 4095 in analogue to digital units (ADU) values which corresponds to charge capacity of 20,000 electron from CCD specifications shown in Figure 7.3. The dark current is 140 electrons/s and, based on the specifications ~143 seconds should be required to saturate a pixel, which is much larger than the standard operating exposures. The standard operating exposures during SHARPeR measurements ranges from 0.5 ms to 100 ms to which dark current noise should contribute typically 0.07 to 14 electrons. The dark current noise is comparable to the read-out noise of 12 electrons rms at 100 ms exposure.

The CCD images taken in a dark environment with little background light and without laser are shown in Figure 7.4, at different exposures. The rms mean of camera image intensities (rms of all pixels) at exposures 10 ms, 100 ms and 10 s are 29.76, 29.77 and 36.88 respectively. The read noise and dark current noise from specifications cannot explain the measured pixel noise values of 146 electrons (corresponding to intensity level 30), measured in a dark environment at different exposures below 1 sec, which may correspond to a significant background noise still present in the darkened room due to imperfect shielding of various extraneous light sources. Some of the measured pixel noise (of 146 electrons rms mean) could also be from non-zero offset for the ADU of the chip.

The SHARPeR CCD detector is imaged with the enclosure lighting on (but the laser still off) and the images at different exposures are shown in Figure 7.5. The images are taken with and without background image correction corresponding to exposures. The CCD images after background correction are very similar for exposures below 100 ms, as shown in Table 7.1, which corresponds to ~20 electrons rms (or ~4 intensity rms).

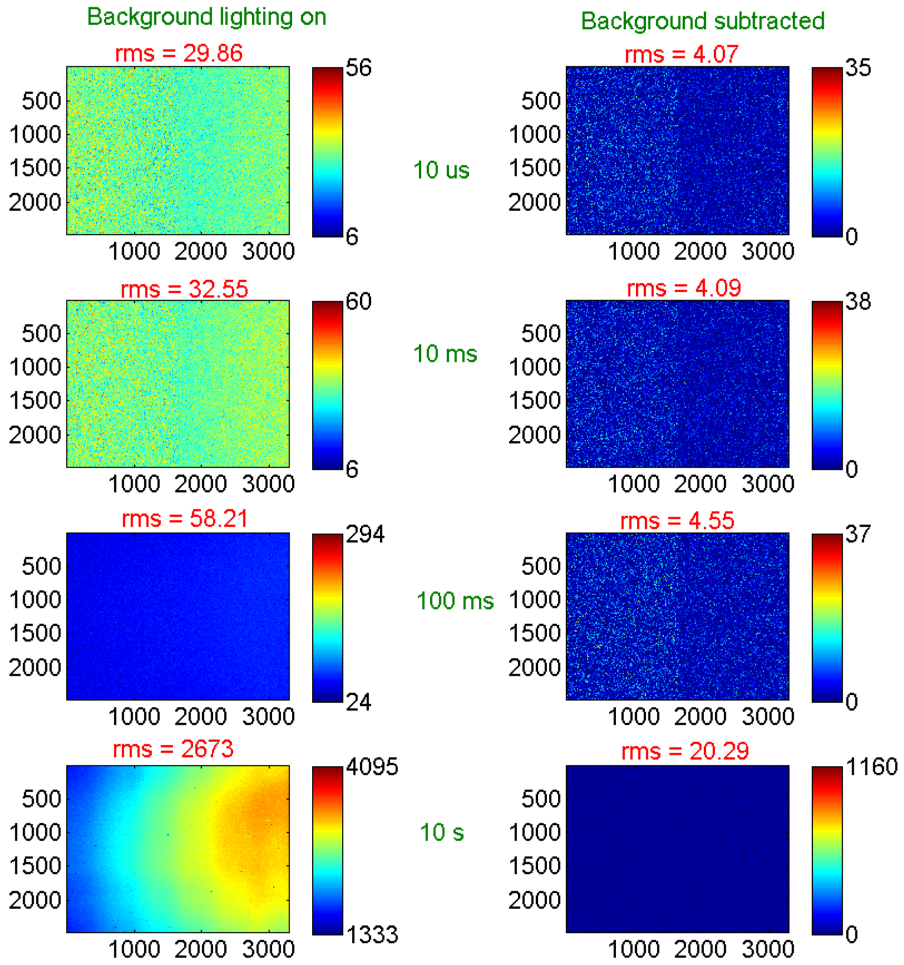

Figure 7.5 : CCD images with background lighting at different exposures with and without background subtraction (a) 10 µs, (b) 10 ms, (c) 100 ms, and (d) 10 s. The image rows denote different exposures (a, b, c, d) and columns with background (column 1) and without background (column 2).

Table 7.1 : CCD rms mean of intensities at different exposures

Exposure	Rms with background	Rms without background
10 μs	29.85	4.07
10 ms	32.55	4.09
100 ms	58.21	4.54
10 s	2673.00	20.30

Slope measurement noise analysis:

Slope noise from read noise:

The readout noise is taken as 20 electrons rms. The focal length (f) is ~300 mm and microlens size (d) is ~1.2 mm. The wavelength (λ) is 405 nm. The pixel size of CCD is 5.5 μm.

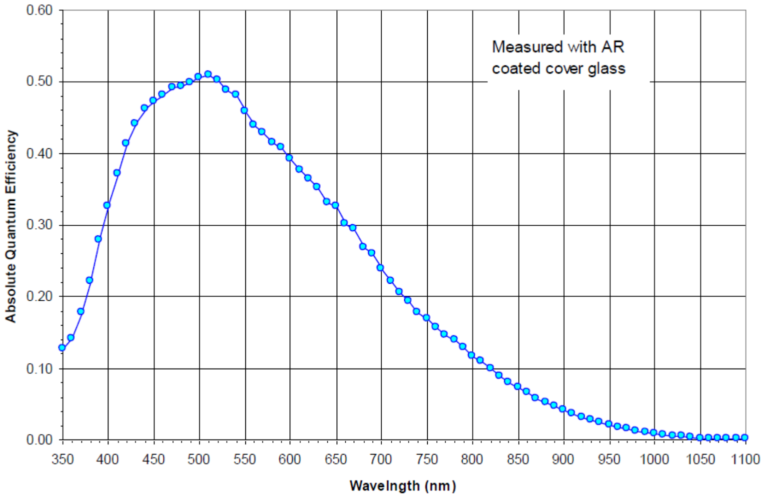

Figure 7.6 : Quantum efficiency of CCD pixels as a function of wavelength [128].

The quantum efficiency ($p2e$ - from Figure 7.6 at 405 nm) and electrons to digital intensity ($e2d$) are given by,

$$p2e = 0.32$$

$$e2d = \frac{20000}{4095} = 4.88$$

Assuming no voltage offset of the CCD ADC, the readout noise (from Table 7.1) in terms of electrons and photons is given by following.

$$\sigma_r = 20\ e^- = 62.5\, p$$

From Cao and Yu [81], corresponding error in centroid determination in X-direction from readout noise is given by,

$$\sigma_{X_{cr}}^2 = \frac{\sigma_r^2}{V^2} ML(\frac{L^2 - 1}{12} + 1.36\sigma_B^2)$$

Where σ_r is the readout noise, V is the total photon count within the microlens region on CCD (217 x 217 pixel grid), L and M are number of pixels in X and Y directions (L=M=217), and σ_B is the rms width of microlens spot for a square aperture which is given by [81] the following.

$$\sigma_B = 0.358\, \lambda\, F^{\#}$$

Where λ is the wavelength (405 nm), and $F^{\#}$ is the f-number of microlens which is given by focal length (f = ~300 mm) and microlens size (d= 1.2 mm) as following.

$$F^{\#} = \frac{f}{d} = \frac{300}{1.2} = 250$$

$$\sigma_B = 36.2475\ \mu m$$

The CCD image taken on a test mirror with acquisition near 90 percent of saturation level is shown in Figure 7.7 (only a few spots are shown). A single microlens spot within its full width at half maximum (FWHM) is shown in Figure 7.8. The FWHM is nearly 16 pixels, with each pixel of size 5.5 µm leads to FWHM of 88 µm. Using a Gaussian approximation for the spot width ($\sigma_{B,m}$ = FWHM / 2.35) is 37.45 µm which is close to the theoretical square aperture rms width.

In order to determine the total photon count within a microlens spot region on CCD, the background image intensity is subtracted and to exclude side lobes a threshold of 10 percent of maximum intensity is applied. The total intensity of all pixels above the threshold is divided by number of microlenses (= 164) to get microlens spot average intensity (V_d).

$$V = \frac{V_d}{e2d * p2e} = 1.52e7$$

The measured typical spot size after applying threshold is length (L) x width (M) of 26 x 26 pixels. The centroid noise is calculated by substituting

$$\sigma_{X_{cr}} = 0.0015\, pix = 8.33\, nm$$

This value contributes to a slope noise of,

$$\sigma_{S_r} = \frac{\sigma_{X_{cr}}}{f} = 28\, nrad$$

Slope noise from photon noise :

The centroiding noise from photon noise is given by [81],

$$\sigma_{X_{cp}} = \frac{\sigma_B}{\sqrt{V}} = 0.0019\, pix = \ 10.7\, nm$$

This value contributes to a slope noise of,

$$\sigma_{S_p} = \frac{\sigma_{X_{cp}}}{f} = 36\, nrad$$

The total slope noise from readout and photon noises is given below.

$$\sigma_S = \ \sqrt{{\sigma_{S_r}}^2 + {\sigma_{S_p}}^2} = 45.6\, nrad$$

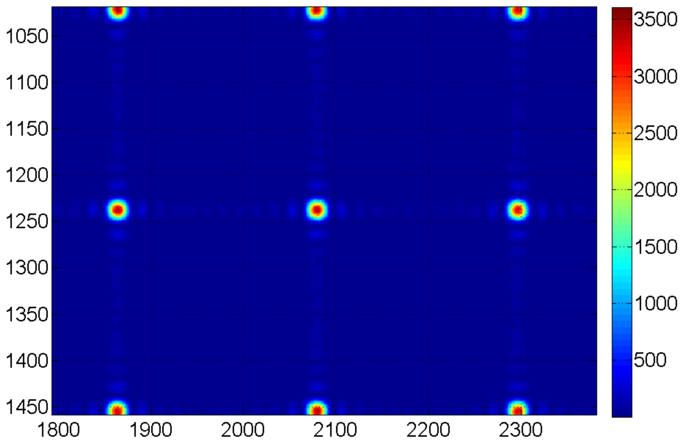

Figure 7.7 : CCD image on a mirror with microlens spots.

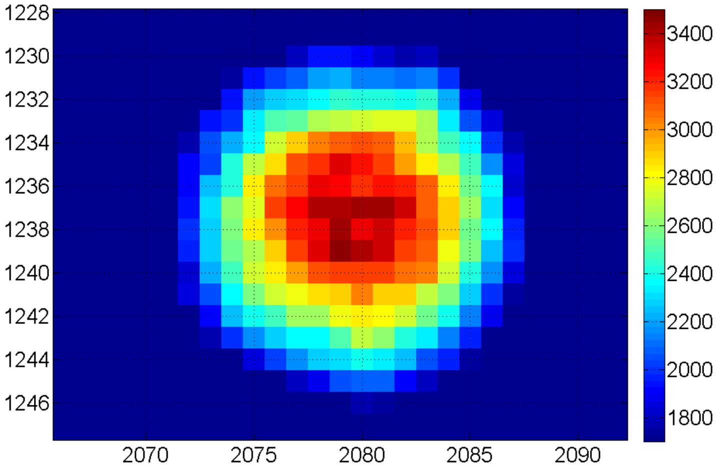

Figure 7.8 : Microlens spot within full width at half maximum (FWHM).

Appendix 4: Characterization of SHARPeR motion stages

The movements of the SHARPeR system as shown in Figure 7.9 were characterized using a standard Michelson interferometer, from the Precision Engineering Laboratory (PEL) at ESRF, made by HP (model 5530 Dynamic Calibrator) with linear accuracy of ±0.4 ppm and angular accuracy of ±0.2% measured value, ± 0.24 µrad/meter of traveled distance.

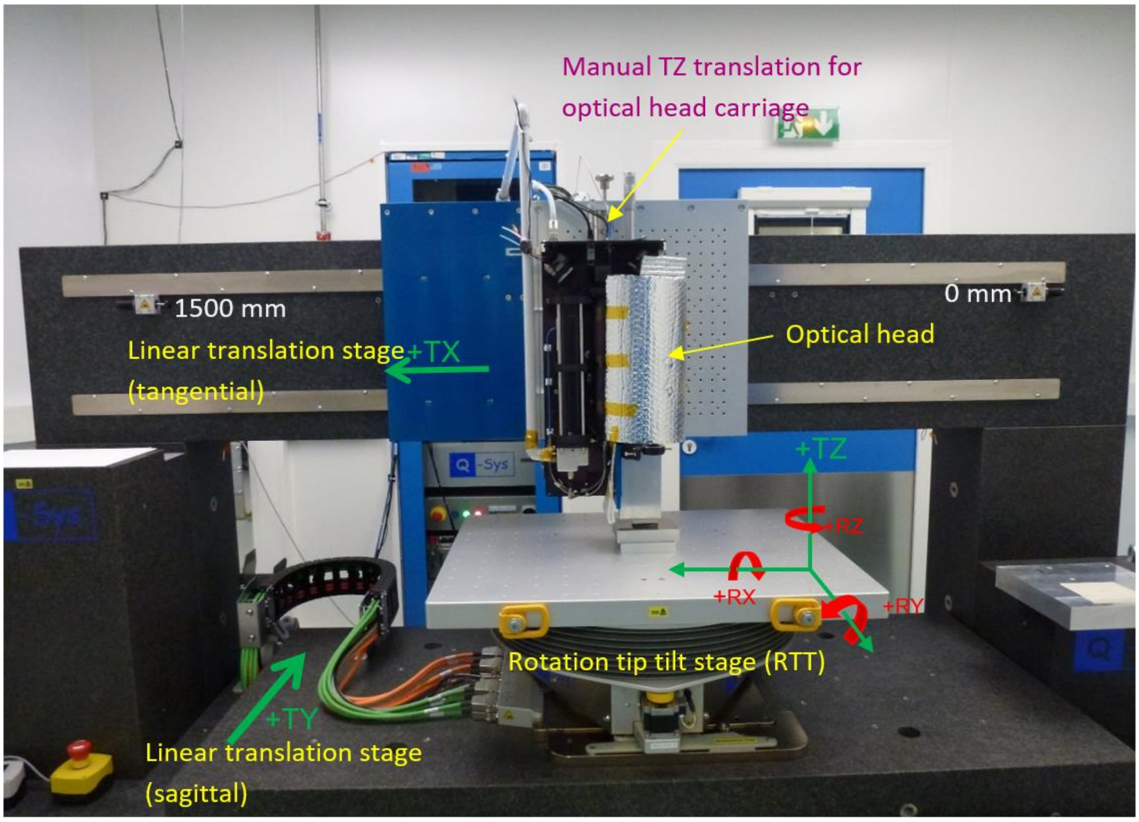

Figure 7.9 : SHARPeR instrument setup.

Linear translation stage TX (tangential):

Positioning errors during translation:

The interferometer was setup as shown in Figure 7.10 to measure the linear positioning error of tangential translation axis (TX). The corner cube reflector was positioned at approximately the same height as the linear encoder scale used in the position control of the TX movement thus minimizing potential Abbe measurement errors. The translation stage was moved from 1 mm to 1400 mm nominal positions in steps of 10 mm (step by step motion), in 3 bidirectional cycles. The zero position of interferometer was set at the zero-reference position of the TX axis.

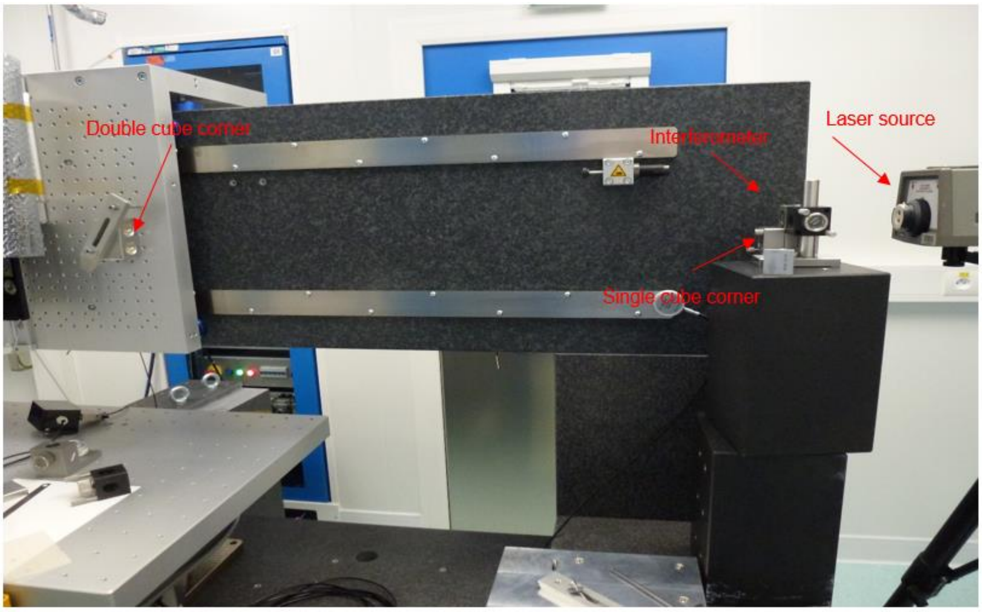

Figure 7.10 : Measurement setup of the linear positioning of TX axis.

The translation stage was moved to a given nominal position and after the motion was finished it was kept in place for three seconds to stabilize. Subsequently the interferometer readout was triggered with a TTL pulse from the SHARPeR motor controller. After a sleep time of 1s the stage was moved to next position. The measurements were recorded for 3 forward and 3 backward scans and the measured calibration errors are shown in Figure 7.11. The calibration error represents the measured stage position value of interferometer minus the nominal position. The errors are smaller than 4 µm peak to valley and the scans have a repeatability of 1.28 µm. The forward and backward scan means show small difference of 0.61 µm peak to valley. The measured accuracy and repeatability errors from the stage translation are much smaller than the wavefront sensor microlens size of ~1.2 mm. Stage positioning errors of few µm are ignored as the spatial frequencies under consideration are smaller than 1 mm^{-1} with SHARPeR.

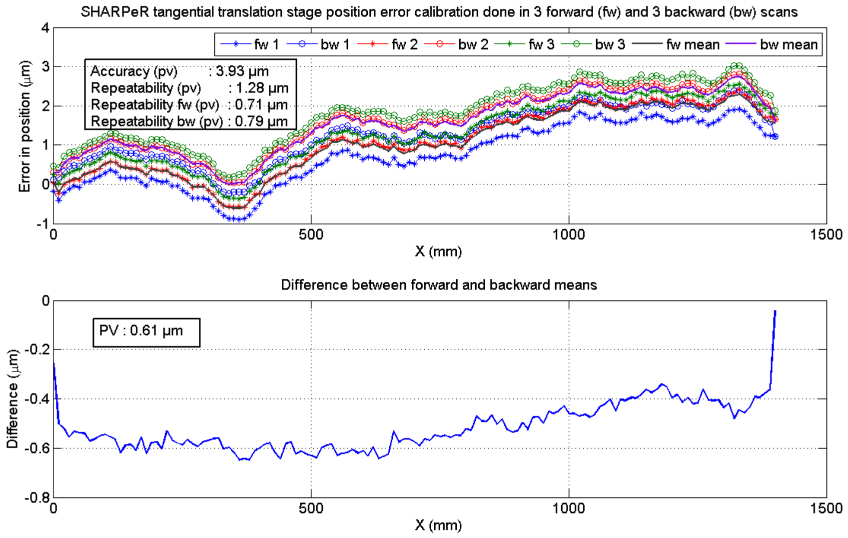

Figure 7.11 : SHARPeR translation stage (tangential) calibration errors in positioning within a range of 1 mm to 1401 mm in steps of 10 mm.

Pitch/roll/yaw errors during translation:

Interferometer is setup as shown in Figure 7.12 to calibrate pitch errors of tangential translation stage along TX axis. The double corner is set in vertical direction for pitch error calibration and in horizontal direction for yaw error calibration.

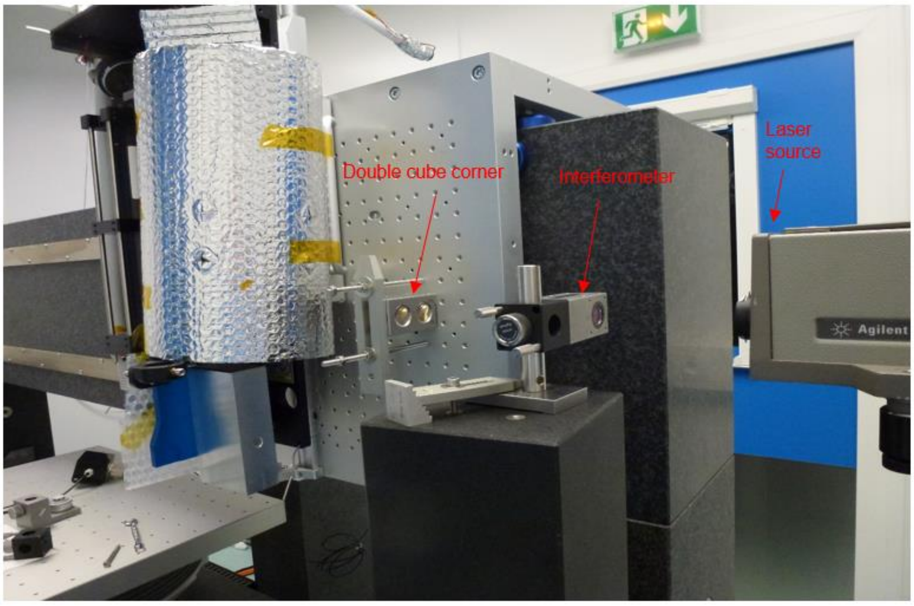

Figure 7.12 : Setup for characterization of the pitch and yaw errors of TX axis.

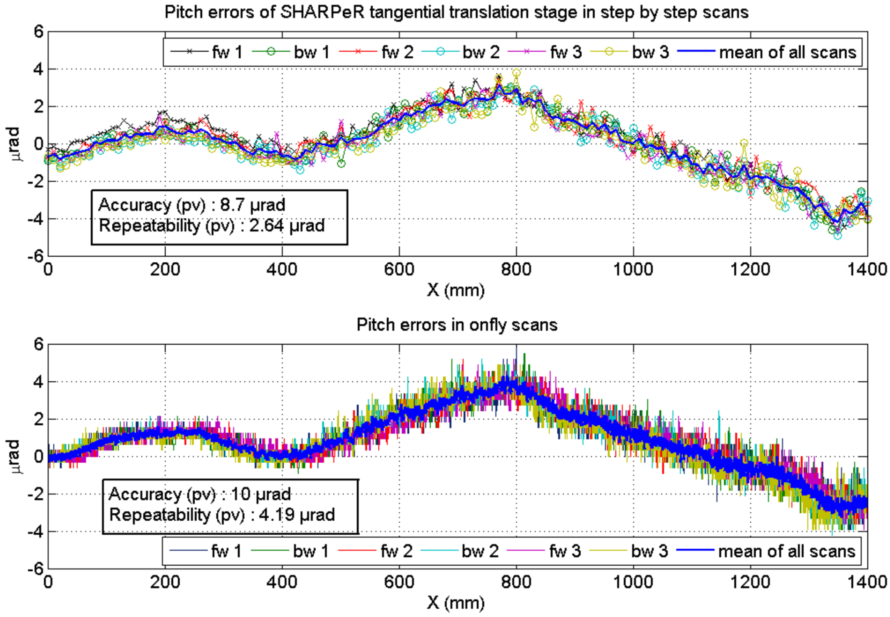

Figure 7.13 : SHARPeR tangential translation stage pitch errors calibration with three forward and three backward scans from 1 mm to 1401 mm in stepwise scans of step 10 mm. The scans are repeated in onfly mode within the same translation range and with 3 mm/s speed.

Figure 7.13 shows the pitch errors measured in stepwise and onfly modes. The stepwise mode measured three bidirectional scans with 10 mm step in the range of positions from 1 mm to 1401 mm. The onfly scans measured every 5 ms with a translation speed of 3 mm/s, i.e. step size of 15 µm, in the same range of positions from 1 mm to 1401 mm. Pitch errors are very similar in stepwise and onfly modes. The accuracy of SHARPeR translation stage for pitch errors is 8.7 µrad in stepwise scans and 10 µrad for onfly scans in the peak to valley terms. Repeatability is slightly worse for onfly scans with 4.19 µrad compared to stepwise with 2.64 µrad, however onfly scans have very high sampling rate. Reducing the sampling to 10 mm for onfly scans results in 8.5 µrad in accuracy and 3.13 µrad in repeatability. The measured onfly scans also have uncertainties in the scan start and end points as the interferometer clock is not synchronized to stage translation, which may be partially responsible for poor repeatability. Errors in yaw were also calibrated using same setup as pitch except with rotating the double cube corner into horizontal direction as shown in Figure 7.12. Calibration of roll errors were not possible with interferometer, and a Talivel electronic level instrument was used for roll error calibration as shown in Figure 7.14.

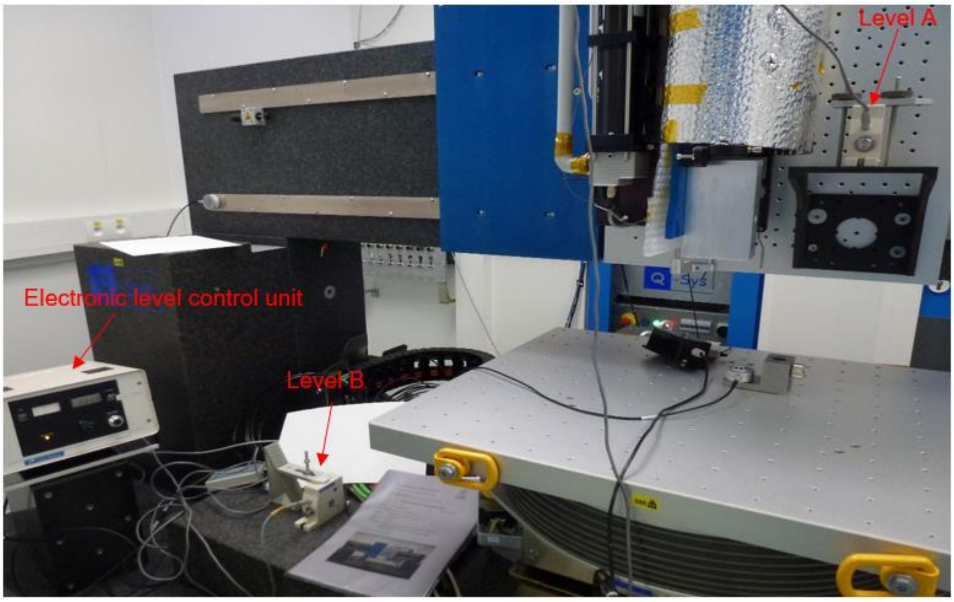

Figure 7.14 : Measurement setup for roll error calibration for SHARPeR tangential translation stage using a Talivel electronic level.

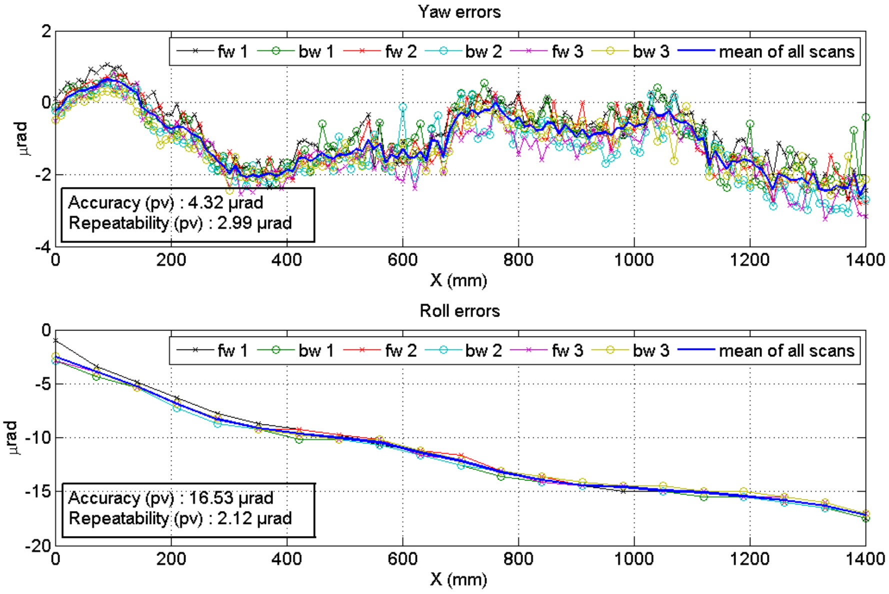

Figure 7.15 : SHARPeR tangential translation stage roll and yaw errors calibration over the length of 1 mm to 1400 mm. The yaw errors were measured in steps of 10 mm and the roll errors were measured in steps of 70 mm. In each case, three bidirectional scans were used in step-by-step mode.

The yaw errors of SHARPeR tangential translation stage, as shown in Figure 7.15, have accuracy of 4.32 µrad and repeatability of 2.99 µrad in peak to valley. The roll errors are much larger compared to pitch and yaw errors with an accuracy of 16.53 µrad and repeatability of 2.12 µrad in peak to valley. Pitch and roll errors are much larger than typical synchrotron mirror which have slope errors below 1 µrad and for high quality mirror slope errors are well below 0.1 µrad. SHARPeR can correct for pitch and roll errors significantly using stitching techniques whereas yaw errors are not corrected. Pitch and roll errors result in offsets in measured slopes in x and y which can be corrected by comparing the overlaps between successive subapertures. Yaw errors would cause in rotation of image and hence a shift in measurement area on the mirror. However, the shift in the farthest microlens from center (i.e. the four corner microlenses), at a maximum yaw error of 4.32 µrad results in a shift of 45 nm, which can be ignored.

Tilt stages (RX and RY):

Figure 7.16 shows the measurement setup for characterizing the angular accuracy of SHARPeR axes RX and RY for tilts along sagittal and tangential directions respectively. The Figure 7.16 shows setup for calibrating RY axis (tangential tilt) where the interferometer, laser and double corner were placed parallel to TX axis. To calibrate the RX axis the whole setup was placed parallel TY axis. The double corner was placed close to the center of Rotation Tip Tilt (RTT) platform.

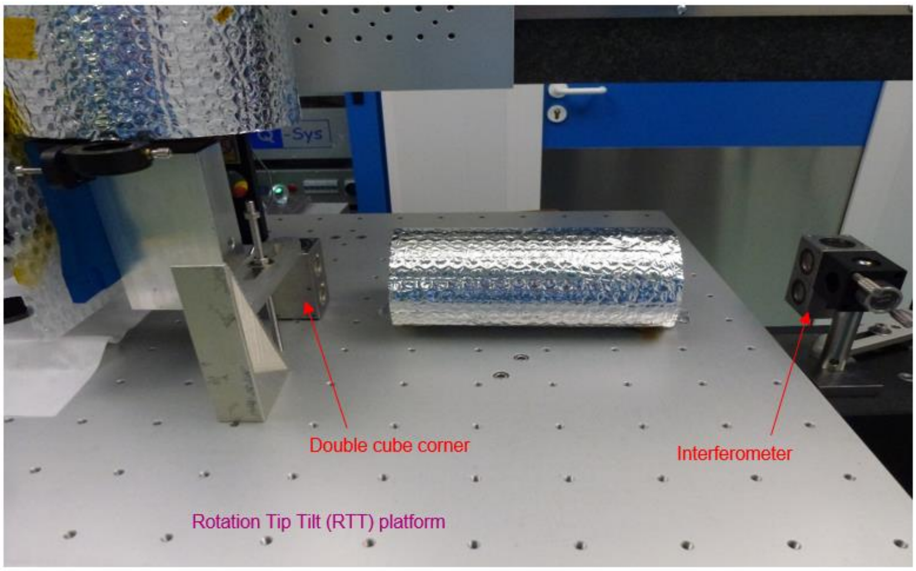

Figure 7.16 : Measurement setup of angular positioning for axes RX and RY.

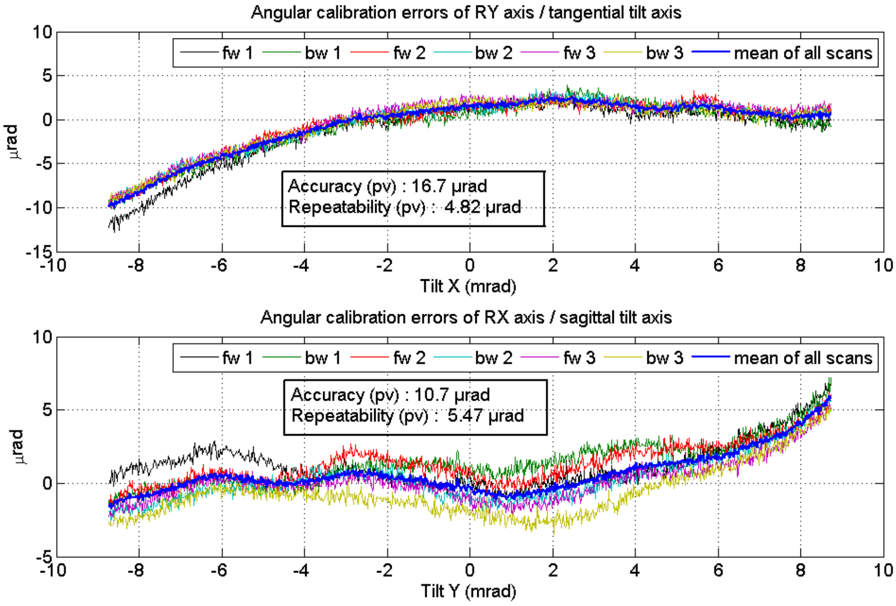

Figure 7.17 : SHARPeR angular calibration errors of RY (tangential) and RX (sagittal) axes of RTT platform. The stage was tilted from -8.7 mrad to 8.7 mrad (-0.5 to 0.5 deg), in steps of 17.45 µrad with 1001 points.

Figure 7.17 shows the angular errors of the RX and RY axes. The accuracy of RY (tangential) axis is 16.7 µrad and for RX (sagittal) axis is 10.7 µrad in peak to valley. The repeatability of RY (tangential) axis is 4.82 µrad and for RX (sagittal) axis is 5.47 µrad in peak to valley. Measurement of flat mirrors usually avoids using any of the SHARPeR motor axes except the tangential translation stage. RTT axes (RX, RY, RZ, and TZ) are usually used only for alignment of the mirror. However, for the measurement of curved mirrors such as spheres and ellipses, normal and multi-incidence techniques were developed which require tilting of RX and RY axes during scans. Angular errors of RX and RY axes in combination with pitch/roll errors of SHARPeR tangential translation stage will be effective tilt errors between subapertures in normal / multi-incidence measurements.

APPENDIX 5: ON THE FLY SCANS

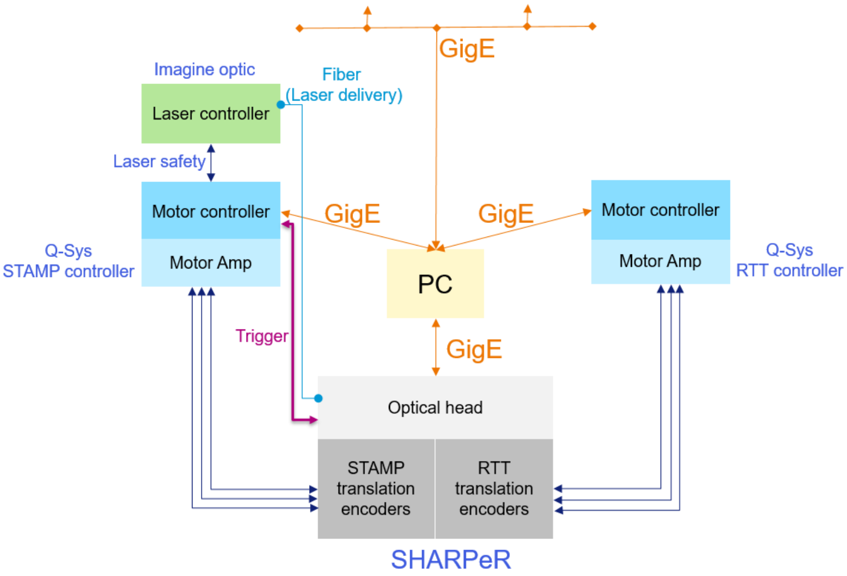

Figure 7.18 : Communication setup between PC, SHARPeR and Q-Sys Delta Tau controller.

The SHARPeR instrument control communication scheme is shown in Figure 7.18 and consists of three principal components (1) Windows 7 PC, (2) Q-Sys Delta Tau (DT) Power PMAC controllers (two controllers one each for STAMP and RTT), mainly for motion control and (3) SHARPeR motors, encoders and camera. Q-Sys controllers also control safety aspects of the system including emergency motor shutdown and laser shutdown. Q-Sys controllers also manage compressed air delivery to the air bearings. The communication channels are also shown in the Figure 7.18. The communications are bidirectional but can be initiated on only one side, from PC to Delta Tau, from Delta Tau to SHARPeR and from PC to SHARPeR. The communications between these different channels during step-by-step and onfly scans are shown in Figure 7.19 and Figure 7.20 respectively.

In the step-by-step mode, PC requests DT (Delta Tau controller) to move TX axis to a list of given positions in sequence. After each request, PC waits for the motion to finish by polling the current TX position, while DT performs motion in parallel. After the motion is finished, PC requests SHARPeR camera to capture and read image and waits until readout is finished (typically 0.3 sec). The camera images are processed for slopes which are saved to *.has files. This whole process continues until all subapertures in a scan are captured.

In the onfly mode, the TX axis is moved at a constant speed (typically 3 mm/s) for the whole scan range. A trigger cable from DT to SHARPeR camera is used which triggers based on positions. DT polls for current positions, and at each position from a predefined list, it sends trigger pulse. The SHARPeR camera captures image at the trigger pulse rising edge. As and when the trigger happens, the PC requests SHARPeR camera to read the captured image (typically ~0.3 sec exposure plus readout time). Later the camera image is processed for slopes, which are stored within the program memory (all the subaperture slopes are saved at the end of scan). PC requests DT whether the scan is finished, if not this process continues in a loop. A second loop runs on the DT in parallel and trigger pulses are generated at regular intervals based on the current position, and the two loops runs synchronously. Hence the scan speed is limited (to typically 3 mm/s for scan step of 1.2 mm), to give enough time for camera images to be read by PC.

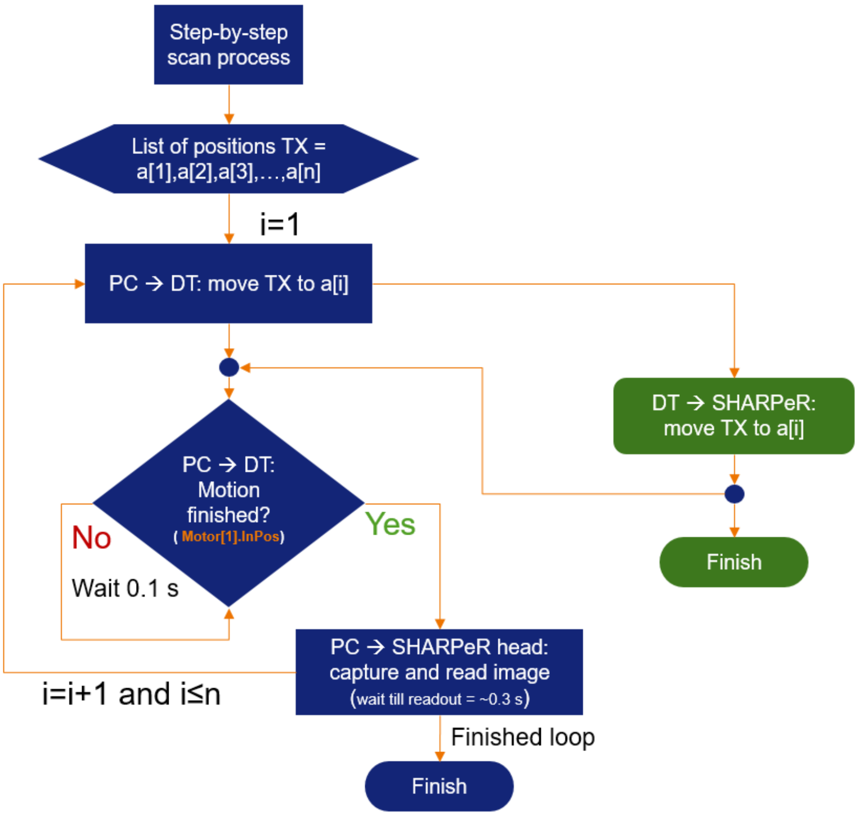

Figure 7.19 : Stepwise scan communication flowchart between PC, DT (delta tau controllers), SHARPeR (motors & encoders) and SHARPeR head (camera).

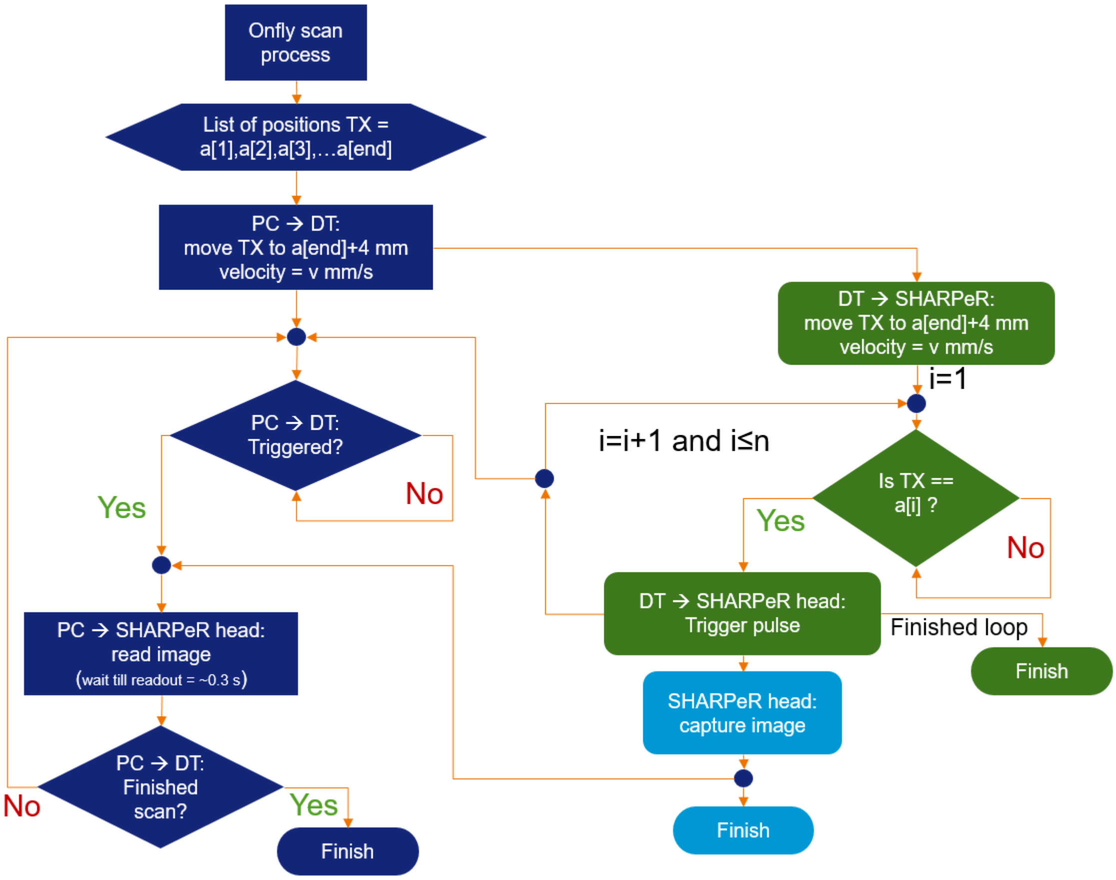

Figure 7.20 : Onfly scan communication flowchart between PC, DT (delta tau controllers), SHARPeR (motors & encoders) and SHARPeR head (camera).

APPENDIX 6: SHARPER DESIGN OPTIMIZATIONS (INTERMEDIATE)

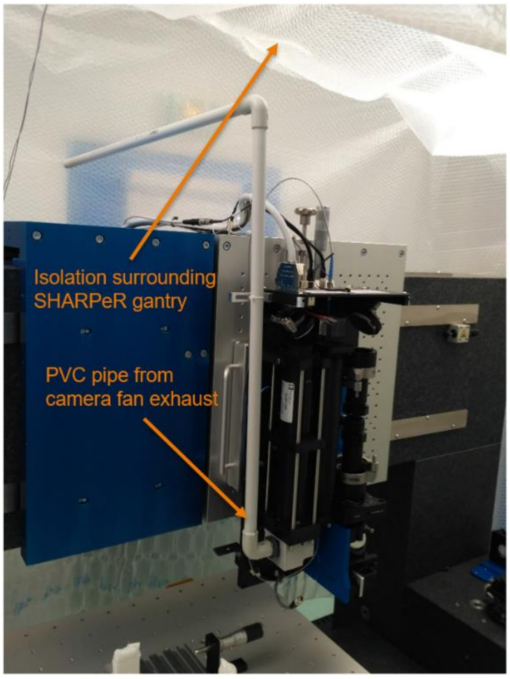

Figure 7.21 : SHARPeR design with no cover on the head, hot air extraction pipe from CCD fan, and insulation shielding SHARPeR from downward airflow from roof.

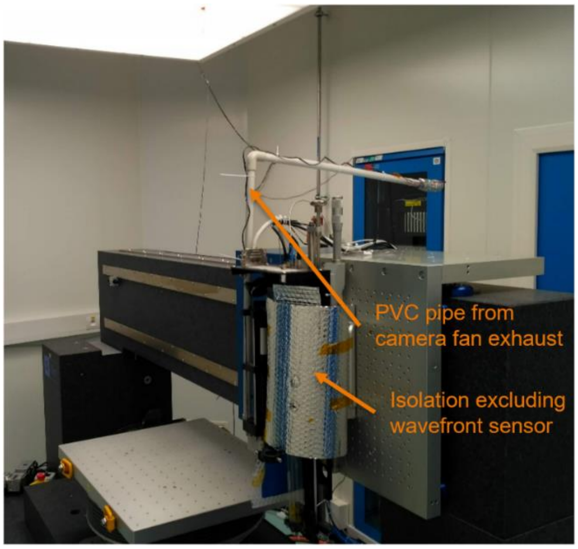

Figure 7.22 : SHARPeR design with insulation of optics without wavefront sensor, hot air extraction pipe from CCD fan and open airflow on SHARPeR from roof.

APPENDIX 7: TYPICAL MIRROR SPECIFICATIONS

A typical flat mirror is shown in Figure 7.23, which was designed by Carl Zeiss SMT and used by ESRF.

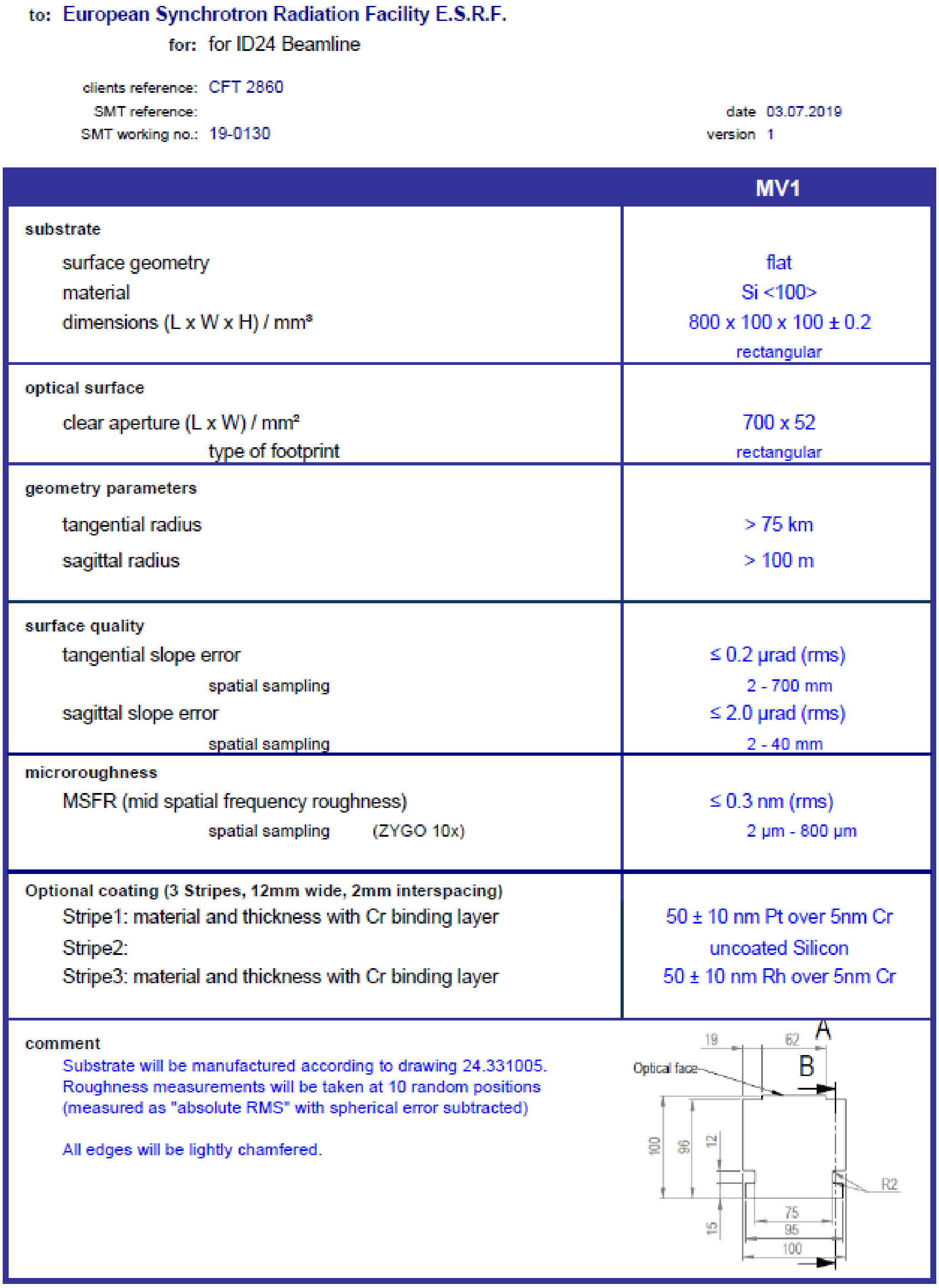

to: European Synchrotron Radiation Facility E.S.R.F.
for: for ID24 Beamline

clients reference: CFT 2860
SMT reference:
SMT working no.: 19-0130

date 03.07.2019
version 1

	MV1
substrate	
surface geometry	flat
material	Si <100>
dimensions (L x W x H) / mm³	800 x 100 x 100 ± 0.2 rectangular
optical surface	
clear aperture (L x W) / mm²	700 x 52
type of footprint	rectangular
geometry parameters	
tangential radius	> 75 km
sagittal radius	> 100 m
surface quality	
tangential slope error	≤ 0.2 µrad (rms)
spatial sampling	2 - 700 mm
sagittal slope error	≤ 2.0 µrad (rms)
spatial sampling	2 - 40 mm
microroughness	
MSFR (mid spatial frequency roughness)	≤ 0.3 nm (rms)
spatial sampling (ZYGO 10x)	2 µm - 800 µm
Optional coating (3 Stripes, 12mm wide, 2mm interspacing)	
Stripe1: material and thickness with Cr binding layer	50 ± 10 nm Pt over 5nm Cr
Stripe2:	uncoated Silicon
Stripe3: material and thickness with Cr binding layer	50 ± 10 nm Rh over 5nm Cr
comment Substrate will be manufactured according to drawing 24.331005. Roughness measurements will be taken at 10 random positions (measured as "absolute RMS" with spherical error subtracted) All edges will be lightly chamfered.	

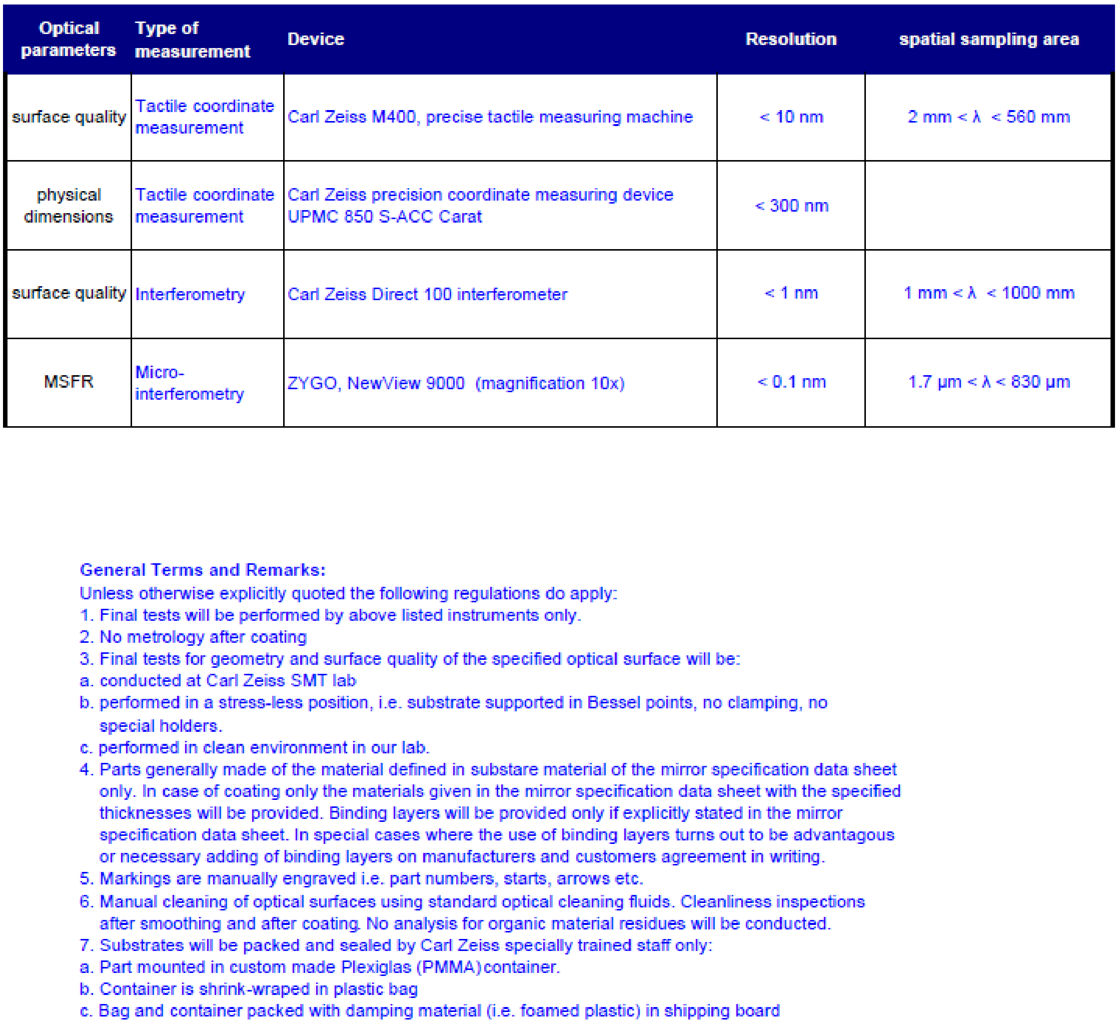

Optical parameters	Type of measurement	Device	Resolution	spatial sampling area
surface quality	Tactile coordinate measurement	Carl Zeiss M400, precise tactile measuring machine	< 10 nm	2 mm < λ < 560 mm
physical dimensions	Tactile coordinate measurement	Carl Zeiss precision coordinate measuring device UPMC 850 S-ACC Carat	< 300 nm	
surface quality	Interferometry	Carl Zeiss Direct 100 interferometer	< 1 nm	1 mm < λ < 1000 mm
MSFR	Micro-interferometry	ZYGO, NewView 9000 (magnification 10x)	< 0.1 nm	1.7 µm < λ < 830 µm

General Terms and Remarks:

Unless otherwise explicitly quoted the following regulations do apply:

1. Final tests will be performed by above listed instruments only.
2. No metrology after coating
3. Final tests for geometry and surface quality of the specified optical surface will be:

a. conducted at Carl Zeiss SMT lab

b. performed in a stress-less position, i.e. substrate supported in Bessel points, no clamping, no special holders.

c. performed in clean environment in our lab.

4. Parts generally made of the material defined in substare material of the mirror specification data sheet only. In case of coating only the materials given in the mirror specification data sheet with the specified thicknesses will be provided. Binding layers will be provided only if explicitly stated in the mirror specification data sheet. In special cases where the use of binding layers turns out to be advantagous or necessary adding of binding layers on manufacturers and customers agreement in writing.
5. Markings are manually engraved i.e. part numbers, starts, arrows etc.
6. Manual cleaning of optical surfaces using standard optical cleaning fluids. Cleanliness inspections after smoothing and after coating. No analysis for organic material residues will be conducted.
7. Substrates will be packed and sealed by Carl Zeiss specially trained staff only:

a. Part mounted in custom made Plexiglas (PMMA) container.

b. Container is shrink-wraped in plastic bag

c. Bag and container packed with damping material (i.e. foamed plastic) in shipping board

Figure 7.23 : Specifications of an 800 mm long flat mirror.

APPENDIX 8: ADDITIONAL RESULTS

i. Measurements on jtec flat mirror

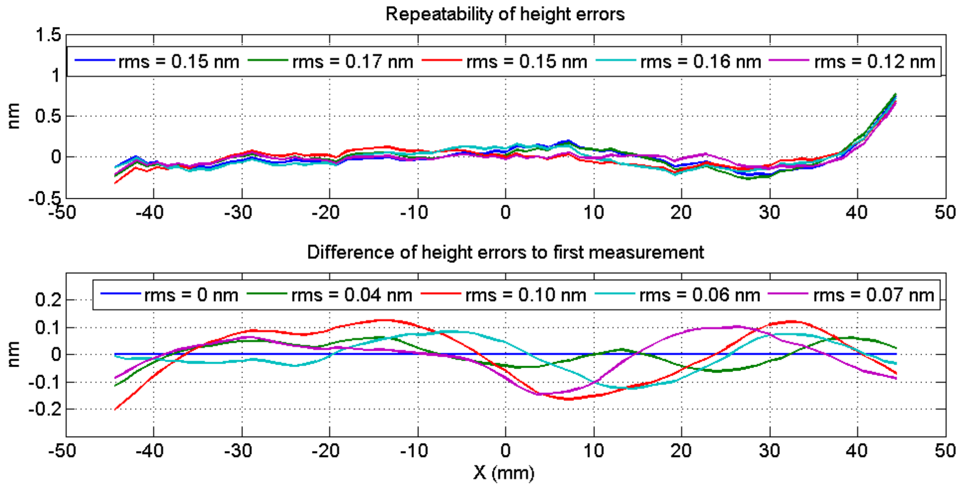

Figure 7.24: Height error repeatability on jtec flat mirror with five ABBA measurements each with 128 total scans.

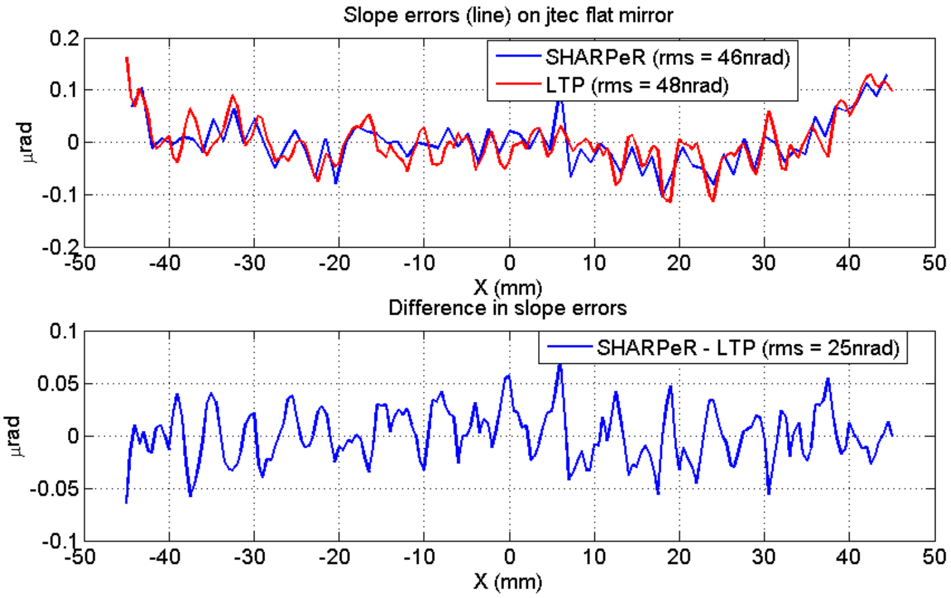

Figure 7.25 : Line slope errors comparison between SHARPeR and LTP.

ii. Measurements on Zeiss sphere

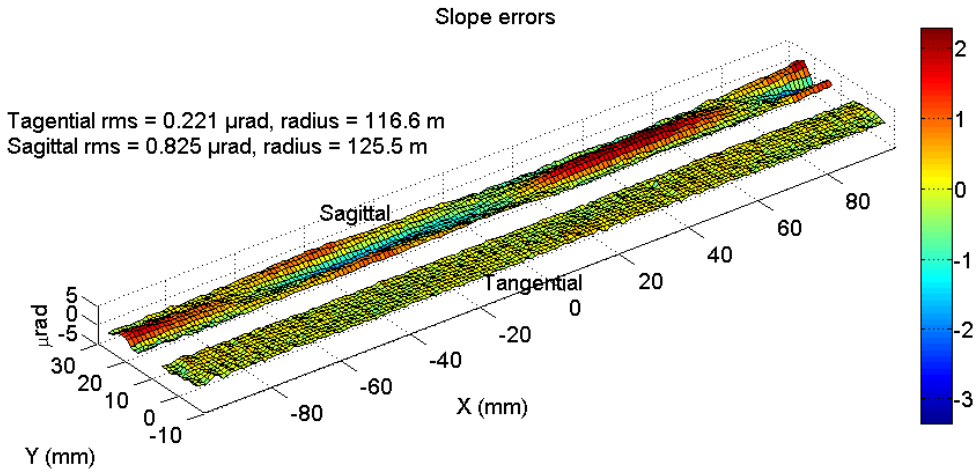

Figure 7.26 : SHARPeR ABBA average slope errors (2D) on the sphere measured in normal incidence.

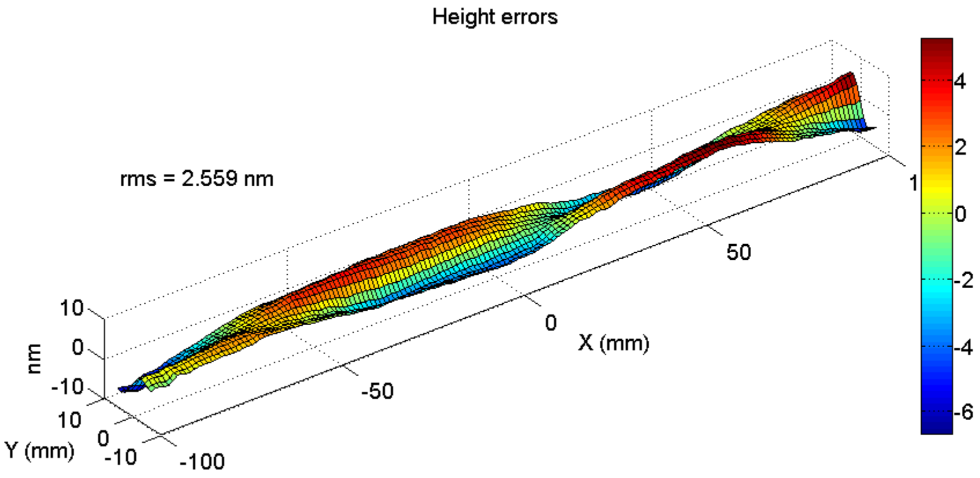

Figure 7.27 : SHARPeR ABBA average height errors (2D) on the sphere measured in normal incidence.